

**EXPERIMENTAL DETECTION OF ACTINIDES IN
HUMAN BODY AND COMPUTATIONAL
INVESTIGATIONS OF THEIR DECORPORATION
MECHANISM**

by

LOKPATI MISHRA

CHEM01201404006

BHABHA ATOMIC RESEARCH CENTRE

A thesis submitted to the

Board of Studies in Chemical Sciences

In partial fulfillment of the requirements

for the degree of

DOCTOR OF PHILOSOPHY

of

HOMI BHABHA NATIONAL INSTITUTE

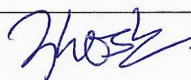
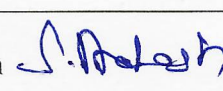
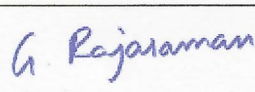
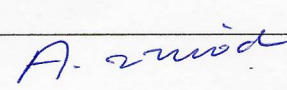
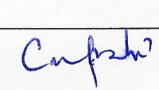
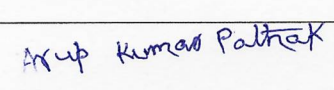


September 2020

Homi Bhabha National Institute¹

Recommendations of the Viva Voce Committee

As members of the Viva Voce Committee, we certify that we have read the dissertation prepared by Lokpati Mishra entitled "Experimental detection of actinides in human body and computational investigations of their decorporation mechanism" and recommend that it may be accepted as fulfilling the thesis requirement for the award of Degree of Doctor of Philosophy.

Chairman - Prof. S. K. Ghosh		Date: 17/9/2020
Guide / Convener - Prof T. Bandyopadhyay		Date: 17-9-2020
Co-guide/ if any Technology Adviser - Dr M. Sundararajan		Date: 17.9.2020
Examiner - Prof G. Rajaraman		Date: 17/09/20
Member 1- Prof Vinod Kumar A.		Date: 17/9/2020
Member 2- Prof C. N. Patra		Date: 17-09-2020
Member 3- Dr A. K. Pathak		Date: 17 09.2020

Final approval and acceptance of this thesis is contingent upon the candidate's submission of the final copies of the thesis to HBNI.

I/We hereby certify that I/we have read this thesis prepared under my/our direction and recommend that it may be accepted as fulfilling the thesis requirement.

Date: 17/09/2020

Place: Mumbai

Co-guide (if applicable)


<Signature> 17/9/20



<Signature>

Guide

¹ This page is to be included only for final submission after successful completion of viva voce.

STATEMENT BY AUTHOR

This dissertation has been submitted in partial fulfillment of requirements for an advanced degree at Homi Bhabha National Institute (HBNI) and is deposited in the Library to be made available to borrowers under rules of the HBNI.

Brief quotations from this dissertation are allowable without special permission, provided that accurate acknowledgment of source is made. Requests for permission for extended quotation from or reproduction of this manuscript in whole or in part may be granted by the Competent Authority of HBNI when in his or her judgment the proposed use of the material is in the interests of scholarship. In all other instances, however, permission must be obtained from the author.

September 2020



LOKPATI MISHRA

DECLARATION

I, hereby declare that the investigation presented in the thesis has been carried out by me.
The work is original and has not been submitted earlier as a whole or in part for a degree
/ diploma at this or any other Institution / University.

September 2020



LOKPATI MISHRA

List of Publications arising from the thesis

Publications in Refereed Journal:

a. Published

1. Equilibrium MD simulation of Cm (III) and Th (IV) release from Human Transferrin binding cleft at endosomal pH; Lokpati Mishra, Mahesh Sundararajan and Tusar Bandyopadhyay; Proteins, 2020, accepted.
2. Molecular Dynamics Simulations of Plutonium Binding and its Decorporation from the Binding-Cleft of Human Serum Transferrin; Lokpati Mishra, Mahesh Sundararajan and Tusar Bandyopadhyay; J. Biol. Inorg. Chem., 2020, 25, 213–231.
3. Binding of Cm (III) and Th (IV) with Human Transferrin at Serum pH: Combined QM and MD Investigations; Lokpati Mishra, Pramilla Damodar Sawant, Mahesh Sundararajan and Tusar Bandyopadhyay; J. Phys. Chem. B, 2019, 123, 2729–2744.
4. Quantum chemical studies of structures and spin Hamiltonian parameters of iron transferrin using isolated and embedded clusters models; Lokpati Mishra, M Sundararajan J. Chem. Sci. 2019, 131, 15.
5. Comparing lungs, liver and knee measurement geometries at various times post inhalation of ^{239}Pu and ^{241}Am ; Lokpati Mishra, I. S. Singh, H. K. Patni, D. D. Rao Radiat. Prot. Dosim. 2018, 181, 168–177.
6. Applying low energy HPGe detector gamma ray spectrometric technique for the evaluation of Pu/Am ratio in biological samples; I.S. Singh, Lokpati Mishra, J. R. Yadav, M.Y. Nadar, D. D. Rao and K.S. Pradeepkumar; Appl. Radiat. Isot. 2015, 104, 49–54.

Other Publications:

a. Conference/Symposium

1. Molecular dynamics and metadynamics study for binding and decorpoartion of plutonium in serum transferrin; Lokpati Mishra, P. D. Sawant, and Tusar Bandyopadhyay, presented at Workshop and Symposium on Advanced Simulation Methods: DFT, MD and Beyond, ASM2019 held at IIT Delhi, New Delhi, India during March 6-10, 2019.
2. Binding of Th (IV) and Cm (III) with 3,4,3, (1-2) LiHOPO: A Density Functional Theory Study; Lokpati Mishra, Mahesh Sundararajan, P. D. Sawant, Journal of Radiation and Cancer Research 9 (1), 48-64.
3. Estimation of cross talk between lungs and liver for ^{241}Am using phoswich detector; Lokpati Mishra, M Y Nadar, IS Singh, PD Sawant - Proceedings of the 33rd IARP international conference, IARPIC2018, held at DAE convention centre, Anushaktinagar, Mumbai during January 16-18, 2018, p 228.
4. Uncertainty in lung activity estimation of ^{241}Am due to angular variation in Phoswich and HPGe array detector; MY Nadar, J Chakraborty, Lokpati Mishra, IS Singh, Pramilla D Sawant, Proceedings of the 33rd IARP international conference, IARPIC2018, held at DAE convention centre, Anushaktinagar, Mumbai during January 16-18, 2018, p 229.
5. Experience with HPGe detector-based actinide lung monitoring system; Singh, I.S., Nadar, M.Y., Mishra, Lokpati, Kalyan, G.N. Proceedings of the 33rd IARP international conference, IARPIC2018, held at DAE convention centre, Anushaktinagar, Mumbai during January 16-18, 2018, p 224.
6. Standardization of actinide lung monitor for broad energy spectrum; Lokpati Mishra, IS Singh, DD Rao - Proceedings of the 13th DAE-BRNS nuclear and radiochemistry symposium, NUCAR2017 held at KIIT Bhubaneswar (India) during February 6-10, 2017, p 670-671.
7. A methodology for estimation of ^{241}Pu in biological samples by low energy HPGe detector; Lokpati Mishra, IS Singh, S Anilkumar, DD Rao - Proceedings of the 7th DAE-BRNS biennial symposium on emerging trends in separation science and technology, SESTEC2016 held at IIT-Guwahati, India during May 17-20, 2016, p 191.

Lokpati Mishra

8. In-vivo measurement of Pu/Am activity in liver using an array of HPGe detector; Lokpati Mishra, IS Singh, DD Rao - Proceedings of the 32nd IARP international conference, IARPIC2016 held at IGCAR, Tamilnadu, during February 22-25, 2016, p 95.
9. Comparison of counting efficiencies of phoswich detector using various realistic thorax phantoms for ²⁴¹Am; MY Nadar, Lokpati Mishra, IS Singh, DD Rao - Proceedings of the 32nd IARP international conference, IARPIC2016 held at IGCAR, Tamilnadu during February 22-25, 2016, p 210.
10. Quantum chemical studies for the binding of Am (III) and Pu (IV) with transferrin protein; Lokpati Mishra, Sadhu B. and Sundararajan M., Proceedings of DAE BRNS symposium on Multiscale Modelling of Materials and Devices symposium, MMMD2014 held at BARC, Mumbai during October 30 - November 2, 2014, p116.
11. Binding of Th (IV) & Cm (III) with transferrin protein: A DFT study; Lokpati Mishra, Sundararajan M. and D. D. Rao, presented at theoretical chemistry symposium, TCS2014 held at CSIR-NCL, Pune during December 18- 21, 2014.
12. Measurement of contribution of radioactivity in Liver to Lung; Lokpati Mishra, I. S. Singh, Minal Nadar, G. N. Kalyane and D. D. Rao, Book of abstracts of DAE-BRNS fifth symposium on nuclear analytical chemistry, NAC-V held at BARC, Mumbai during January 20-24, 2014, p160.
13. Assessment and Determination of Inhomogeneous distribution of Pu/Am in Lungs; I.S. Singh, L. Mishra, M. Y. Nadar, D. D. Rao and K. S. Pradeepkumar, Proceedings of 31st IARP national conference, IARPNC2014 held at BARC, Mumbai during March 19-21, 2014, p 138.
14. In-vivo Measurement of Pu/Am activity in liver using phoswich detector; Lokpati Mishra, I. S. Singh, Minal Nadar, D. D. Rao and K.S. Pradeepkumar, Proceedings of 31st IARP national conference, IARPNC2014 held at BARC, Mumbai during March 19-21, 2014, p 120.

Lokpati Mishra

Dedicated to my Parents, Parents-in-law, Wife and Sons

ACKNOWLEDGEMENTS

Today I have great pleasure in achieving one of my life goals, completing PhD thesis, as it was very challenging and difficult for me to finish this journey. I would like to acknowledge the help, guidance, support and encouragement of all the people who have immensely contributed in making it possible. I am thankful to the Almighty God for successful PhD journey and everything happening in my life.

At first, it is my great privilege to acknowledge my Guru (my guide), Dr. Tusar Bandyopadhyay who has shown me the path to achieve this goal. I am thankful to my technology advisor Dr. Mahesh Sundararajan from the bottom of my heart who helped in each and every step of this journey. Both of them have introduced me several methods in computational chemistry *viz.* Density functional theory, molecular dynamics, metadynamics, umbrella sampling, hydrogen bond and water bridge dynamics so-and-so on. Their guidance always kept me motivated and immensely helped throughout this journey. I can not pay off for their precious time they have given to listen my ideas and removing all the hurdles by putting sincere efforts and sharing their experiences.

I would like to thank Shri R. M. Suresh Babu, Associate Director, Health, Safety and Environment Group (HS&EG) and Dr. K. S. Pradeepkumar, Ex-Associate Director, HS&EG for motivating me to complete PhD. I would like to take this opportunity to thank Shri Probal Chaudhury, Head RSSD, BARC for his moral support and continuous encouragement. I would also thank to Dr. D. D. Rao, Ex-Head, IDS, RSSD for his support. I am fortunate and thankful to Dr. P. D. Sawant, Head IDS, RSSD, and Dr. I. S. Singh, RSSD for creating beautiful working environment in the lab and for providing their positive thoughts, support and motivation to make the journey enjoyable.

This thesis was never possible without availability of ANUPAM parallel computing facility in BARC and HBNI. My special thanks to Shri Vaibhav Kumar, CD, BARC for their spontaneous help in running the simulation jobs and software related help.

I sincerely acknowledge the respected members of doctoral committee Prof. S. K. Ghosh, Prof. C. N. Patra, Prof. Vinod Kumar A., Prof. C. Majumdar and Dr. A. K. Pathak for their critical comments during annual review and pre-synopsis presentation, which helped immensely in upgrading the level of research work. I would also like to thank my colleague Dr. M. Y. Nadar, Shri H. K. Patni, Shri R. Sankhla, Shri D. K. Akar and Dr. B. Sadhu, Prof. S.K. Ghosh, Ex-Head TCS, BARC for their selfless moral

support and fruitful discussion throughout the PhD. thesis work.

I would like to express my heartiest gratitude to my parents Shri Shivakant Mishra and Smt Sudha Mishra for giving me complete freedom in choosing my career and their endless love and blessings which helped me a lot to keep focus on my life goals. I can not forget my parents-in-law specially Dr. T. N. Dubey who always encouraged and motivated me for the thesis. My special thanks to my wife Pratiksha who was always there like pillar of support to pursue my dreams. During this PhD journey there were several occasions when I was not sure about completing the thesis, but she always helped and supported like anything. I am thankful to her and both of my kids because I was unable to give my full attention and time which they deserved. Thank you all from the bottom of my heart.

September 2020


LOKPATI MISHRA

Synopsis	ix
List of Abbreviations	xxvii
List of Figures	xxix
List of Tables	xxxvii
1 Introduction to <i>In-vivo</i> Detection of Actinides and <i>In-Silico</i> Investigations of their Decorporation	1
1.1 BASICS OF INTERNAL DOSIMETRY	3
1.2 MIRD METHODOLOGY FOR INTERNAL DOSE ESTIMATION	8
1.2.1 Specific effective energy SEE(T←S)	8
1.2.2 Number of transformations in source organs, $U_s(50)$	9
1.2.3 Committed equivalent dose	10
1.2.4 Committed effective dose	10
1.2.5 Dose coefficient	11
1.2.6 Annual limit on intake (ALI)	11
1.3 MATHEMATICAL SOLUTION OF A BIOKINETIC MODEL	12
1.4 In-vivo Method	14
1.5 PRACTICAL APPROACH FOR CED ESTIMATION	15
1.5.1 Estimation of activity	15
1.5.2 Estimation of intake	16
1.5.3 Estimation of committed Effective Dose	16
1.6 DECORPORATION OF ACTINIDES	18
1.6.1 Drug development process	19
1.6.2 Serum transferrin	21
1.7 MULTI-SCALE MODELLING	22

List of Contents

1.8	DENSITY FUNCTIONAL THEORY (DFT)	23
1.8.1	Hohenberg and Kohn theorems	25
1.8.2	Kohn-Sham equations	26
1.8.3	Various approximations for exchange correlation functional	27
1.8.4	Self-consistent way for DFT	29
1.8.5	Basis set	31
1.8.5.1	Contracted Gaussian-type orbitals (<i>CGTOs</i>)	32
1.8.5.2	Designations of basis set size	32
1.8.5.3	Diffuse functions	33
1.8.5.4	Polarization functions	33
1.8.5.5	Split valence basis set	34
1.8.5.6	Pople-style basis set	35
1.8.5.7	Basis sets of Ahlrichs and Karlsruhe	36
1.8.6	Effective core potential	36
1.8.7	Solvation effects	37
1.9	MOLECULAR DYNAMICS	38
1.9.1	The ergodic hypothesis	38
1.9.2	Newton's second law	40
1.9.3	Potential energy function	41
1.9.3.1	E_{bonded}	41
1.9.3.2	$E_{\text{non-bonded}}$	43
1.9.4	Periodic boundary conditions	43
1.9.5	Setting up and running a molecular dynamics simulation	45
1.10	ENHANCED SAMPLING METHODS	47
1.10.1	Metadynamics	48
1.10.2	Well tempered metadynamics	48
1.10.3	Umbrella sampling simulations	50
1.10.4	Hydrogen bond and water bridge correlation functions	51
1.11	OBJECTIVE AND OUTLINE OF THE THESIS	52
2	Quick Estimation of Pu/Am in Biological Samples using Low Energy HPGe Detector	54
2.1	INTRODUCTION	56
2.2	MEASUREMENT TECHNIQUES	60
2.2.1	Measurement of photons	60
2.2.2	Calibration of the system	60
2.2.2.1	Determination of Pu/Am activity	61
2.2.3	Procedure of biological sample analysis	62
2.2.4	Determination of MDA	63

List of Contents

2.3	RESULTS AND DISCUSSION	63
2.3.1	Estimation of depth of activity embedded in the sample	63
2.3.2	Measurement of embedded Pu/ ²⁴¹ Am activity	68
2.3.3	Quick estimation of ²⁴¹ Pu in biological samples	70
2.3.3.1	Correcting interference due to ²⁴¹ Pu in measurements for ²³⁹ Am	72
2.4	CONCLUSIONS	74
3	Optimum Measurement Geometry for <i>In-vivo</i> Assessment of ²³⁹Pu/²⁴¹Am	76
3.1	INTRODUCTION	78
3.2	MEASUREMENT TECHNIQUES	80
3.2.1	Measurement of photons	80
3.2.2	The efficiency and MDA	81
3.2.2.1	Method of in-vivo measurement of ²³⁹ Pu and its intake estimation	82
3.2.3	Computer software used for computations of organ contents of ²³⁹ Pu and ²⁴¹ Am	84
3.3	RESULTS AND DISCUSSION	85
3.3.1	Cross – talk between ²⁴¹ Am in lungs, liver and skeleton.	87
3.3.2	Estimation of CED using ICRP-66 HRTM, ICRP-30 GI tract model and ICRP 67 biokinetic model of Pu and Am at MDA level of ²⁴¹ Am measured in lungs, liver and skeleton.	87
3.3.3	Effect of revised HRTM, HATM and Leggett’s systemic biokinetic model of Plutonium on intake estimation.	91
3.3.4	Estimation of intake and CED from in-vivo measurement after acute inhalation intake of ²⁴¹ Am.	92
3.4	CONCLUSIONS	95
4	Quantum Chemical Studies of Iron Transferrin	97
4.1	INTRODUCTION	99
4.2	COMPUTATIONAL STRATEGY	101
4.3	RESULTS AND DISCUSSION	103
4.3.1	Gas phase vs. embedded optimized geometries	103
4.3.2	MB and EPR spin Hamiltonian parameters	104
4.4	CONCLUSIONS	108

List of Contents

5	Multi-scale Modeling for Binding of Cm(III) and Th(IV) with sTf at Serum pH	109
5.1	INTRODUCTION	111
5.2	METHODS	115
5.2.1	Molecular dynamics study	116
5.2.2	Well-tempered metadynamics	120
5.2.3	Quantum mechanical study	121
5.3	RESULTS AND DISCUSSION	123
5.3.1	Protein in closed conformation	123
5.3.2	Structural analysis of An-loaded sTf binding cleft	126
5.3.2.1	Water penetration into the binding cleft.	126
5.3.2.2	Coordination sphere of Th (IV), Cm(III) in the cleft.	127
5.3.2.3	Swapping of An ions in the sTf binding cleft.	133
5.3.3	The binding and exchange energetics of metal ions at the cleft	137
5.3.3.1	Ion binding :	137
5.3.3.2	Ion exchange energetics with DFT calculations	141
5.4	CONCLUSIONS	146
6	Equilibrium MD Simulations for Binding of Cm(III) and Th(IV) with sTf at Endosomal pH	147
6.1	INTRODUCTION	149
6.2	METHODS	154
6.2.1	Molecular dynamics	154
6.2.2	Umbrella sampling simulations	156
6.2.3	Hydrogen bond and water bridge correlation functions	157
6.3	RESULTS AND DISCUSSIONS	157
6.3.1	Structure and dynamics of the An-sTf systems.	158
6.3.2	Water penetration into the binding cleft.	165
6.3.3	Actinide release and their potential of mean force.	167
6.4	CONCLUSIONS	174
7	<i>In-silico</i> Investigations for Pu(IV) Binding and its Decorporation from sTf	176
7.1	INTRODUCTION	178
7.2	METHODS	183
7.2.1	Docking of ligands at the binding cleft of sTf	184

List of Contents

7.2.2	Equilibrium molecular dynamics	185
7.2.3	Hydrogen bond and water bridge dynamics	185
7.2.4	Well-tempered metadynamics	185
7.3	RESULTS AND DISCUSSION	186
7.3.1	Binding of Pu(IV) with human serum transferrin	186
7.3.1.1	Binding without ligand	186
7.3.1.2	Binding with ligand	195
7.3.2	Unbinding of Pu(IV) at serum pH	199
7.3.2.1	Without ligand	200
7.3.2.2	With HOPO	203
7.3.2.3	With CAM	204
7.3.3	DFT calculations for ion exchange energetics	206
7.4	CONCLUSIONS	208
8	Summary and Future Scope	210
8.1	SUMMARY AND FUTURE SCOPE	212

SYNOPSIS

Actinides such as Th, U, Np, Pu, Am, and Cm are routinely handled in various processes of front and back-end of nuclear fuel cycle. Although there are stringent safety measures during these processes, the possibility of internal contamination due to these radionuclides cannot be ruled out. They can enter into human body through any of the routes, namely inhalation, ingestion, cuts/wounds and skin absorption. Internal contamination of these radionuclides has the potential to induce both radiological and chemical toxicity under acute or chronic exposure conditions. Irrespective of the entry route, they are first absorbed into and then transported via blood prior to deposition in the target organs (e.g. thyroid, kidney, liver, bones etc).¹⁻⁵ Upon entry into the blood,⁶ actinides are mainly transported to various tissues/organs by serum transferrin (sTf),⁷⁻¹⁴ an iron carrier protein.¹⁵ sTf mainly binds dietary iron, transports it in the blood serum and delivers it to cells through a process of receptor mediated endocytosis. The sTf protein is present at a concentration of approximately 3mg/ml in human serum and is about 30% saturated with Fe(III). While this renders the blood serum accessible for certain therapeutic metal ions to bind and transport, it also become vulnerable for other toxic metals to follow the major iron acquisition pathway via the receptor-mediated endocytosis.¹⁵⁻¹⁸ About 30 other metal ions including actinides are found to make complexes with sTf.¹⁹

Since most of the actinides are man-made and do not exist throughout the evolution of the earth, our body is not used to tackle these elements, as they do not have, unlike some other trace elements, any essential role in biochemical reactions occurring in our body as well as other living organisms, plants and animals. Actinides, when present inside our body, can be detected, identified and quantified using various bioassay techniques. Internal contamination of actinides can be monitored using direct (*in vivo*) or indirect (*in vitro*) methods.^{5,20} These methods provide information about amount of radioactivity present in the body of the person and committed effective dose due to these isotopes. However, these methods do not provide information about the structure, speciation, and mechanism that our body uses to bind and transport actinides. In order to have information about actinide speciation in biological media, several *in vitro*

speciation tools like genomics, transcriptomics and proteomics can be applied.

The transferrin molecule undergoes a significant conformational change when binding and releasing iron: from open (the iron free apo-protein)–to closed (iron loaded at physiological serum pH)–to open (releasing iron upon binding to transferrin receptor at the endosomal pH) conformations. Conformational changes in the sub-domains of sTf orchestrate sequence of events in metal regulation. For example, sTf binds metals tightly at serum pH in closed form, whereas during metal release at endosomal pH, sTf is converted to open form which involves parting away of the sub-domains accompanied by a rigid body rotation around the hinge segment.²¹ Opening of the protein at endosomal acidic medium (pH=5.5), measured by center of mass separation (COM) between NI and NII sub-domains of the protein could be observed during tens of ns of equilibrium MD simulation.²²

One naively expects that the coordination of all metal ions to be the same as that of iron; differing only on their affinity to sTf, depending on their charge/mass ratio. Indeed, the actinides form stable complexes with transferrin in the following order: $\text{Pu}^{4+} > \text{Th}^{4+} > \text{Np}^{4+} \gg \text{U}^{\text{VI}}\text{O}_2^{2+} > \text{Cf}^{3+} > \text{Am}^{3+} > \text{Cm}^{3+}$.²³ Experimental studies regarding the interactions of transferrin have been carried out with a variety of actinide (An) ions.^{7–11,24–26} It is observed from these experimental studies that tetravalent An ions are more tightly bound to sTf and also their coordination with the binding site of sTf is different to that of trivalent An ions. Even in the case of tetravalent ions, while Pu(IV) is reported bound to transferrin in the iron sites,²⁷ two Th(IV) ions have been reported to bind at two non-equivalent sites.²⁸ Although a huge amount of information is available for transferrin to bind and transport non-iron metal ions,¹⁷ there is hardly any specific information at the molecular level, especially for the An ions. To the best of our knowledge crystal structures of An loaded sTf are not yet available. Whereas this is an important issue to be probed at the molecular level, since it relates to the biological fate of An trafficking in human body through sTf. In effect, the structural and thermodynamic properties of An-sTf systems are of enormous importance in providing guidance on the structures, affinities, and design of potential specific chelating agents that might be used

to eliminate an incorporated radionuclide before the initiation of toxic effects.

Isotopes of Pu/Am are mostly alpha emitters and have high linear energy transfer (LET) depositing large amount of energy per unit length of the medium. Therefore, biological damage due to these isotopes is more, and they are assigned high dose coefficients. Hence very small value of their intake will correspond to the annual average dose limit of 20 mSv decided by atomic energy regulatory board (AERB). Annual limit of intake (ALI) values for Type M compounds of Pu/Am is less than 750 Bq and for Type S compounds it is about 2400 Bq. If one calculates committed effective dose (CED) after 180 days post intake of minimum detectable activity (MDA) level of activity using various techniques, in several cases the CED exceeds the dose limit of 20 mSv. The question arises if any radiation worker has internal contamination at ALI level or more what actions should be taken to reduce the dose received by the worker. In case of external contamination, principle of time, distance and shielding applies to reduce the received dose. But in case of internal contamination radioactive source is present inside the person's body hence these principles are not effective and the most effective method to reduce internal dose is by enhancing the biological excretion of systemic activity. In case of actinides, chelation mechanism is used for enhancing the radionuclide excretion. Chelating compounds bind with the radionuclide in a ring-like highly stable structure and gets eliminated by urinary excretion path.

At present trisodium salt of Calcium diethylene triamine penta acetic Acid (Ca-DTPA) is the only FDA approved chelating agent which is used for Pu/Am decorporation. It is given to the person either through nebulizer or through intravenous (IV) administration or intramuscular (IM) routes. Ca-DTPA binds Pu/Am present in the body fluids in elemental form and the chelated complex is excreted. There are several limitations of this drug as follows (1) it cannot be administered through oral path in the form of tablets or capsules. (2) when there is intake due to several mixed radionuclides (viz. Uranium and Pu/Am) Ca-DTPA is not much effective. (3) Also, it cannot penetrate cells hence the radioactive material deposited inside bones, liver or other cells cannot be easily removed with this drug.

There is a need to develop new drugs or chelation mechanism which can overcome these difficulties. Drug development is very tedious process which needs a host of related chemical compounds to be studied at different level. The main challenge is to choose a lead compound among more than 10^{20} drug like compounds. With the advancement in computational hardware as well as theoretical models, computer aided drug designing has emerged as a new field in drug development process. In the pursuit of molecular details of binding, a combination of density functional theory (DFT) and molecular dynamics (MD) simulation is a very attractive avenue and this is extensively used in this work.^{29,30}

The aim of this thesis is to develop experimental direct monitoring methodologies to quickly estimate Pu/Am in biological samples as well as optimize various measurement geometries so that minimum MDA and CED can be evaluated. If these heavy metals are detected inside the body and found to be above recommended levels, they need to be decorporated before their deposition to various organs. In this endeavour, molecular level understanding of the binding, transport and chelation mechanism is of utmost importance. The present thesis extensively focuses on the molecular level details about binding, structural, speciation, dynamical and thermodynamic properties of the actinide ions bound to sTf. In an effort to find better chelating agents for their decorporation, the efficacy of two potential chelators, hydroxypyridinone (HOPO) and catecholamide (CAM) for the decorporation of Pu(IV) from binding cleft of sTf is studied (*in-silico*) and found that fragmented form of catecholamide (CAM) has the potential to detach Pu(IV) from the BS of sTf.

Present thesis is divided into eight chapters. The first chapter, is introductory in nature which describes the direct method of internal dose assessment, basics of quantum mechanics (QM) especially DFT, equilibrium MD simulation and enhance sampling methods. Second chapter focuses on development of a methodology for quick estimation of isotopes of Pu and Am in biological samples using HPGe array.³¹ The third chapter describes optimization of various measurement geometries to know the most sensitive organ at different time interval post inhalation intake.⁵ In the fourth chapter, model QM

structure for native Fe-sTf is studied using DFT. QM calculations for structures and spin Hamiltonian parameters of Fe-sTf using isolated and embedded clusters models are presented in this chapter.³² Fifth chapter focuses on multi-scale modelling to study structural and thermodynamic behaviour of complexes of Th(IV) and Cm(III) with sTf at serum pH.³³ In the sixth chapter, equilibrium MD Simulation are performed to study binding of Cm(III) and Th(IV) with sTf at acidic endosomal pH. The seventh chapter describes binding of plutonium Pu(IV) with sTf at various protonation states of the protein using equilibrium MD simulations. In an effort to remove it from sTf binding cleft, fragmented form of HOPO and CAM ligands are docked at the BS and well tempered MD simulations are performed to study chelation mechanism of the Pu(IV) ion at serum pH. And the final chapter of the thesis is about conclusions and future scope of the present work. The aim and scope of each of the eight chapters of the present thesis work is further presented below:

Chapter 1: Introduction to *In-vivo* Detection of Actinides and *In-Silico* Investigations for their Decorporation

The first chapter, is introductory in nature which describes the direct method of internal dose assessment, important dosimetric quantities, method to solve biokinetic models and estimate committed effective dose using methodology given by committee on medical internal radiation dose (MIRD). Current methods for decorporation of important actinides and their limitations are also discussed. Various multi-scale modelling techniques used in this work are also introduced in this chapter e.g. basics of QM especially DFT, basis sets, equilibrium MD simulations and enhanced sampling methods like umbrella sampling (US), well-tempered metadynamics (WtMetaD), hydrogen bond (HB), water bridge (WB) dynamics etc. Finally, objectives and goals of the present thesis are discussed. If Pu/Am goes inside our body how to carry out quick estimation in biological samples?? This problem and developed methodology is addressed in the second chapter.

Chapter 2: Quick Estimation of Pu/Am in Biological Samples using Low Energy HPGe Detector

This chapter describes a methodology developed for quick estimation of Pu/Am in biological samples using HPGe detectors and its comparison with

conventional technique based on radio-chemical separation followed by alpha counting. In this work, gamma/x-rays detection method is applied to estimate Pu and ^{241}Am deposited in biological sample. First, depth of contaminant in biological sample is estimated by comparing relative transmission of 26.3 and 59.5 keV photons emitted by ^{241}Am . Then ^{241}Am activity is estimated using calibration factor at calculated depth. Finally, Pu activity is estimated by applying appropriate correction for ^{241}Am contribution in 17.2 keV L_{β} X-rays region and Pu/ ^{241}Am ratio is calculated. Also, methodology for estimating ^{241}Pu in small biological sample is standardized without any chemical analysis. The method is fast as it does not involve chemical separation of Pu and Am as required in the alpha-spectrometric method. This study will be useful for assessment and medical management of Pu/ ^{241}Am embedded in tissue of workers.³¹ If Pu/Am enter the body it gets trans-located to various organs like lungs, liver, skeleton etc. Direct measurements can be carried out at any of the organs but which organ should be used for monitoring at different time intervals post inhalation is the main aim of the third chapter.

Chapter 3: Optimum Measurement Geometry for In-Vivo Assessment of $^{239}\text{Pu}/^{241}\text{Am}$ *In-vivo* measurement of Pu/ ^{241}Am in workers is carried out by placing suitable detector above lungs, liver and skeleton, as major fraction of Pu/Am is transferred to liver and skeleton, after its retention in entry organ. In this work, CED corresponding to MDA for Type M and S $^{239}\text{Pu}/^{241}\text{Am}$ deposited in these organs are estimated and a monitoring protocol of organ measurement giving the lowest CED at different time intervals post inhalation is described. It is observed, for Type M compounds, lung measurement is the most sensitive method during initial days after inhalation exposure. Liver measurement yields the lowest CED between 100 to 2000 d and beyond that bone measurement gives the lowest CED. For Type S compounds, lung measurement remains the most sensitive method even up to 10,000 d post inhalation. This study is expected to be useful for the assessment of CED due to internally deposited $^{239}\text{Pu}/^{241}\text{Am}$ in radiation workers.⁵ As Pu/Am are deposited to various organs but what is the mechanism for its transport is yet not very clear. sTf, iron carrier protein, is found to be one of the proteins

for their transport. Before studying actinide loaded sTf complexes, a QM model structure for Fe-sTf is standardized using DFT and discussed in next chapter.

Chapter 4: Quantum Chemical Studies of Iron Transferrin It is observed that iron carrier sTf also acts as the transport protein for various metal ions including several actinides. Before studying structural, speciation, binding and thermodynamic characteristics of actinide bound sTf complexes, DFT based calculations using large cluster models are carried out to elucidate the ground state electronic structure of iron bound transferrin. In this chapter, the results of electronic structure calculations are presented to understand the much-debated geometric structure of Fe-sTf. It is found that the use of gas phase geometry optimization predicts a wrong penta-coordinated geometric structure and thus an incorrect electronic structure, whereas the geometry predicted within the continuum solvation model is hexa-coordinate which is also found in the crystal structure. Our computed Mössbauer parameters are in line with the experimental data only when O_{Y188} is bound to Fe. Further, ¹⁷O HFCC of Y188 is very large (−14.5 MHz) when bound to Fe as compared to unbound state (−1.5 MHz), which can be measured with paramagnetic NMR experiments.³² This study helped a lot in selecting suitable computational solvation models, basis sets and other parameters which can be used for QM studies on actinide bound sTf complexes as discussed in next chapters.

Chapter 5: Multi-scale Modelling for Binding of Cm(III) and Th(IV) with sTf at Serum pH In this chapter, an extensive multi-scale modelling of two An [Cm(III) and Th(IV)] ions' binding with sTf at serum physiological pH is presented. From structural, dynamical and binding studies of the two An ions it is observed that sTf binds both the heavy ions in a closed conformation with carbonate as synergistic anions and the An loaded sTf maintains its closed conformation even after 100 ns of equilibrium molecular dynamics (MD) simulations. This mechanism closely follows that of the ferric ion trafficking pathway at serum pH. It is observed that in tandem with carbonate ion, Th(IV) is present in octa-dentate mode while Cm(III) prefers a hepta-dentate mode of coordination in the protein binding site. In line with reported experimental observations,

well-tempered metadynamics results of the ions' binding energetics show that the studied An-sTf complexes are less stable than Fe-sTf. Additionally, Cm(III) is found to bound more weakly than Th (IV). As a result, it will be more difficult to release thorium(IV) from the binding cleft, which might suggest its lower cytotoxicity when compared with curium (III). This result in particular emphasizes that interaction between the An ions and sTf in the presence of explicit water molecules is mainly the Coulomb interaction between them, which gives rise to the difference in the binding characteristics of the ions. In total, this chapter provides the atomistic detail of An ions' interaction with sTf at serum pH, which in future may prove to be useful for effective design of their decorporating therapeutics.³³ Mujika *et al.*²² have investigated the release of metal from an Fe(III) and Al(III) loaded N-lobe of serum transferrin by MD simulations. They have observed that in addition to the variations in the protonation state of the dilysine pair (K206 and K296), the protonation of Y188 is indispensable for prompting the conformational change of the protein and release of the metal ions. Whether similar mechanism will hold true in the case of release of An ions is yet to be explored. Sixth chapter of the thesis addresses this issue.

Chapter 6: Equilibrium MD Simulations for Binding of Cm(III) and Th(IV) with sTf at Endosomal pH In this chapter, several 100 ns equilibrium MD simulations of sTf bound to Cm(III) and Th(IV) at various protonation states of the protein are performed to explore the possibility of the two An ions release and speciation. The results demonstrate that like in Fe(III)-sTf system at the acidic endosomal pH, variation in protonation state of dilysine pair (K206 and K296) and the tyrosine (Y188) residue is necessary for the opening of Cm(III)-bound protein and the release of this trivalent ion. For Th(IV), protonation of dilysine pair alone is found to be sufficient to cause conformational changes in protein for opening of the sub-domains. However, in none of the protonation states of the protein investigated, Th(IV) is found to be released. The findings are further supported by the evaluation of potential mean force (PMF) of An ions' release. In this endeavour, the US runs along the chosen reaction coordinates, the ergodicity is maintained throughout. This is because in both the steps, diffusive dynamics of the

systems are maintained with a reasonable computational effort in the spirit of an equilibrium run. This chapter provides the molecular detail of An ions' interaction with sTf, which in future may prove to be useful for effective design of their decorporating therapeutics which is the subject matter of next chapter.

Chapter 7: *In-silico* Investigations for Plutonium Binding and its Decorporation

from sTf In the seventh chapter, equilibrium MD simulations of Pu(IV) binding with human serum transferrin at physiological and at endosomal acidic pH are discussed. Results unravel that Pu(IV) is bound to sTf in closed conformation at extracellular serum pH with carbonate as synergistic anions, and change in protonation state of dilysine (K206 and K296)-trigger and carbonate ion at endosomal pH induces conformational changes in protein, conducive for the heavy ion to be released, however strong electrostatic interaction between D63 and Pu(IV) does not allow the ion to be free. The possibility of two chelators: fragmented form of hydroxypyridinone and catecholamide ligands, to act as suitable unbinding agents for Pu(IV) in blood serum is discussed. The equilibrium MD simulations of the docked chelators in Pu(IV)-sTf system show variedly rich HB and WB dynamics, which significantly differ from each other. The metadynamics simulation results along the chosen collective variables (CVs) show differential unbinding pattern of the metal ion from the sTf cleft by the two ligands. The free energy barriers associated with the inter-basin transitions along the transition pathways are also found to be different. Following the discovered PMF profiles for the ion's unbinding, it is concluded that catecholamide based ligands could be promising chelator for the Pu(IV) ion decorporation. While any comment on the chemical toxicity of these compounds is beyond the scope of present study, this study may help in understanding the Pu(IV) chelation mechanism in blood serum and designing new decorporating agents.

Chapter 8: Summary and Future Scope In the final and concluding chapter, the objectives and findings of the various studies for the thesis are summarized and its future scope is discussed. The present thesis is aimed to develop a methodology for quick estimation of Pu/Am in biological samples as well as to optimize various measurement

geometries to find most sensitive organ for in-vivo monitoring. Much debated structure of the binding cleft of iron loaded sTf structure is studied using isolated and embedded clusters models and spin Hamiltonian parameters are estimated. Using this study, it is observed that tyrosine Y188 is bound to Fe. This thesis extensively discusses the speciation, binding and structures of various actinide ions present in the binding cleft of the sTf at serum pH. It is found that trivalent Cm(III) and tetravalent Th(IV) ions behave differently at the sTf binding cleft. Their binding and release mechanism are totally different. In an endeavour to decorporate plutonium ion Pu(IV), fragmented molecular form of hydroxypyridinone (HOPO) and catecholamide (CAM) based ligands are docked at the binding site (BS) of the sTf protein and metadynamics simulations are conducted to find the efficacy of the ligands for Pu(IV) decorporation. Pu(IV) binding at BS is found to be so strong that it is not detached from BS with the docked HOPO. However, for the identical set of simulation parameters, CAM is found to facilitate dislodging the heavy ion from the protein's binding influence. Differential behaviour of the two chelators are further explored. We have also discussed how the findings of present thesis can in principle be useful in future for effective design of its decorporating therapeutic based on CAM or its derivatives.

References

- [1] *International commission on radiological protection. Dose coefficients for intake of radionuclides by workers. ICRP Publication 68.*; 1994; Vol. 24.
- [2] *International commission on radiological protection. Individual monitoring for internal exposure of workers. ICRP Publication 78.*; 1997; Vol. 27.
- [3] *International commission on radiological protection. Age-dependent doses to members of the public from intake of radionuclides: Part 2. Ingestion dose coefficients. A report of a Task Group of Committee 2 of the International Commission on Radiological Protection. ICRP Publication 67.*; 1993; Vol. 23.
- [4] *International commission on radiological protection. Guide for the practical application of the ICRP human respiratory tract model. ICRP Supporting Guidance 3*; 2002; Vol. 32.
- [5] Mishra, L.; Singh, I. S.; Patni, H. K.; Rao, D. D. *Radiat. Prot. Dosim.* **2018**, *181*, 168–177.
- [6] Taylor, D. M. *J. Alloys Compd.* **1998**, *271*, 6–10.
- [7] Jeanson, A.; Ferrand, M.; Funke, H.; Hennig, C.; Moisy, P.; Solari, P.; Vidaud, C.; Den Auwer, C. *Chem.: Eur. J* **2010**, *16*, 1378–1387.
- [8] Taylor, D. M.; Farrow, L. C. *Int. J. Radiat. Appl. Instrum. Part B* **1987**, *14*, 27–31.
- [9] Bauer, N.; Frohlich, D. R.; Panak, P. J. *Dalton Trans.* **2014**, *43*, 6689–6700.
- [10] Bauer, N.; Panak, P. J. *New J. Chem.* **2015**, *39*, 1375–1381.
- [11] Bauer, N.; Smith, V. C.; MacGillivray, R. T. A.; Panak, P. J. *Dalton Trans.* **2015**, *44*, 1850–1857.
- [12] Benavides-Garcia, M. G.; Balasubramanian, K. *Chem. Res. Toxicol.* **2009**, *22*, 1613–1621.
- [13] Peter, E.; Lehmann, M. *Int. J. Radiat. Biol.* **1981**, *40*, 445–450.
- [14] Taylor, D.; Duffield, J.; Williams, D.; Yule, L.; Gaskin, P.; Unalkat, P. *Eur. J. Solid State Inorg. Chem.* **1991**, *28*, 271–274.
- [15] Sun, H.; Li, H.; Sadler, P. J. *Chem. Rev.* **1999**, *99*, 2817–2842.
- [16] Ansoborlo, E.; Prat, O.; Moisy, P.; Den Auwer, C.; Guilbaud, P.; Carriere, M.; Gouget, B.; Duffield, J.; doizi, D.; Vercouter, T.; Moulin, C.; Moulin, V. *Biochimie* **2006**, *88*, 1605–1618.
- [17] Vincent, J. B.; Love, S. *Biochim. Biophys. Acta, Gen. Subj* **2012**, *1820*, 362–378.
- [18] Harris, W. R.; Messori, L. *Coord. Chem. Rev.* **2002**, *228*, 237–262.
- [19] Dennis Chasteen, N. *Coord. Chem. Rev.* **1977**, *22*, 1–36.

- [20] Sharma, R. C.; Surendran, T.; Haridasan, T. K.; Sunta, C. M. *Bull. Radiat. Prot.* **1989**, *12*, 41–56.
- [21] Rinaldo, D.; Field, M. J. *Biophys. J.* **2003**, *85*, 3485–3501.
- [22] Mujika, J. I.; Escribano, B.; Akhmatskaya, E.; Ugalde, J. M.; Lopez, X. *Biochemistry* **2012**, *51*, 7017–7027.
- [23] Durbin, P. W. *The chemistry of the actinide and transactinide elements. Springer, Heidelberg, 3rd Edition; 2006; p 3339.*
- [24] Sturzbecher-Hoehne, M.; Goujon, C.; Deblonde, G. J.-P.; Mason, A. B.; Abergel, R. J. *J. Am. Chem. Soc.* **2013**, *135*, 2676–2683.
- [25] Michon, J.; Frelon, S.; Garnier, C.; Coppin, F. *J. Fluoresc.* **2010**, *20*, 581–590.
- [26] Racine, R.; Moisy, P.; Paquet, F.; Metivier, H.; Madic, C. *Radiochim. Acta* **2003**, *91*, 115.
- [27] Li, H.; Sadler, P. J.; Sun, H. *Eur. J. Biochem.* **1996**, *242*, 387–393.
- [28] Harris, W. R.; Carrano, C. J.; Pecoraro, V. L.; Raymond, K. N. *J. Am. Chem. Soc.* **1981**, *103*, 2231–2237.
- [29] Sadhu, B.; Sundararajan, M.; Bandyopadhyay, T. *J. Phys. Chem. B* **2015**, *119*, 12783–12797.
- [30] Sadhu, B.; Sundararajan, M.; Bandyopadhyay, T. *Phys. Chem. Chem. Phys.* **2017**, *19*, 27611–27622.
- [31] Singh, I. S.; Mishra, L.; Yadav, J. R.; Nadar, M. Y.; Rao, D. D.; Pradeepkumar, K. S. *Appl. Radiat. Isot.* **2015**, *104*, 49–54.
- [32] Mishra, L.; Sundararajan, M. *J. Chem. Sci.* **2019**, *131*, 15.
- [33] Mishra, L.; Sawant, P. D.; Sundararajan, M.; Bandyopadhyay, T. *J. Phys. Chem. B* **2019**, *123*, 2729–2744.

List of Figures

1.1	Routes of the entry of radionuclides, their deposition and clearance pathways are shown.	3
1.2	Schematic diagram for several source and target organ configurations.	9
1.3	Representation of the compartments in a biokinetic model.	13
1.4	Steps involved in the internal dosimetry for CED estimation.	17
1.5	Schematics for decorporation of metal using chelation mechanism	19
1.6	Schematics for decorporation of metal using chelation mechanism	20
1.7	Computational ‘microscopy’ and its different levels of resolution. A computational ‘microscope’ uses computational resources and the underlying physicochemical relationships between atoms to study cell membranes at an unrivalled level of detail. The computational ‘microscope’ can use different computational modelling methods depending on the resolution (length and time scales) required. Reproduced / adapted with permission from Journal of Cell Science. ¹	24
1.8	Flow chart of the self-consistent iteration scheme for DFT.	30
1.9	A double zeta basis allows for different bonding in different directions to consider diffusion and polarization of the orbitals	34
1.10	representation of periodic boundaries along a cubic cell is shown. Atoms moving away from the cell are entered through other side of the boundary.	44
1.11	FlowChart of the steps in an MD simulation	46
1.12	Schematic diagram of the process of metadynamics. Panel (A) shows that first the system evolves according to a normal dynamics (A), then a Gaussian potential is deposited (solid blue line), which lifts the system and modifies the free-energy landscape (dashed blue line) in which the dynamics evolves; shown in pannel (B). After a while the sum of Gaussian potentials fills up the first metastable state and the system moves into the second metastable basin pannel (C). After this the second metastable basin is filled, at this point, the system evolves in a flat landscape (D). The summation of the deposited bias (solid gray profile) provides a first rough negative estimate of the free-energy profile. ² (reproduced here with permission form John Wiley & Sons, Ltd)	49

List of Figures

2.1	Relative transmission of mono-energetic photons through a 50 mm thickness of tissue with different adipose contents (with permission from Journal of the ICRU, 2003).	58
2.2	Pulse height spectrum of ^{241}Am in the same counting geometry with (—) and without (. .) 10 mm tissue equivalent absorber recorded with HPGe detector.	59
2.3	HPGe pulse height spectrum of biological sample containing Pu isotopes and ^{241}Am .	64
2.4	Distance dependence of the ratio of counts in different energy regions are shown in the upper panel whereas in the lower panel Counting efficiency (CE) for HPGe array for important Pu/Am photon energies at various tissue depth are presented. ³	65
2.5	Spectrum of $^{238+239}\text{Pu}$ of the biological sample after radiochemical analysis followed by alpha spectroscopy.	69
2.6	Decay scheme of ^{241}Pu and its daughters	71
2.7	Variation of Detector efficiency of detector with Energy for point source is shown in the efficiency curve	72
2.8	Background subtracted Spectrum of the biological sample obtained with HPGe detector	74
3.1	Actinide monitoring system, consists of an array of three HPGe detectors placed above lungs of the LLNL phantom inside totally shielded steel room.	80
3.2	Predicted values (Bq per Bq intake) in lungs, liver and skeleton following acute inhalation intake of Type S ^{239}Pu using default ICRP metabolic parameters. The values marked with * denotes results obtained with revised HRTM, new HATM and Leggett's Pu biokinetic model.	94
3.3	Predicted values (Bq per Bq intake) in lungs, liver and skeleton following acute inhalation intake of Type M ^{239}Pu using default ICRP metabolic parameters. The values marked with * denotes results obtained with revised HRTM, new HATM and Leggett's Pu biokinetic model.	95
4.1	Active site structure of sTf.	101
4.2	Optimized structures of (a) isolated and (b) embedded models.	104
4.3	Optimized structures of Cu-sTf using embedded model(Units in Å).	106
5.1	Schematic view of the metal-bound ($\text{M}^{n+}=\text{Fe}^{3+}$, Cm^{3+} , Th^{4+}) human transferrin and its binding site in the protein cleft at serum pH. The left panel shows the ribbon presentation of the N-lobe (NI sub-domain in red, NII sub-domain in blue, hinge region in yellow) of the protein bound to a metal ion, which is utilized during the all-atom molecular dynamics simulations. The right panel shows the zoomed in view of the metal-bound first and the second coordination shells of the protein binding cleft, which has been utilized to perform DFT calculations. The suffixes I and II used in the labels of binding site residues indicate sub-domains I and II of the N-lobe that they belong to.	113

List of Figures

-
- 5.2 Flowchart of all the MD and QM calculations performed. 118
- 5.3 Time dependence of the radius of gyration, R_g (upper panel) of protein heavy atoms and RMSD of its C^α atoms (lower panel) from the crystal structure of the iron loaded (cyan) serum transferrin during the 100 ns equilibrium MD simulation is shown. Also shown are the same when Fe^{3+} ion in the binding cleft is replaced with Th^{4+} (blue), Cm^{3+} (green) and the equilibrated structures of Cm -sTf and Th -sTf are replaced with Th^{4+} (Cm^{3+} -to- Th^{4+} , red) and Cm^{3+} (Th^{4+} -to- Cm^{3+} , black) ions, respectively. 124
- 5.4 MD time evolution of distance between centre of mass of the NI and NII sub-domains of N-lobe of sTf, bound to the metal ions as indicated. Color legends are same as in Figure 5.3. 125
- 5.5 Water penetration into the protein's binding cleft for the case of metal-loaded sTf. Radial distribution function (RDF), $g_{M-O_{H_2O}}(r)$, calculated from 100 ns simulation data for the metals bound to the sTf protein as indicated are shown. From top to bottom panels: for Fe^{3+} , Fe^{3+} replaced with Th^{4+} and Cm^{3+} , MD-equilibrated Cm^{3+} structure is replaced with Th^{4+} , and MD-equilibrated Th^{4+} structure is replaced with Cm^{3+} . 128
- 5.6 Temporal profiles of distances between metal cations and the atoms of the residues lining the first coordination shell of the protein binding pocket are shown as indicated. Since after initial 10 ns the distances vary monotonously for each of the MD runs, only the first 10 ns of a representative 100 ns MD data are plotted here. Also shown are distances between metal cations and the centre of mass separation of the first coordination shell. Colour legends shown for the variety of protein-bound metal ions considered are the same as in Figure 5.3. 129
- 5.7 DFT optimized structures consisting of first and second coordination shell residues of sTf protein bound with the (A) Fe^{3+} , (B) Cm^{3+} , and (C) Th^{4+} ions. Various hydrogen bonds and their lengths are also depicted. 130
- 5.8 Temporal profiles of interatomic distances between oxygen atoms of the synergistic ion (CO_3^{2-}) and hydrogen atoms of residues in the second coordination shell, forming hydrogen bonds (a: $HH21_{R124}-O1_{CO_3}$, b: $HE_{R124}-O1_{CO_3}$, c: $HG1_{T120}-O3_{CO_3}$) and that between nitrogen atoms of K206 and K296 residues (d: $N_{K206}-N_{K296}$). Colour legends shown for the variety of protein-bound metal ions are the same as in Figure 5.3. Since after initial 10 ns the distances varies monotonously for each of the MD runs, only the first 10 ns of a representative 100 ns MD data are plotted here. 132

List of Figures

- 5.9 DFT optimized structures consisting of first and second coordination shell residues of actinide-bound sTf protein when structures, presented in Figure 5.7 of: Cm³⁺ is replaced with Th⁴⁺, [Cm_{-to}-Th-sTf]_{QM} (A); Th⁴⁺ is replaced with Cm³⁺, [Th_{-to}-Cm-sTf]_{QM} (B). The bottom panel shows the same when An ions in the equilibrated structures of An-bound sTf are first swapped with one another, MD equilibrated and then the truncated structures of An-bound binding cleft are DFT optimized: (C) [Cm_{-to}-Th_{MD}]_{QM}, (D) [Th_{-to}-Cm_{MD}]_{QM}. Various hydrogen bonds and their lengths are also depicted. 135
- 5.10 Well-tempered metadynamics-discovered free energy contour surface as a function of protein-ion centre of mass separation and centre of mass separation between the NI and NII sub-domain of sTf for unbinding transition of: (A) Cm³⁺, (B) Th⁴⁺ and (C) Fe³⁺ in polarizable water medium are shown. Isoenergy lines are drawn every 15 kJ/mol as indicated by color bar. Green colored regions show the bound state of the ions; in contrast to trivalent ions, tetravalent thorium(IV) ion can be seen to remain attached to the transferrin at various locations even when NI and NII sub-domains are far apart and the protein is in the open state. 138
- 5.11 Left panel shows the PMF profiles of actinides (Th⁴⁺ and Cm³⁺) and Fe³⁺ unbinding from the sTf binding cleft as a function of centre of mass separation between the residues in the first coordination shell of the protein's MBS and the metal ions, synergistically attached with the CO₃²⁻ ion. The profiles are obtained by reweighting⁴ the well-tempered metadynamics results in a polarizable water medium. Also shown at the right are ions' separation from centre of mass of first coordination shell of the MBS as a function of time. 141
- 6.1 The first and the second coordination shells of metal ions (Mⁿ⁺= Cm³⁺, Th⁴⁺) in human serum transferrin binding cleft is shown schematically. Various protonation states of the residues in the shells, for which equilibrium MD simulations are performed, are summarized in Table-6.1. 150
- 6.2 Time dependence of the RMSD of backbone C^α atoms of the An-sTf systems from their starting structures during the 100 ns equilibrium MD simulation. Upper panel shows the RMSD profiles for Cm(III)- and lower panel for Th(IV)-loaded sTf systems. Colour labels representing different protonation states (*cf.* Table-6.1) of the coordination shells of the An ions in the protein binding cleft are (i) red; *acid I*, (ii) blue: *acid II*, and (iii) cyan: *acid III*. 158
- 6.3 MD time evolution of distance between center of mass of the NI and NII sub-domains of An-sTf systems in various protonation states: (from top to bottom) *acid I*, *acid II* and *acid III*. Lines in red colour are for Th(IV)-loaded and blue ones are for Cm(III)-loaded sTf. Also shown the same in black line for the metal-free apo-sTf system at *acid III* protonation state. 161

List of Figures

- 6.4 Time dependence of HB lifetime correlation function for the hydrogen bonds formed by the residues in the binding cleft of sTf in *acid III* protonation state of the protein are shown for metal-free (black line) and Th(IV)-sTf (red lines) systems. Higher HB lifetimes in the case of metal-free condition implies that the protein maintains its closed and compact structure in this acidic state, while Th(IV)-loaded protein opens up (*cf.* Figures 6.3) with less number of similar HBs to report upon. 162
- 6.5 Water penetration into the binding cleft of the An-bound protein in *acid I* protonation state. Radial distribution function (RDF), $g_{M-O_{H_2O}}(r)$ of water around the An ions (Th(IV) in black and Cm(III) in red line), calculated from 100 ns simulation data are shown. Opening up of the protein while bound to Th(IV) ion is evident. 164
- 6.6 Time dependence of WB lifetime correlation function of the residues in the sTf binding cleft in *acid I* protonation state is shown. Red and black lines represents $C_{WB}(t)$ for Th(IV)- and Cm(III)-loaded sTf systems, respectively. Opening of the protein (Figure 6.3) at this acidic condition in Th(IV)-sTf system allows extensive WB formation due to abundance of water molecules in the protein interior in comparison to Cm(III)-loaded sTf. 165
- 6.7 Temporal profile of the COM separation of the actinides (solid lines) and the synergistic HCO_3^- ion (dashed lines) from the protein in acidic conditions: *acid I*, *acid II*, and *acid III*, as indicated. Red lines are for Th(IV)-loaded and black lines are for Cm(III)-loaded sTf systems. The synergistic effect of HCO_3^- ion is seen to be lost as the An ions moves out of binding cleft. 168
- 6.8 Hydrogen bond correlation function between HCO_3^- ion and residues of sTf in *acid I* protonation state is shown. Hydrogen bonds between all possible donor-accepter pairs are considered. Red and black lines represent $C_{HB}(t)$ for Th(IV)- and Cm(III)-loaded sTf, respectively. Extensive nature of hydrogen bonding of HCO_3^- with residues in Th(IV)-sTf system imply that the synergistic anion is detached from An ion while the later forms strong electrostatic interaction with D63 residue in the first coordination shell (see below). This renders Th(IV) not to leave the protein interior even though the protein opened up in *acid I* protonation state (*cf.* Figure 6.3) and Th(IV) is freed from the synergistic influence of the bicarbonate ion (*cf.* Figure 6.7). 169
- 6.9 Short-range electrostatic interaction energy between Th(IV) and D63 and between Cm(III) and D63 are plotted as a function of time in *acid I* (blue lines) and *acid III* (red lines) protonation states of sTf. Strong electrostatic interaction between D63 and Th(IV) in both the protonation states of sTf does not allow the An ion to completely come out of the protein interior (*cf.* Figure 6.7), even though the protein opens up in both the acidic situations (*cf.* Figure 6.3). Whereas, Cm(III), in particular at *acid III* condition is free from such interaction and hence can be released from the protein. 170

List of Figures

- 6.10 Potential of mean force (PMF) profiles for distance between COM of NI and NII sub-domains, characterizing the opening of sTf protein in *acid III* protonation state is shown. Red line is for Th(IV)- and black line is for Cm(III)-loaded protein. The profiles are obtained by performing US simulation along the NI-NII distance coordinate, as obtained from equilibrium MD simulations and shown in Figure 6.3. 171
- 6.11 PMF profiles of An ions' unbinding transitions from the sTf protein as obtained through US runs. Red line represents PMF for Th(IV) unbinding in *acid I*, while black line represents Cm(III) unbinding in *acid III* protonation state of the protein. The US simulations were performed along the COM separation coordinate between the protein and the An ions (*cf.* equilibrium MD results in Figure 6.7). 172
- 7.1 Schematic view of the binding-cleft of Pu(IV)-bound human serum transferrin at serum pH are presented (A) without ligand, and with the fragmented (B) HOPO, and (C) CAM ligands. The suffixes I and II in the residue labels point to the sub-domains I and II of the N-lobe of the protein that they belong to. 179
- 7.2 Schematic view of the ligand-free binding-cleft of Pu(IV)-bound human serum transferrin are presented in (A) *acid I*, (B) *acid II*, and (C) *acid III* protonation states of the protein. The suffixes I and II in the residue labels point to the sub-domains I and II of the N-lobe of the protein that they belong to. 183
- 7.3 Water penetration into the ligand-free protein's binding cleft. Radial distribution function, $g_{M-O_{H_2O}}(r)$, of water around the Pu(IV) ion during the 100 ns simulation for various protonation states of the protein, as indicated: *phys* at serum pH (black), and at acidic endosomal pH *acid I* (red), *acid II* (blue), and *acid III* (green), are shown. Opening up of the protein in *acid I* protonation state can be seen to be most prominent. 187
- 7.4 Time dependence of root mean square deviation (RMSD) of backbone C_α atoms (upper panel) and the radius of gyration, R_g of protein heavy atoms (lower panel) from the starting structure of the ligand-free and Pu(IV)-loaded serum transferrin during the 100 ns equilibrium MD simulation are shown at various protonation states of the protein binding-cleft. Colour legends are same as in Figure 7.3. 189
- 7.5 MD time evolution of distance between the tetravalent metal ion and centre of mass (COM) of residues in the binding site (BS) cleft (upper panel), and the COM separation between NI and NII sub-domains (lower panel) of the ligand-free and Pu(IV)-loaded sTf protein are shown at various protonation states of the cleft: *phys* at serum pH (black), and at acidic endosomal pH *acid I* (red), *acid II* (blue), and *acid III* (green). 190

List of Figures

- 7.6 Time dependence of HB (Short-range electrostatic interaction energy of Pu(IV) with D63 and with the binding site (BS) residues of ligand-free sTf are plotted as a function of time in *phys* serum and *acid I* protonation states. Stronger electrostatic interaction as experienced by Pu(IV) both with BS and with D63 residue at *phys* protonation state compared with the *acid I* variant is evident. Note that in *acid I* state, Pu(IV)-BS interaction strength reduces to that prevailing between Pu(IV) and D63 at about 80 ns. However, interaction strengths are always seen to be attractive, which does not allow the An ion to completely come out of the protein interior, even though the protein opens up in *acid I* protonation state (*cf.* Figure 7.5) for the tetravalent ion to be released. 192
- 7.7 Time dependence of HB (upper panel) and WB (lower panel) lifetime correlation functions between residues of ligand-free sTf, bound to the tetravalent ion, are shown in all the four protonation states of the protein. Results for D-A pairs (as indicated) which are extensively engaged in HB and WB formation in polarizable water medium are presented. Colour legends, as indicated are same as in Figure 7.5. 193
- 7.8 Time dependence of HB lifetime correlation functions between residues of sTf which are extensively engaged in HB formation with the synergistic ion (carbonate and bicarbonate) are shown for ligand-free Pu(IV)-sTf bound system at all four protonation states of the protein. Colour legends used are as mentioned. 194
- 7.9 Time dependence of HB lifetime correlation functions between residues of sTf which are extensively engaged in HB formation between themselves and with the ligand molecules are shown for Pu(IV)-sTf bound system at *phys* serum pH. The results are presented without (black lines) and with ligands (red lines: HOPO, blue lines: CAM). HB formation pattern in presence of the two ligand molecules can be seen to be strikingly different from each other. HB formation between all possible D-A pairs are considered in polarizable water. 196
- 7.10 (upper panel, A) Time dependence of WB lifetime correlation functions between residues of sTf which are extensively engaged in WB formation between themselves are shown for Pu(IV)-sTf bound system at *phys* serum pH. (lower panel, B) Same as panel (A) except that WB between residues of sTf with the synergistic ion, CO_3^{2-} are shown. Colour legends are same as in Figure 7.9. Remarkable difference in WB formation behaviour due to single-atom nitrogenation of catechol-based CAM ligand in hydroxypyridinone-based HOPO ligand is quite evident. 198

List of Figures

- 7.11 Two-dimensional contour plot for the unbinding transition of Pu(IV) from the binding-cleft of serum transferrin at serum pH are shown (A) without ligand, (B) with HOPO, and (C) with CAM ligands. The 2D free-energy landscape is generated from WtMetaD runs, employing ordinate and abscissa of the plots as CVs. Isoenergy lines are drawn every 15 kJ/mol. Numerals without and with prime indicate major basins and barriers along the unbinding pathway. See Figures 7.13, 7.14, 7.15 for structural snapshots of them. 200
- 7.12 PMF profile for the unbinding transition by employing COM separation between protein binding-cleft and Pu(IV) ion as a CV (*cf.* abscissa in Figure 7.11) are shown without and with the ligands. Colour legends are same as in Figure 7.10. The PMF profile are generated from the converged WtMetaD simulation. 201
- 7.13 Snapshots of the two energetic basins, as marked in Figure 7.11 (A) for the unsuccessful attempt of unbinding transition of Pu(IV) without the ligands in polarizable water medium are shown. Only those residues of sTf that stabilizes these states and are responsible for Pu(IV) binding are depicted. The dotted lines marked with separation distance (Å) indicate HBs and WBs. 202
- 7.14 Snapshots of the energetic basins and barriers, as marked in Figure 7.11 (B) for an attempt to unbind Pu(IV) from sTf cleft when docked with HOPO ligand in polarizable water medium are shown. Only those residues of sTf that stabilizes these states and are responsible for Pu(IV) binding are depicted. The dotted lines marked with separation distance (Å) indicate HBs and WBs. 203
- 7.15 Snapshots of the energetic basins and barriers, as marked in Figure 7.11 (C) for successful unbinding of Pu(IV) from sTf cleft when docked with CAM ligand in polarizable water medium are shown. Only those residues of sTf that stabilizes these states and are responsible for Pu(IV) binding are depicted. The dotted lines marked with separation distance (Å) indicate HBs and WBs. 205

List of Tables

1.1	Radiation weighting factors, w_R for different radiation types.	7
1.2	Tissue weighting factors, w_T for different organs.	7
1.3	Estimated CED Values for MDA equivalent inhaled activity of Pu/Am at different monitoring frequency.	17
1.4	Contracted and primitive basis functions for some Pople style basis sets for hydrogen, second and third row elements.	36
2.1	Radiological properties of Pu and ^{241}Am and half value thickness of its photon energy in the soft tissue (ICRU, 1989 ⁶⁷).	57
2.2	Variation of detector efficiency and MDA of HPGe detector for the measurement of ^{241}Am embedded in tissue at various depth for monitoring time of 600 seconds.	66
2.3	Detector efficiency (counts photon ⁻¹) and MDA (Bq) of Pu and ^{241}Am at various energies and 10 mm depth for monitoring period of 600 seconds.	68
2.4	Values of constants given in equation 2.7	71
2.5	Efficiency of the HPGe detector for ^{241}Am and ^{241}Pu	72
3.1	The efficiency and MDA (50 minutes measurement time) of HPGe array at 59.5 keV photon of ^{241}Am distributed in the lungs and liver of LLNL phantom with various overlay thicknesses.	85
3.2	The intake and CED from MDA equivalent Type M ^{241}Am measured in lungs, liver and skeleton at various days post inhalation. Intake and CED is calculated using ICRP-66 HRTM, ICRP 30 GIT and ICRP 67 biokinetic model of americium with default ICRP parameter for occupational workers.	88
3.3	The intake and CED from MDA equivalent ^{241}Am embedded in Pu oxide (Type S) and measured in lungs, liver and skeleton at various days post inhalation. Intake and CED is calculated using ICRP-66 HRTM, ICRP 30 GIT and ICRP 67 biokinetic model of americium with default ICRP parameter for occupational workers.	89
3.4	The intake and CED of Type M ^{239}Pu from MDA equivalent ^{241}Am measured in lungs, liver and skeleton at various days post inhalation. The $^{239}\text{Pu}/^{241}\text{Am}$ ratio of 3 is taken for the calculation. The values are calculated using ICRP-66 HRTM, ICRP 30 GIT and ICRP 67 biokinetic model of Pu with default ICRP parameter.	90

List of Tables

3.5	The intake and CED of Type S ^{239}Pu from MDA equivalent ^{241}Am measured in lungs, liver and skeleton at various days post inhalation. The $^{239}\text{Pu}/^{241}\text{Am}$ ratio of 3 is taken for the calculation. The values are calculated using ICRP-66 HRTM, ICRP 30 GIT and ICRP 67 biokinetic model of Pu with default ICRP parameter.	90
3.6	Estimated intake of Type M ^{239}Pu from MDA equivalent ^{241}Am measured in lungs, liver and skeleton at various days post inhalation. The Pu/ ^{241}Am ratio of 3 is taken for the calculation of intake. Intake is calculated using ICRP-130 HRTM, ICRP-100 HATM and Leggett's biokinetic model of Pu with default parameters for occupational workers.	92
3.7	Estimated intake of Type S ^{239}Pu from MDA equivalent ^{241}Am measured in lungs, liver and skeleton at various days post inhalation. The Pu/ ^{241}Am ratio of 3 is taken for the calculation of intake of ^{239}Pu . Intake is calculated using ICRP-130 HRTM, ICRP-100 HATM and Leggett's biokinetic model of Pu with default parameters for occupational workers.	93
4.1	Optimized first coordination parameters (in Å) around the iron center of Fe-sTf.	104
4.2	Computed MB (isomer shift (δ), quadrupolar splitting (ΔE_q) (mm s^{-1}) and super hyperfine coupling constants (MHz).	105
4.3	Optimized first coordination parameters (in Å) around the binding cleft of Cu-sTf.	106
4.4	Computed EPR Parameters for Cu-sTf	107
5.1	Mean and standard deviations of bond lengths (Å) of the metal ions ligated with atoms of the residues in the first coordination shell as calculated by averaging over five independent 100 ns MD simulations	129
5.2	DFT optimized bond lengths (Å) of the metal ions ligated with atoms of the residues in the first coordination shell of protein's binding cleft	136
5.3	Optimized range of M-O _{water} bond lengths and hydration free energies of metal hydrated systems	143
5.4	Calculated ion exchange energetics (kJ/mol) in the first binding shell of the protein cleft at different dielectric constant of the medium	145
6.1	Protonation states of residues in the first and second coordination shells of the metal ions in the protein binding cleft. Only changes in protonation states with respect to the crystal structure (PDB ID: 1A8E) are indicated	151
6.2	Mean and standard deviations of distances (Å) between the An ions and the ligating atoms of the residues in the first coordination shell of the protein during 100 ns MD simulations at various protonation states	159
7.1	Mean and standard deviations of bond lengths (Å) of the metal ions ligated with atoms of the residues in the first coordination shell as calculated from MD simulations	188

List of Tables

7.2	Estimated ion exchange, Fe(III) \rightarrow Pu(IV) free energies (in kJ/mol) by the chelating ligands, in the absence of sTf binding cleft, at different dielectric constant of the medium.	207
7.3	Estimated ion exchange, Fe(III) \rightarrow Pu(IV) free energies (in kJ/mol) by the chelating ligands, inside the sTf binding cleft, at different dielectric constant of the medium	207
8.1	Ionic potential and non-bonded parameters of the investigated metal ions	216

Thesis Highlight

Name of the Student: Lokpati Mishra
Name of the CI/OCC: BARC, Mumbai

Enrolment No.: CHEM01201404006
Date of viva voce: 17/09/2020

Thesis Title: "Experimental detection of actinides in human body and computational investigations of their decorporation mechanism"

Discipline: Chemical Sciences

Sub-Area of Discipline: Multiscale modelling for actinide's biochemistry

Actinides (An) such as Th, U, Pu, Am, and Cm etc. are routinely handled in various processes of front and back-end of nuclear fuel cycle. Although there are stringent safety measures during these processes, the possibility of internal contamination due to these radionuclides cannot be ruled out. They can enter into human body through any of the routes, namely inhalation, ingestion, cuts/wounds and skin absorption. Internal contamination of these radionuclides has the potential to induce both radiological and chemical toxicity under acute or chronic exposure conditions. Irrespective of the entry route, they are first absorbed into and then transported via blood prior to deposition in the target organs (e.g. thyroid, kidney, liver, bones etc). Upon entry into the blood, actinides are mainly transported to various tissues, organs by serum transferrin (sTf), an iron carrier protein. sTf mainly binds dietary iron, transports it in the blood serum and delivers it to cells through a process of receptor mediated endocytosis.

The aim of this thesis is to develop direct monitoring methodologies to quickly estimate Pu/Am in biological samples as well as optimize various measurement geometries so that the deposited radioactivity and corresponding committed effective dose (CED) to the person can be assessed at the trace level, well below the regulatory

limits. If these heavy metals are detected inside the body and found to be above recommended levels, they need to be decorporated before their deposition to various organs. In this endeavor, molecular level understanding of the binding, transport and removal mechanism is of utmost importance. The thesis work reveals that tetravalent Pu(IV), Th(IV) binds at the sTf site more strongly than trivalent Cm(III) at serum pH conditions. Also in endosomal pH conditions, variations in the protonation states of dilysine pair (K206 and K296) and the tyrosine (Y188) residue is necessary for the opening of Cm(III)-bound protein and the release of this trivalent ion. For Th(IV), protonation of dilysine pair alone is found to be sufficient to cause conformational changes in protein for opening of the sub-domains. In an effort to find better chelating agents for their decorporation, the efficacy of two potential chelators, hydroxypyridinone (HOPO) and catecholamide (CAM) for decorporating Pu(IV) from binding cleft of sTf is studied in-silico. It has been found that fragmented form of catecholamide (CAM) has the potential to detach Pu(IV) from the binding cleft of sTf. In short, the thesis highlights the in-vivo detection methods of actinide contamination and focuses on the multi-scale modeling of actinide biochemistry, which could pave the way for discovering potential decorporating agents of actinides.

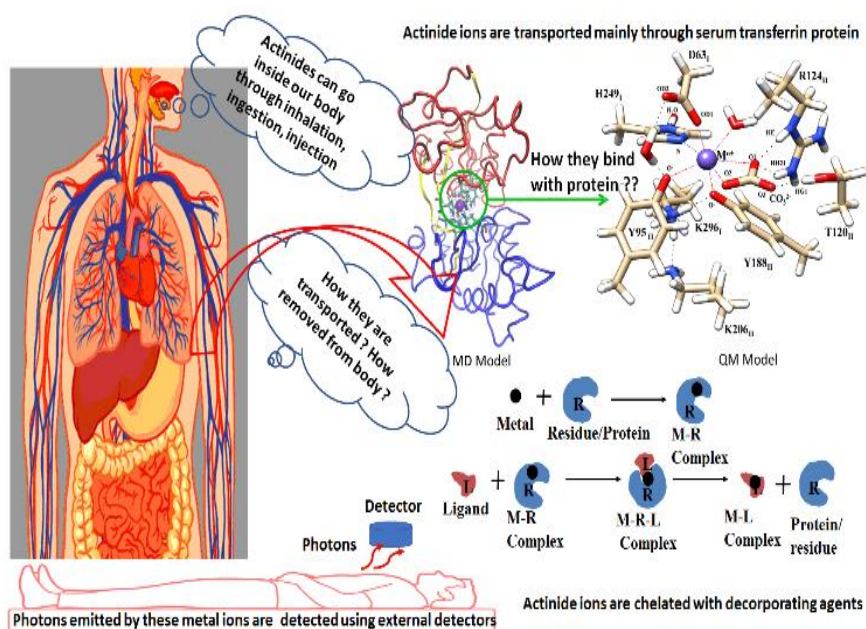
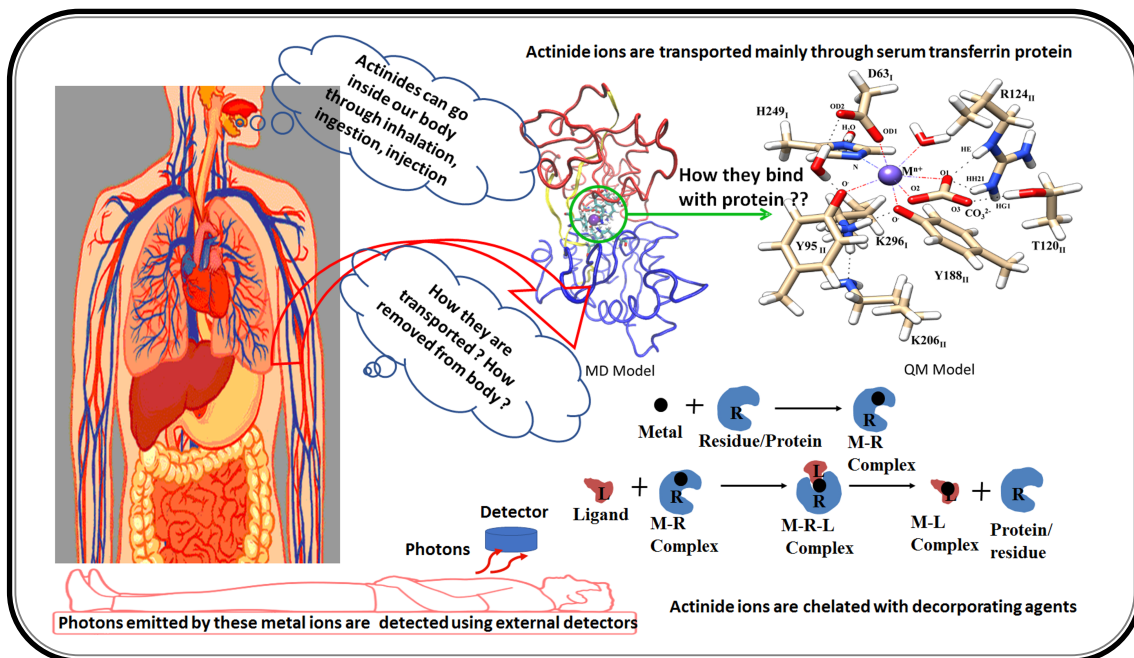


Figure 1. Schematics of entry routes of Th, Pu, and Cm into human body, their in-vivo detection and their transport to various organs via blood by serum transferrin (sTf) carrier protein is shown. Also shown in the figure how Metal ion (M) bound to a protein residue (R) can be removed by chelating ligand (L).

CHAPTER 1

Introduction to *In-vivo* Detection of Actinides and *In-Silico* Investigations of their Decorporation



HIGHLIGHTS

- Actinides are handled at various stages of nuclear fuel cycle. In spite of stringent safety measures the probability of internal contamination cannot be ruled out. They can go inside our body through inhalation, ingestion and injection route. Depending on their biochemistry they are deposited at various organ sites and are transported mainly through iron carrier serum transferrin (sTf) protein in blood serum.
- Gamma and x-ray photons emitted by these radionuclides are measured using external detectors placed outside the body and activity present in the body is estimated. These methods do not give information about the molecular interactions of these ions with various biomolecules.
- Once detected they are decorporated from the body using chelating agent, Ca-DTPA/Zn-DTPA is used at present. These ligands have several limitations, therefore study for designing new chelating agents is required.
- Multi-scale modelling using density functional theory, molecular dynamic simulations, well-tempered metadynamics and docking is carried out to study, structural, binding and thermodynamic properties of actinides complexed with sTf at various pH.
- Two new ligands, fragmented catecholamide (CAM) and hydroxypyridinone (HOPO), are studied for plausible chelation of Plutonium Pu(IV) ion from sTf at serum pH condition using equilibrium MD simulations. Basic introduction about these methods is given in this chapter.

1.1 BASICS OF INTERNAL DOSIMETRY

Studies on actinides are carried out at various stages of nuclear fuel cycle programs. There are stringent safety measures during their handling, yet the risk of internal contamination due to these radio-nuclides cannot be neglected. The Major routes of entry of a radioactive contaminant in our body are: through inhalation of airborne radioactivity (aerosols) via nasal route, ingestion of contaminated food or water through oral path, injection by any sharp contaminated object penetrating the skin and direct skin absorption. These routes of intakes of radioactive materials along with the metabolic pathways are schematically illustrated in Figure 1.1. The amount of radioactivity entered to our body through any of these routes is called as ‘intake’.⁵ The deposition and clearance of radioactivity in various parts of the entry route viz. respiratory tract, gastrointestinal (GI) tract, wound site can be understood by their respective biokinetic models. In inhalation case, Inhaled activity is deposited in various regions of respiratory

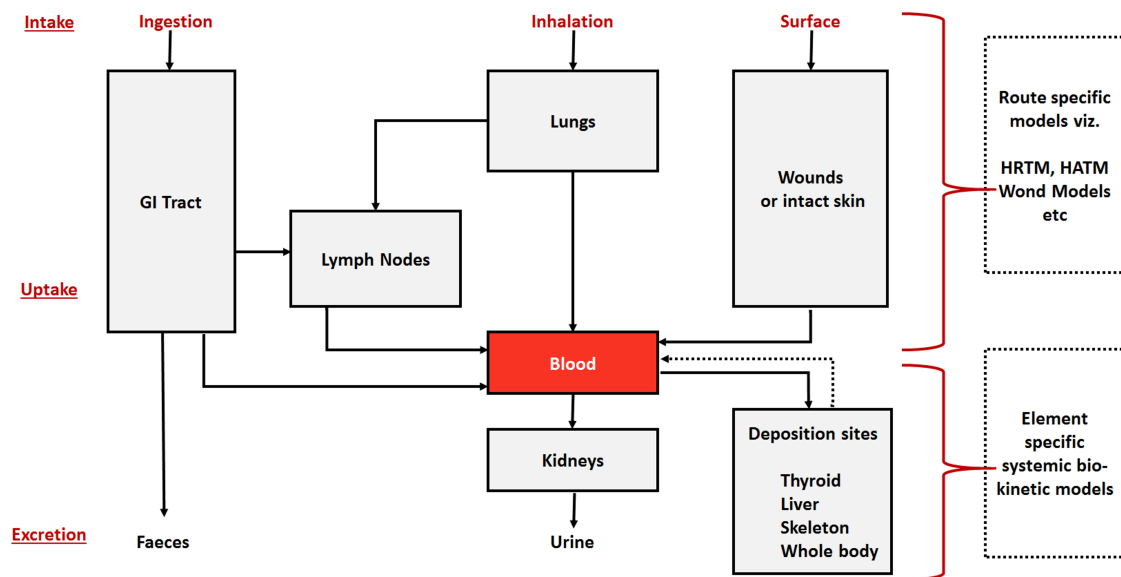


FIGURE 1.1: Routes of the entry of radionuclides, their deposition and clearance pathways are shown.

tract and a fraction is absorbed to blood and other fraction is transferred to alimentary tract/lymph nodes through particle transport mechanism. Absorption to blood depends

on the solubility of inhaled material which is classified as fast (Type F), moderate (Type M) and slow (Type S) categories. Human respiratory tract model (HRTM) provides details of deposition and clearance from various parts of respiratory tract.⁶ In ingestion case, ingested activity is transferred through various regions of GI tract.⁷ A fraction, f_1 , of the ingested activity is absorbed in to the blood from small intestine and rest is excreted through feces. Human alimentary tract model (HATM) describes in details about entry, transfer, deposition and clearance of ingested radioactivity.⁸ Similarly, in wound contamination case, radionuclide is either locally deposited at the wound site or absorbed to the blood depending on its nature (viz. soluble, particle aggregates and bound state (PABS), trapped particle aggregates (TPA), fragment type, or colloidal intermediate state (CIS)). Deposition of the material at the wound site, its absorption to blood or clearance from body can be modeled by National commission on radiation protection (NCRP) wound model.⁹

In all the routes of the internal contamination, a fraction is absorbed to the blood which is also known as ‘uptake’ or systemic radioactivity as it is present in the circulatory body fluids. Once radionuclide reaches blood, its distribution within the body and its route and rate of elimination is determined by various and often complex metabolic processes. The organs where radioactivity is deposited are termed as ‘source organs’ and the nearby organs getting irradiated by them as ‘target organs’. It should be noted here that source and target organs can and can’t be the same. The distribution of systemic activity depends mainly on the biochemical nature of the material in the body, it can either be diffused and/or relatively homogeneous, e.g. with tritiated water, or it can be organ specific distribution e.g. with iodine (thyroid), alkaline earth metals (bone) and plutonium (bone and liver).

Deposited material in the body is removed principally by urinary and fecal excretions. Material from the plasma and extra-cellular body fluids is removed through urine in urinary excretion path whereas, removal of systemic material unabsorbed

through the gastrointestinal tract is represented by fecal excretion. International commission on radiation protection (ICRP) provides details of systemic biokinetic models for various important radioactive elements.^{5,10}

The processes involved in physical movement of radionuclides in the body following intake and deposition of materials that constitute exposure can be described mathematically with the help of biokinetic models. These models can be used to calculate intake, uptake and retained activity in any organ at different time intervals post exposure. Also, number of transformations (radioactive decays of atoms) that take place in a given time after intake in any part of the body or whole body can be calculated with the help of biokinetic models. Important organs where radionuclide reaches is represented by one or many compartments and rate of transfer of activity between these compartments is assigned along with their fractional distribution. Transfer of the radioactivity from one compartment to another is represented by transfer rates (per day, d^{-1}). These rates are mainly estimated using data of various experimental studies performed on animals and human being. If fraction of activity deposited in each compartment and inter-compartment transfer rates are known, the biokinetic model can be represented by first order kinetics and can be solved mathematically to calculate various parameters.

Radionuclides due to their unstable nature emit various ionizing radiations viz. energetic alpha, beta particles or x-ray/gamma ray photons which can either ionize or excite the atoms of the medium where radionuclide is present. Ionization and excitation of the atoms mainly depends on the type and energy of the emitted radiation as well on the atomic number Z and electron density of the atoms present in the medium. For example, alpha particles produce more ionization compared to beta particles or gamma photons. Ionization or excitation of atoms in the body due to these radiations can induce some stochastic or deterministic effects in the body. To quantify these effects, dosimetric model is used in which we can calculate how much of the emitted energy is absorbed in

each tissue or organ, and hence the committed doses received to the organ. The organ in which radionuclide is located is called as ‘source organ’ and the organ where emitted energy is absorbed termed as ‘target organ’.

The primary physical quantity of interest for internal dosimetry is absorbed dose and it is the measure of energy deposited to unit mass of the target medium. ICRP defines absorbed dose, D , as “mean energy imparted by ionizing radiation to matter in a small volume element having mass dm ” and is given by.¹¹

$$D_{T,R} = d\bar{\epsilon}/dm; \quad (1.1)$$

where $d\bar{\epsilon}$ represents the mean energy imparted by ionizing radiation to the matter in a small volume element having mass dm . The SI unit of absorbed dose is joule per kilogram (J/kg), known as Gray (Gy). Absorbed dose cannot be estimated practically, therefore it is not used for practical application in radiation protection.

Radiation induced effects produced in any organ will differ for the same absorbed dose due to different radiation type as ionization of atoms in the medium is highly radiation dependent. Linear energy transfer (LET), “the amount of energy that an ionizing particle transfers to the material traversed per unit distance”, is used to compare ionizing power of radiation type. LET is measured in kilo-electron-volts per micrometer ($\text{keV } (\mu\text{m})^{-1}$) or mega-electron-volts per centimeter (MeV cm^{-1}). Organ or tissue absorbed dose is weighted by a dimensionless factor to account for the higher biological effectiveness of high-LET radiations compared with low-LET radiations. This factor is called as radiation weighting factor w_R and its values for important radiation types are given in Table 1.1. Highly charged particles such as alpha, due to its high LET, will produce more biological effects and hence are assigned high value of w_R . Absorbed dose is multiplied by radiation weighting factor to derive the ‘equivalent dose’ averaged over a tissue or organ. The equivalent dose, H_T , in tissue or organ is given by

$$H_T = \sum_R w_R D_{T,R}; \quad (1.2)$$

TABLE 1.1: Radiation weighting factors, w_R for different radiation types.

Radiation type and energy Range	Radiation weighting factor, w_R
Photon, all energies	1
Electrons and muons, all energy	1
Neutrons, energy $E_n < 1$ MeV	$2.85 + 18.2 \exp[-(\ln E_n)^2/\sigma]$
Neutrons, energy $E_n \geq 1$ MeV	$5.0 + 17.0 \exp[-(\ln 2E_n)^2/\sigma]$
Protons and charged pions	2
Alpha particles, fission fragments, heavy nuclei	20

TABLE 1.2: Tissue weighting factors, w_T for different organs.

Tissue	w_T	$\sum w_T$
Bone Marrow, Breast, Colon, Lung, Stomach, Remainder Tissues* (13 Tissue)	0.12	0.72
Gonads	0.08	0.08
Bladder, Oesophagus, Liver, Thyroid	0.04	0.16
Bone Surface, Brain, Salivary Glands, Skin	0.01	0.04
Total		1

*Remainder tissue: lymphatic nodes, muscle, oral mucosa, adrenals, extra thoracic (ET) region, pancreas, prostate, small intestine, spleen, thymus, uterus/cervix, gall bladder, heart, kidneys.

The SI unit of equivalent dose is same as for absorbed dose i.e. the joule per kilogram (J/kg) but it is called Sievert (Sv).

Organs/tissues have different sensitivity for ionizing radiation, even when irradiated with the same type and energy of the radiation i.e. if same equivalent dose is given to different tissues, the induced biological effects will not be the same. To account for varying radio-sensitivity of the organs, tissue weighting factor, w_T is used. The sum of the weighted equivalent doses in all the tissues and organs of the body is called as 'effective dose'.

$$E = \sum_T w_T H_T = \sum_T w_T \sum_R w_R D_{T,R}; \quad (1.3)$$

Its units are similar to equivalent dose i.e. joule per kilogram (J/kg) or Sievert (Sv) but its physical significance is different. Effective dose represents whole body dose whereas equivalent dose corresponds to organ specific dose. If whole body is uniformly irradiated then relative contribution of any tissue in the total detriment is represented by w_T which

is a dimensionless factor by which equivalent dose in the tissue or organ is weighted. The recent values¹¹ of w_T adopted by ICRP for various tissues / organs are given in Table 1.2

1.2 MIRD METHODOLOGY FOR INTERNAL DOSE ESTIMATION

Radiations emitted by the radioactive material present in the source organ, S, will create ionization or excitation of the atoms in the target organ, T, by depositing their energy. There can be different possibilities for source and target organ configurations as represented in Figure 1.2. Below we describe how to calculate committed effective dose (CED) received by a person. First, absorbed fraction $AF(T \leftarrow S)_R$ is estimated then specific effective energy $SEE(T \leftarrow S)$ is calculated which is multiplied by total number of transformations U_s to get committed equivalent dose $H_T(50)$ for any target organ T. $H_T(50)$ is weighted for appropriate w_T and summed over all the source organs to estimated CED. The various terms are detailed below.

1.2.1 Specific effective energy $SEE(T \leftarrow S)$

$SEE(T \leftarrow S)$ is defined as the energy, modified by the radiation weighting factor for radiation type R, absorbed in the target organ T from each transformation in the source organ S; it is expressed in MeV g⁻¹. The specific effective energy is calculated as:

$$SEE(T \leftarrow S) = \sum_R \frac{Y_R E_R w_R AF(T \leftarrow S)_R}{m_T}; \quad (1.4)$$

where, Y_R , E_R and w_R are respectively yield, energy and radiation weighting factor of the radiation type R per transformation of the radionuclide. m_T is the mass of target organ,

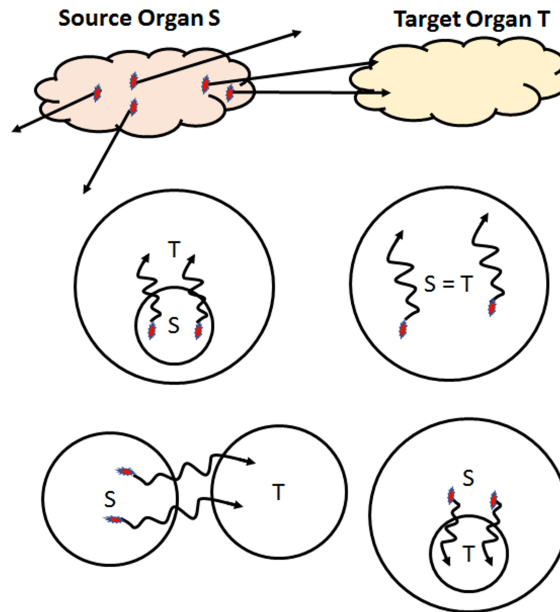


FIGURE 1.2: Schematic diagram for several source and target organ configurations.

T (in grams, g). ‘Absorbed fraction $AF(T \leftarrow S)_R$ ’ is the fraction of energy absorbed in the target organ T per emission of radiation type R in the source organ S. Alpha and beta particles have less penetrating power hence AF will be zero if S and T are not the same whereas AF will be unity if S and T are the same. In case of gamma or x-ray photons AF will always be a fractional value which is calculated by Monte Carlo simulations methods for photon transport in a medium.¹¹

1.2.2 Number of transformations in source organs, $U_s(50)$

Number of Transformations in Source Organs, U_s , is defined as the number of atoms of radionuclides that decay in each source organ S during the 50-year period over which the committed equivalent dose is defined following single intake. This number is equal to the time integral of the activity of the radionuclide in the organ over this period. Radioactive materials are transported to various tissues and organs (depends on metabolism of the element which is described by biokinetic models) via body fluids,

where they enter following inhalation or ingestion. The activity at any time t , is given by

$$A(t) = A(0)e^{-\lambda t}$$

The number of transformation $U_S(50)$, during 50 years period, following 1 Bq intake is given as follows

$$U_S(50) = \int_0^{50} A(t)dt = A(0) \int_0^{50} e^{-\lambda t} dt = \frac{A(0)}{\lambda} [1 - e^{-\lambda t}]$$

1.2.3 Committed equivalent dose

When radionuclide is present inside body, it will keep on irradiating the tissues till it is fully cleared from the body either through radioactive decay or biological removal. Therefore, body is committed to receive internal dose for a period T. ICRP recommends this period as 50 years for occupational workers and 70 years for members of public. Total number of radioactive transformations occurring in this time period is denoted by U_S as defined above. The committed equivalent dose to the target organ T from the entire source organs S, over which the introduced radionuclide is distributed, is estimated by the summation of product of $SEE(T \leftarrow S)_R$ and U_S over all source organs S:

$$H_T(50) = \sum_S U_S(50) SEE(T \leftarrow S); \quad (1.5)$$

Where $U_S(50)$ is the total number of nuclear transformations in 50 years in source region S following an acute intake.

1.2.4 Committed effective dose

Committed Effective Dose (CED) represents effective dose that a person is committed to receive for a period T. CED is defined as the summation of the product of committed equivalent dose of a tissue and appropriate tissue weighting factor w_T for all the target

organ in the body. Unit of CED is same as effective dose i.e. Sv. It is whole body dose for a committed period T. CED is calculated as follows:

$$E(50) = \sum_T w_T H_T(50) \quad (1.6)$$

If a person receives 50 mSv CED it signifies that he will get 50 mSv in 50 years, each year a fraction (radionuclide dependent) of 50 mSv will be received. Although worker will receive CED over period of 50 years, but for radiation protection purpose CED will be assigned to the year in which intake has occurred for dose records.

1.2.5 Dose coefficient

Dose coefficient is defined as the CED received for unit Bq intake of radioactivity. It is expressed in Sv.Bq⁻¹. One Bq of intake is taken into consideration and biokinetic model of a radionuclide is solved to get time dependent retained activity in various organs. Us is calculated for time period T and $SEE(T \leftarrow S)_R$ is calculated using absorbed fractions $AF(T \leftarrow S)_R$ for all important source and target organs and finally CED is estimated using equation 1.6. Value of CED estimated in this case will be dose coefficient for the radionuclide as we have considered 1 Bq intake.

1.2.6 Annual limit on intake (ALI)

ALI for a radionuclide is defined as, intake activity (Bq) that would result in the maximum recommended annual dose if inhaled or ingested. In case of occupational radiation workers, ICRP recommends a primary dose limit of 100 mSv over a 5 year period, with a maximum in any one-year of 50 mSv or an average of 20 mSv per year.¹¹ According to ICRP, *ALI* is the annual intake that would lead to committed effective dose (a 50 year dose commitment) not exceeding 20 mSv. The ALI for ingestion and

inhalation are thus calculated by:

$$ALI = \frac{0.02}{\sum_T w_T H_T(50)} Bq \quad (1.7)$$

Where, denominator is the CED per unit intake of radionuclides by ingestion or inhalation.

1.3 MATHEMATICAL SOLUTION OF A BIOKINETIC MODEL

Any biokinetic model is represented by various compartments representing different parts of the body organs. Compartment is a term introduced for an organ, part of an organ or a group of organs. If activity removal rate from a organ follows multi component decay then the organ is divided into various compartments corresponding to each component of the decay rate. Environment is also one of the compartments to take care of intake or excretion.

Clearance of a radionuclide from a compartment is governed by its metabolic clearance rate (biological) and radioactive decay rates λ_B and λ_R respectively. Both the processes are characterized independently by their respective half-lives.

Biological half-life, T_B : The time taken for a biological system, such as a tissue compartment or the whole body, to eliminate, 50% of the activity of a radionuclide that has entered it by natural biological processes other than radioactive decay.

Effective half-life, T_{eff} : The time taken for the amount of a radionuclide deposited in a living organism to be reduced by 50% as a result of the combined action of radioactive decay and biological elimination.

$$T_B = \frac{0.693}{\lambda_B}; \quad T_R = \frac{0.693}{\lambda_R}$$

the effective rate of clearance λ_{eff} from compartment is given by,

$$\lambda_{eff} = \lambda_B + \lambda_R = \frac{0.693}{T_{eff}}$$

where,

$$T_{\text{eff}} = \frac{T_R T_B}{T_R + T_B}$$

If there are n compartments to represent a biokinetic model, then rate of change of number of atoms N_i in i^{th} compartment is given by following equation:

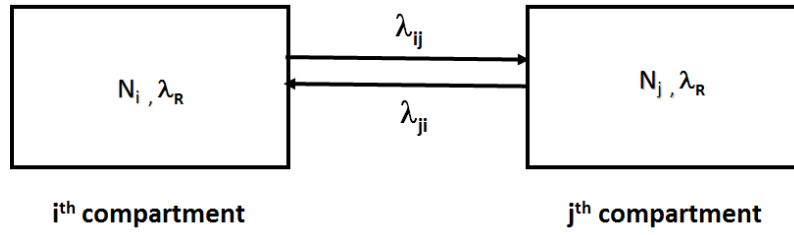


FIGURE 1.3: Representation of the compartments in a biokinetic model.

$$\frac{dN_i}{dt} = \sum_{\substack{j=1 \\ j \neq i}}^n \lambda_{ji} N_j - \sum_{\substack{j=1 \\ j \neq i}}^n \lambda_{ij} N_i - \lambda_R N_i \tag{1.8}$$

to solve this equation, it is rearranged in the following form:

$$\frac{dN_i}{dt} = \sum_{\substack{j=1 \\ j \neq i}}^n r_{ij} N_j + r_{ii} N_i = \sum_{i=1}^n r_{ij} N_i \tag{1.9}$$

where,

$$r_{ij} = \lambda_{ji}; \quad r_{ii} = - \sum_{\substack{j=1 \\ j \neq i}}^n \lambda_{ij} - \lambda_R$$

equation 1.9 can be written as

$$\frac{dN}{dt} = RN \Rightarrow N = e^{Rt} N_{(t=0)} \tag{1.10}$$

here, N is column matrix $N = \begin{bmatrix} N_1 \\ \cdot \\ \cdot \\ N_n \end{bmatrix}$ and R is another $n \times n$ matrix $R = \begin{bmatrix} r_{11} & \dots & \dots & r_{1n} \\ \cdot & \dots & \dots & \cdot \\ \cdot & \dots & \dots & \cdot \\ r_{n1} & \dots & \dots & r_{nn} \end{bmatrix}$

The main challenge in solving equation 1.10 is in calculation of exponential of a matrix

R . There are several ways to find exponential of matrix, using power series expansion is one of them. The exponential of R , denoted by e^R or $\exp(R)$, is the $n \times n$ matrix given by the power series

$$e^R = \sum_{n=0}^{\infty} \frac{1}{n!} R^n$$

where R^0 is defined to be the identity matrix I_n with the same dimensions as of R . This method gives values of N which can be used for estimation of retained activity in any organ at time t . Retention factors $m(t)$ and number of transformations U_S can be calculated with this method.

1.4 DIRECT METHOD FOR INTERNAL CONTAMINATION MONITORING

Internal doses cannot be measured directly; they can only be assessed from measured quantities such as body/organ activity content, excretion rates or airborne concentrations of radioactive material. The measurement of whole body/ organ content of radionuclides is carried out using external detectors. by whole body/ organ monitoring method which is also called direct method or in-vivo monitoring. Intake and committed effective dose (CED) (also referred as internal dose) from these measured quantities is estimated using appropriate biokinetic and dosimetric models published by ICRP.⁵ In-vivo or direct method involves direct measurement of gamma or x-ray photons emitted from internally deposited radionuclides using external detection systems. This method is also known as in vivo monitoring, body/organ activity measurements, whole body monitoring, lung counting or whole body counting. Gamma or X- rays (including bremsstrahlung by high energy β emitted by the radionuclide) of energies greater than few (keV) can be used for direct measurements as these can penetrate the body and reach the detector placed above the body of the person. Isotopes of Uranium, Plutonium, Americium and other actinides

in addition to fission and activation products (e.g. ^{60}Co , ^{137}Cs , ^{131}I , ^{239}Pu , ^{241}Am , ^{235}U , ^{238}U etc.) can be detected by this method. Direct method offers the advantage of a rapid and convenient estimate of the total activity in the body or a defined part of the body at the time of measurement; when it is sufficiently sensitive. In-vivo measurements are less dependent on biokinetic models than in-vitro measurements, but they suffer from calibration uncertainties, especially for low energy photon emitters. There are certain requisites of In-vivo measurement which involve shielding for background reduction, radiation detectors, electronic instrumentation setup, phantoms for calibration, counting geometry/technique and data analysis (computational set up).

1.5 PRACTICAL APPROACH FOR CED ESTIMATION

Dosimetric quantities described above cannot be estimated practically as we cannot measure energy deposited in each tissue or organ. To overcome this problem, first activity is measured in any organ/whole body using direct method. This measured activity at time t , M_t , is divided by appropriate retention factor $m(t)$ to estimate intake I , activity entered the body at time $t = 0$. Finally, Intake is multiplied by dose coefficient to get committed effective dose, i.e., the effective dose received by the worker by internally deposited radionuclides in period of 50 years since intake.¹¹ Schematics of steps involved estimation of internal dose received by a person is given in Figure1.4. These steps are described below:

1.5.1 Estimation of activity

Activity present at the time of monitoring is calculated by dividing net count rate (cps) in an energy region of interest (ROI) with the respective counting efficiency (cps/Bq) of the detection system determined using realistic phantom measurements.

$$\text{Measured Activity, } M(\text{Bq}) = \frac{\text{Net count rate (cps)}}{\text{Counting Efficiency (cps Bq}^{-1}\text{)}} \quad (1.11)$$

1.5.2 Estimation of intake

The activity present at the time of measurement is used to estimate intake by using appropriate retention factors which depend on the biokinetic behavior of the radionuclide. The retention factors for important radionuclides, for different routes of intake are given in ICRP 78.⁵ The intake for any person can be evaluated directly from the measured result i.e. from the retained activity in any organ or whole body.

$$\text{Intake, } I(\text{Bq}) = \frac{M(\text{Bq})}{m(t)}$$

Where, M is measured activity at the time of monitoring and $m(t)$ is retention factor at time t . For routine monitoring, it is assumed that for all exposures, intake took place in the midpoint of the monitoring interval of T days and $m(t)$ will be $m(T/2)$. In case of special monitoring when time of intake is known $m(t)$ value corresponding to that time is used.

1.5.3 Estimation of committed Effective Dose

Intake due to any radionuclide is multiplied with the respective dose coefficient (CED per unit intake), to calculate committed effective dose. Finally, CED is given as:

$$CED(\text{Sv}) = \text{Intake}(\text{Bq}) * \text{Dose Coefficient}(\text{SvBq}^{-1}) \quad (1.12)$$

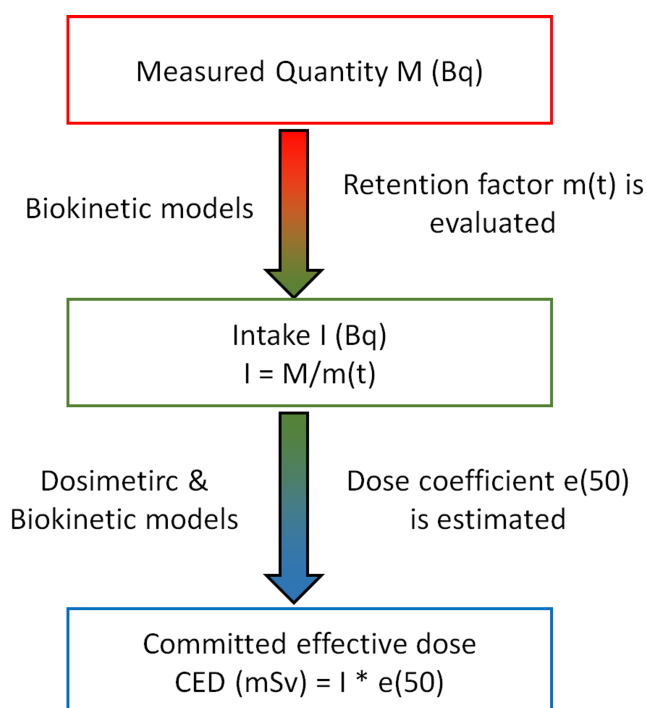


FIGURE 1.4: Steps involved in the internal dosimetry for CED estimation.

TABLE 1.3: Estimated CED Values for MDA equivalent inhaled activity of Pu/Am at different monitoring frequency.

Radionuclide	MDA (lungs) Bq	ALI Bq	Absorption type	Corresponding CED (mSv) 180 days post intake	Corresponding CED (mSv) 7 days post intake
^{241}Am (in-vivo)	5	740	Type-M	11	2.6
^{239}Pu (in-vivo with ^{241}Am as tracer) (Pu: Am = 3:1)	15	(625)	Type-M	40	9
	15	(2400)	Type-S	4	2
^{239}Pu (in-vivo with ^{241}Am as tracer) (Pu: Am = 10:1)	50	(625)	Type-M	133	31
	50	(2400)	Type-S	13	7
^{239}Pu (direct Pu in-vivo measurement)	2000	(625)	Type-M	5333	1231
	2000	(2400)	Type-S	519	277
^{239}Pu (in vitro)	0.5 mBq d ⁻¹	(625)	Type-M	3	1
	0.5 mBq d ⁻¹	(2400)	Type-S	26	14

1.6 DECORPORATION OF ACTINIDES

Isotopes of Pu/Am are having very high dose coefficients, hence their ALI values are very less as given in Table 1.3. ALI values for Type M compounds of Pu/Am is less than 750 Bq and for Type S compounds ALI is about 2400 Bq. If we calculate CED after 180 days post intake of MDA level of activity using various techniques, we can observe from the Table 1.3 that in several cases the CED exceeds the dose limit of 20 mSv . The question arises if any radiation worker has internal contamination at ALI level or more what actions should be taken to reduce the dose received by the worker. In case of external contamination, principal of time, distance and shielding applies to reduce the received dose (i.e. minimize the time of exposure, increase the distance between the person and radioactive source or provide appropriate shielding). But in case of internal contamination radioactive source is inside the body of the person hence these principles are not effective and the most effective method to reduce internal dose is by enhancing the biological excretion of systemic activity. In case of actinides, chelation mechanism is used for enhancing the radionuclide excretion. Chelating compounds bind with the radionuclide in a ring like highly stable structure and gets eliminated by urinary excretion path. Figure 1.5 shows schematic representation of chelation mechanism for decorporation of any metal.

At present trisodium salt of Calcium di-ethylene tri-amine penta-acetic Acid (Ca-DTPA) is the only FDA approved chelating agent which is used for Pu/Am decorporation. It is given to the person either through nebulizer or through intravenous (IV) administration by IV or intramuscular (IM) routes. Ca-DTPA binds Pu/Am present in the body fluids in elemental form and the chelated complex is excreted. There are several limitations of this drug as follows (1) it cannot be administered through oral path in the form of tablets or capsules. (2) when there is intake due to several mixed radionuclides (viz. Uranium and Pu/Am) Ca-DTPA is not much effective. (3) Also it cannot penetrate cells hence the radioactive material deposited in side bones, liver or

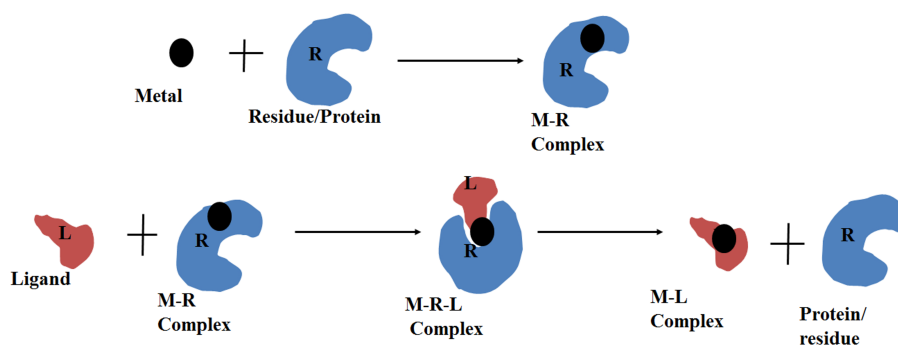


FIGURE 1.5: Schematics for decorporation of metal using chelation mechanism

other cells cannot be easily removed with this drug.

There is a need to develop new drugs or chelation mechanism which can overcome these difficulties. drug development is very tedious process which needs lots of chemical compounds to be studied at different level so that it can be used as drug. The main challenge is to choose a lead compound among more than 10^{20} drug like compounds. With the advancement in computational hardware as well as theoretical models, computer aided drug designing has emerged as a new field in drug development process.

1.6.1 Drug development process

In any drug discovery or development process first, we need to know about the disease, its target organ/protein, its root cause. Once we isolate the protein or other biological residue responsible for the disease then various chemical compounds can be tested which can cure the changes occurred in that protein. If the lab scale results are satisfactory then pre-clinical testing on animals is carried out. In the next step the drug or compound is formulated in larger scale and investigational new drug application is filed for approval of human clinical trials. Satisfactory results lead the tested drug to be used for disease by getting the food and drug administration (FDA) approval. The whole process can take decades for any new drug development. In the whole process computational chemistry

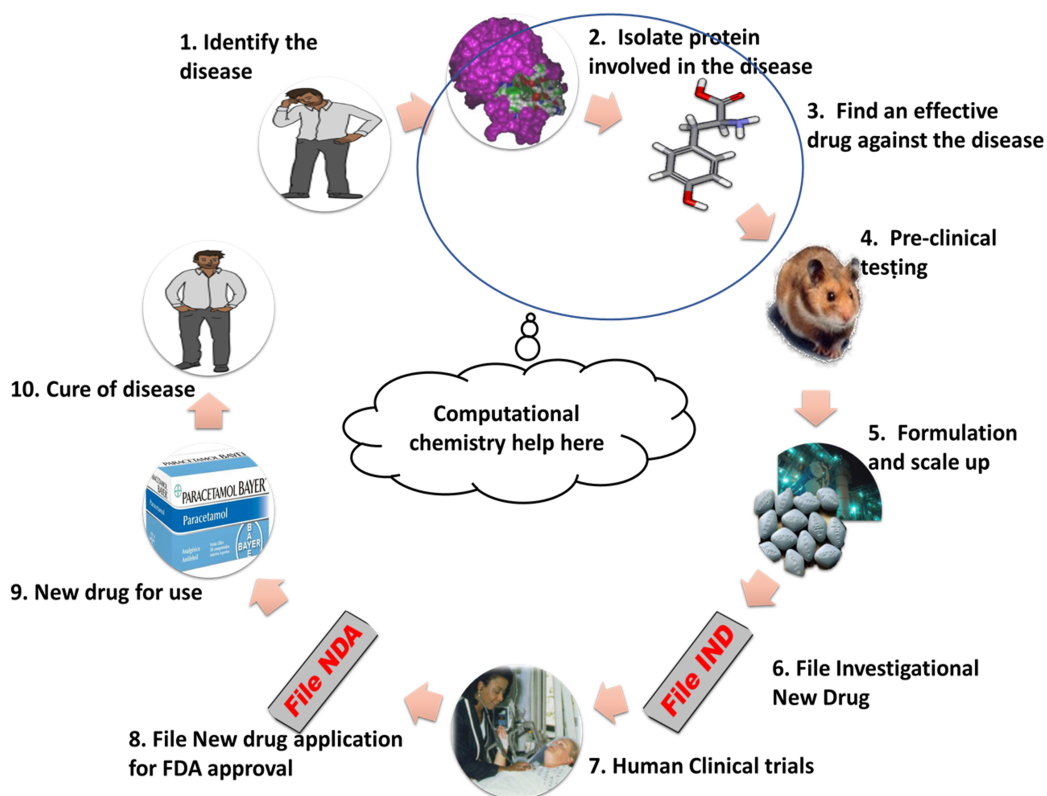


FIGURE 1.6: Schematics for decorporation of metal using chelation mechanism

can help delineating the structural, binding, kinetic and thermodynamic aspects of various biomolecules/proteins with and without drug compounds. Multi scale modelling approach can help in predicting plausible lead compounds as well as in speciation studies of various chemical and biomolecules.

Pu and other actinides in general are deposited to various organs *viz.* liver, lungs, skeleton etc. Biochemistry of these radionuclides is still very promising field of research as most of the molecular reaction mechanism are unexplored. Iron carrier serum transferrin (sTf) is found to bind several actinides but molecular level understanding of the reaction mechanisms is still obscure. sTf is one of the important proteins responsible for the trafficking of actinide ions within the body. Interaction of sTf with Pu(IV), Th(IV) and Cm(III) at serum and endosomal pH conditions is investigated *in-silico* in this thesis.

1.6.2 Serum transferrin

In this work complexes of actinides with serum transferrin (sTf) are investigated in serum and acidic pH conditions using multi-scale modelling approach. Also, *in-silico* investigations are carried out to find suitable chelating compounds for decorporation of Pu from our body. sTf is an important member of the homologous iron-binding glycoprotein family called as transferrins which is responsible for control of iron level in the body. Dietary iron in our body is mainly bound to sTf, then transported in the blood serum and finally delivered to cells through a process of receptor mediated endocytosis. sTf protein is present at a concentration of approximately 3mg/ml in human serum and is about 30 % saturated with Fe (III). While this renders the blood serum accessible for certain therapeutic metal ions to bind and transport, it also become vulnerable for other toxic metals to follow the major iron acquisition pathway receptor mediated endocytosis.¹²⁻¹⁵ About 30 other metal ions including thorium, curium, plutonium are found to make complexes with sTf.¹⁶

Stability of the complexes formed by actinides with sTf is found to be in following order: $\text{Pu}^{4+} > \text{Th}^{4+} > \text{Np}^{4+} \gg \text{U}^{\text{VI}}\text{O}_2^{2+} > \text{Cf}^{3+} > \text{Am}^{3+} > \text{Cm}^{3+}$.¹⁷ Several experimental studies focused on the interactions of transferrin with a variety of actinide (An) ions are reported in literature.¹⁸⁻²⁵ It is observed from these experimental studies that tetravalent An ions interact differently compared to trivalent ions. Complexes of sTf loaded with tetravalent actinides are more stable and their coordination with the sTf binding site is different to that of trivalent An ions. Even in the case of tetravalent ions, Pu(IV) and Th(IV) have been reported to bind differently.^{26,27} Although non-iron metal ions are studied at large scale for their interactions with sTf and huge amount of data is available,¹⁴ yet sTf loaded with An ions are not much explored as hardly any specific information at the molecular level is available. Crystal structures of An loaded sTf are not yet reported to the best of our knowledge. Similarly, how physiological carbonate ion

work in tandem with sTf to bind An ion is obscure. Whereas this is an important issue to be probed at the molecular level, since it relates to the biological fate of An trafficking in human body through sTf. In effect, the structural and thermodynamic properties of An-sTf systems are of enormous importance in providing guidance on the structures, affinities, and design of potential specific chelating agents that might be used to eliminate an incorporated radionuclide before the initiation of toxic effects. Experiments on biochemical studies of these radionuclides are sometimes limited due their radioactive nature as these studies require various radiological safety measures to prevent their radioactive contamination. In the pursuit of molecular details of binding, a combination of DFT and MD simulation is a very attractive avenue.^{28,29} Various computational methods are used to study the biological interactions at different scales of time and length corresponding the type of process as briefed in following section. In this thesis multi-scale modeling is used to study interactions of Plutonium, Thorium and Curium with sTf at molecular level.

1.7 MULTI-SCALE MODELLING IN BIOLOGICAL SYSTEMS

Various biological processes occur in a wide range of length and time scales in biomolecules; for example, atomic fluctuations, side chain motions and loop motions categorized as local motion and occur between (0.01 to 5 Å) length scale and (10^{-15} to 10^{-1} s) time scales respectively. Helix Motions, domain motions (hinge bending) and subunit motions, called as rigid body motions occur between (1 to 10 Å) length scale and (10^{-9} to 1 s) timescale. Whereas helix coil transitions, dissociation/association, folding and unfolding, called as Large-scale motions occur in length scale over 5Å and timescale range of (10^{-7} to 10^4 s). Various length and time scales and appropriate modelling techniques used in these scales are shown in Figure 1.7. Quantum mechanics (QM) is needed to study processes involving bond making and bond breaking

phenomenon and other internal molecular conformations. All-atom molecular mechanics MM is used to study various biological processes which describe H-bond networks and various protein/lipid interactions. A Coarse-grain (CG) molecular dynamics (MD) is used to explore various large-scale dynamic distribution of lipids and proteins, as well as lipid phase separation. Even supra-coarse-grain methods or continuum modelling is being used for larger scales, such as lipid-mediated protein organization or modelling the processes involving whole-cell.¹

There are various disciplines in the field of computational chemistry which vary in their sophistication: Cheminformatics, Molecular mechanics, Semi-empirical methods and Ab initio quantum chemistry etc. are among them. All these methods, except ab initio methods, rely on empirical information (parameters, energy levels, force fields, etc.). In this thesis work, specially Density functional theory(DFT), molecular dynamics (MD) and metadynamics are used for studying interaction of actinides with serum transferrin protein.

1.8 DENSITY FUNCTIONAL THEORY (DFT)

If we try to solve Schrödinger equation for N-body system using ab initio methods without any approximation it becomes practically impossible as such an approach will be beyond the current computational infrastructure capabilities. Wave function theory will be very difficult to use and interpret for many body systems. Therefore, we must involve some approximations to render the problem soluble albeit tricky. In spite of using wave function, an approximate physical observable can be used to get ground state energy of the system. Density functional is such an observable which is used to obtain an approximate solution to the Schrödinger equation of a many-body system. A Functional is a function of function. Electron density is measure of probability of any electron being present at any location.

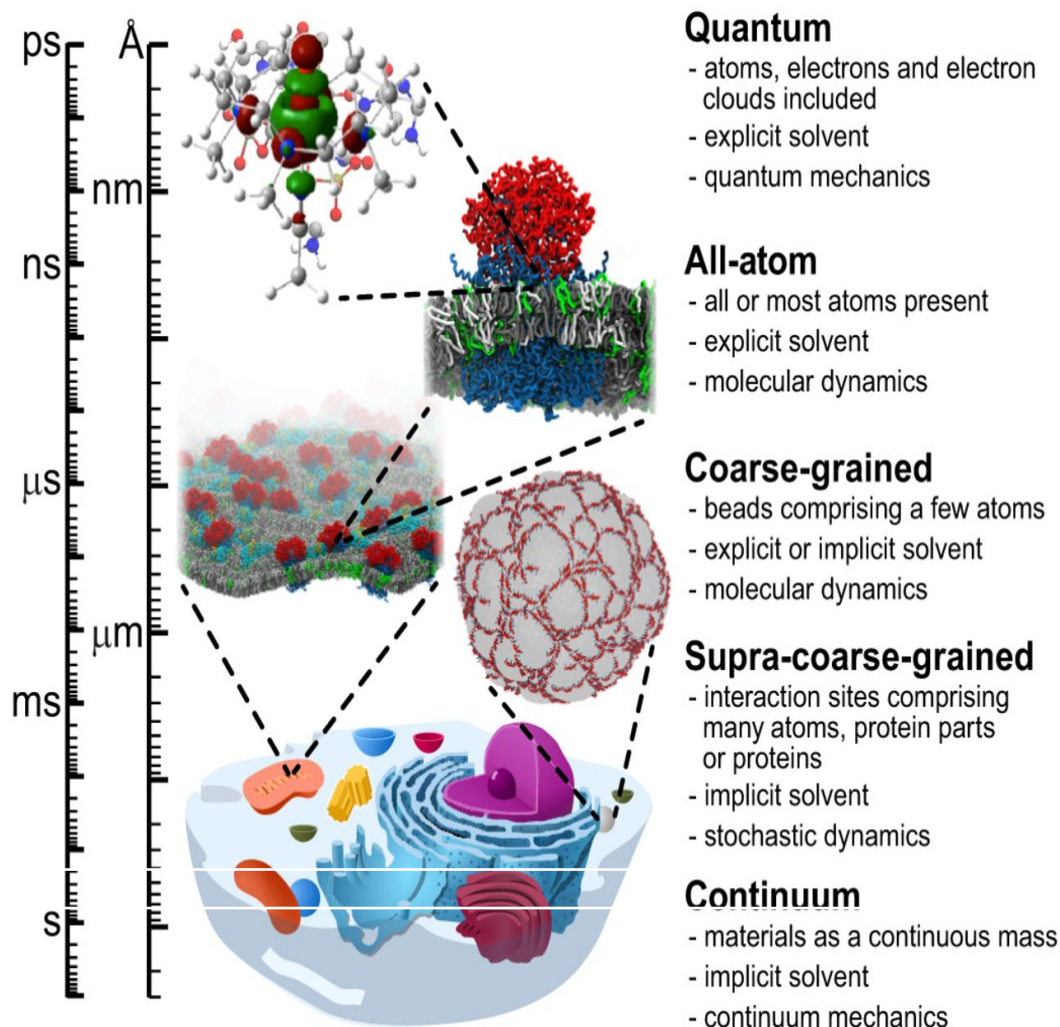


FIGURE 1.7: Computational ‘microscopy’ and its different levels of resolution. A computational ‘microscope’ uses computational resources and the underlying physicochemical relationships between atoms to study cell membranes at an unrivalled level of detail. The computational ‘microscope’ can use different computational modelling methods depending on the resolution (length and time scales) required. Reproduced / adapted with permission from Journal of Cell Science.¹

Number of electrons per unit volume in a given state is the electron density for that state.

$$\rho(\mathbf{r}) = N \int \dots \int \Psi(r, x_2, \dots, x_N) \Psi(r, x_2, \dots, x_N) dx_2 \dots dx_N$$

ρ integrated over all space gives N: $N = \int \rho(r) dr$

1.8.1 Hohenberg and Kohn theorems

In 1964, Hohenberg and Kohn³⁰ have proved two theorems which establish DFT as a robust most widely used quantum chemical methodology. Electrons interact with one another and with an external potential.

Theorem 1

“The external potential is a unique functional of the electron density in the ground state, and therefore the total energy is also a functional of the ground state electron density.”

$$E[\rho] = F[\rho] + \int V_{\text{ext}}(r)\rho(\mathbf{r})dr$$

A consequence of the first Hohenberg-Kohn theorem is that all properties of a system are determined from only the ground state electron density.

Corollary: the ground state density uniquely determines the potential and thus all properties of the system, including the many-body wave function. In particular, the H–K functional, defined as $F[\rho] = T[\rho] + U[\rho]$, is a universal functional of the density (not depending explicitly on the external potential).

Theorem 2

This theorem is based on the principle that the density obeys a variational principle.

“The functional that delivers the ground state energy of the system gives the lowest energy if and only if the input density is the true ground state density.” For any positive integer N and potential $v(\mathbf{r})$, a density functional $F[\rho]$ exists such that

$$E_{(v,N)}[\rho] = F[\rho] + \int v(\mathbf{r})\rho(\mathbf{r})d^3r$$

obtains its minimal value at the ground-state density of N electrons in the potential $v(\mathbf{r})$.

The minimal value of $E_{(v,N)}[\rho]$ is then the ground state energy of this system.

1.8.2 Kohn-Sham equations

The many-electron wave function used to solve Schrödinger equation will be of the form

$$\Psi(x) = \Psi(r_1, r_2, \dots, r_N)$$

using wave function approach to estimate total energy of the many body system will be almost impossible. Kohn-Sham (KS) in 1965 proposed an ansatz³¹ to replace the fully interacting system with fictitious system of non-interacting electrons. In this assumption the wave function is decomposed into a product of single-electron orbitals $\Psi_i(r)$ and this ansatz corresponds to a mean-field approach. Due to this simplification energy contribution due to correlation and antisymmetric exchange of electrons is neglected. Therefore, as a correction, an exchange correlation term is introduced in the Hamiltonian. The functional $E_{XC}[\rho(r)]$ term does not only account for the correlations but also for the unconsidered exchange interactions. The modified Hamiltonian yields a single-particle Schrödinger equation on applying the variation principle to it. This single particle equation is also referred to as Kohn-Sham equation in DFT. The following KS equation includes an effective potential $v_{eff}(r)$, which is produced by the Coulomb forces of all other electrons and nuclei and incorporates the exchange and correlation interactions.

$$\left(-\frac{\hbar^2}{2m_e} \nabla^2 + v_{\text{eff}}(\mathbf{r}) \right) \psi_i^{KS}(\mathbf{r}) = \varepsilon_i^{KS} \psi_i^{KS}(\mathbf{r}) \quad (1.13)$$

where,

$$v_{\text{eff}}(\mathbf{r}) = V_{\text{eN}}(\mathbf{r}) + V_{\text{ee}}(\mathbf{r}) + V_{\text{XC}}(\mathbf{r}) \quad (1.14)$$

$$V_{\text{XC}}(\mathbf{r}) = \frac{\delta E_{\text{XC}}[\rho_0(\mathbf{r})]}{\delta \rho(\mathbf{r})}$$

and

$$V_{\text{ee}}(\mathbf{r}) = \int \frac{\rho_0(r')}{|r - r'|} dr'$$

KS wave function ψ_i^{KS} is estimated by solving above equation 1.13 and electron density $\rho(\mathbf{r})$ can be estimated as follows

$$\rho(\mathbf{r}) = \sum_i^N |\psi_i^{KS}(\mathbf{r})|^2 \quad (1.15)$$

Total energy of the system can be estimated from the electron density given in equation 1.15 as follows

$$E = E[\rho(\mathbf{r})]$$

$$E[\rho] = T_s[\rho] + \int d\mathbf{r} v_{\text{ext}}(\mathbf{r})\rho(\mathbf{r}) + E_H[\rho] + E_{xc}[\rho]$$

If we assume electrons are mutually non-interacting in Hartee-Fock sense that is each electron sees average of all other electrons and correlation of electrons is not taken into account then kinetic energy term can be written as follows

$$T_s[\rho] = \sum_i^N \int d\mathbf{r} \psi_i^{KS*}(\mathbf{r}) \left(-\frac{\hbar^2}{2m} \nabla^2 \right) \psi_i^{KS}(\mathbf{r})$$

E_H is the Hartree (or Coulomb) energy, which represent electron-electron repulsive interaction term

$$E_H = \frac{e^2}{2} \int d\mathbf{r} \int d\mathbf{r}' \frac{\rho(\mathbf{r})\rho(\mathbf{r}')}{|\mathbf{r} - \mathbf{r}'|}$$

1.8.3 Various approximations for exchange correlation functional

There are different approximations for exchange and correlation terms

Local density approximation LDA

In this approach where the value of E_{xc} , at some position \mathbf{r} , can be computed exclusively from the value of density ρ at that position, i.e., the ‘local’ value of ρ . a local-density approximation for the exchange-correlation energy is written as

$$E_{xc}^{\text{LDA}}[\rho] = \int \rho(\mathbf{r})\epsilon_{xc}(\rho(\mathbf{r})) d\mathbf{r}$$

where ρ is the electronic density and ϵ_{xc} is the exchange-correlation energy per particle of a homogeneous electron gas of charge density ρ . The exchange-correlation energy is decomposed into exchange and correlation terms linearly, so that separate expressions for E_x and E_c are sought.

$$E_{xc} = E_x + E_c$$

Local spin density approximation LSDA

The extension of density functional to spin-polarized systems is straightforward for exchange, where the exact spin-scaling is known, but for correlation further approximations must be employed. A spin polarized system in DFT employs two spin-densities, ρ_α and ρ_β with $\rho = \rho_\alpha + \rho_\beta$, and the form of the local-spin-density approximation (LSDA) is

$$E_{xc}^{\text{LSDA}}[\rho_\alpha, \rho_\beta] = \int \mathbf{dr} \rho(\mathbf{r}) \epsilon_{xc}(\rho_\alpha, \rho_\beta)$$

Generalized gradient approximation GGA

As the LDA approximates the energy of the true density by the energy of a local constant density, LDA approximates fail in situations where the density undergoes rapid changes such as in molecules. In such cases gradient of the electron density is also considered in the functional, the so-called Generalized Gradient Approximation (GGA). Symbolically this can be written as

$$E_{xc} = E_{xc}[\rho(\mathbf{r}), \nabla\rho(\mathbf{r})].$$

GGA approximation leads to a large improvement over LDA results with accuracy approaching that of correlated wave function methods such as MP2 and in some cases surpassing these.³² Contrary to only one LDA there are several parametrization of the GGA. Some of these are semi-empirical, while others are found entirely from first principles. A commonly used functional is the PW91 functional, due to Perdew and Yang.³³

Hybrid functional approximation

If a portion of exact exchange from Hartree–Fock theory is incorporated with the rest of the exchange–correlation energy from other sources (ab initio or empirical), hybrid functionals are derived. The exact exchange energy functional is expressed in terms of the Kohn–Sham orbitals rather than the density, so is termed an implicit density functional.

B3LYP functional

One of the most commonly used hybrid functional is B3LYP, which stands for “Becke, 3-parameter, Lee–Yang–Parr”. B3LYP exchange-correlation functional is³⁴

$$E_{xc}^{B3LYP} = (1 - a_0)E_x^{LSDA} + a_0E_x^{HF} + a_x\Delta E_x^{B88} + a_cE_c^{LYP} + (1 - a_c)E_c^{VWN3} \quad (1.16)$$

where $a_0 = 0.20$, $a_x = 0.72$, and $a_c = 0.81$. E_x^{B88} and E_c^{LYP} are generalized gradient approximations: the Becke88 exchange functional³⁵ and the correlation functional of Lee, Yang and Parr³⁶ for B3LYP respectively. E_c^{VWN3} is the VWN local-density approximation to the correlation functional.³⁷ Exchange and correlation energy contribution can be separated as E_x^{B3LYP} and E_c^{B3LYP} respectively and can be written as follows :

$$E_x^{B3LYP} = 0.8E_x^{LDA} + 0.2E_x^{HF} + 0.72\Delta E_x^{B88}$$

$$E_c^{B3LYP} = 0.19E_c^{VWN3} + 0.81E_c^{LYP}$$

1.8.4 Self-consistent way for DFT

A schematic representation of a self-consistent loop in this numerical method is depicted in Figure 1.8. For a given system first a initial guess of the electron density is made then effective potential is calculated using equation 1.14 and Kohn-Sham equation 1.13 is solved to find KS wave function. Finally, electron density and total energy of the system is estimated checked if total energy is converged to the minimum E or not. If it is not converged then this self-consistent cycle is repeated for several iterative steps till

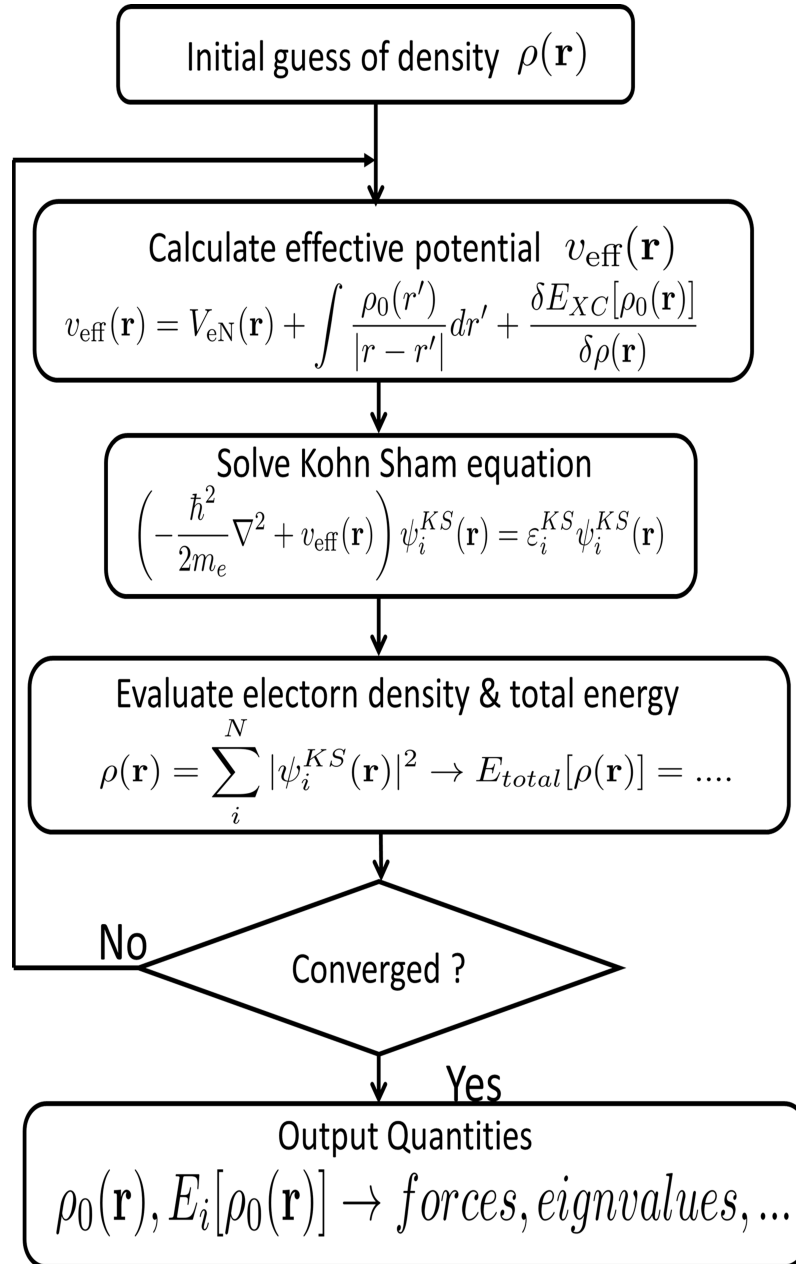


FIGURE 1.8: Flow chart of the self-consistent iteration scheme for DFT.

convergence is achieved. The obtained energy minima correspond to the stable configurations, which are physically realized and thus important for the determination of stable defect configurations. Then using this converged structure desired quantities like density, energy, Eigen values, forces etc. or estimated.

1.8.5 Basis set

In quantum chemistry, the “basis set” usually refers to the set of (non-orthogonal) single-electron wave functions which is used to make molecular orbitals. Individual molecular orbital can be expressed as linear combination of finite set of N prescribed one electron functions called as basis functions. If $\phi_1, \phi_2, \dots, \phi_N$ are the basis functions then individual molecular orbital ψ_i can be written as follows

$$\psi_i = \sum_{\mu=1}^N c_{\mu i} \phi_{\mu}$$

where $c_{\mu i}$ are molecular orbital expansion coefficients. There are two types of basis functions (also called Atomic Orbitals (AO)) commonly used in electronic structure calculations: Slater Type orbitals (*STO*) and Gaussian Type orbitals (*GTO*). *STO* can be written in the functional form shown below in equation 1.17

$$\begin{aligned} \chi_{\zeta,n,l,m}(r, \theta, \phi) &= NY_{l,m}(\theta, \phi) r^{n-1} e^{-\zeta r} \\ \chi_{\zeta,l_x,l_y,l_z}(x, y, z) &= Nx^{l_x} y^{l_y} z^{l_z} e^{-\zeta r} \end{aligned} \quad (1.17)$$

Here N is a normalization constant and $Y_{l,m}$ represents spherical harmonic functions. ζ controls the width of the orbital (large ζ gives tight function, small ζ gives diffuse function). l_x, l_y and l_z controls angular momentum

$$L = l_x + l_y + l_z$$

Whereas *GTOs* are represented using polar or cartesian coordinates as shown in eq 1.18

$$\begin{aligned} \chi_{\zeta,n,l,m}(r, \theta, \phi) &= NY_{l,m}(\theta, \phi) r^{2n-2-l} e^{-\zeta r^2} \\ \chi_{\zeta,l_x,l_y,l_z}(x, y, z) &= Nx^{l_x} y^{l_y} z^{l_z} e^{-\zeta r^2} \end{aligned} \quad (1.18)$$

STOs are considered superior to the *GTOs* in two respects due to the r^2 dependence in its exponential term. (1) *STO* has a “cusp” (discontinuous derivative) whereas a *GTO*

has zero slope at the nucleus, hence *GTOs* poorly represent the proper behaviour near the nucleus. (2) The “tail” of the wave function is poorly represented in *GTO* as it falls off too rapidly in comparison to *STO* at larger distances from the nucleus. A complete basis can be formed with *STOs* and *GTOs* both, but more *GTOs* are required compared with *STOs* for achieving a certain accuracy. As a thumb rule, for reaching a given level of accuracy as obtained with single *STO*, thrice *GTOs* are required.³⁸

1.8.5.1 Contracted Gaussian-type orbitals (*CGTOs*)

The radial derivatives in the *GTOs* vanish at the nucleus whereas the derivatives of *STOs* are non-zero, therefore, *GTO* function does not correctly represent the behaviour near nucleus. To overcome this weakness of *GTO* functions, contracted *GTO* is used in which two, three, or more *GTOs* are combined, with combination coefficients which are fixed and not treated as LCAO-MO parameters. A series of loose, medium and tight *GTOs* (represented by *GTOs* with small, medium, and large ζ values, respectively) are multiplied by contraction coefficients and summed to produce a *CGTO*. Such a *CGTO* helps in defining the proper ‘cusp’ (i.e., non-zero slope) at the nuclear center.

$$\chi(\text{CGTO}) = \sum_i^k (a_i \chi_i(\text{GTO}))$$

1.8.5.2 Designations of basis set size

Minimal basis set: One basis function (*STO*, *GTO*, or *CGTO*) is used for each atomic orbital in each atom.

Double-zeta (DZ) basis set: two basis functions for each AO are used.

Triple-zeta (TZ) basis set: three basis functions for each AO are used similarly for quadruple-zeta (QZ), 5Z, 6Z, ... respectively four, five and six basis functions are used for each AO. The presence of different-sized functions allows the orbital to get bigger or

smaller when other atoms approach it, adds flexibility to adequately describe anisotropic electron distribution in molecules.

1.8.5.3 Diffuse functions

Normal basis sets are often inadequate when the electron density exists far from nuclear centers. Diffuse functions with small zeta exponents are added in the basis sets to hold the electron far away from the nucleus. Diffuse functions are most required for anions, electronegative atoms (fluorine) with a lot of electron density. These are also necessary for accurate polarizabilities or binding energies of van der Waals complexes which are bound by dispersion. Let us consider H-C and C-N bonding in the HCN molecule. The H—C bond will primarily consist of the hydrogen's s-orbital and the p_z-orbital of carbon atom. The π -bond between C and N will consist of the p_x (and p_y) orbitals of C and N, and this bond will have a more diffuse electron distribution than the σ -bond between H and C atoms. Thus, the exponent for carbon's p-orbital will be smaller along the x-direction than along the z-direction. If only a minimum basis set is available (single set of p-orbitals), bond will not be properly represented and a compromise will be made. However, a DZ basis set, have two sets of p-orbitals having different exponents. The tighter function (with larger exponent) can represent the H—C σ -bond with a large coefficient, whereas the more diffuse function (with small exponent) can be used for describing the C—N π -bond. Thus, if we double the number of basis functions, a much better description of non-uniform electron distribution in different directions can be made.

1.8.5.4 Polarization functions

An atom's orbitals tend to slightly shift to one side or the other when surrounding atoms approach due to polarization. Polarization of an s orbital in one direction can be represented by mixing it with a p orbital. p orbitals can polarize if it is mixed with d

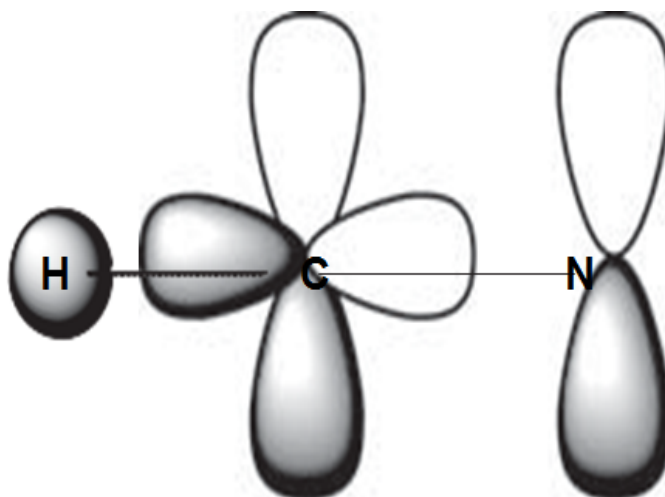


FIGURE 1.9: A double zeta basis allows for different bonding in different directions to consider diffusion and polarization of the orbitals

orbitals. In general, to polarize a basis function with angular momentum l , it is mixed with basis functions of angular momentum $l + 1$. Let us consider again the bonding in HCN in Figure 1.9 as described above. The bond between H and C is primarily represented by the s -orbital(s) of hydrogen and s and p_z -orbitals of carbon. The electron distribution along the bond and perpendicular to the bond will be different. Non-uniform electron distribution cannot be described if only s -functions are present on the hydrogen. However, if a set of p -orbitals is added to hydrogen, its p_z component will improve the description of the H—C bond. This way the p -orbitals introduces a polarization of the s -orbital(s). Similarly, d orbitals and f -orbitals can be used for polarizing p -orbitals and d -orbitals respectively.

1.8.5.5 Split valence basis set

Valence orbitals are more influenced by the surrounding compare to core orbitals. In split-valence basis only one basis function for each core AO and multiple basis for the valence AOs are used.

1.8.5.6 Pople-style basis set

These basis sets are developed by the late Nobel Laureate, John Pople, and mostly used by the Gaussian programs. Notation of these basis sets looks like: k-nlm++G** or k-nlm++G(idf,jpd).

STO-nG basis sets

These are Slater-type orbitals consisting of n primitive *GTOS* (*PGTOs*).³⁹ This is a single zeta (SZ)-type basis set and STO-3G basis is a widely used SZ basis set.

k-nlmG basis sets

In these basis sets k *PGTOs* for core electrons, n *PGTOs* for inner valence orbitals, l *PGTO* for medium valence orbitals and m *PGTO* for outer valence orbitals are used to describe AOs. * are used to for Polarization functions as follows single * indicates one set d polarization functions is added to non-H heavy atoms * is alternatively represented by (d) and two ** indicate one set d polarization functions added to heavy atoms and one set p polarization functions added to H atom, (d,p) is also used in place of **. If i set d and one set f polarization functions added to heavy atoms is indicated by idf whereas idf,jpd indicates i set d and one set f polarization functions is added to non-hydrogen atoms and j set p and one set d polarization functions added to hydrogen atom. For representation of diffuse functions + symbol is used. If one set p diffuse functions added to heavy atoms (non-H) single + is used whereas double ++ is used if one set p diffuse functions added to non-hydrogen heavy atoms and 1 s diffuse function is added to hydrogen atom.

Let us count primitive and contracted basis function for methane CH₄ molecule

6-31G(d,p): Here 6 Gaussians (G) are added to core electrons, 4G (3G+1G) are added to valence electrons, d polarization is added to the non-hydrogen atoms and p polarization to the hydrogen ones.

C— 1s (6G), 2s (3G+1G), 2p_x, 2p_y, 2p_z ([3G+1G] three times) + 6G (d polarizations- dxx, dyy, dzz, dxy, dyz, dxz)—total 28 gaussians

TABLE 1.4: Contracted and primitive basis functions for some Pople style basis sets for hydrogen, second and third row elements.

Basis	Hydrogen		Second row elements		Third row elements	
	Contracted	Primitive	Contracted	Primitive	Contracted	Primitive
STO-3G	1s	3s	2s1p	6s3p	3s2p	9s6p
3-21G	2s	3s	3s2p	6s3p	4s3p	9s6p
6-31G(d,p)	2s1p	4s	3s2p1d	10s4p	4s3p1d	16s10p
6-311G(2df,2pd)	3s2p1d	5s	4s3p2d1f	11s5p	6s4p2d1f ^a	13s9p ^a

^aMcLean–Chandler basis set.⁴⁰

H– 1s (3G+1G) + 3G (p-polarizations–px, py, pz)—total 7 gaussians for one H

so, for CH₄— 28 + 7x4 = 56 gaussians

1.8.5.7 Basis sets of Ahlrichs and Karlsruhe

R. Ahlrichs and group members have developed basis sets having similar quality as of DZ, TZ and QZ for elements up to Kr. In their basis sets, the Split Valence Polarized (SVP) basis set is represented as [3s2p] contraction of (7s4p) set of primitive functions (contraction 5,1,1 and 3,1), whereas the Triple Zeta Valence (TZV) basis set is a [5s3p] contraction of an (11s6p) set of primitive functions (contraction 6,2,1,1,1 and 4,1,1).^{41,42} The series is extended by a Quadruple Zeta Valence (QZV) basis set, being a [7s4p] contraction of a (15s8p) set of primitive functions with the contraction 8,2,1,1,1,1 and 5,1,1,1,. Later this work also included a general update of the SVP and TVP to produce the so-called Def2-SVP, Def2-TZVP, Def2-TZVPP, Def2-QZVP etc. basis sets.^{43,44}³⁸

1.8.6 Effective core potential

Ab initio methods including DFT are successfully applied to smaller systems containing first-row atoms. As atomic number increases, number of electrons also increases and for atoms further down the periodic table, these methods face a great computational

challenge. For atoms with large Z , computational time is enhanced manifold as $T \propto Z^{5.5}t_0Z^{6.5}$. To solve this problem, inner core electrons which are less influenced with the surroundings are represented by approximate pseudo potentials, called as effective core potential or (ECP), in spite of explicit basis functions. However, the valence electrons are treated explicitly. Use of ECPs is useful in most cases as molecular geometries as well as many chemical properties such as bond strengths, polarizabilities, electron affinities, and ionization potential are determined by valence electrons. With use of ECPs, computation time reduces as it depends on the screened nuclear charge, $Z^{\text{eff}} = Z - N_{\text{core}}$, where N_{core} is the number of electrons in some pre-defined core. Moving across a row of the periodic table, Z^{eff} increases like Z . The computation time-dependence is estimated to be approximately $T \propto (Z^{\text{eff}})^{3.4}$ which is significantly lower power than the previous $Z^{6.5}$. Effective core potentials (ECPs) are categorized small core, medium core, or large core ECP. ECPs are not only used for replacing the core, but also to represent relativistic effects, which are more prominent in large Z elements (some d block and f block elements) and confined to the core.

Taking bromine as an example, the all-electron calculation treats all 35 electrons explicitly ($1s^22s^22p^63s^23p^64s^23d^{10}4p^5$). In “small-core” ECP, 10 innermost electrons ($1s^22s^22p^6$) are replaced with pseudo potential, leaving the remaining 25 electrons to be treated explicitly. If complete block of ($1s^22s^22p^63s^23p^63d^{10}$) electrons is included then ECP leads to a “large-core” ECP replacing 28 electrons. This latter choice leaves the 7 ($4s^24p^5$) electrons to be treated explicitly:

1.8.7 Solvation effects

Most of the biological processes take place in some medium other than gas phase *viz.* either in aqueous, protein or some other. If we use gas phase QM calculations then estimated properties will not represent the actual system. To account for environmental conditions

solvation models are used. Two type of solvation is considered as follows:

Implicit solvation model: Implicit solvation model represent solvent as a continuous medium of permittivity ϵ surrounding the solute molecules outside a molecular cavity. The system is inserted by making a cavity in the continuum solvation. In this work continuum model having dielectric constant of water ($\epsilon=80$) and protein ($\epsilon = 5$) are used.

Explicit solvation model: In this model solvent molecule are added explicitly to provide proper solvation to the system. This method requires plenty of water molecules to be added explicitly hence increases the system size. This method is mostly used in molecular dynamics simulations.

1.9 MOLECULAR DYNAMICS

Molecular dynamics (MD) simulations is one of the important techniques in the theoretical study of biological systems in the field of biochemistry or biophysics. In this method, the time dependent behaviour of a molecular system is evaluated. With the advancements in the computer hardware and simulation algorithms MD simulations are now routinely used to investigate the structural, kinetic and thermodynamic properties of biomolecules and their complexes. MD simulations have helped in getting detailed information on various biological processes like fluctuations and conformational changes of proteins and nucleic acids metal ions transport in biological medium. They are also used for computer aided drug designs.

1.9.1 The ergodic hypothesis

An experiment performed in laboratory is usually a macroscopic sample which contains an extremely large number of atoms or molecules (\geq Avogadro number) sampling an enormous number of conformations. Averages corresponding to experimental observable

are defined in terms of ensemble averages in statistical mechanics. In statistical mechanics, ensemble averages are defined as follows:

$$\langle A \rangle_{\text{ensemble}} = \int \int A(\mathbf{p}^N, \mathbf{r}^N) \rho(\mathbf{p}^N, \mathbf{r}^N) d\mathbf{p}^N d\mathbf{r}^N \quad (1.19)$$

where $A(\mathbf{p}^N, \mathbf{r}^N)$ is the observable of interest which is a function of positions, \mathbf{r} and momenta, \mathbf{p} of the system. The integration is over all the possible \mathbf{r} and \mathbf{p} variables. $\rho(\mathbf{p}^N, \mathbf{r}^N)$ is probability density of the ensemble given as follows

$$\rho(\mathbf{p}^N, \mathbf{r}^N) = \frac{1}{Q} \exp\left[-\frac{H(\mathbf{p}^N, \mathbf{r}^N)}{k_B T}\right] \quad (1.20)$$

where k_B is Boltzmann's constant, T is the temperature, H is the Hamiltonian and Q is the partition function given below

$$Q = \int \int \exp\left[-\frac{H(\mathbf{p}^N, \mathbf{r}^N)}{k_B T}\right] d\mathbf{p}^N d\mathbf{r}^N \quad (1.21)$$

This integral is practically very difficult to calculate and time-consuming because all possible states of the system should be considered for calculation. If we take any point (microscopic ensemble) in the system then over a period of time this point will represent different states of the system. In a molecular dynamics (MD) simulation, we calculate the points in the ensemble sequentially in time, so for the estimation of an ensemble average, the MD simulations must pass through all possible states corresponding to the particular thermodynamic constraints. Therefore, time average of the observable A is calculated in lieu of ensemble average in MD simulations. Time average of observable A , is expressed as follows

$$\langle A \rangle_{\text{time}} = \lim_{\tau \rightarrow \infty} \frac{1}{\tau} \int_{t=0}^{\tau} A(\mathbf{p}^N(t), \mathbf{r}^N(t)) dt \approx \frac{1}{M} \sum_{t=1}^M A(\mathbf{p}^N, \mathbf{r}^N) \quad (1.22)$$

where $A(\mathbf{p}^N, \mathbf{r}^N)$ is the instantaneous value of observable A , M is the number of time steps in the simulation and t is the simulation time.

The ergodic hypothesis states that the “time average equals the ensemble average” and is one of the most fundamental hypotheses of statistical mechanics. this axiom solves

the dilemma that calculated time averages by MD simulation can be used for estimating experimental observable which are assumed to be ensemble averages.

$$\langle A \rangle_{\text{ensemble}} = \langle A \rangle_{\text{time}}$$

$$\textit{Ensemble - average} = \textit{Time - average} \quad (1.23)$$

Idea behind this hypothesis is that if we allow the system to evolve in time indefinitely, then system will pass through all the possible states. Therefore, in MD simulations, simulation time should be long enough to represent large number of conformations such that this equality is satisfied. In such scenario experimentally observed information concerning structural, kinetic and thermodynamic properties can be calculated using a feasible computational infrastructure.

1.9.2 Newton's second law

Newton's second law or the equation of motion, is the basis for molecular dynamics simulation method. It states that force (\mathbf{F}) exerted on the particle is equal to product of the mass(m) of that particle and its acceleration (\mathbf{a}). i.e $\mathbf{F} = m\mathbf{a}$. If we integrate this equation of motion then a trajectory can be generated which describes positions, velocities and accelerations of the particles as they vary with time. Also, the average values of properties can be determined from this trajectory. This method is deterministic in nature as states of the system can be predicted at any time in the future or the past once the positions and velocities of each atom are known. MD simulations can be computationally expensive and time-consuming. However, as computers are getting faster and cheaper, we can perform simulations of solvated proteins up to the nanosecond timescale or even in microseconds and milliseconds regime. Newton's equation of motion is given by

$$\mathbf{F}_i = m_i \mathbf{a}_i \quad (1.24)$$

where F_i is the force exerted on i th particle, m_i and a_i are the mass and acceleration of particle i . Alternatively the force can also be expressed as the negative gradient of the potential energy,

$$\mathbf{F}_i = -\nabla_i V \quad (1.25)$$

If we combine these two equations, it yields

$$-\frac{dV}{dr_i} = m_i \frac{d^2 r_i}{dt^2} \quad (1.26)$$

where V is the potential energy of the system. using this equation, we can then relate positional derivative of the potential energy to the changes in position with time.

1.9.3 Potential energy function

The value of the energy is calculated as a sum of two components respective for bonded and non-bonded interactions. Energy term for internal, or bonded, terms E_{bonded} , describe the bonds, angles and rotations of bonds in a molecule. Whereas $E_{\text{non-bonded}}$, energy term for external or non-bonded interactions, account for interactions between atoms separated by 3 or more covalent bonds or non-bonded atoms.

$$V(R) = E_{\text{bonded}} + E_{\text{non-bonded}} \quad (1.27)$$

1.9.3.1 E_{bonded}

The E_{bonded} term can be written as a sum of three terms corresponding to three types of atom movement as given below;

$$E_{\text{bonded}} = E_{\text{bond-stretch}} + E_{\text{bond-bend}} + E_{\text{rotate-along-bond}} \quad (1.28)$$

The first term represents the interaction between atomic pairs where atoms are separated by one covalent bond, i.e., 1,2-pairs and is called as harmonic potential. This term represents

the energy of a bond as a function of displacement from the equilibrium, b_0 . The strength of the bond is determined by force constant, K_b . Both equilibrium bond lengths b_0 and force constants K_b depend on chemical type of atoms making bond, and they are specific for each pair of bound atoms.

$$E_{\text{bond-stretch}} = \sum_{1,2\text{pairs}} K_b (b - b_0)^2 \quad (1.29)$$

Values of force constant K_b are often estimated from experimental values of infra-red stretching frequencies or calculated from quantum mechanical studies. Whereas bond lengths can be evaluated from microwave spectroscopy data or high-resolution crystal structures.

The second term in the above equation is related with the deviation of bond angles theta from an ideal equilibrium value θ_0 , which is also represented by a harmonic potential as described in below equation 1.30.

$$E_{\text{bond-bend}} = \sum_{\text{angles}} K_\theta (\theta - \theta_0)^2 \quad (1.30)$$

Values of θ_0 and K_θ depend on chemical type of bonds making the angle. $E_{\text{bond-stretch}}$ and $E_{\text{bond-bend}}$ describe the deviation from an equilibrium geometry and in a perfectly optimized structure, the sum of these terms should be near to zero.

The third term, $E_{\text{rotate-along-bond}}$ represents the dihedral angle potential function for modelling 1,4 pairs interactions i.e the presence of steric barriers between atoms separated by 3 covalent bonds. This potential is often expressed as a cosine function and is assumed to be periodic.

$$E_{\text{rotate-along-bond}} = \sum_{1,4\text{pairs}} K_\phi (1 - \cos(n\phi)) \quad (1.31)$$

1.9.3.2 $E_{\text{non-bonded}}$

The energy term representing the contribution of non-bonded interactions has generally two components, the Van der Waals interaction energy and the electrostatic interaction energy. Some other non bonded potential functions also include an additional term to account for hydrogen bonds. For example, in the AMBER and CHARMM potential energy function, these interactions are accounted by the electrostatic and Van der Waals interactions.

$$E_{\text{non-bonded}} = E_{\text{van-der-Waals}} + E_{\text{electrostatic}} \quad (1.32)$$

The van der Waals interactions are one of the most important for the MD simulations of the biological molecules. Lennard-Jones 6-12 potential, given below, is used to model the van der Waals interaction. It expresses the interaction energy using the atom-type dependent constants A and C . Values of A and C may be determined by a variety of methods, like gas-phase scattering measurements and non-bonding distances in crystals.

$$E_{\text{van-der-Waals}} = \sum_{\substack{\text{non-bonded} \\ \text{pairs}}} \left(\frac{A_{ik}}{r_{ik}^{12}} - \frac{C_{ik}}{r_{ik}^6} \right)$$

Coulomb potential is used to represent electrostatic interaction between a pair of atoms. If the two atoms having charges q_i and q_k are separated by distance r in a medium with effective dielectric constant D then the electrostatic energy term will be written as

$$E_{\text{electrostatic}} = \sum_{\substack{\text{non-bonded} \\ \text{pairs}}} \frac{q_i q_k}{D r_{ik}}$$

1.9.4 Periodic boundary conditions

In experiments the atoms/molecules are present in the bulk; such a large system will be very time-consuming and it will be difficult to simulate. To simplify the problem periodic boundary conditions are used which help in performing a simulation with a relatively small

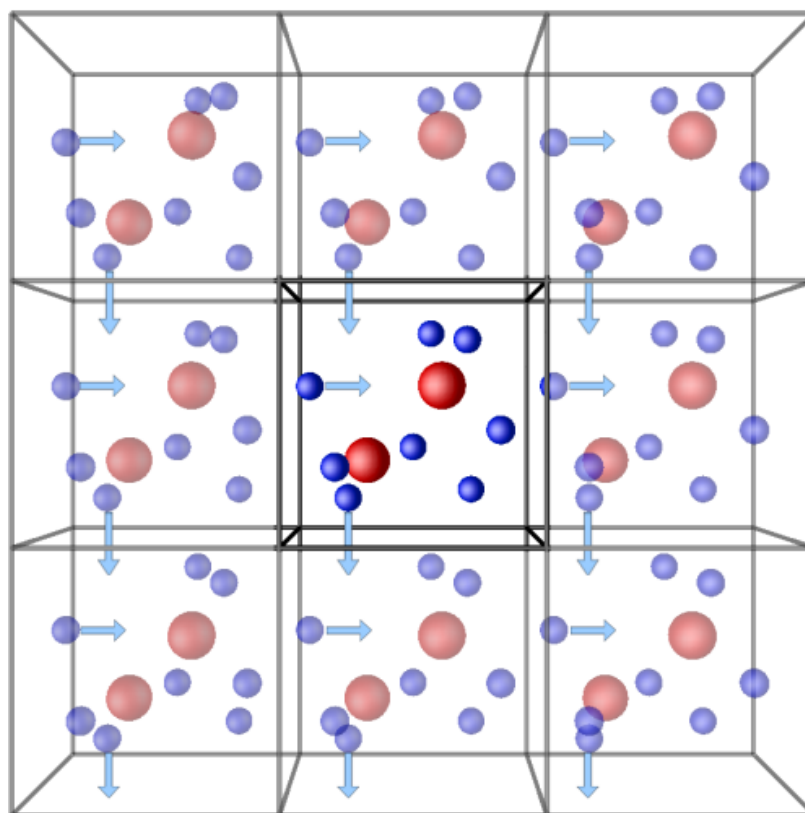


FIGURE 1.10: representation of periodic boundaries along a cubic cell is shown. Atoms moving away from the cell are entered through other side of the boundary.

number of particles in such a way that the particles experience similar forces as they are in the bulk solution. A sketch of the periodic boundaries for a cubic cell is shown in the Figure 1.10. The simplest box used in MD simulation is cubic box, if we look into the Figure 1.10, the central box is surrounded by eight similar neighbours. The coordinates of the image particles, present in the surrounding box are correlated with the particles in the primary box by simple translation. Forces on the primary particles are estimated from particles present in the same box as well as in the surrounding box. The cut-off is chosen so that a particle in the primary box does not view its image in the neighbouring boxes. If during MD simulations any particle leaves the primary cell then simultaneously image particle will enter from opposite neighbouring cell and total number will be unchanged.

1.9.5 Setting up and running a molecular dynamics simulation

In molecular dynamics simulation, the time dependent trajectory describing position and velocities of any system is evaluated by integrating Newton's equations of motion using potential energy functions and a numerical integrator. The trajectory or the path followed by each atom in accordance with Newton's laws of motion will describe a time series of conformations of the system. MD simulations are mostly performed either under constant N, V, and E conditions or even at constant N, P, and T condition to mimic actual experimental conditions. Below in the text the steps taken to set up and run a typical MD simulation are described in brief.

Initialization: The first step is a starting point, at $t=0$, i.e. an initial configuration of the system, mostly taken from an x-ray crystal structure or an NMR structure. In simulations of biomolecules, initial structure is obtained from pdb database mostly Brookhaven Protein Data Bank (<http://www.rcsb.org/pdb/>). If crystal structure is not available then a theoretical structure developed by homology modelling can be used. The initial configuration must be carefully chosen as it can influence the quality of the overall simulation. A configuration close to the state intended for the simulation is often used as a good practice. A simulation cell (cubic or other) is defined, periodic boundary conditions and cutoffs are chosen.

Energy minimization: It is recommended to minimize the energy of the structure prior to starting MD simulation. Energy minimization will remove any existing strong van der Waals interactions, which might result in an unstable simulation due to local structural distortion. If some water molecules are present in the starting x-ray crystal structure and it is not a part of the binding site or other important structural feature, they are removed and explicit water molecules are added to solvate the protein. Electric charge of the total system is neutralized by adding appropriate number of ions of opposite charge using either KCl or NaCl. Another energy minimization is performed

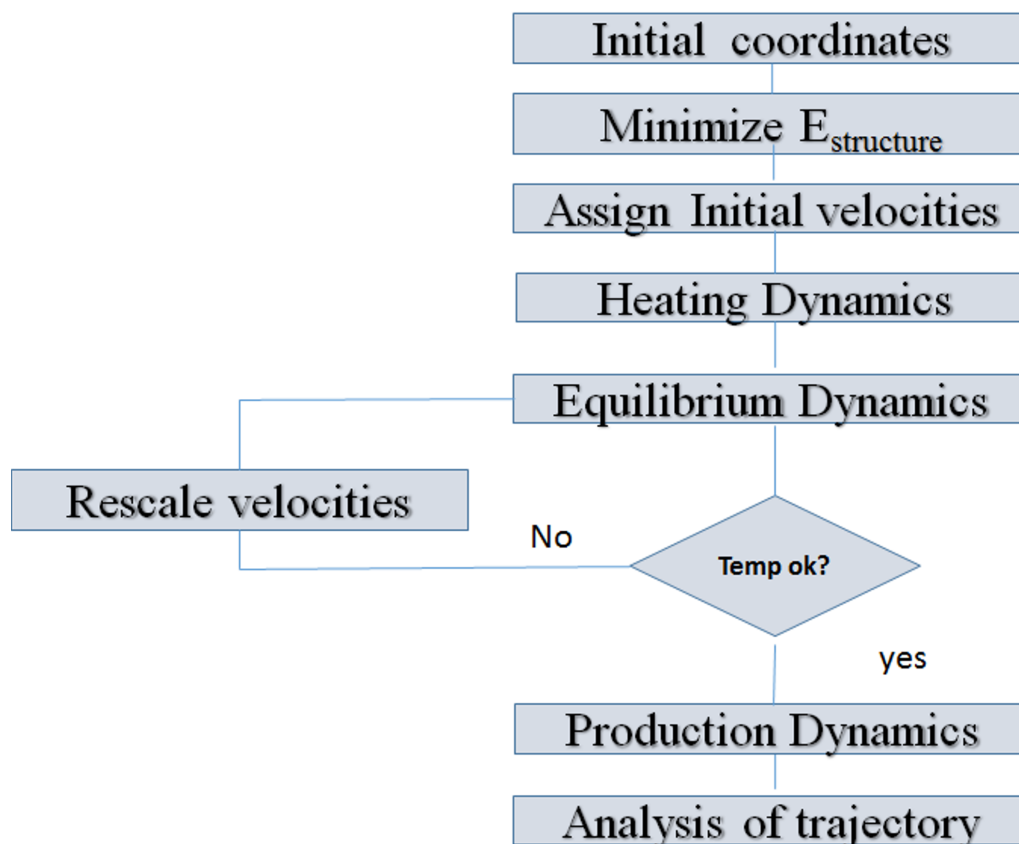


FIGURE 1.11: FlowChart of the steps in an MD simulation

with the protein fixed in its energy minimized position so that water molecules readjust themselves inside the protein molecule.

Heating the system: The temperature of the overall system is increased gradually first at a low temperature, initial velocity is assigned to each atom of the system and equations of motion are integrated to propagate the system with time. Generally, water molecules are heated first by fixing the protein position so that water molecules adjust to the presence of the protein. Afterwards the temperature of the whole system is increased. During the heating phase, first initial velocities are assigned at a low temperature and periodically, new velocities are assigned at a slightly higher temperature until the desired temperature is reached during the simulation.

Equilibration: When the desired temperature is achieved, other important

properties like pressure, energy, temperature etc are monitored and varied to get desired values during simulation so that canonical ensemble (NVT) or isothermal–isobaric (NPT) ensemble conditions are maintained. The main aim of this phase is to run the simulation until these properties become stable with respect to time.

Production phase: Once the system is in equilibrium, all the constraints are removed and simulation is carried out in “production” phase for the desired time length which can be from hundreds of ps to ns or even more.

Analysis of MD simulation trajectory: Trajectory produced during MD simulation, contains information about coordinates and velocities of the system at several time steps. Using this information, various time dependent properties can be estimated and displayed graphically. Property of interest viz. energy, rmsd, rmsf, Rg, rdf, etc. are plotted against time as X axis. The trajectory can be also used to analyze various non-bonding interactions like hydrogen bonds water bridges etc. MD simulations can help in visualizing and understanding various conformational changes occurring at an atomic level using molecular graphics programs like VMD, chimera. These programs can display the temporal profile of various structural parameters of interest.

1.10 ENHANCED SAMPLING METHODS

In molecular dynamics simulations of biological system, various complex processes (viz conformational changes, protein folding etc.) can create rough energy landscape with many local minima separated by high-energy barriers. In such systems, insufficient sampling often limits the application of equilibrium MD simulations. Sampling such complicated processes may be time-consuming and commonly beyond the ability of straightforward MD simulations. In the past few decades several enhanced sampling methods such as metadynamics, umbrella sampling and replica-exchange molecular dynamics (REMD) have been developed for this purpose.

1.10.1 Metadynamics

In metadynamics, history-dependent external bias potential is applied as a sum of small Gaussian kernels along the selected degrees of freedom $\vec{s}(q)$, generally called collective variables (CVs).⁴⁵

$$V(\vec{s}, t) = \sum_{k\tau < t} W(k\tau) \exp\left(-\sum_{i=1}^d \frac{(s_i - s_i(q(k\tau)))^2}{2\sigma_i^2}\right) \quad (1.33)$$

where τ is the Gaussian deposition stride, σ_i the width of the Gaussian for the i th CV, and $W(k\tau)$ the height of the Gaussian. Applied external bias potential pushes the system away from local minima and helps in visiting new regions of the phase space. The bias potential converges to minus the free energy as a function of the CVs over long time limits.

$$V(\vec{s}, t \rightarrow \infty) = -F(\vec{s}) + C \quad (1.34)$$

In standard metadynamics, height of the Gaussian kernels is kept constant during entire course of a simulation. Eventually the system is pushed to explore the high energy regions (barriers or transition states) and problem in convergence of the simulation arises and the estimated free energy from the bias potential oscillates around the true value. To circumvent the issue of convergence well-tempered version of metadynamics method has been developed.

1.10.2 Well tempered metadynamics

In well-tempered metadynamics,⁴⁶ the height of the Gaussian is not kept constant but it is decreased with simulation time according to:

$$W(k\tau) = W_0 \exp\left(-\frac{V(\vec{s}(q(k\tau)), k\tau)}{k_B \Delta T}\right) \quad (1.35)$$

where k_B the Boltzmann constant, W_0 is an initial Gaussian height and ΔT is an input parameter with the dimension of a temperature and estimate by the applied bias factor

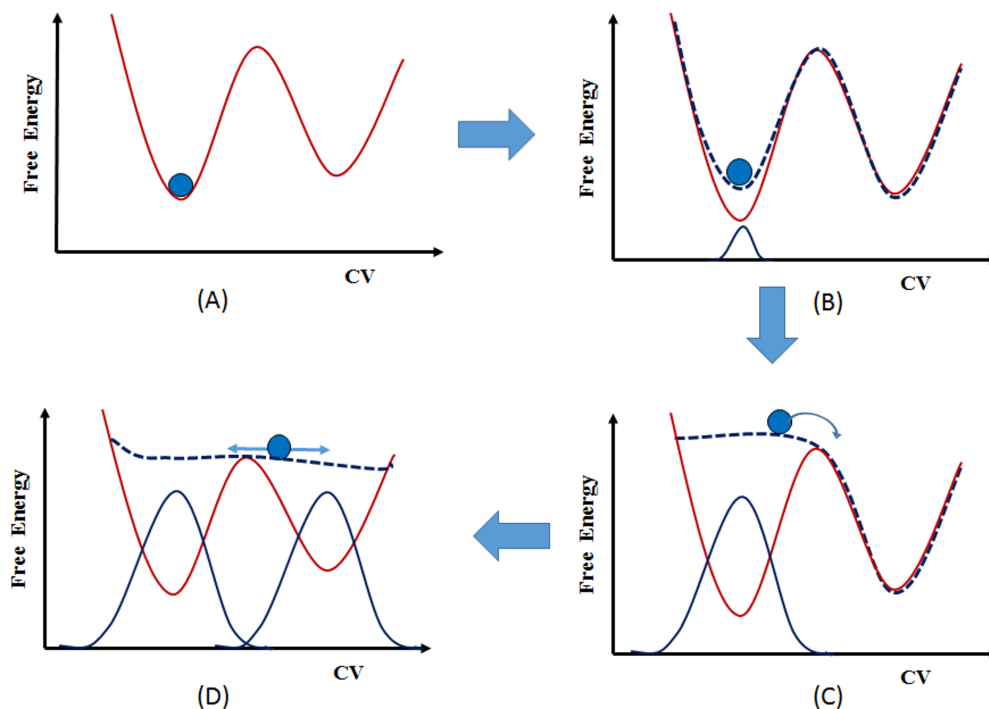


FIGURE 1.12: Schematic diagram of the process of metadynamics. Panel (A) shows that first the system evolves according to a normal dynamics (A), then a Gaussian potential is deposited (solid blue line), which lifts the system and modifies the free-energy landscape (dashed blue line) in which the dynamics evolves; shown in panel (B). After a while the sum of Gaussian potentials fills up the first metastable state and the system moves into the second metastable basin panel (C). After this the second metastable basin is filled, at this point, the system evolves in a flat landscape (D). The summation of the deposited bias (solid gray profile) provides a first rough negative estimate of the free-energy profile.²(reproduced here with permission from John Wiley & Sons, Ltd)

as defined below in equation 1.37. When Gaussian height is rescaled using bias factor γ , the bias potential smoothly converges in the long time limit. Applied bias potential underestimate the underlying free energy which can be corrected by bias factor as follows:

$$V(\vec{s}, t \rightarrow \infty) = -\frac{\Delta T}{T + \Delta T} F(\vec{s}) + C \quad (1.36)$$

$$\gamma = \frac{T + \Delta T}{T} \quad (1.37)$$

The bias factor should be chosen carefully for efficient estimation of the relevant free-energy surface.

1.10.3 Umbrella sampling simulations

Umbrella sampling (US),⁴⁷⁻⁴⁹ is one of the methods to explore the rare events/processes that require extremely long simulation times either due to large energy barrier between two states or due very complex nature of the free energy profile. In umbrella sampling, several simulations along evenly distributed windows for the chosen reaction coordinate are carried out. A biasing potential, $V_b(\chi)$, is added to the total energy to enhance the sampling of certain regions of conformational space. A harmonic form is often chosen for the biasing potential and is defined as.^{50,51}

$$V_b(\chi_i) = \frac{1}{2}k(\chi - \chi_i)^2 \quad (1.38)$$

where k is the force constant and χ_i is the target position. The separate simulations are then combined to obtain the unbiased $\rho(\chi)$ and its associated potential of mean force (PMF). The average distribution function or the unbiased $\rho(\chi)$ or (eq ..), along some reaction coordinate χ is defined as the Boltzmann weighted average:⁵²

$$\langle \rho(\chi) \rangle = \frac{\int dq \delta(\chi'(q) - \chi) e^{-V(q)/k_B T}}{\int dq e^{-V(q)/k_B T}} \quad (1.39)$$

where $V(q)$ is the total energy of the system as a function of the conformation q and $\chi' \chi'(q)$ is the functional dependence of the reaction coordinate on the conformation. The (PMF) $W(\chi)$, or the change in free energy along the coordinate χ , can be defined as^{50,53}

$$W(\chi) = -k_B T \ln \langle \rho(\chi) \rangle \quad (1.40)$$

The weighted histogram analysis method (WHAM) proposed by Kumar *et al.*⁵⁴ uses all the information present in the umbrella sampling without discarding the overlapping regions. The WHAM method among the various approaches to combine the simulation results,^{48,49,55-57} is a practical and most used approach to obtain average $\rho(\chi)$ and the PMF. The whole process, for which US is to be carried out, is evenly divided into several windows along the reaction coordinate. This distribution of the windows is

generally carried out either by steered MD, replica exchange or other biased/non-equilibrium simulation methods.

1.10.4 Hydrogen bond and water bridge correlation functions

We have used geometric criterion for the hydrogen bonding to investigate hydrogen bond (HB) dynamics.^{58,59} We have analyzed the hydrogen-bond time-correlation function, which quantifies the extent to which hydrogen bonds found at time $t = 0$ survive to subsequent times t^{60} to investigate hydrogen-bond rearrangements between protein and hydration water. A hydrogen bond is formed when the distance between the hydrogen bond donor (D) and acceptor (A) is less than 3.5 Å, and the D–H–A angle is less than 35°. A water molecule forming concurrent hydrogen bonds with two atoms of the protein is called bridging water and such interaction is defined as water bridge(WB). We have considered only those WBs, in which both the bonds satisfy the aforesaid criteria. The HB lifetime correlation function, $C_{\text{HB}}(t)$, is measured as

$$C_{\text{HB}}(t) = \sum_{mn} \frac{\langle A_{mn}(0)A_{mn}(t) \rangle}{\langle A_{mn} \rangle} \quad (1.41)$$

where $A_{mn}(t)$ is the HB population operator. The values of A_{mn} stipulate HBs between all donor–acceptor (D–A) pairs involving all the participating amino acid residues of the sTf at time t . $A_{mn}(t)$ is equal to 1 when the particular HB is unbroken at time t and it becomes zero when the same HB breaks. Similarly, the water bridge (WB) lifetime correlation function, $C_{\text{WB}}(t)$, is measured as

$$C_{\text{WB}}(t) = \sum_{i=1}^n \frac{\langle P(0)P(t) \rangle}{\langle P \rangle} \quad (1.42)$$

where n is the number of possible WBs formed between the protein residues. $P(0)$ and $P(t)$ are the WB population operator at time 0 and t , respectively. $P(t)$ is equal to 1 when the two associated HBs of the water bridge are intact at time t , but it becomes zero when

either of the HBs break. The angular bracket denotes the average over all water bridge forming water molecules.

1.11 OBJECTIVE AND OUTLINE OF THE THESIS

The main objective of the present work is to provide the solutions for recent challenges in the direct monitoring of actinides and to understand, at molecular level, the biochemical behaviour of various actinide ions during their transport inside the human body and to find new probable chelating compounds for their decorporation. Gamma ray spectroscopy with hyper pure germanium (HPGe) array for detection and quantification of actinides is used, and their dosimetric assessment is carried out. Multi-scale modelling approach based on DFT, MD, Mtd and docking is applied to study structural and thermodynamic behaviour of these ions. The following two chapters are based on the work based on recent challenges faced in experimental detection of actinides and its dosimetry. Whereas four subsequent chapters are based on the computational study carried out for various complexes of serum transferrin protein with native iron and actinide ions mainly Th(IV), Pu(IV), Cm(III) using multi-scale modelling approach. In total the outline of the thesis chapters is as follows:

- (1) The first chapter, is introductory in nature which describes the direct method of internal dose assessment, basics of QM especially DFT and also molecular dynamics simulation basics.
- (2) Second chapter is based on the in-vivo detection and quantification of Pu/ Am in workers. In this chapter a methodology is developed for quick estimation of isotopes of Pu and Am in biological samples using HPGe array. Results obtained with new methodology are compared with the conventional technique of radiochemical separation followed by alpha counting.
- (3) The third chapter is based on the dosimetric assessment of the estimated activity in

radiation workers at several organs viz. lung, liver and skeleton. Various measurement geometries are optimized to know the most sensitive geometry at different time interval post inhalation intake.

(4) In the fourth chapter QM results for structures and spin Hamiltonian parameters of iron transferrin using isolated and embedded clusters models are presented.

(5) In the fifth chapter multi-scale modelling of structural and thermodynamic behaviour of complexes of Th(IV) and Cm(III) with sTf at serum pH are carried out. Density functional theory, molecular dynamics, and well tempered metadynamics simulations are used in this study.

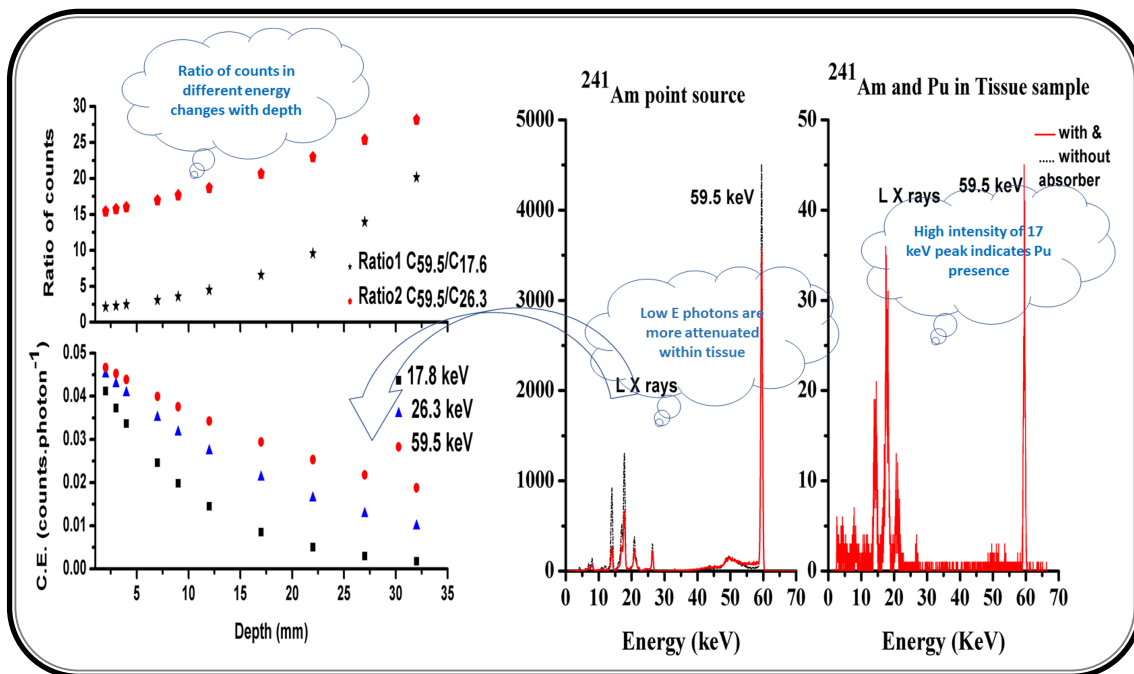
(6) In Chapter 6, equilibrium MD Simulation are performed to study binding of Cm(III) and Th(IV) with sTf at acidic endosomal pH. umbrella sampling, hydrogen bond dynamics and water bridge dynamics are analyzed on equilibrium MD simulation trajectories.

(7) In seventh chapter binding of plutonium Pu(IV) with sTf binding site at various protonation states of the protein is studied using equilibrium molecular dynamics. In order to remove Pu(IV) from sTf BS, fragmented decorporating agents are docked at the BS and well tempered MD simulations are performed to study chelation mechanism of the Pu(IV) ion at serum pH and also to understand its possible decorporation mechanism.

(8) The eighth and final chapter is dedicated to conclusion and future scope of the present thesis work.

CHAPTER 2

Quick Estimation of Pu/Am in Biological Samples using Low Energy HPGe Detector



HIGHLIGHTS

- The estimation of Pu/²⁴¹Am ratio in the biological samples is an important input for the assessment of internal dose received by the workers.
- The radiochemical separation of Pu isotopes and ²⁴¹Am in a sample followed by alpha spectrometry is a widely used technique for the determination of Pu/²⁴¹Am ratio. However, this method is time-consuming and many times quick estimation is required.
- High resolution gamma ray spectroscopy technique with low energy HPGe detector is used for the measurement of Pu isotopes and ²⁴¹Am in biological samples.
- Results obtained with gamma ray spectroscopy compared well with the results obtained from radiochemical analysis of sample followed by α -spectroscopy.
- This study will be useful for assessment and medical management of Pu/²⁴¹Am embedded in tissue of workers. Part of the work presented in this chapter is published in Applied radiation and isotopes⁶¹ and included here with permission.

2.1 INTRODUCTION

Plutonium isotopes and their compounds are handled in front and back end of the nuclear fuel cycle. Despite elaborate and stringent radiation protection controls at the plants, cases of internal contamination of plutonium cannot be ruled out. The internal contamination of plutonium can be measured by in-vivo, in-vitro measurements, or a combination of these techniques.⁵ In-vivo measurement of plutonium in occupational workers is carried out by suitable detectors *viz.* phoswich or an array of high-purity germanium (HPGe) detectors installed inside a totally shielded steel room.⁶²⁻⁶⁴ Although inhalation is the most common route of intake of radionuclides for the workers yet, there is a probability that radioactive substances might enter into human body through cuts and wounds in rare circumstances. In such scenario, direct measurement of Pu isotopes and ²⁴¹Am deposited in wound is an important task to quantify radioactive material present and to provide guidance for medical management of the injury.⁹ The ICRP has published dose per unit intake of various radionuclides for different routes of intake using latest biokinetics and dosimetric models.¹⁰ The dose per unit intake for Pu is among the highest due its high linear energy transfer (LET) in the tissues; therefore it should be measured at the lowest possible detection level. Pu isotopes are mainly alpha emitters which cannot penetrate the body tissues hence its gamma rays or x-rays of its daughter are used for in-vivo measurements. The intensity of gamma rays emitted by Pu is of the order of 10⁻³ %, which is too low to be useful for the measurement of low level of plutonium in biological/environmental samples.

In biological sample (tissue, nasal swab, urine, faecal etc.), low level of ²³⁹Pu and its other isotopes are detected by L x-rays of its daughter ²³⁵U which emits 13.6, 17.2 and 20.2 keV photons with a total yield of 4.6%. These U L x-ray photons emitted by Pu isotopes are not energetic enough to get transmitted through if activity is deposited deep in biological sample. Figure 2.1 gives relative transmission of mono-energetic photons through 50 mm thickness of tissue with different adipose contents.⁶² It is obvious from

TABLE 2.1: Radiological properties of Pu and ^{241}Am and half value thickness of its photon energy in the soft tissue (ICRU, 1989⁶⁷).

Radio-nuclide	Half-Life (Y)	Alpha Energy (keV)	Emission Probability (%)	Photon Emission	Photon Energy (KeV)	Emission Probability (%)	HVL of photon in soft tissue (mm)
^{238}Pu	87.7	5499.03	70.91	U L α	13.6	4.17	6
		5456.3	28.98	U L β	17.2	5.17	7
				U L γ	20.3	1.15	8
^{239}Pu	24110	5156.59	73.3	U L α	13.6	1.65	6
		5144.3	15.1	U L β	17.2	2.27	7
		5105.5	11.5	U L γ	20.3	0.56	8
^{240}Pu	6363	5168.17	72.8	U L α	13.6	3.95	6
		5123.68	27.1	U L β	17.2	5.04	7
				U L γ	20.3	1.1	8
^{241}Am	432.2	5485.56	84.5	Np L α	13.9	13.02	6
		5442.8	13	Np L β	17.6	18.6	7
				Np L γ	20.8	4.81	8
				Gamma	26.3	2.4	18
				Gamma	59.5	35.9	35

the figure that most of the low energy photons are getting absorbed and the fraction of transmitted photons ($E \leq 30\text{keV}$) is even less than 10^{-1} . Therefore, minimum detectable activity (MDA) of Pu is quite high if we use only its x or gamma ray photons. Fortunately, trace amount of ^{241}Am is also present along with Pu in most of the samples from various nuclear fuel cycle operations. ^{241}Am is produced from the beta decay of ^{241}Pu and the amount of ^{241}Am present with Pu depends upon the amount of ^{241}Pu initially present and also on the time elapsed after the purification of plutonium. By using ^{241}Am as a tracer we can achieve lower MDA for Pu measurements. Therefore, direct measurement of Pu in biological sample is carried out using ^{241}Am as a tracer and by measuring its 59.5 keV γ -rays having 36 % yield. The detection limit for 59.5 keV photon emitted by ^{241}Am is superior compared to L x-ray photons because it is less absorbed in the biological sample than the low energy x-rays. The knowledge of Pu/ ^{241}Am ratio in the contaminant can be used for estimation of plutonium activity. The Pu/ ^{241}Am ratio is commonly estimated from radiochemical analysis of a representative sample from workplace or faecal sample of the worker⁶⁵ followed by alpha spectroscopy. Assessment of committed effective dose due to internally deposited Pu, is carried out by direct measurement of ^{241}Am and making use of isotopic composition of

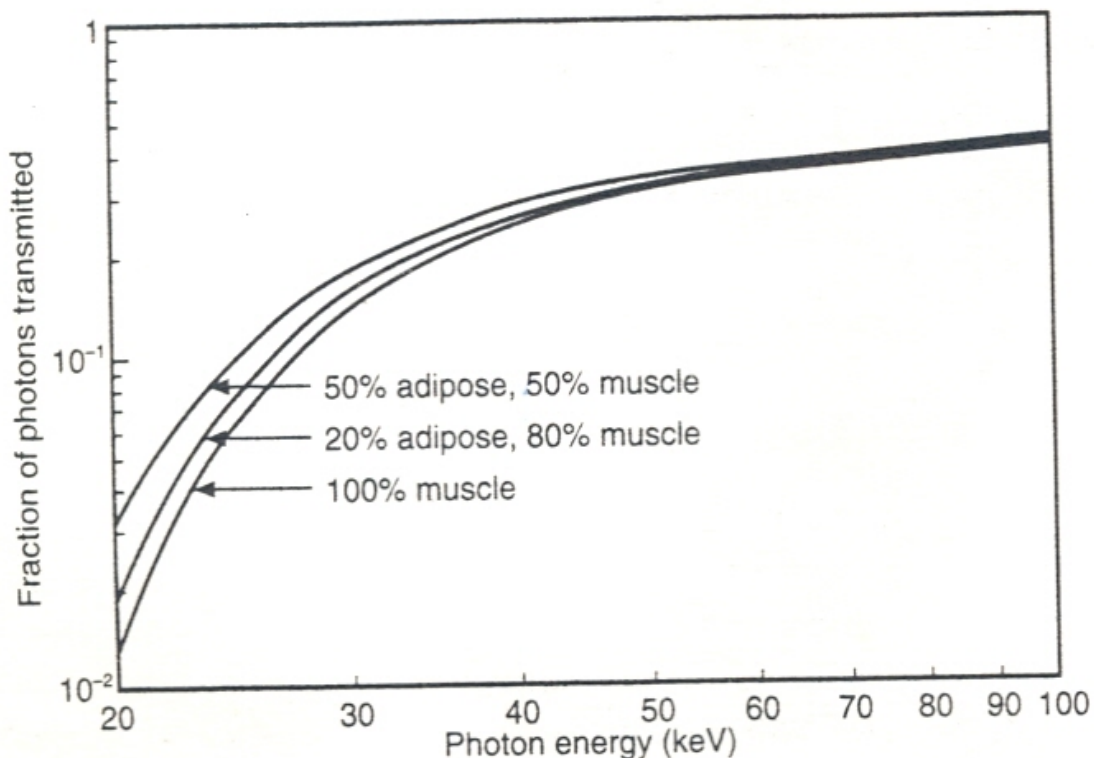


FIGURE 2.1: Relative transmission of mono-energetic photons through a 50 mm thickness of tissue with different adipose contents (with permission from Journal of the ICRU, 2003).

Pu and Pu/²⁴¹Am ratio.⁵ The radiochemical analysis of biological sample followed by alpha spectroscopy for the measurement of Pu and ²⁴¹Am is time-consuming and needs minimum one working week time for completion. Also, for the assessment of Pu/²⁴¹Am ratio, the selected sample for the radiochemical analysis should be true representative of the contaminant.

The direct gamma-ray spectrometry of biological sample or contaminated wound gives better isotopic composition of the contaminant and this will not be affected by different metabolic behavior of Pu and Am⁶⁶ as well as by interferences due to radiochemical sample preparation. In case of wound contamination, deposition takes place near the surface of skin and characteristic x-rays emitted by Pu isotopes and ²⁴¹Am

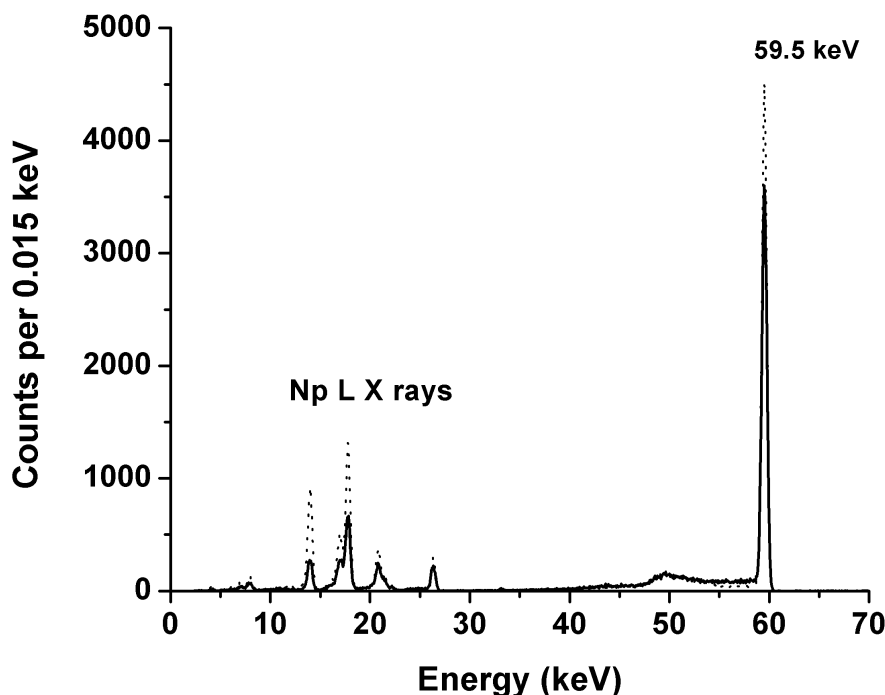


FIGURE 2.2: Pulse height spectrum of ^{241}Am in the same counting geometry with (—) and without (. . .) 10 mm tissue equivalent absorber recorded with HPGc detector.

(average energy 17 keV) are easily measurable as there is little attenuation by overlying soft tissue (half value thickness 7 mm). The important x-ray/gamma ray energies emitted by plutonium and americium with their yields and half value thicknesses in tissue are given in Table 2.1. In emergency situations when quick decisions have to be taken for the wound contamination management, quick estimate of Pu/Am in sample is required, therefore direct gamma ray spectroscopy technique will be more useful than traditional radiochemical analysis. In this work, important isotopes of the Plutonium and ^{241}Am are detected and their radioactivity is quantified using gamma ray spectroscopy. Also, a quick method is standardized for estimation of Pu: ^{241}Am ratio in biological samples and results are compared with those obtained from radiochemical analysis of sample followed by alpha spectroscopy. However, potential for using radiochemical method for Pu/Am ratio estimation still exists when concentration of deposits is too low

to be determined by direct counting method.

2.2 MEASUREMENT TECHNIQUES

2.2.1 Measurement of photons

In this work an array of three 70 mm dia. and 25 mm thick n-type HPGe detectors (Canberra Model No. EGMP3x70-25) installed inside a totally shielded steel room, is used for the measurement of γ/x -rays of Pu and ^{241}Am in biological sample.^{63,64} The three detectors of the array named as A, B, and C are enclosed in a 20 cm diameter hollow copper cylinder, positioned at 120 degree apart, their centers lie on the circumference of 10 cm dia. and each have 0.8 mm thick carbon window. The signals from each detector are analyzed separately using three multichannel analyzer (MCA) cards and the sum of spectrum of three detectors is used for the estimation of total activity. The summing of three detector spectra is carried out using Interwinner 4.1 and Winnerdose software procured from M/s Canberra Eurisys, France which displays sum of all the detector spectrum as well as individual spectrum on the computer screen. Energy summing of the counts is carried out using WinnerDose software after acquisition of individual detector spectrum. The full width at half maxima (FWHM) of each detector is about 0.6 keV at 59.5 keV photon energy. During the measurement, the samples are placed 10 cm below the detector window, to minimize the error due to the positioning of the sample.

2.2.2 Calibration of the system

The HPGe detector array is calibrated with standard point source of ^{241}Am placed beneath tissue equivalent absorber made of polymethyl methacrylate (Lucite/Perspex) and ICRU

soft tissue material⁶⁷ having various thickness of the material. The thickness of soft tissue material is varied from 1 to 30 mm to simulate activity embedded in the tissue at different depths. Figure 2.2 shows the pulse height spectra of ²⁴¹Am with and without absorber thickness of 10 mm tissue equivalent material. The counting efficiency at various photon energies of ²⁴¹Am i.e. 17.6, 26.3 and 59.5 keV is evaluated from 0 to 30 mm depths of tissue equivalent material.^{68,69}

2.2.2.1 Determination of Pu/Am activity

Although HPGe is having superior energy resolution of 0.6 keV at 59.5 keV, yet it cannot resolve 17.2 keV U L_β x-ray of Pu and 17.6 keV Np L_β x-rays of ²⁴¹Am, therefore same energy region of interest from 16.0-18.5 keV is selected for both of these energies. Other important photon energy is 59.5 keV which is emitted as gammas only from ²⁴¹Am. Pulse height spectrum of biological sample having both Pu and Am is shown in Figure 2.3. The amount of ²⁴¹Am present in the biological sample, is estimated using following equation.

$$A_{Am} = \frac{(C_{Am,59.5} - C_{bkg})}{E_{59.5} \cdot T \cdot Y_{(i,Am59.5)}}, \quad (2.1)$$

Where, A_{Am} is the amount of ²⁴¹Am (Bq) present in the sample, $E_{59.5}$ and $Y_{(i,Am59.5)}$ are the efficiency of the detection system (counts photon⁻¹) and gamma intensity of ²⁴¹Am at 59.5 keV respectively. $C_{Am,59.5}$ and C_{bkg} are the sample and background counts in the 59.5 keV energy region of ²⁴¹Am in counting time T seconds. The predicted counts due to estimated ²⁴¹Am activity in 17 keV energy region is evaluated as

$$C_{(Am,17.6)} = A_{Am} \cdot E_{17} \cdot Y_{(i,Am17.6)} \cdot T, \quad (2.2)$$

Where, $C_{(Am,17.6)}$ and $Y_{(i,Am17.6)}$ are the counts and intensity of 17.6 keV photons emitted by ²⁴¹Am respectively. E_{17} is the total detection efficiency of the system at 17 keV Energy and T is the counting time in seconds.

The counts due to Pu activity in the 17 keV energy region is evaluated as follows,

$$C_{P(u,17.2)} = (C_{(17,Pu+Am)} - C_{(Am,17.6)} - C_{bkg}) \quad (2.3)$$

Where, $C_{P(u,17.2)}$, $(C_{(17,Pu+Am)})$ and C_{bkg} are the counts due to only Pu, due to both Am + Pu and due to background at 17 keV energy region respectively.

The total amount of Pu in the sample is evaluated as follows,

$$A_{Pu} = \frac{C_{(Pu,17.2)}}{E_{17.2} \cdot T \cdot Y_{(i,Pu17.2)}}, \quad (2.4)$$

Where, $E_{17.2}$ and $Y_{(i,Pu17.2)}$ are the efficiency and gamma intensity of Pu at 17.2 keV respectively and T is measurement time in seconds.

2.2.3 Procedure of biological sample analysis

After direct gamma ray spectroscopy, the biological (tissue) samples are fused by adding NaOH, NaNO₃ and Na₂CO₃ in the ratio of 5:2:1 in stainless steel dish. Fused mass is heated on a hot plate with the addition of distilled water and is centrifuged. Supernatant is collected in a separate beaker and iron hydroxide co-precipitation is performed. The iron hydroxide precipitate along with the carbonate residue of centrifuged material are dissolved in concentrated HNO₃, transferred to 100 ml capacity glass beaker and dried on hot plate. The residue is taken in 2M HNO₃, filtered and collected in plastic bottle of 100 ml capacity (this geometry is selected which is congruous to the one used during efficiency calibration procedure) and counted under HPGe for ²⁴¹Am estimation. Depending on the activity level, appropriate aliquot of the sample from the total prepared sample volume is analyzed for americium and plutonium estimation by the standardized TRU column extraction chromatography and anion exchange radiochemical procedure respectively,^{70,71} followed by activity estimation by alpha spectrometry using passivated ion implanted planar silicon (PIPS) semiconductor detector. The energy resolution and efficiency of detector for α -particle measurement is about 50 keV and 22% respectively.

The detection limit of the system for ^{238}Pu , $^{239+240}\text{Pu}$ and ^{241}Am is 0.5 mBq.^{72,73} Spectrum of plutonium isotopes obtained by alpha spectrometry is presented in Figure 2.5. In routine bioassay sample for chemical recovery estimation, tracers namely ^{236}Pu and ^{243}Am of the order of 5 to 10 mBq are added. The average chemical recovery observed at our laboratory for Pu and Am estimation in biological samples is about 60% and 73% respectively and same values are used for the activity estimation in the sample. The radiochemical analysis of the sample is completed within a week after γ/x -ray spectroscopy and expected decay of ^{241}Pu during this period is less than 0.1%, therefore in growth of ^{241}Am due to the decay of ^{241}Pu is ignored.

2.2.4 Determination of MDA

Currie's equation, given below, is used to estimate minimum detectable activity (MDA) of the system at 95% confidence level.⁷⁴

$$MDA = \frac{(4.65 \sigma_B + 2.7)}{E.R.Y.T} \quad (2.5)$$

Where σ_B is the standard deviation in the appropriate blank, E is the counting efficiency, R is the chemical recovery, Y is the emission probability of the photon and T is the time of counting. In case of direct gamma spectroscopy of the sample the chemical recovery, R is unity.

2.3 RESULTS AND DISCUSSION

2.3.1 Estimation of depth of activity embedded in the sample

Low energy photons are more attenuated compared to high energy photons when activity is embedded in the tissues. To verify this, a pulse height spectrum of ^{241}Am is recorded with an array of HPGe detectors in the same counting geometry with and without 10 mm

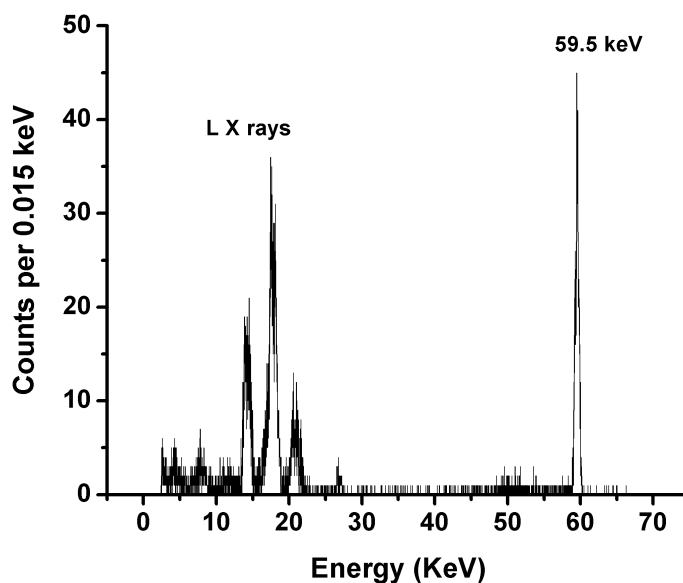


FIGURE 2.3: HPGe pulse height spectrum of biological sample containing Pu isotopes and ^{241}Am .

tissue equivalent absorber and shown in Figure 2.2. More absorption of low energy x-rays in tissue absorber compared to 59.5 keV photons can be observed from Figure 2.2. In another study,³ empirical equations for variation of ratios of counts in the 17.6, 26.3 and 59.5 keV energy region of the spectrum with depth of ^{241}Am activity deposited in the tissue are established. For this, known amount of ^{241}Am at various depth of tissue equivalent material is placed and measurements are carried out using HPGe array. Dependence of the ratios of counts in different energy regions on the depth of the embedded activity and variation of counting efficiency at various energies with respect to depth are shown in Figure 2.4.

Embedded ^{241}Am activity in the biological sample is measured using HPGe detector by placing it at a distance of 10 cm below detector window. Figure 2.3 shows the pulse height spectrum of the measurement. Generally, in a gamma ray spectrum of only ^{241}Am as a point source, intensity of the 17.6 keV peak is less than half the intensity of 59.5 keV peak (*cf.* Table 2.1). When ^{241}Am is embedded in the tissue, intensity of 17

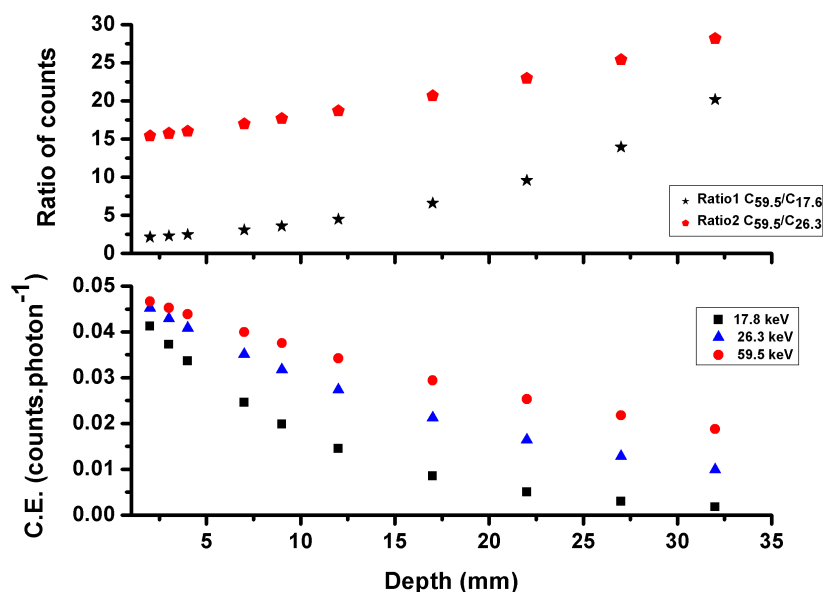


FIGURE 2.4: Distance dependence of the ratio of counts in different energy regions are shown in the upper panel whereas in the lower panel Counting efficiency (CE) for HPGe array for important Pu/Am photon energies at various tissue depth are presented.³

keV peak decreases more and ratio of 17 keV to 59.5 keV peak intensity goes up to 0.3 or even less. But here, in this spectrum (*cf.* Figure 2.3) higher intensity of 17 keV peak confirms the presence of Pu along with ²⁴¹Am. Therefore, to avoid the interference due to Pu in depth estimation, we have used C_{59.5} : C_{26.3}, ratio of counts in 59.5 keV and 26.3 keV energy regions which are the gamma photons emitted only due to ²⁴¹Am. For the activity embedded in the sample C_{59.5} : C_{26.3} is about 19.6. By comparing this ratio with the empirical equations the estimated depth of the deposited activity comes out about 10 mm of tissue equivalent material.^{3,68}

Table 2.2 shows the response of the system for known amount of ²⁴¹Am embedded at different tissue thicknesses and corresponding MDAs for a monitoring period of 600 seconds. The efficiency of the system varies from 4.94×10^{-2} counts photon⁻¹ to 2.73×10^{-2} counts photon⁻¹ and MDA varies from 1.7 Bq to 3 Bq as tissue thickness increases from 0 to 30 mm. The counting efficiency of the system at 59.5 keV photon energy of

TABLE 2.2: Variation of detector efficiency and MDA of HPGe detector for the measurement of ^{241}Am embedded in tissue at various depth for monitoring time of 600 seconds.

Depth of activity (mm)	Efficiency for 59.5 keV (counts photon ⁻¹)	MDA (Bq)
0	4.94×10^{-2}	1.7
5	4.53×10^{-2}	1.8
10	4.13×10^{-2}	2.0
15	3.56×10^{-2}	2.3
20	3.35×10^{-2}	2.4
30	2.73×10^{-2}	3.0

the ^{241}Am deposited at various depths inside tissue can be obtained from the following fitted equation.

$$Y = 0.5e^{(-0.02 X)}, \quad (2.6)$$

Where Y is counting efficiency (counts photon⁻¹) at ' X ' mm of tissue depth. With increase in the tissue thickness, attenuation of the photons increases hence the efficiency of the system decreases or MDA increases (ref: equation 2.5) Genicot *et al.* (1995)⁷⁵ carried out depth assessment of the Pu/ ^{241}Am contamination in wound by comparing the intensity of the gamma ray photon of 59.5 keV with x-rays between 13 and 25 keV. These results are only valid for the intake of chemically pure Pu or ^{241}Am , but in case of exposure to mixture of Pu isotopes and ^{241}Am , the combination of energies of 17.2, 17.6, 26.3 and 59.5 keV are needed to be used. The L_{β} x-ray energy coming from Pu (17.2 keV) and ^{241}Am (17.6 keV) are indistinguishable by HPGe detector with energy resolution of 0.6 keV at 17.6 keV photon energy. The counts recorded by HPGe detector in the 17 keV energy region are due to both uranium L_{β} x-ray from Pu isotopes (17.2 keV) and neptunium L_{β} x-ray (17.6 keV) of ^{241}Am . Therefore, depth of contaminant is estimated by comparing the intensity of the gamma photon of 59.5 keV and 26.3 keV, which are free from interference of Pu x-rays. Palmer and Rodes⁷⁶ determined the ratio of ^{239}Pu to ^{241}Am in the wound by measuring the 20.16 keV U L_{γ} X-rays resulting from

of ^{239}Pu to ^{241}Am in the wound by measuring the 20.16 keV U L_γ X-rays resulting from ^{239}Pu decay and 20.78 keV Np L_γ x-rays resulting from ^{241}Am decay with a Si(Li) detector. The Si(Li) planar detector provides sufficient photo peak resolution to resolve both L_γ X-rays coming from ^{239}Pu and ^{241}Am decay. The small size of the Si(Li) detector and use of L_γ x-rays, which are less abundant than the L_β x-rays, resulted in the poor detection limit for ^{239}Pu , which is estimated to be approximately 700 Bq. Therefore, this methodology can be useful while estimating high level of radioactivity in the sample. The ratio of photo peak area to total area of HPGe detector is approximately 14 times higher than Si(Li) detector at 17.6 keV energy, thus HPGe detector has the advantage for the measurements of low level of activity in biological/environmental samples.⁷⁷ Therefore, to achieve better detection limit, HPGe detector is used in this work. The atomic fraction of ^{238}Pu , ^{239}Pu and ^{240}Pu in the sample is 0.119, 73.08, and 22.98%⁷⁸ and respective alpha activities are 17.3, 38.5, and 44.2%. The L x-rays emission probability of each Pu isotopes is different.⁷⁹ Using isotopic composition of sample and x-ray yield of each Pu isotopes present in the sample (Table 2.1), weighted yield of 17.2 keV U L_β x-ray of Pu comes out 3.99% and this value is used for the estimation of Pu activity. In this work, Pu refers to total Pu α activity present in the sample which is the sum of ^{238}Pu , ^{239}Pu and ^{240}Pu activity. The x-ray energies of Pu and ^{241}Am are close and their absorption coefficients in tissue are similar.⁶⁷ Therefore, to evaluate detector efficiency for Pu isotopes, only yield correction is applied to detector efficiency for 17.6 keV of ^{241}Am . Table 2.3 shows detector efficiency (counts photon⁻¹) and MDA (Bq) of the system for alpha emitting Pu isotopes and ^{241}Am embedded at 10 mm depth of tissue. It can be seen from Table 2.3 that using 59.5 keV photons at 10 mm depth about 2 Bq of ^{241}Am can easily be detected by this system. The MDA of the system for ^{241}Am at photon energies of 17.6, 26.3 and 59.5 keV are 9.5, 33.4 and 2 Bq respectively. Estimated MDA of the system for Pu measurement in the sample using 17.2 keV photon energy is 44.30 Bq for 600 seconds measurement time.

TABLE 2.3: Detector efficiency (counts photon⁻¹) and MDA (Bq) of Pu and ²⁴¹Am at various energies and 10 mm depth for monitoring period of 600 seconds.

Radionuclide	Photon Energy (keV)	Detector Efficiency (counts photon ⁻¹)	MDA (Bq)
Pu	17.2	2.25×10^{-2}	44.3
²⁴¹ Am	17.6	2.25×10^{-2}	9.5
	26.3	3.67×10^{-2}	33.4
	59.5	4.13×10^{-2}	2.0

2.3.2 Measurement of embedded Pu/²⁴¹Am activity

Measurement of activity in the biological sample is carried out by placing the sample 10 cm below HPGe detector enclosure and the γ /x-ray spectrum thus obtained is shown in Figure 2.3. This spectrum is compared with the spectrum obtained with ²⁴¹Am activity embedded in tissue equivalent material (*cf.* Figure 2.2). The ratio of counts recorded for L_{β} x-rays in 17 keV energy region to 59.5 keV energy region having only ²⁴¹Am activity is about 0.285 (*cf.* Figure 2.2), but this ratio is 1.10 with biological sample (*cf.* Figure 2.3). The higher ratio of counts in this energy region, indicate the presence of Pu along with ²⁴¹Am in the spectrum. The methodology described in equations 2.1 to 2.4 is used for the estimation of Pu and ²⁴¹Am in the sample. The counts recorded in 17 keV L_{β} x-ray energy region is due to all alpha-emitting isotopes of Pu. Therefore, weighted yield of all alpha emitting Pu isotopes is taken for the estimation of activity present in the sample. The direct gamma ray spectrometry, measured value of Pu and ²⁴¹Am activity in the sample are 1789.7 ± 52.4 and 125.1 ± 3.4 Bq respectively. radiochemically analyzed results in combination with alpha spectroscopy for ²³⁸⁺²³⁹⁺²⁴⁰Pu and ²⁴¹Am are 1158.0 ± 36.7 and 93.7 ± 1.1 Bq respectively. Figures 2.3 and 2.5 are gamma and alpha spectra of the same sample measured by HPGe and PIPS detector respectively. The estimated activity in the sample by radio-analytical method are about 25% and 35% lower than those obtained from direct gamma ray analysis for Pu and ²⁴¹Am respectively. The Pu/²⁴¹Am ratios estimated

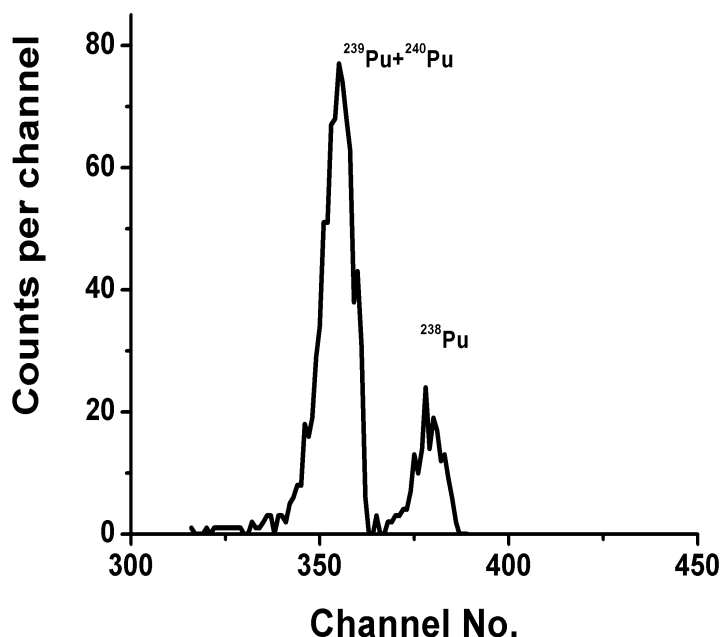


FIGURE 2.5: Spectrum of $^{238+239}\text{Pu}$ of the biological sample after radiochemical analysis followed by alpha spectroscopy.

by gamma and alpha spectroscopy are 14.0 ± 0.6 and 12.4 ± 0.4 respectively. The ratio obtained by gamma spectroscopy method is about 13.5% higher than results obtained from radio-analytical method. The same sample when it is at a depth of about 10 mm from surface, direct measurement with HPGe detector resulted in a Pu/ ^{241}Am ratio of 9.5 ± 0.2 . This value is about 23.2% lower than the results obtained from radio-analytical method. This is because higher uncertainty in the measurement of L x rays due to irregular sample matrix and distribution of activity at 10 mm of depth. It is observed that, Pu and ^{241}Am ratio calculated by gamma-ray spectrometry method matches within reasonable limit (<14% for biological sample and 23.2% if activity is deposited at 10 mm depth in the tissue) with the results obtained from radiochemical analysis of sample followed by alpha spectroscopy. With the increase in depth of contaminant deviation in the direct measurement result of the Pu to ^{241}Am ratio could be higher compared to the results obtained by radiochemical method.

2.3.3 Quick estimation of ^{241}Pu in biological samples

In direct method of assessment of internal contamination due to Pu/Am (discussed above), first ^{241}Am activity is estimated by measuring its 59.5 keV gamma ray photons then applying Pu/Am ratio, Pu alpha activity is estimated. Directly this method does not account for the activity due to ^{241}Pu . Activity due to ^{241}Pu is separately estimated using its composition in the fuel. Due to high burn up of the fuel in power reactors fractional composition of ^{241}Pu in the power reactor is more compared to that in research reactors. ^{241}Pu decays to ^{237}U and ^{241}Am with a branching fraction of 0.00246 % and 99.998 % respectively. Both the daughters of ^{241}Pu viz. ^{237}U and ^{241}Am decay to same isotope ^{237}Np and populate the same excited states of ^{237}Np . Decay scheme of ^{241}Pu and its daughters is shown in Figure 2.6. Gamma rays of ^{237}U can be used as a measure of ^{241}Pu . But both the daughters of ^{241}Pu viz. ^{237}U and ^{241}Am decay to same isotope ^{237}Np and populate the same excited states of ^{237}Np . Hence most of the gamma rays of ^{237}U are having contributions from the gamma rays of ^{241}Am and therefore a correction is required before using $^{241}\text{Pu} - ^{237}\text{U}$ peaks for calculation of ^{241}Pu activity. Energy of important gamma ray photons emitted by ^{241}Am and $^{241}\text{Pu} - ^{237}\text{U}$ with their respective yield is given in Figure 2.6. Counts due to 59.5 keV and 208 keV photons emitted by these radionuclides are used in this study. Efficiency of the system is estimated at these energies and appropriate yield correction are applied to estimate activity due to ^{241}Am and ^{241}Pu . To estimate Efficiency ϵ_{ij} , efficiency calibration of the HPGe detector is carried out using point sources of ^{241}Am , ^{133}Ba and ^{152}Eu . All the measurements are carried out in standard geometry holder keeping a fixed source to detector distance. Efficiency of the system for point sources at several important energies are calculated and shown in Figure 2.7. Data points in the above graph are fitted as a polynomial to get an empirical equation 2.7 in the energy range 60 keV-1460 keV.

$$CE(E) = B_0 * E^0 + B_1 * E^1 + B_2 * E^2 + B_3 * E^3 + B_4 * E^4 + B_5 * E^5 \quad (2.7)$$

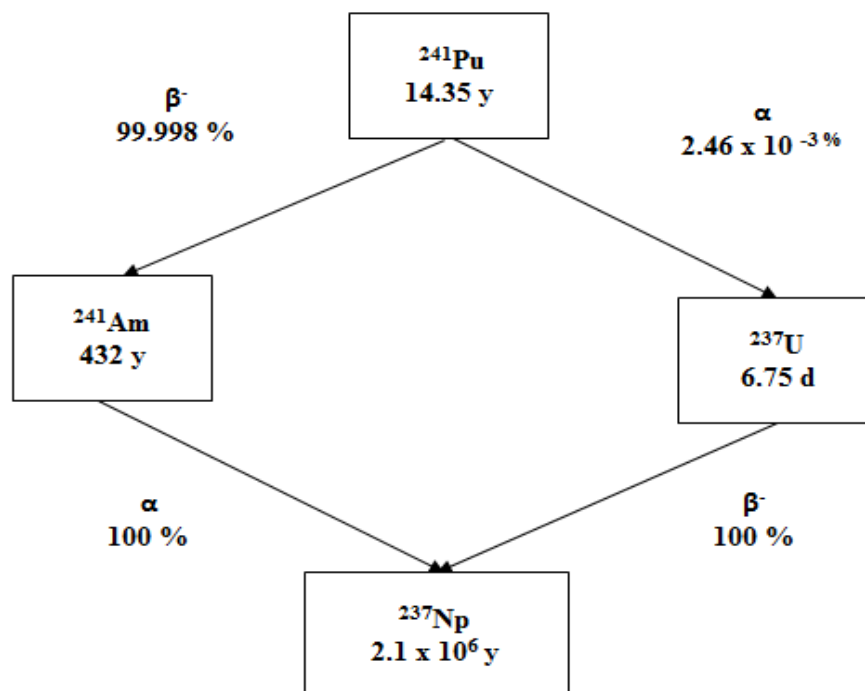
FIGURE 2.6: Decay scheme of ^{241}Pu and its daughters

TABLE 2.4: Values of constants given in equation 2.7

Multiplier	B0	B1	B2	B3	B4	B5
Value	3.81700E-02	-1.63742E-04	3.13328E-07	-2.95934E-10	1.34310E-13	-2.32900E-17

The values of the constant multipliers are given in the Table 2.4. Efficiency at 59.5 keV and 208 keV is estimated using this empirical equation and applying yield correction for ^{241}Am and ^{241}Pu their respective efficiency is given in Table 2.5. Initially the efficiency at 60 keV is at maximum as almost all the photons are fully absorbed in the detector. As the energy of the photons increases, the number of photons absorbed in the detector volume decreases rapidly up to about 400 keV then slowly. Thickness of the HPGe detector is 25mm hence fraction of the photons transmitted without depositing its energy in the detector increases rapidly and beyond 400 keV most of the photons are transmitted as unabsorbed in the detector.

TABLE 2.5: Efficiency of the HPGe detector for ^{241}Am and ^{241}Pu

Energy (keV)	Yield corrected efficiency for ^{241}Am (cps Bq $^{-1}$)	Yield corrected efficiency for ^{241}Pu (cps Bq $^{-1}$)
59.5	1.06×10^{-02}	2.50×10^{-07}
208	1.21×10^{-07}	8.13×10^{-08}

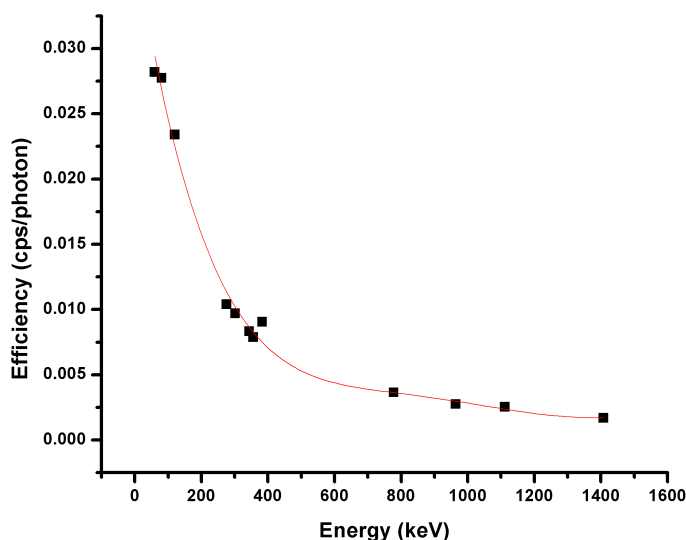


FIGURE 2.7: Variation of Detector efficiency of detector with Energy for point source is shown in the efficiency curve

2.3.3.1 Correcting interference due to ^{241}Pu in measurements for ^{239}Am

Detector arranged to measure the sample record counts from all the photons emitted by all the radionuclides present in the sample interacting within the sensitive volume of the detector. For example, with detector positioned to measure the sample, the total counts recorded in energy region E_i (here 59.5 keV and 208 keV) may originate from ^{241}Am as well as ^{241}Pu . The count rate (counts s^{-1} , cps) measured by the detector at any energy region E_i is a function of the quantity of activity, Q_j , due to each of the radionuclide j :

$$C_{E_i} = \sum_j \epsilon_{E_i,j} \cdot Q_j \quad (2.8)$$

where, C_{E_i} is the count rate in energy region E_i , Q_j is the activity of the radionuclide j , and $\epsilon_{E_i,j}$ is the detector efficiency in the energy region E_i due to radionuclide j . Expanding the above equation 2.8 for 59.5 keV and 208 keV

$$C_{59.5} = \epsilon_{(59.5,^{241}\text{Am})} \cdot Q_{^{241}\text{Am}} + \epsilon_{(59.5,^{241}\text{Pu})} \cdot Q_{^{241}\text{Pu}} \quad (2.9)$$

$$C_{208} = \epsilon_{(208,^{241}\text{Am})} \cdot Q_{^{241}\text{Am}} + \epsilon_{(208,^{241}\text{Pu})} \cdot Q_{^{241}\text{Pu}} \quad (2.10)$$

Writing the coefficient matrices for these equations,

$$D_{(^{241}\text{Am})} = \begin{bmatrix} C_{59.5} & \epsilon_{(59.5,^{241}\text{Pu})} \\ C_{208} & \epsilon_{(208,^{241}\text{Pu})} \end{bmatrix}; D_{(^{241}\text{Pu})} = \begin{bmatrix} \epsilon_{(59.5,^{241}\text{Am})} & C_{59.5} \\ \epsilon_{(208,^{241}\text{Am})} & C_{208} \end{bmatrix} \text{ and,}$$

$$D = \begin{bmatrix} \epsilon_{(59.5,^{241}\text{Am})} & \epsilon_{(59.5,^{241}\text{Pu})} \\ \epsilon_{(208,^{241}\text{Am})} & \epsilon_{(208,^{241}\text{Pu})} \end{bmatrix}$$

$Q_{^{241}\text{Am}}$ and $Q_{^{241}\text{Pu}}$ can be estimated as follows

$$Q_{^{241}\text{Am}} = \frac{|D_{^{241}\text{Am}}|}{|D|} \quad \text{and} \quad Q_{^{241}\text{Pu}} = \frac{|D_{^{241}\text{Pu}}|}{|D|} \quad (2.11)$$

A biological sample as a point source is counted in the standard geometry and gamma spectrum of the measurement is shown in Figure 2.8. Net counts in the 59.5 keV and 208 keV are used and applying corrections as discussed above, $^{241}\text{Pu}/^{241}\text{Am}$ activity present in a biological sample is estimated using this methodology. Results obtained with this method are in good agreement with those obtained from radiochemical analysis. This method is having its own pros and cons. We do not need any sample preparation or radiochemical analysis just a tiny point sample can be placed in a standard geometry and count with the detector, apply corrections and estimate ^{241}Pu activity. Due to very low yield of 208 keV photons the MDA is about 4 kBq.⁸⁰

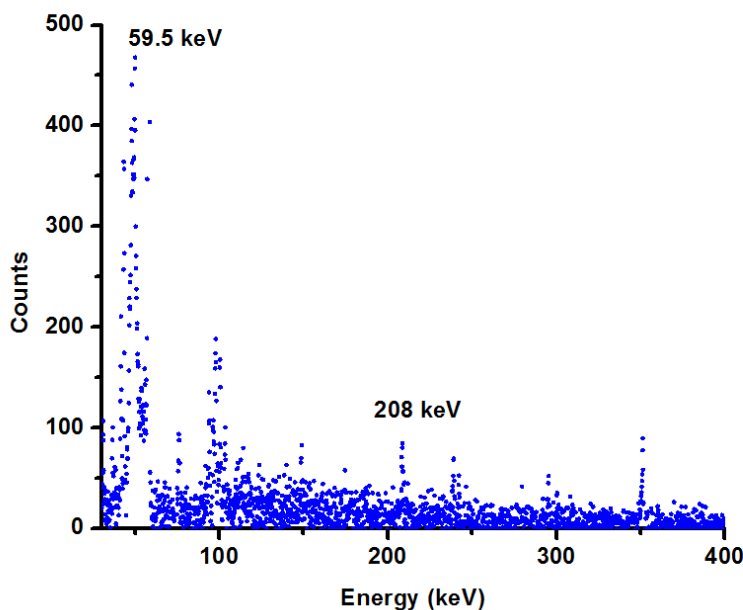


FIGURE 2.8: Background subtracted Spectrum of the biological sample obtained with HPGe detector

2.4 CONCLUSIONS

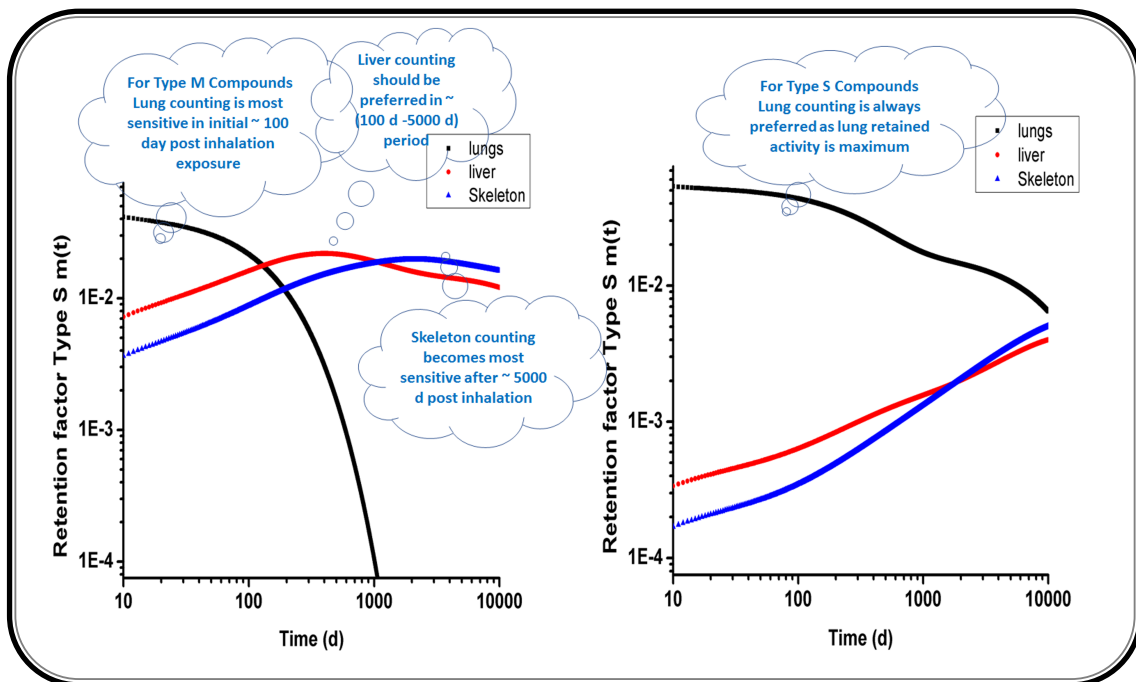
This work describes the methodology of direct measurement of Pu and ^{241}Am in biological samples using HPGe detector. Generally radiochemical analysis of biological or workplace sample followed by alpha spectroscopy is used to determine Pu/ ^{241}Am ratio in the contaminant. In this work, gamma/x-rays detection method is applied to estimate Pu and ^{241}Am deposited in biological sample. First, depth of contaminant in biological sample is estimated by comparing relative transmission of 26.3 and 59.5 keV photons of ^{241}Am . Then ^{241}Am activity is estimated using calibration factor at calculated depth. Finally, Pu activity is estimated by applying appropriate correction for ^{241}Am contribution in 17.2 keV L_{β} X-rays region and Pu/ ^{241}Am ratio is calculated. Also, methodology for estimating ^{241}Pu in small biological sample is standardized without any chemical analysis. The measured value is compared with results obtained from radiochemical separation of sample followed by alpha spectroscopy and both the results

found to agree well. The method is fast as it does not involve chemical separation of Pu and Am as required in the alpha spectrometry method. Results of this study will be useful for assessment and medical management of Pu/Am embedded in wound.

CHAPTER 3

Optimum Measurement Geometry for *In-vivo*

Assessment of $^{239}\text{Pu}/^{241}\text{Am}$



HIGHLIGHTS

- **In-vivo measurement of Pu/²⁴¹Am in workers is carried out by placing suitable detector above lungs, liver and skeleton, as major fraction of Pu/Am is transferred to liver and skeleton, after its retention in entry organ.**
- **In this work, committed effective dose (CED) corresponding to minimum detectable activity (MDA) for Type M and S ²³⁹Pu/²⁴¹Am deposited in these organs are presented and a monitoring protocol of organ measurement giving the lowest CED at different time intervals post inhalation is described.**
- **We have observed, for Type M compounds, lung measurement is the most sensitive method during initial days after inhalation exposure. Liver measurement yields the lowest CED between 100 to 2000 days and beyond that bone measurement gives the lowest CED.**
- **For Type S compounds, lung measurement remains most sensitive method even up to 10,000 days post inhalation. This study will be useful for the assessment of CED due to internally deposited ²³⁹Pu/²⁴¹Am in the workers. This work is published in radiation protection dosimetry⁸¹ and presented here with permission.**

3.1 INTRODUCTION

In the previous chapter a methodology to quickly detect and quantify Pu/Am in biological samples is discussed. If compounds of these radionuclides are measured inside the body, what will be internal dose received? Out of various measurement geometries which will be the most sensitive one, providing the lowest possible intake and committed effective dose assessment is the main aim of this work.

Plutonium is handled in fuel fabrication facilities and reprocessing plants, where, in spite of stringent safety measures, risk of internal contamination in workers due to plutonium cannot be ruled out.⁶¹ In-vivo measurements, excreta monitoring or a combination of these techniques⁵ can be used for the assessment of internally deposited ²³⁹Pu, other isotopes of plutonium and ²⁴¹Am. Initially, these isotopes are deposited at the route of entry (respiratory tract, alimentary tract, skin or wound site) and then gets translocated to other organs depending on their chemical and physical properties. In working areas of Pu/Am handling facility, inhalation is the most common route of intake to the worker. Inhaled activity is deposited in various regions of respiratory tract and a fraction is absorbed to blood and/or transferred to alimentary tract/ lymph nodes through particle transport mechanism. Absorption to blood depends on the solubility of the inhaled material which is classified as fast (Type F), moderate (Type M) and slow (Type S) categories. Human respiratory tract model (HRTM) provides details of deposition and clearance from various parts of respiratory tract.⁶ In case of moderately soluble plutonium (e.g. nitrates and all unspecified compounds)^{5,66} and all americium compounds, the deposited lung activity is absorbed into the blood with a biological half-time of about 140 days. But, oxides of ²³⁹Pu and ²⁴¹Am embedded in plutonium matrix behaves as lung absorption Type S⁶⁵ and are retained in the lungs for years which are subsequently absorbed to the blood with a biological half-time of about 7000 days.

There have been a number of updates to the International Commission on Radiological Protection (ICRP) publication 66 HRTM based on new data involving

experiments on animals and humans. The revised HRTM is published in ICRP Publication 130.⁸² In revised HRTM, deposition in parts of extra thoracic region, rates of particle transport and absorption to blood are modified. According to ICRP publication 67 biokinetic model, 80% of systemic activity of plutonium and americium is transferred to liver and skeleton. In case of plutonium, about 30% of systemic activity is transferred to the liver. Based on various studies⁸³⁻⁸⁷ carried out after ICRP 67 publication, an improved biokinetic model for plutonium is developed by Leggett *et al.*,⁸⁸ which is being incorporated in new ICRP publication.⁸⁹ In this improved biokinetic model of plutonium, initially 60% of systemic activity is transferred to liver and 30% to the skeleton. ICRP says, the bioassay predictions obtained with new model gives better fits to the measured data. Therefore, measurement of ²³⁹Pu and ²⁴¹Am deposited at the organs associated with the route of entry (lungs, wound, stomach) and organs where it is transferred and retained for long time (skeleton and liver) is an important aspect of radiation protection program. The measurement of ²³⁹Pu and ²⁴¹Am long time post exposure can be carried out by measuring activity deposited in the skeleton and liver. The skeleton measurement is performed by placing detector above knee or skull.⁹⁰ Total skeleton activity is estimated using the fraction of skeleton mass in knee or skull.

In this work, efficiency calibration of an actinide lung monitor is carried out using Lawrence Livermore National Laboratory (LLNL) thorax phantom for ²⁴¹Am deposited in the lungs and liver. The calibration factor for ²⁴¹Am, deposited in bone is taken from the earlier results on knee phantom measurement carried out under International Atomic Energy Agency (IAEA) inter-comparison exercise.⁹¹ The biokinetic model of ²³⁹Pu and ²⁴¹Am is solved to evaluate its retention in lungs, liver and skeleton at different time interval post inhalation. For direct measurement, to identify which measurement geometry will give lower intake and CED estimate, internal dose is estimated at various days post inhalation using lung, liver and skeleton measurement data of ²⁴¹Am at MDA level. Intake and CED values are calculated first using ICRP-66 HRTM, ICRP-30 GI



FIGURE 3.1: Actinide monitoring system, consists of an array of three HPGe detectors placed above lungs of the LLNL phantom inside totally shielded steel room.

tract model⁷ and ICRP -67 biokinetic mode,⁶⁶ then intake values are calculated using revised ICRP-130 HRTM,⁸² ICRP-100 human alimentary tract model (HATM)⁸ and new plutonium biokinetic model published by Leggett et al.⁸⁸ The results of this study will be useful to identify the organ whose in-vivo measurement will give the lowest intake and CED at various days post inhalation.

3.2 MEASUREMENT TECHNIQUES

3.2.1 Measurement of photons

An array of three 70 mm dia. and 25 mm thick n-type HPGe detectors (Make: Canberra Eurisys S.A.) installed inside totally shielded steel room is used for the measurement of γ/x -rays of Pu/²⁴¹Am and U.^{63,64} The three detectors of the array are enclosed in a 20 cm diameter hollow copper cylinder, positioned at 120 degrees apart. Their centers lie on

the circumference of 10 cm dia. and each has 0.8 mm thick carbon window. The total area of all the three detectors is 115.4 cm². The signals from each detector are acquired separately through three multi-channel analyzer cards, which can be summed into a single spectrum as per the requirement. Inter Winner gamma ray spectrometry software is used for analyzing the spectra. The full width at half maxima of each detector is about 0.6 keV at 59.5 keV photon energy. Figure 3.1 shows actinide monitoring system, consists of an array of three HPGe detectors placed above lungs of the LLNL phantom inside totally shielded steel room.

3.2.2 The efficiency and MDA

Efficiency calibration of in-vivo monitoring system used in this study is carried out using realistic LLNL thorax phantom⁹² for lungs and liver measurement geometry. The LLNL phantom is a physical thorax phantom based on a Caucasian man with mass 76 kg and height 177 cm.⁹³ This phantom has a simulated rib cage, removable lungs, heart, liver, major trachea and bronchial lymph nodes. Four numbers of 100% muscle equivalent chest overlay plates are available with the phantom. The overlay plates were used for placement over phantom for the representation of individuals with different tissue thicknesses above chest and liver. Thickness of the overlay plates above lungs varies from 1.77 cm to 6.18 cm and thickness above liver varies from 1.33 cm to 5.76 cm. For measurement of activity deposited in lungs, detectors are placed tangentially to supra sternal notch covering maximum lungs area and for liver measurement; detectors are placed near right sub-costal area covering liver. The counting efficiency (CE), K (cps Bq⁻¹) of the detection system at X cm of chest wall thickness (CWT) for photon energy, E_i is estimated using following equation:

$$K_{X,E_i} = \frac{(C - C_{\text{bkg}})}{A \cdot T} \quad (3.1)$$

where, A is the amount of activity (Bq) present in the lungs or liver of LLNL phantom, C and C_{bkg} are the total counts and background counts in energy region E_i recorded with lung/liver sets in respective energy region and T is measurement time. Measurement geometry is kept same for the phantom as well as for the person.

The minimum detectable activity (MDA) of the system at 95% confidence level is evaluated using following equation:⁷⁴

$$MDA = \frac{(4.65 \sigma_B + 2.7)}{K.T} \quad (3.2)$$

where, σ_B is the standard deviation in the gross counts of reference energy band of an uncontaminated person measured in appropriate geometry, K is the counting efficiency (cps Bq^{-1}); and T is the counting time.

The efficiency and MDA of the detection system for ^{241}Am in the skeleton is evaluated from our results of IAEA inter-comparison exercise. Under this exercise the leg phantom distributed with an unknown amount of ^{241}Am was received by the laboratory. The measurement of activity was carried out with phoswich detector and results were reported to IAEA. Later on, the actual amount of ^{241}Am distributed in the knee phantom was published.⁹¹ Using this value, efficiency and MDA of the phoswich detector is evaluated. To evaluate efficiency of HPGe detector, measurements were carried out for ^{241}Am deposited in the knee of a worker with phoswich and HPGe array and counts obtained by both the systems were compared to derive efficiency of HPGe detector. The results were also verified with Monte Carlo simulation of knee voxel phantom.⁹⁴

3.2.2.1 Method of in-vivo measurement of ^{239}Pu and its intake estimation

The in-vivo measurement of ^{239}Pu can be carried out by detecting L X-rays of its daughter ^{235}U which emits 13.5, 17.2 and 20.2 keV photons with a total yield of 4.6%. These U L-X rays are not energetic enough to get transmitted through lungs and liver

overlay tissues. Therefore, the detection limit of in-vivo monitoring system for the measurement of ^{239}Pu using its X-ray energy is about 2000 Bq, which is quite high compared to relevant reference level. Therefore, direct measurement of Pu in various organs is carried out using ^{241}Am as a tracer and by measuring its 59.5 keV gamma-rays having 36% yield. Then using following method amount of ^{239}Pu present in the organ or its intake is estimated:

(1) In the case of inhalation of ^{239}Pu , if ^{241}Am is measured in the lungs then it is assumed that ^{241}Am is embedded in plutonium matrix and follows biokinetics of plutonium in the lungs.⁹⁵ Using $^{239}\text{Pu}/^{241}\text{Am}$ ratio obtained from radiochemical analysis of fecal/workplace sample, and measured activity of ^{241}Am , total amount of ^{239}Pu present in the lung is estimated. The $^{239}\text{Pu}/^{241}\text{Am}$ ratio depends on burn-up of the fuel and also the time elapsed after the purification of ^{239}Pu . Typically, the $^{239}\text{Pu}/^{241}\text{Am}$ ratio found for high burn-up fuel is about three.⁹⁶ Therefore, in this work for the evaluation of ^{239}Pu , from MDA level of ^{241}Am measured in the lungs of worker $^{239}\text{Pu}/^{241}\text{Am}$ ratio of three is used. Then using ICRP-78 methodology intake of plutonium is estimated.

(2) When ^{241}Am is measured in liver or skeleton, the $^{239}\text{Pu}/^{241}\text{Am}$ ratio cannot be used directly for the estimation of ^{239}Pu deposited in the measured organ. This is because, according to ICRP, plutonium and americium follow their own biokinetics and deposition in liver and skeleton will be different from actual radionuclide composition of this material at the time of intake. Therefore, from measured ^{241}Am in liver and knee, first intake of ^{241}Am is estimated, then this value is multiplied by the $^{239}\text{Pu}/^{241}\text{Am}$ ratio to evaluate ^{239}Pu intake.⁹⁷

The measured ^{241}Am in lungs, liver and skeleton can be residual activity from intake of ^{241}Am as well as due to in-growth from ^{241}Pu ($T_{1/2} = 14.35$ y) decay. The ^{241}Pu activity can vary from 84 - 97 % of the total plutonium activity in irradiated nuclear fuel.⁹⁸ In-growth of ^{241}Am can take place in the organ where activity is deposited after intake as well as systemically. The ICRP publication 130 recommends that if ^{241}Am is

born systemically then americium biokinetics should be used in place of plutonium for dosimetric calculations. If measured ^{241}Am without in-growth correction is used for plutonium dose estimation it will lead to overestimation of intake and CED values. Hence, first in-growth of ^{241}Am from ^{241}Pu should be evaluated using isotopic composition of inhaled material at the time of intake, then, after its correction, ^{241}Am values should be used for intake and CED estimation.⁹⁸

3.2.3 Computer software used for computations of organ contents of ^{239}Pu and ^{241}Am

A computer program based on Birchall's algorithm⁹⁹ for compartmental analysis with recycling is developed and standardized.^{100,101} This program can be used for biokinetic studies of various radionuclides for any input parameters. The method incorporates the compartmentalized forms of biokinetic model of a selected radionuclide. It provides a solution for the complete compartmental model and can compute the daily urinary excretion and the amount of radioactivity retained in any organ at any time for both acute and for chronic intake by inhalation and ingestion. The transfer rate constants of plutonium and americium, d^{-1} , (defined as the fractional flow per unit time between different compartments) for the HRTM, the GI tract and systemic biokinetic models were taken from ICRP Publication 66,⁶ 78⁵ and 67⁶⁶ respectively. The above-mentioned methodology is applied to compute ^{239}Pu and ^{241}Am content in different organs for inhaled particle of $5\mu\text{m}$ activity median aerodynamic diameter (AMAD) of absorption Type M and S for acute intake. For the purpose of the quality assurance of the software used, estimated ^{239}Pu and ^{241}Am content in lungs and its daily urinary excretion were compared with the values given in the ICRP publication 78⁵ for respective categories. An excellent agreement is observed.

Also, we have estimated retained fractions after inhalation of Type M and S plutonium compounds in lungs, liver and skeleton at different time interval post

TABLE 3.1: The efficiency and MDA (50 minutes measurement time) of HPGe array at 59.5 keV photon of ^{241}Am distributed in the lungs and liver of LLNL phantom with various overlay thicknesses.

Chest wall thickness (cm)	Efficiency (cps Bq ⁻¹)	MDA (Bq)	Liver overlay thickness (cm)	Efficiency (cps Bq ⁻¹)	MDA (Bq)
1.77	2.60E-03± 3.17E-05	6.00	1.33	5.55E-03± 5.90E-06	4.00
2.84	1.81E-03± 5.10E-05	9.10	2.31	3.96E-03± 1.03E-05	4.50
3.50	1.41E-03± 6.27E-05	11.70	3.04	3.12E-03± 1.35E-05	5.00
4.32	1.04E-03± 7.74E-05	15.9	3.87	2.36E-03± 1.72E-05	7.00
6.18	6.31E-04± 7.92E-05	26.20	5.76	1.29E-03± 2.56E-05	12.80

inhalation by solving the improved plutonium biokinetic model developed by Leggett *et al.*⁸⁸ incorporated with ICRP-130 revised HRTM⁸² and ICRP-100 HATM.⁸

3.3 RESULTS AND DISCUSSION

Efficiency and MDA of HPGe array based in-vivo monitoring system for lungs and liver measurement geometry, are estimated using LLNL phantom with various overlay thicknesses above these organs and given in Table 3.1 for ^{241}Am . The MDA of the system is calculated using average value of background counts obtained in energy region of interest (ROI) of 30 non-radiation workers monitored for 3000 seconds in the lungs, liver and knee measurement geometry. The mean value of muscle equivalent chest wall thicknesses (MEQ-CWT) for Indian worker is 1.77 ± 0.31 cm.¹⁰² The basic LLNL phantom is having MEQ-CWT of 1.77 cm (which is equivalent to mean MEQ-CWT for Indian worker) and liver overlay thickness of 1.33 cm. Therefore, efficiency and MDA values corresponding to the basic overlay plate in the LLNL phantom were used for the interpretation of measurement results in terms of intake and CED. The efficiency and MDA of the system are 2.60E-03 cps Bq⁻¹ and 6.0 Bq for ^{241}Am in lungs and 5.55E-03 cps Bq⁻¹ and 4.0 Bq for ^{241}Am in liver with basic LLNL phantom. The total surface area of lungs and liver of the LLNL phantom is about 2109 cm² and 946 cm² respectively.¹⁰³

It is observed that liver geometry gives better efficiency and lower MDA compared to lungs geometry. This is because, active volume of the detector sees larger fraction of liver area than lungs and also due to lower overlying tissues thickness above liver (1.33 cm) as compared to lungs (1.77 cm), photons are less attenuated in liver geometry. We can observe from Table 3.1 that with increase in the thickness of overlay tissues above lungs and liver of the phantom, efficiency of the system decreases and MDA increases. Decrease in the efficiency is due to higher attenuation of photons with increase in the overlay thickness.

Overlying tissue thicknesses above lungs and liver of different workers are person specific, hence same counting efficiency cannot be used for all the workers, because for same amount of radio-activity present inside body, attenuation of the photons in their body will differ. In order to get person specific counting efficiency of the system, various chest overlay plates in the LLNL phantom were used and CE is estimated at several thicknesses of the overlying tissues. From these data, empirical equations are derived to estimate efficiency at a particular overlay thickness for lungs and liver geometry. Efficiency of HPGe detector based system at 59.5 keV photon energy of ^{241}Am in lungs and liver with X cm overlay thickness can be evaluated respectively by equations 3.3 and 3.4.

$$Y_{(\text{HPGe, lung, 59.5})}(X) = 0.00474e^{(-0.34 X)} \quad (3.3)$$

$$Y_{(\text{HPGe, liver, 59.5})}(X) = 0.00863e^{(-0.33 X)} \quad (3.4)$$

The efficiency and MDA of the HPGe system for ^{241}Am in the knee were $4.5\text{E-}3$ cps Bq^{-1} and about 3.0 Bq respectively. Considering that knee contains 9.3% of the total bone mass, 94 30 Bq of the ^{241}Am in skeleton can be measured using this system. The above results show that MDA of in-vivo monitoring system for ^{241}Am deposited in lungs, liver and skeleton of worker having average physique are 6.0 Bq, 4.0 Bq and 30.0 Bq respectively for measurement time of 3000 seconds. Using these values, intake and

CED at various days post inhalation is evaluated to determine sensitivity of the techniques used for the measurement.

3.3.1 Cross – talk between ^{241}Am in lungs, liver and skeleton.

It is known that ^{241}Am gets transferred to liver and skeleton as time passes after intake, which interferes in estimating correct amount of activity deposited in lungs and liver. The cross talk between lungs, liver and skeleton (ribs) should be calculated before estimating amount of activity in any of these organs. The cross talk between liver and lungs for the system, used in this work, is estimated using LLNL phantom for ^{241}Am . These values between lungs and liver is found to be less than 8% of the counting efficiency of that organ.^{104,105} Also, Lobaugh *et al.* have carried out extensive study for estimation of cross talk between lungs and other organs (ribs, lymph nodes, and liver) in thorax region. Analysis of their results show that contribution to the measured organ due to activity in the source organ is less than 5 % of the counting efficiency for the source organ.¹⁰⁶ Therefore, if in-vivo measurement of ^{241}Am is conducted long time after intake, cross – talk from the activity deposited in other organs in the thorax region should be considered before estimating activity.

3.3.2 Estimation of CED using ICRP-66 HRTM, ICRP-30 GI tract model and ICRP 67 biokinetic model of Pu and Am at MDA level of ^{241}Am measured in lungs, liver and skeleton.

Tables 3.2 and 3.3 give intake and CED calculated at MDA level of ^{241}Am measured in the lungs, liver and skeleton at various days since inhalation for absorption Type M and S compounds respectively. The dose coefficients of these radionuclides are taken from ICRP-68.¹⁰ If intake of Type M ^{241}Am occurs one day prior to lung measurement, 2.8

TABLE 3.2: The intake and CED from MDA equivalent Type M ^{241}Am measured in lungs, liver and skeleton at various days post inhalation. Intake and CED is calculated using ICRP-66 HRTM, ICRP 30 GIT and ICRP 67 biokinetic model of americium with default ICRP parameter for occupational workers.

Days (Post exposure)	Absorption Type M					
	Lungs		Liver		Skeleton	
	Intake (Bq)	CED (mSv)	Intake (Bq)	CED (mSv)	Intake (Bq)	CED (mSv)
1	1.04E+02	2.81E+00	3.20E+02	8.64E+00	3.97E+03	1.07E+02
2	1.07E+02	2.90E+00	2.92E+02	7.88E+00	3.62E+03	9.77E+01
5	1.12E+02	3.04E+00	2.71E+02	7.33E+00	3.35E+03	9.04E+01
10	1.21E+02	3.26E+00	2.59E+02	7.00E+00	3.17E+03	8.56E+01
20	1.38E+02	3.73E+00	2.41E+02	6.52E+00	2.90E+03	7.84E+01
50	1.94E+02	5.24E+00	2.08E+02	5.63E+00	2.40E+03	6.48E+01
100	2.97E+02	8.01E+00	1.83E+02	4.93E+00	1.97E+03	5.32E+01
200	5.69E+02	1.54E+01	1.65E+02	4.47E+00	1.58E+03	4.27E+01
500	3.30E+03	8.92E+01	1.76E+02	4.74E+00	1.21E+03	3.26E+01
1000	5.93E+04	1.60E+03	2.40E+02	6.49E+00	1.03E+03	2.79E+01
2000	-	-	4.24E+02	1.15E+01	9.49E+02	2.56E+01
5000	-	-	1.03E+03	2.78E+01	1.02E+03	2.76E+01
10000	-	-	1.84E+03	4.97E+01	1.25E+03	3.38E+01

Note: Intake and CED values are not given if CED exceeded 2.0 Sv.

mSv CED can be estimated. The CED estimated using MDA level of ^{241}Am measured in liver and skeleton after one day of intake is about 8.6 mSv and 107.0 mSv respectively. This shows that lung measurement of ^{241}Am is the most sensitive method for Type M compounds during initial days post inhalation. The estimated CED values at 100 days after inhalation for ^{241}Am measured in lungs, liver and skeleton were 8.01 mSv, 4.93 mSv and 53.2 mSv respectively. Thus, measured ^{241}Am deposited in the liver yields lower CED than lung measurement data at 100 days post inhalation intake. Table 3.2, therefore indicates that post 100 to 5000 days, liver measurement becomes sensitive, while post 5000 days, skeleton measurement becomes sensitive as it yields the lowest CED among three geometries. From Table 3.3, it can be observed that for ^{241}Am embedded in Type S plutonium matrix, lung geometry yields the lowest CED even up to 10,000 days post inhalation compared to other two geometries. If measurements are

TABLE 3.3: The intake and CED from MDA equivalent ^{241}Am embedded in Pu oxide (Type S) and measured in lungs, liver and skeleton at various days post inhalation. Intake and CED is calculated using ICRP-66 HRTM, ICRP 30 GIT and ICRP 67 biokinetic model of americium with default ICRP parameter for occupational workers.

Days (Post exposure)	Absorption Type S					
	Lungs		Liver		Skeleton	
	Intake (Bq)	CED (mSv)	Intake (Bq)	CED (mSv)	Intake (Bq)	CED (mSv)
1	9.33E+01	7.75E-01	1.88E+04	1.56E+02	2.33E+05	1.94E+03
2	9.57E+01	7.94E-01	1.69E+04	1.40E+02	2.09E+05	1.74E+03
5	9.89E+01	8.20E-01	1.55E+04	1.28E+02	1.91E+05	1.58E+03
10	1.04E+02	8.60E-01	1.45E+04	1.21E+02	1.78E+05	1.48E+03
20	1.13E+02	9.37E-01	1.32E+04	1.09E+02	1.59E+05	1.32E+03
50	1.37E+02	1.14E+00	1.06E+04	8.83E+01	1.23E+05	1.02E+03
100	1.64E+02	1.36E+00	8.53E+03	7.08E+01	9.31E+04	7.73E+02
200	1.92E+02	1.60E+00	6.58E+03	5.46E+01	6.50E+04	5.39E+02
500	2.57E+02	2.13E+00	4.61E+03	3.83E+01	3.59E+04	2.98E+02
1000	3.98E+02	3.30E+00	3.93E+03	3.26E+01	2.23E+04	1.85E+02
2000	8.32E+02	6.90E+00	4.33E+03	3.59E+01	1.49E+04	1.24E+02
5000	2.71E+03	2.25E+01	7.60E+03	6.31E+01	1.15E+04	9.57E+01
10000	7.04E+03	5.84E+01	1.26E+04	1.05E+02	1.18E+04	9.81E+01

conducted up to initial 200 days post inhalation, estimated CED will not be more than 1.6 mSv.

Intake and CED of absorption Type M and S ^{239}Pu calculated from MDA equivalent ^{241}Am measured in lungs, liver and knee of a worker at various days post inhalation intake are given in Tables 3.4 and 3.5. In the case of Type M ^{239}Pu , lung monitoring is the most sensitive technique during initial days after inhalation up to 100 days. About 9-10 mSv of CED from measured ^{239}Pu can be estimated if measurements are conducted within a week after inhalation. Table 3.4, therefore indicates that post 100 days, measurement of activity deposited in the liver becomes most sensitive method, while post 5000 days, skeleton measurements become most sensitive as it yields the lowest CED out of the three geometries. From Table 3.5, it can be observed that for Type S ^{239}Pu lung geometry yields the lowest CED even up to 10,000 days post inhalation compared to other two geometries. If lung measurements are conducted for ^{241}Am up to initial 200 days post inhalation, estimated ^{239}Pu CED will not be more than 4.8 mSv.

TABLE 3.4: The intake and CED of Type M ^{239}Pu from MDA equivalent ^{241}Am measured in lungs, liver and skeleton at various days post inhalation. The $^{239}\text{Pu}/^{241}\text{Am}$ ratio of 3 is taken for the calculation. The values are calculated using ICRP-66 HRTM, ICRP 30 GIT and ICRP 67 biokinetic model of Pu with default ICRP parameter.

Days (Post exposure)	Absorption Type M					
	Lungs		Liver		Skeleton	
	Intake (Bq)	CED (mSv)	Intake (Bq)	CED (mSv)	Intake (Bq)	CED (mSv)
1	3.12E+02	9.99E+00	9.60E+02	3.07E+01	1.19E+04	3.82E+02
2	3.22E+02	1.03E+01	8.76E+02	2.80E+01	1.09E+04	3.47E+02
5	3.37E+02	1.08E+01	8.14E+02	2.61E+01	1.00E+04	3.21E+02
10	3.63E+02	1.16E+01	7.78E+02	2.49E+01	9.52E+03	3.05E+02
20	4.15E+02	1.33E+01	7.24E+02	2.32E+01	8.71E+03	2.79E+02
50	5.82E+02	1.86E+01	6.25E+02	2.00E+01	7.20E+03	2.30E+02
100	8.90E+02	2.85E+01	5.48E+02	1.75E+01	5.91E+03	1.89E+02
200	1.71E+03	5.46E+01	4.96E+02	1.59E+01	4.74E+03	1.52E+02
500	9.91E+03	3.17E+02	5.27E+02	1.69E+01	3.62E+03	1.16E+02
1000	1.78E+05	5.69E+03	7.21E+02	2.31E+01	3.10E+03	9.93E+01
2000	-	-	1.27E+03	4.07E+01	2.85E+03	9.11E+01
5000	-	-	3.09E+03	9.90E+01	3.06E+03	9.80E+01
10000	-	-	5.52E+03	1.77E+02	3.75E+03	1.20E+02

Note: Intake and CED values are not given if CED exceeded 2.0 Sv.

TABLE 3.5: The intake and CED of Type S ^{239}Pu from MDA equivalent ^{241}Am measured in lungs, liver and skeleton at various days post inhalation. The $^{239}\text{Pu}/^{241}\text{Am}$ ratio of 3 is taken for the calculation. The values are calculated using ICRP-66 HRTM, ICRP 30 GIT and ICRP 67 biokinetic model of Pu with default ICRP parameter.

Days (Post exposure)	Absorption Type S					
	Lungs		Liver		Skeleton	
	Intake (Bq)	CED (mSv)	Intake (Bq)	CED (mSv)	Intake (Bq)	CED (mSv)
1	2.80E+02	2.32E+00	5.64E+04	4.68E+02	-	-
2	2.87E+02	2.38E+00	5.06E+04	4.20E+02	-	-
5	2.97E+02	2.46E+00	4.64E+04	3.85E+02	-	-
10	3.11E+02	2.58E+00	4.36E+04	3.62E+02	-	-
20	3.39E+02	2.81E+00	3.95E+04	3.28E+02	-	-
50	4.11E+02	3.41E+00	3.19E+04	2.65E+02	-	-
100	4.91E+02	4.08E+00	2.56E+04	2.13E+02	-	-
200	5.77E+02	4.79E+00	1.97E+04	1.64E+02	1.95E+05	1.62E+03
500	7.71E+02	6.40E+00	1.38E+04	1.15E+02	1.08E+05	8.94E+02
1000	1.19E+03	9.90E+00	1.18E+04	9.78E+01	6.68E+04	5.54E+02
2000	2.50E+03	2.07E+01	1.30E+04	1.08E+02	4.47E+04	3.71E+02
5000	8.13E+03	6.75E+01	2.28E+04	1.89E+02	3.46E+04	2.87E+02
10000	2.11E+04	1.75E+02	3.79E+04	3.14E+02	3.55E+04	2.94E+02

Note: Intake and CED values are not given if CED exceeded 2.0 Sv.

3.3.3 Effect of revised HRTM, HATM and Leggett's systemic biokinetic model of Plutonium on intake estimation.

For inhalation of Type M and S ^{239}Pu , the ICRP-130 revised HRTM, ICRP-100 HATM and revised ICRP-67 systemic biokinetic model of plutonium published by Leggett *et al.* is integrated together and solved for default parameters of reference radiation worker. These models were used to calculate retention fractions in lungs, liver and skeleton at various days after inhalation. ICRP has not published dose coefficient using revised biokinetic models, therefore only intake values were estimated. CED can be calculated by multiplying these intake values with new dose coefficients whenever it will be available. The retained values in lungs, liver and skeleton is compared with those obtained with earlier models and are presented in Figure 3.3 and Figure 3.2 for absorption Type M and S ^{239}Pu respectively. It is observed from Figure 3.3 that with previous models, initially lower amount of systemic activity is transferred to liver than skeleton. In revised model, larger fraction of plutonium is transferred to liver than skeleton in initial days. At 1,000 days post inhalation skeleton deposit exceeds liver deposit. For Type M ^{239}Pu after 100 days since inhalation, liver deposit exceeds lung deposit. Therefore, measurements carried out after 100 days post inhalation of Type M ^{239}Pu , the liver measurement gives lower intake. Figure 3.2 shows, for Type S ^{239}Pu lung retention is similar with both models up to 600 days, afterwards lung retention is higher with the new model. The higher lung retention obtained with new model than previous model is likely to results into higher lung dose. The initial deposition in liver and skeleton are lower with revised model than earlier. In the revised model for Type S ^{239}Pu , liver content is higher than skeleton up to 4,000 days, after that skeleton content is higher. For Type S compounds of plutonium, lung retention is higher than liver and skeleton even up to 10,000 days. Intake values at MDA level of activity measured in lungs, liver and skeleton based on revised ICRP models are estimated and these values

TABLE 3.6: Estimated intake of Type M ^{239}Pu from MDA equivalent ^{241}Am measured in lungs, liver and skeleton at various days post inhalation. The Pu/ ^{241}Am ratio of 3 is taken for the calculation of intake. Intake is calculated using ICRP-130 HRTM, ICRP-100 HATM and Leggett's biokinetic model of Pu with default parameters for occupational workers.

Days(Post exposure)	Absorption Type S		
	Lungs Intake (Bq)	Liver Intake (Bq)	Skeleton Intake (Bq)
1	2.89E+02	9.98E+04	-
2	2.98E+02	6.02E+04	-
5	3.18E+02	3.76E+04	-
10	3.36E+02	3.21E+04	-
20	3.51E+02	2.95E+04	-
50	3.75E+02	2.50E+04	-
100	4.13E+02	2.05E+04	2.24E+05
200	4.94E+02	1.60E+04	1.58E+05
500	7.42E+02	1.17E+04	9.01E+04
1000	1.03E+03	1.02E+04	5.70E+04
2000	1.25E+03	9.74E+03	3.54E+04
5000	1.72E+03	1.02E+04	1.93E+04
10000	2.90E+03	1.30E+04	1.35E+04

Note: Intake values are not given if exceeds MBq.

are given in Table 3.6 and 3.7 for absorption Type M and Type S ^{239}Pu respectively. It is observed from Table 3.6 that for Type M ^{239}Pu , with revised model also, in-vivo measurement of lungs is the most sensitive technique up to 200 days post inhalation, after that liver measurement is the most sensitive method. After 5,000 days, knee/skeleton measurement result yields the lowest intake. In case of Type S ^{239}Pu lungs measurement remains the most sensitive method even up to 10,000 days post inhalation compared to other two geometries.

3.3.4 Estimation of intake and CED from in-vivo measurement after acute inhalation intake of ^{241}Am .

We have used a case study to show that follow-up measurement data of various geometries such as lungs, liver and skeleton should be used for intake and CED

TABLE 3.7: Estimated intake of Type S ^{239}Pu from MDA equivalent ^{241}Am measured in lungs, liver and skeleton at various days post inhalation. The $\text{Pu}/^{241}\text{Am}$ ratio of 3 is taken for the calculation of intake of ^{239}Pu . Intake is calculated using ICRP-130 HRTM, ICRP-100 HATM and Leggett's biokinetic model of Pu with default parameters for occupational workers.

Days(Post exposure)	Absorption Type S		
	Lungs Intake (Bq)	Liver Intake (Bq)	Skeleton Intake (Bq)
1	2.89E+02	9.98E+04	-
2	2.98E+02	6.02E+04	-
5	3.18E+02	3.76E+04	-
10	3.36E+02	3.21E+04	-
20	3.51E+02	2.95E+04	-
50	3.75E+02	2.50E+04	-
100	4.13E+02	2.05E+04	2.24E+05
200	4.94E+02	1.60E+04	1.58E+05
500	7.42E+02	1.17E+04	9.01E+04
1000	1.03E+03	1.02E+04	5.70E+04
2000	1.25E+03	9.74E+03	3.54E+04
5000	1.72E+03	1.02E+04	1.93E+04
10000	2.90E+03	1.30E+04	1.35E+04

Note: Intake values are not given if exceeds MBq.

calculation. Kathren *et al.* have described a case involving a person who was exposed while examining an old 370 MBq shield ^{241}Am sources on 1st February 1996.¹⁰⁷ Long term follow-up measurement (up to six years) of ^{241}Am deposited in lungs, liver and skeleton of this worker was carried out. The authors¹⁰⁷ have interpreted this material primarily being Type S perhaps mixed with Type M material. Based on this interpretation, they have estimated intake as 6.3 kBq. This case is also listed in IDEAS internal dosimetry database; Case Id 20637. The intake and CED estimated by IDEAS is 7.2 kBq and 116.0 mSv respectively. We have estimated retention factors for lungs and liver and calculated CED using ICRP 78 methodology (dose coefficient and biokinetic model) from lungs and liver measurement data, assuming material behaving as absorption Type M and S. The calculated CED assuming Type M material using lung and liver data are 1753.0 mSv and 70.0 mSv respectively. If inhaled material is assumed as

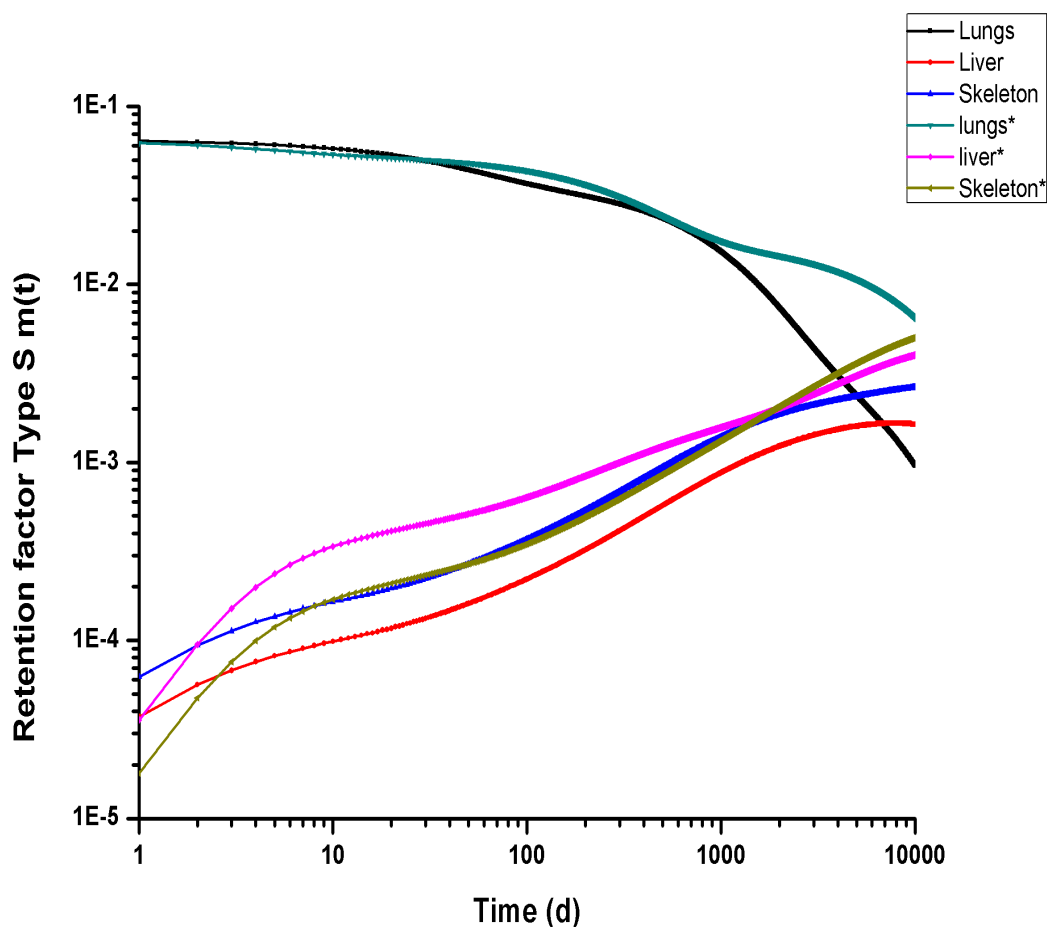


FIGURE 3.2: Predicted values (Bq per Bq intake) in lungs, liver and skeleton following acute inhalation intake of Type S ^{239}Pu using default ICRP metabolic parameters. The values marked with * denotes results obtained with revised HRTM, new HATM and Leggett's Pu biokinetic model.

Type S, estimated CED using lung and liver data are 54.9 mSv and 705.6 mSv respectively. Though the lung data support Type S behavior, liver measurement supports Type M behaviour of inhaled compound which indicates it to be a mixture of Type S and Type M materials. Therefore, while estimating CED, importance should be given not only to lungs measurement data but also to other organ measurement data. Using integrated modules for bioassay (IMBA)¹⁰⁸ software, best estimated intake and CED for this case are 7.1 kBq and 128.0 mSv respectively.

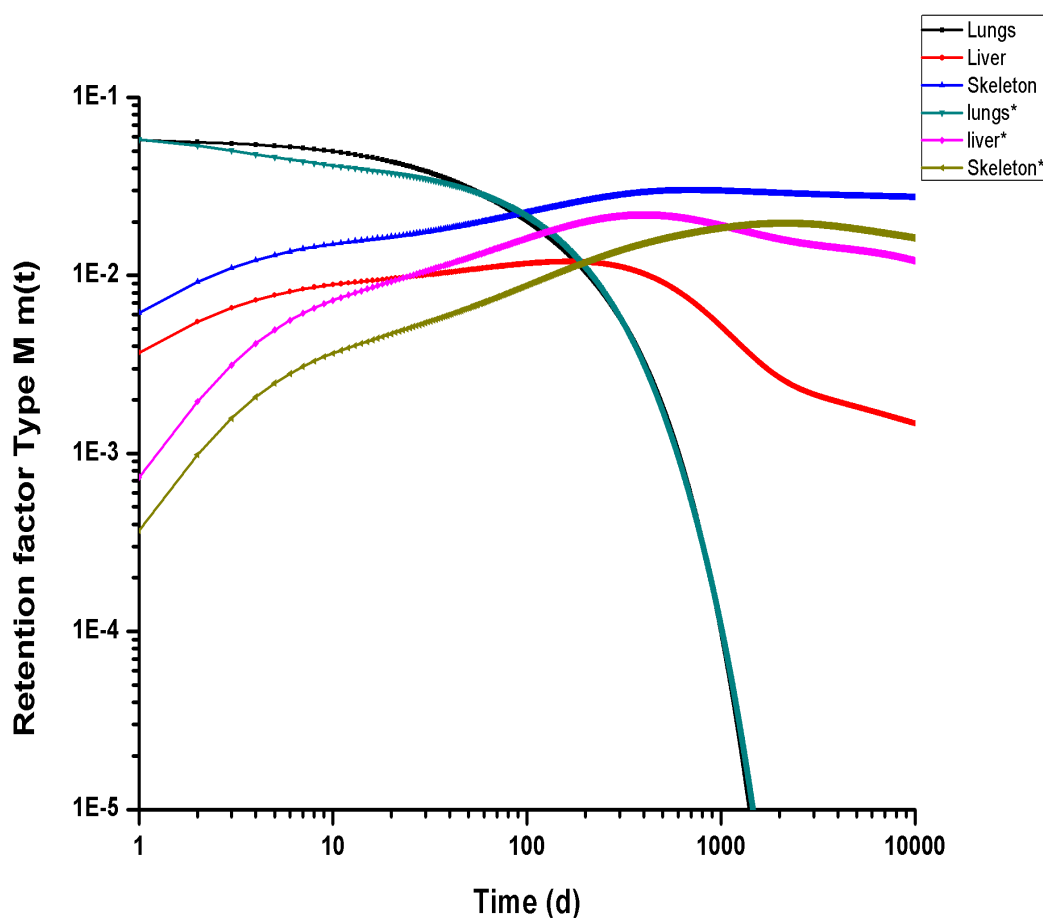


FIGURE 3.3: Predicted values (Bq per Bq intake) in lungs, liver and skeleton following acute inhalation intake of Type M ^{239}Pu using default ICRP metabolic parameters. The values marked with * denotes results obtained with revised HRTM, new HATM and Leggett's Pu biokinetic model.

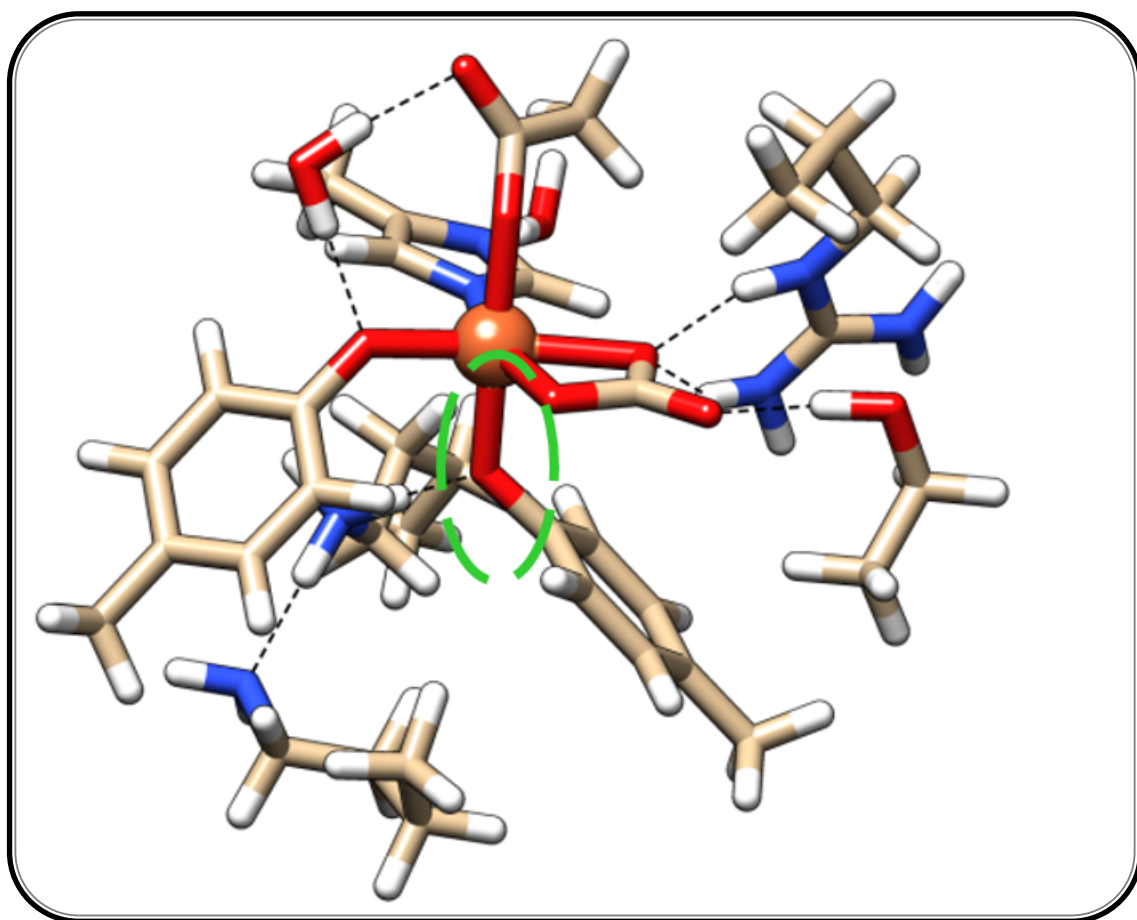
3.4 CONCLUSIONS

The CEDs corresponding to MDA equivalent activity measured in lungs, liver and knee of worker for absorption Type M and S ^{239}Pu and ^{241}Am are estimated. The efficiency and MDA of HPGe array based in-vivo monitoring system for ^{241}Am deposited in lungs, liver and skeleton are estimated using LLNL phantom and IAEA leg phantom. Retained fractions in lungs, liver and skeleton at different time post inhalation are estimated using HRTM, GI tract model and ICRP-67 systemic model of ^{239}Pu and ^{241}Am . Retained values

in these organs were compared with those obtained from the improved biokinetic model for plutonium developed by Leggett et al. incorporating ICRP-130 revised HRTM and HATM. The evaluated CED at MDA level of ^{239}Pu and ^{241}Am present in lungs, liver and skeleton show for absorption Type M compounds, lung measurement is the most sensitive method, if measurements were carried out during initial days post inhalation, but after 100 days, liver measurement yields the lowest CED. After 5000 days post inhalation, knee measurement gives the lowest CED. For Type S ^{239}Pu , lung measurement remains the most sensitive method even up to 10,000 days post inhalation intake. Results of this study will be useful in the assessment of internal dose due to intake of ^{239}Pu and ^{241}Am in the case of old exposure.

CHAPTER 4

Quantum Chemical Studies of Iron Transferrin



HIGHLIGHTS

- **Density functional theory (DFT) based calculations using large cluster models are used to elucidate the ground state electronic structure of iron bound transferrin. Explicit incorporation of second coordination amino acid residues and crystallographic water molecules anchor the active site.**
- **Electronic structure calculations clearly suggest tyrosine amino acid (Y188) residue is bound to iron when the structures are optimized within the continuum solvation model. However, in the gas phase optimized structure, we note that Y188 is unbound to Fe (by more than 3Å).**
- **The Mössbauer isomer shift (δ) and quadrupolar splitting (ΔE_q) of iron transferrin are in line with the experimental data only when Y188 is bound to Fe(III). Further, the computed oxygen hyperfine coupling constant value is very large (-14.5 MHz) when bound to iron which can be verified through ^{17}O NMR experiments.**
- **It is observed that Y188 is strongly bound to Fe(III) at physiological pH, which needs to be protonated (acidic pH) to weaken this bond, thus the metal release pathway can be possible only in acidic conditions.**
- **This work is published in the journal of chemical sciences¹⁰⁹ and presented here with permission.**

4.1 INTRODUCTION

In previous 2nd and 3rd chapters, biokinetic and dosimetric aspects of Pu/Am compounds have been discussed. It is observed that these radionuclides are deposited to various organs *viz.* lungs, liver, bones etc. Iron carrier protein serum transferrin (sTf) is found to be one of the responsible agents for their transport within the body. Methods discussed in the preceding chapters provide information on the amount of activity present in the body and corresponding committed effective dose received by the person. These methods are unable to throw light on the reaction mechanism responsible for transport of these metal ions inside our body especially their biochemical interaction with sTf. To understand molecular mechanism of their transport within the body several *in-silico* investigations have been carried out and presented in subsequent chapters. This thesis not only focus extensively on studying the binding and chelation mechanism of plutonium with sTf as carrier, but also two other actinide ions Th(IV) and Cm(III) are investigated for their interaction with sTf at different pH conditions. Before starting the multi-scale modelling of sTf complexes with plutonium and other actinide ions, a model structure of the binding site of sTf protein loaded with the native iron Fe(III) has been standardized and various structural, EPR and spin Hamiltonian (SH) parameters are evaluated and compared with available experimental data. In this chapter density functional theory DFT based calculations are presented to elucidate the ground state electronic structure of iron bound transferrin.

Serum transferrin (sTf) is the protein that transports iron through the blood between sites of uptake, utilization, and storage. The major function of these proteins is to control the level of free iron in physiological fluids by binding and sequestering Fe(III) cations.^{110–112} Active site iron in Fe-sTf is octahedron geometry coordinated by two tyrosines (Y95, Y188), a histidine (H249), an aspartate (D63) and bidentate inorganic carbonate (CO_3^{2-}) ion as synergistic anion as shown in Figure 4.1.^{113–115} Further, there are a number of amino acid residues in the second coordination shell such as

arginine (R124), salt-bridged lysine (K206 and K296), threonine (T120) and several water molecules anchor the first coordination shell. It is now well-known that at physiological pH the Fe^{3+} binding strength to the protein is very strong ($K_a = 10^6 \text{ M}^{-1}$). Only 30% of the sTf is occupied by Fe^{3+} , whereas the remaining vacant sites can be accommodated by a variety of metal ions such as other 3d transition metal ions (e.g., Cu^{2+} , Zn^{2+} , Co^{3+} and Ni^{3+} to name a few) and inner transition elements (e.g., Eu^{3+} , Am^{3+} , Cm^{3+} , Pu^{4+} , Th^{4+} , Np^{5+} , UO^{2+}).^{18,20,22,116–126} A number of experimental studies have been carried out to understand the geometric and electronic structure and the ion release pathway of sTf.^{114,115,124,127,128} As the magnetic anisotropy is very small ($<0.5 \text{ cm}^{-1}$) due to half-filled d^5 iron,^{129–133} the isomer shift and quadrupolar splitting of Fe derived from Mössbauer spectroscopy (MB) are often used to elucidate the electronic structure of the active site.^{134–136} As far as ion transmission pathways are concerned, several molecular dynamics simulations are carried out by varying the protonation state of the nearby amino acids such as salt bridged lysines K206- K296, tyrosine Y188, and carbonate.¹³⁷ A number of computer studies are carried out on the geometric structures of iron-transferrin using small cluster models.^{122,137,138} Rinaldo and Field¹³⁹ carried out the very first gas phase density functional theory (DFT) based calculations and suggested that salt bridged K206 – K296 could be vital for ion transmission due to the automatic proton transfer from K296 to the bound Y188 which weakens the Fe-Y188 interaction. However, recent molecular dynamics (MD) and QM/MM/MD simulations in physiological and in acidic pH suggest that Fe-Y188 interaction weakens only in acidic pH.^{137–140} A plethora of spin Hamiltonian parameters (SH) derived from MB spectroscopy and EPR spectroscopy are available which can directly reveal the electronic structure of iron sTf in physiological pH.^{117,130–133,135,136,141–144} Computing these SH parameters can directly reveal the coordination environment of Fe(III) in sTf which was never attempted before. Thus, the question arises what is the geometric and electronic structure of iron bound sTf in physiological pH ? In this work, this important question has been attempted to solve

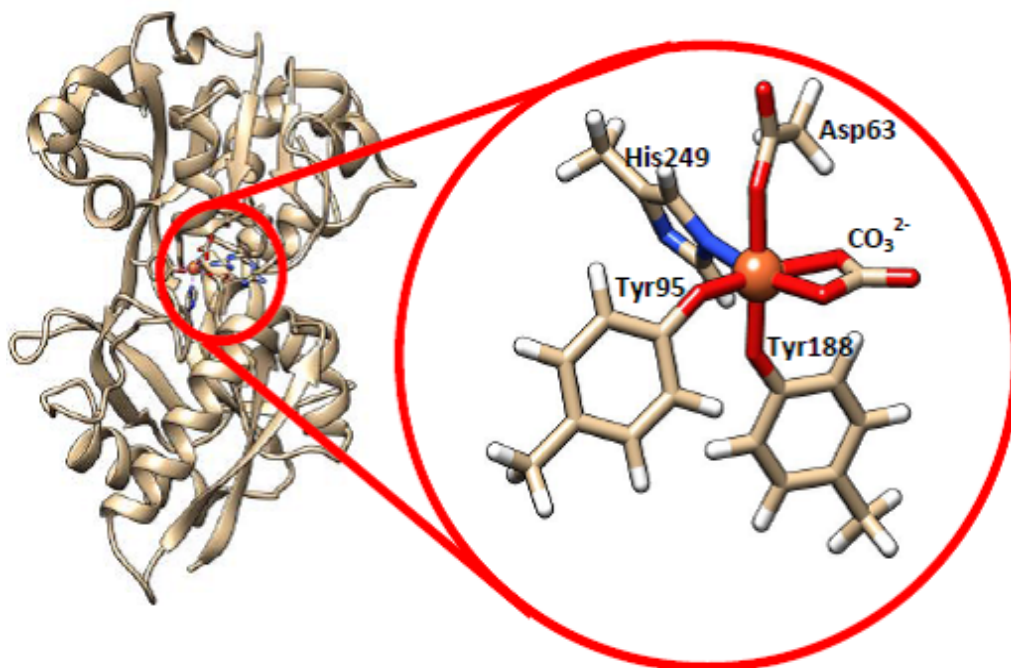


FIGURE 4.1: Active site structure of sTf.

through the computation of SH parameters derived from EPR and MB spectroscopy.^{145–149} From the results of the study it is proposed that the oxygen (^{17}O) hyperfine coupling constant (HFCC) values of Y188 are very large ($>13\text{MHz}$) when bound to Fe(III) and very small ($<2\text{MHz}$) when it is unbound. These variations can be used as fingerprint values to distinguish the binding nature of Y188 to Fe(III) ion.

4.2 COMPUTATIONAL STRATEGY

The N lobe structure of sTf is used for this computational study (PDB Code: 1A8E, 1.6 Å resolution).¹¹⁴ In addition to the first coordination shell (D63, Y95, Y188, H249, and carbonate), important second shell residues viz. dilysine salt bridge (K206 and K296), hydrogen bonded residues such as R124 (to carbonate), T120 (to carbonate) and two crystallographic water molecules have also been incorporated. It should be noted that the salt bridge (K296 and K206) is strongly hydrogen bonded to Y188 (Figure 4.2). In the

calculations, all amino acids have been truncated between C β –C α positions. The C α carbons are fixed to crystallographic positions to mimic the steric effect of the protein. We have used large size cluster models which can be treated as an alternative to QM/MM models in line with our earlier studies and in the pioneering works by Siegbahn *et al.*^{150–152} We have earlier used large cluster models to understand the electronic structure of several metalloproteins which are comparable to QM/MM simulations.^{35,41,153} The choice of density functional is crucial for the accurate prediction of geometry. In this area, both B3LYP and BP86 functionals are commonly applied to model metalloproteins. The structures are optimized in both vacuum (gas phase) and in protein dielectric ($\epsilon = 5$) using dispersion corrected (D3BJ) BP86 functional in conjunction with TZVP^{41,42} basis set for all atoms. This functional is successfully used to model the electronic structure of several iron and copper containing metalloproteins.^{146–149} In this work additional calculations with neutral and anionic histidine's have also been carried out. The protein dielectric calculation is carried out using the COSMO continuum solvation model as implemented in TURBOMOLE 6.6.¹⁵⁴ EPR and MB calculations are carried out at the DFT level using the B3LYP functional.^{36,155} The choice of using this functional is well-known that functionals containing HF-exchange tend to predict the spin Hamiltonian parameters better than the pure functionals. Particularly for MB parameters, the standard deviation of B3LYP functional is smaller than the BP86 functional. For these calculations, a CP(PPP)¹⁵⁶ (for Fe) and TZVP (for all atoms) basis set have been used. The technical details on the computation of SH parameters are discussed in detail in references.^{157,158} The isomer shift (δ) and the quadrupolar splitting (ΔE_q) are closely related to the electron density distribution of the iron nucleus. To validate the computed SH parameters, the EPR parameters for copper transferrin have been computed, where the experimental data are known.^{147–149} (see Table:4.4). Based on this study, the predicted geometries as well as the g-tensor and hyperfine coupling constants (HFCC) of Cu and N (H249) are found to be in excellent agreement with the experimental data.¹³¹

4.3 RESULTS AND DISCUSSION

4.3.1 Gas phase vs. embedded optimized geometries

The optimized structures of Fe-sTf with isolated (gas phase) model and embedded models (optimized within the continuum solvation model) are very different (Figure 4.2 and Table 4.1). Significant geometric changes within the first coordination shell are observed for the two optimized structures. Particularly, a five-coordinated species is found in the optimized isolated gas phase model with a long Fe-O_{Y188} (more than 3 Å, Figure 4.2a). The longer Fe-O_{Y188} is attributed to the direct proton transfer from the neighbouring salt bridge (K296) during optimization and consequently, the Fe-O_{D63} bond (1.927 Å) is shortened. These geometric variations are also observed in the gas phase geometry optimizations of Rinaldo and Field.¹³⁹ Further, the carbonate is asymmetrically bound to Fe(III) (2.032 to 2.227 Å) due to strong hydrogen bonding from R124 and T120 (Figure 4.2). It is observed that one water molecule is anchoring Y95 and D63 through a hydrogen bond, whereas the second water molecule is hydrogen bonded to anionic H249 (δ or ϵ). However, in the optimized embedded model, Y188 is found to be strongly bound to Fe(III) (2.078 Å) and the proton is strongly intact with K296. Further, there is no proton transfer from salt bridged K296 to Y188 (1.663 Å) which lead to conclude the hexacoordinated Fe(III) active site geometry. It is observed that even if calculations are started with Y188 as protonated form, the proton simultaneously transferred back to K296 which is ≈ 9 kcal mol⁻¹ lower in energy than when Y188 is protonated. These variations are consistent with the recent MD simulations study of Mujika et al.,¹³⁷ where they have suggested that only at low pH, the metal release is possible. Finally, the Fe-O_{D63} bond length in the embedded model is elongated as compared to the isolated model by 0.12 Å. The other Fe-ligand bond lengths in the embedded and isolated models are very similar (Table 4.1). Further, neutral H249 has also been considered in the study which weaken the Fe-N bond and alters the geometry significantly. Indeed, Rinaldo et al., reported that H249 should be

TABLE 4.1: Optimized first coordination parameters (in Å) around the iron center of Fe-sTf.

Models	X—O _{D63}	X—O _{Y95}	X—O _{Y188}	X—N _{H249}	X—O _{1CO3}	X—O _{2CO3}
Isolated	1.93	1.92	5.03	2.04	2.03	2.23
Embedded	2.04 (2.03)	2.11 (1.96)	2.08 (2.06)	2.11 (2.19)	2.07 (2.04)	2.21 (2.20)
X-ray	2.02	1.99	1.90	2.10	2.06	2.24

Note: Values given in the brackets are for optimized embedded structure with neutral H249.

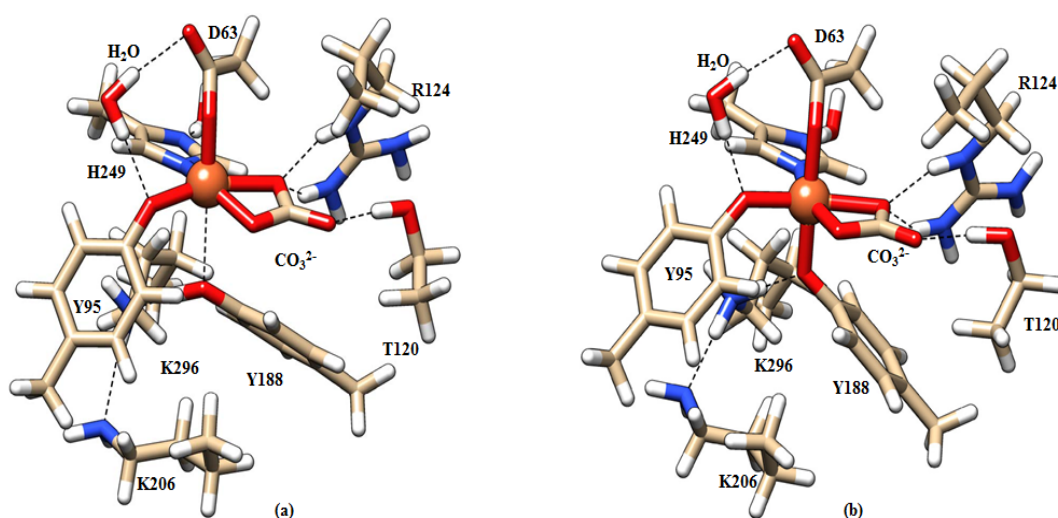


FIGURE 4.2: Optimized structures of (a) isolated and (b) embedded models.

deprotonated.¹³⁹ Other protonation sites such as D63 are beyond the scope of the work as this study is focused only on physiological pH. Within the two clusters, it is found that the embedded model (CPCM-B3LYP/TZVP//CPCM-BP86//TZVP) is more stable than the isolated cluster (CPCM-B3LYP/ TZVP//BP86//TZVP) by 6.97 kcal mol⁻¹.

4.3.2 MB and EPR spin Hamiltonian parameters

Isomer shift (δ), quadrupolar splitting (ΔE_q) and HFCC of the coordinating ligands (¹⁴N and ¹⁷O) of both the optimized structures have been computed. The trivalent oxidation state of iron is a high spin state (⁶A_{1g}) with half-filled d-orbitals. The computed spin Hamiltonian parameters using B3LYP functional for both isolated and embedded models

TABLE 4.2: Computed MB (isomer shift (δ), quadrupolar splitting (ΔE_q) (mm s^{-1})) and super hyperfine coupling constants (MHz).

Models	IS(δ)	QS (ΔE_q)	Fe Aiso	O _{D63} Aiso	O _{Y95} Aiso	O _{Y188} Aiso	N _{H249} Aiso	O1 _{CO3} Aiso	O2 _{CO3} Aiso
Isolated	0.478	1.241 (1.145)	-17.0	-17.3	-15.2	-1.5	-8.3	-7.9	-7.7
Embedded	0.519	-0.578 (-0.587)	-18.5	-14.0	-15.3	-14.5	-8.2	-7.7	-7.3
Expt30	0.38	0.75							

are compared with experimental data (Table 4.2). The SH parameters for the embedded cluster are also computed with neutral H249 as well. The computed δ of both isolated (0.478 mm s^{-1}) and embedded (0.519 mm s^{-1}) models are in agreement with the experimental value (0.38 mm s^{-1}) which is characteristic of high spin ferric species. However, the computed ΔE_q is very different for the two species. It should be noted that for high spin ferric systems, the ΔE_q should be minimal due to the absence of an electric field gradient. Between the two models, ΔE_q is found to be large (1.241 mm s^{-1}) for the isolated model, whereas for the embedded model this value is small (-0.578 mm s^{-1}) and in line with experimental value (0.75 mm s^{-1}). The major component in the ΔE_q , is the electric field gradient which may be positive or negative. This depends on the type of asymmetry of the electronic charge distribution. These variations are perhaps due to large geometric variations in the isolated model (penta-coordinated iron) as compared to the embedded model (hexa-coordinated iron) which will be more prominently reflected in the HFCC of the ligands. To our knowledge, the HFCC parameters derived from EPR spectroscopy in both experiment and in theory of native Fe-sTf was never measured or computed before. However, some insights on Cu bound sTf are known at least experimentally.¹³¹ To gauge the computational protocol in this study, the EPR SH parameters of Cu-sTf have been computed using the embedded model as described for Fe-sTf and compared with the experimental values. The optimized structural parameters and geometry are shown in Table 4.3 and Figure 4.3. The Cu-O_{Y188} bond is found to be

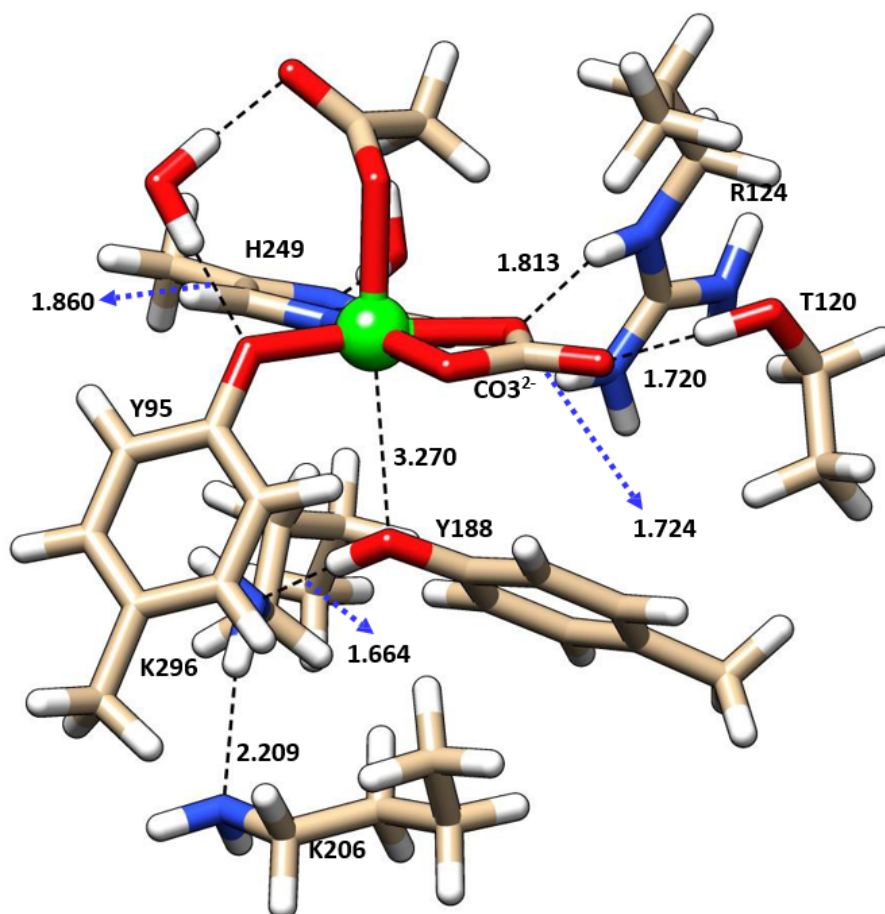


FIGURE 4.3: Optimized structures of Cu-sTf using embedded model (Units in Å).

TABLE 4.3: Optimized first coordination parameters (in Å) around the binding cleft of Cu-sTf.

Models	X—O _{D63}	X—O _{Y95}	X—O _{Y188}	X—N _{H249}	X—O _{1CO3}	X—O _{2CO3}
Optimized	2.32 (2.24)	2.02 (1.99)	3.27 (4.47)	1.99 (2.01)	2.06 (2.04)	2.14 (2.13)
X-ray	2.0	2.0	2.84	2.0	1.9	2.2

Note: Values given in the brackets are for optimized embedded structure with neutral H249.

weak in both X-ray (≈ 2.8 Å) and in optimized structure (≈ 3.2 Å) which is expected due to the Jahn-Teller nature of Cu(II) ion.¹⁴⁵ Computed the EPR SH parameters of Cu-sTf using the embedded model as described for Fe-sTf are given in Table 4.4. An axial type g-tensor predicted in the calculations ($g^{\parallel} = 2.225$ and $g^{\perp} = 2.071$) are found to be in line

TABLE 4.4: Computed EPR Parameters for Cu-sTf

	g^{\perp}	g^{\parallel}	$^{\parallel}A_{Cu}$	O_{D63} Aiso (HCC in MHz)	O_{Y95} Aiso	O_{Y188} Aiso	$O1_{CO3}$ Aiso	$O2_{CO3}$ Aiso
Computed	2.071 (2.068)	2.225 (2.223)	-429 (-467)	1.6	-43.5	-0.2	-28.6	-36.2
Experiment²⁵	2.062	2.312	420					

with the experimental estimates of ($g^{\parallel} = 2.312$ and $g^{\perp} = 2.062$).^{117,124,141-143,159} It is now well-known that metal HFCC is very hard to predict due to the limitations of DFT itself. Nevertheless, the computed Cu HFCC are corrected as discussed in the detailed investigation of Sinnecker and Neese.¹⁶⁰ The predicted Cu HFCC is now in excellent agreement with the experimental data with 10 MHz which shows the reliability of our computational tool employed here even for challenging biomolecules.

As far as Fe-sTf is concerned, the computed HFCC of the directly bound amino acid ligands to the Fe(III) center is shown in Table 4.2. For both isolated and embedded models, the ^{17}O HFCC of carbonates (≈ -7 to 8 MHz), Y95 (≈ -15 MHz) and ^{14}N of H249 (≈ -8.2 MHz) are very similar. However, the computed HFCC of ^{17}O Y188 in the isolated model is very small (-1.5 MHz) due to very long Fe- O_{Y188} (more than 3 Å) thus the oxygen interaction with high spin Fe(III) is rather weak. However, the Fe- O_{Y188} bond is very strong (2.1 Å) in the embedded model which lead to very large HFCC (-14.5 MHz) due to stronger Fe- O_{Y188} interaction. Conversely, ^{17}O HFCC of D63 in the embedded model is smaller (-14.0 MHz) as compared to the isolated model (-17.3 MHz). These variations are due to stronger Fe- O_{D63} bond in the isolated model (≈ 1.9 Å), whereas in the embedded model this distance is slightly longer (≈ 2.1 Å). These variations in super-HFCC of oxygen can be estimated through high field EPR and NMR studies.¹⁶¹⁻¹⁶⁴

The quantum chemical study presented here provide valuable insights to understand the electronic structure of iron-transferrin at physiological pH. Incorrect modeling such as neglecting the second coordination amino acid residues, solvation and explicit incorporation of water molecules can lead to biased conclusions is clear from this study. Further, from a biochemistry perspective, this study suggests that at physiological pH, Fe^{3+} remain strongly bound and an external perturbation such as lowering of pH. In acidic conditions, Y188 amino acid will be protonated and can weaken its interaction with Fe^{3+} , thus releasing the iron.

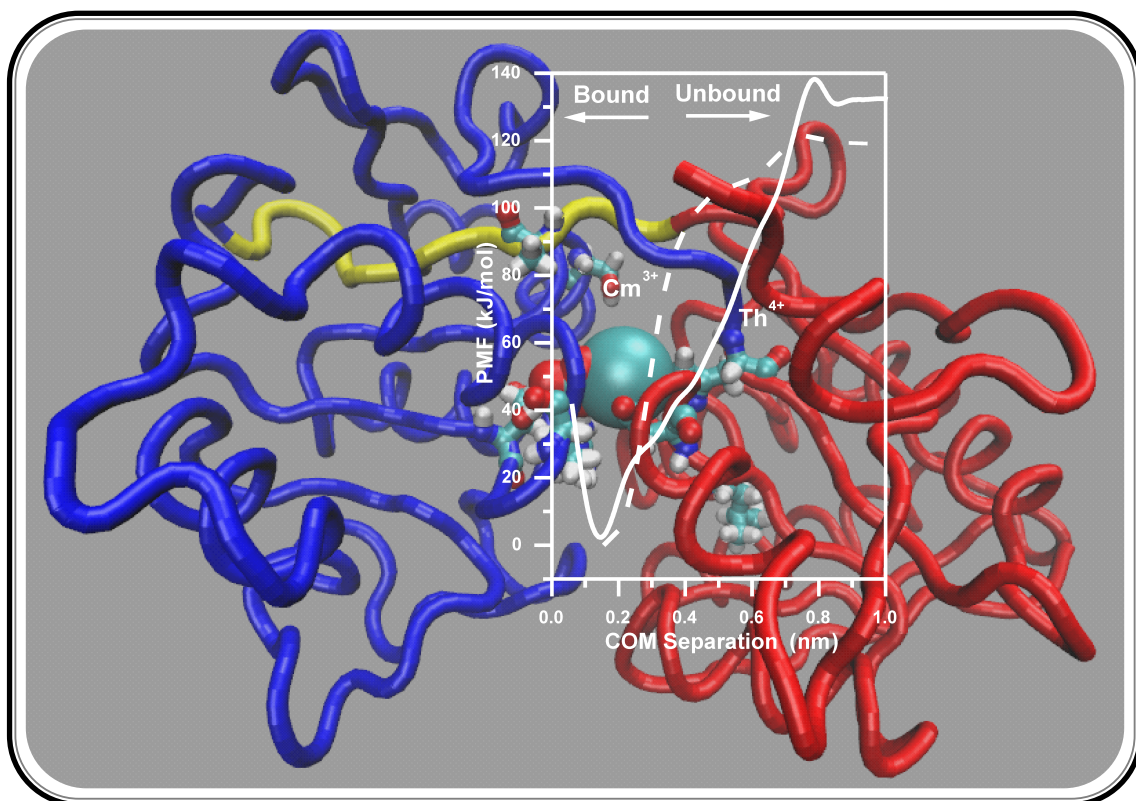
4.4 CONCLUSIONS

In this work, electronic structure calculations are carried out to understand the debatable geometric structure of Fe-sTf. It is observed from the study that use of gas phase geometry optimization predicts a wrong penta-coordinated geometric structure and thus an incorrect electronic structure, whereas the geometry predicted within the continuum solvation model is hexa-coordinate which is similar to the experimentally observed crystal structure. This study predicts that Fe in sTf is hexa-coordinated with a bound O_{Y188} at physiological pH. The computed MB parameters are in line with the experimental data only when O_{Y188} is bound to Fe. Further, ^{17}O HFCC of Y188 is very large (-14.5 MHz) when bound to Fe as compared to unbound state (-1.5 MHz) which can be measured with paramagnetic NMR experiments. Computational benchmark of this study is used in the subsequent work of the thesis.

CHAPTER 5

Multi-scale Modeling for Binding of Cm(III) and Th(IV)

with sTf at Serum pH



HIGHLIGHTS

- **Iron carrier serum transferrin (sTf) protein can also function as a non-iron metal transporter, since only 30% of it is typically saturated with ferric ion. While this function of sTf can be fruitfully utilized for targeted delivery of certain metal therapeutics, it also runs the risk of trafficking the lethal radionuclides into cells.**
- **Several actinides are found to bind with sTf, yet molecular level understanding of their binding is unclear. Understanding the radionuclide interaction with sTf is a primary step towards future design of their decorporating agents.**
- **In this chapter, an extensive multi-scale modelling of two An [Cm(III) and Th(IV)] ions' binding with sTf at serum physiological pH is reported. It is observed that sTf binds both the heavy ions in a closed conformation with carbonate as synergistic anion and the An loaded sTf maintains its closed conformation even after 100 ns of equilibrium molecular dynamics (MD) simulations.**
- **In line with reported experimental observations, well-tempered metadynamics results of the ions' binding energetics show that studied An-sTf complexes are less stable than Fe-sTf. Additionally, Cm(III) is found to bound more weakly than Th (IV). This work is published in the journal of physical chemistry B¹⁶⁵ and presented here with permission.**

5.1 INTRODUCTION

In the previous chapter 4, ground state structure of Serum transferrin sTf loaded with native Fe(III) is studied using quantum chemical calculations. Fe(III) is found to be in hexadentate coordination with amino acid residues at the binding site of sTf. Whether similar binding behaviour will be observed for actinide ions or not? What will be the changes in coordination and binding properties for these metal ions is the topic of investigations for this and subsequent chapters. sTf complexes of not only Pu(IV) but also two other metal ions Th(IV) and Cm(III) are investigated for their interaction with the protein at various protonation states in serum and endosomal pH conditions. In this chapter, results of multi-scale modelling for sTf loaded with Th(IV) and Cm(III) at serum pH conditions are discussed.

Actinides such as Th, U, Np, Pu, Am, and Cm are routinely handled in various processes of front and back-end of nuclear fuel cycle. There are stringent safety measures during these processes, yet these radionuclides can enter into human body through any of the routes, namely inhalation, ingestion, and cuts/wounds. Internal contamination of these radionuclides under acute or chronic conditions has the potential to induce both radiological and chemical toxicity. In all the routes of entry into the human body, they are first absorbed into and then transported *via* blood prior to deposition in the target organs (e.g. thyroid, kidney, liver, bones etc.)^{5,10,65,66,81} Upon entry into the blood,¹⁶⁶ actinides are mainly transported to various tissues/organs by serum transferrin (sTf),^{18,20–22,24,122,167,168} an iron carrier protein.¹³ sTf mainly binds dietary iron, transports it in the blood serum and delivers it to cells through a process of receptor mediated endocytosis. The protein is present at a concentration of approximately 3mg/ml in human serum and is about 30% saturated with Fe(III). While this renders the blood serum accessible for certain therapeutic metal ions to bind and transport, it also becomes vulnerable for other toxic metals to follow the major iron acquisition pathway, receptor-mediated endocytosis.^{12–15} About 30 other metal ions

including actinides are found to make complexes with sTf.¹⁶

Actinides, unlike some other heavy metals, have no known essential role in the normal biochemical reactions occurring in living organisms including plants and animals. Internal contamination of actinides can be monitored using direct (*in vivo*) or indirect (*in vitro*) methods.^{81,95} These methods give information about amount of activity present in the body of the person and committed effective dose received by the person. However, these methods do not provide information about the structure, speciation, and mechanism that the body uses to bind and transport actinides. In order to have information about actinide speciation in biological media, several *in vitro* speciation tools like genomics, transcriptomics and proteomics can be applied. On the other hand analytical speciation tools based on X-ray absorption spectroscopy (XAS), time resolved laser fluorescence spectroscopy (TRLFS), inductively coupled plasma mass spectroscopy (ICP-MS), inductively coupled plasma-atomic emission spectroscopy (ICP-AES), can be used for the biological samples after preliminary separation of unwanted organic compounds (phosphates, carbonates, citrates, oxalates etc.) using liquid chromatography, capillary zone electrophoresis or other suitable separation based technique.

The transferrin molecule undergoes a significant conformational change when binding and releasing iron: from open (the iron free apoprotein)–to closed (iron loaded at physiological serum pH)–to open (releasing iron upon binding to transferrin receptor at the endosomal pH) conformations. sTf is a glycoprotein consisting of a single-chain polypeptide within a molecular mass of 80 kDa, which forms a bilobal structure with its N- and C-lobes that can be further divided into two sub-domains, NI, NII and CI, CII. The sub-domains in each of the lobes form deep cleft and two iron binding sites lie in these inter-domain clefts. The iron is found¹¹⁴ to be ligated with two tyrosine phenolate oxygen atoms, one histidine imidazole nitrogen atom, and one carboxylic oxygen atom from an aspartate residue, forming the first coordination shell of the binding cleft (see

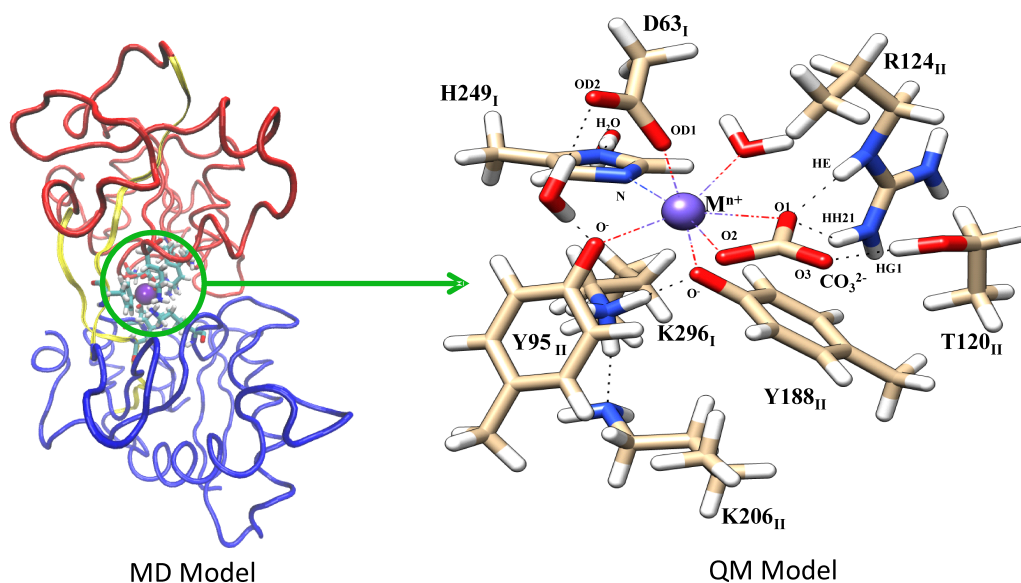


FIGURE 5.1: Schematic view of the metal-bound ($M^{n+} = \text{Fe}^{3+}$, Cm^{3+} , Th^{4+}) human transferrin and its binding site in the protein cleft at serum pH. The left panel shows the ribbon presentation of the N-lobe (N1 sub-domain in red, N2 sub-domain in blue, hinge region in yellow) of the protein bound to a metal ion, which is utilized during the all-atom molecular dynamics simulations. The right panel shows the zoomed in view of the metal-bound first and the second coordination shells of the protein binding cleft, which has been utilized to perform DFT calculations. The suffixes I and II used in the labels of binding site residues indicate sub-domains I and II of the N-lobe that they belong to.

Figure 5.1). A synergistic anion, the bidentate carbonate is also required for completing the coordination sphere of iron at physiological pH. Other synergistic anions in place of carbonate, such as citrate is reported to coordinate with noniron metal ion, Ti(IV) .¹⁶⁹ Numerous inorganic anions which can bind with transferrin are also recently reviewed.¹⁷⁰ Most recently molecular dynamics (MD) simulation of the effects of synergistic and non-synergistic anions on the iron binding cleft has been reported.¹⁷¹ Also complexes of transferrin with few metal ions: Fe^{3+} , $\text{V}^{\text{IV}}\text{O}^{2+}$, UO_2^{2+} have been studied using density functional theory (DFT),^{122,138,172} and QM/MM and MD simulations have been performed to study sTf bound with Fe(III) , Al(III) .^{137,173} Conformational changes in the sub-domains of sTf orchestrate sequence of events in metal regulation. For example, sTf binds metals tightly at serum pH in closed form,

whereas during metal release at endosomal pH, sTf is converted to open form that involves parting away of the sub-domains accompanied by a rigid body rotation around the hinge segment.¹³⁹ Opening of the protein at endosomal acidic medium (pH=5.5), measured by centre of mass separation (COM) between NI and NII sub-domains could be observed during tens of ns of equilibrium MD simulation.¹³⁷

One expects that the coordination of all metal ions to be same as that of iron; differing only on their affinity to sTf, depending on their charge/mass ratio. Indeed, the actinides form stable complexes with transferrin in the following order: $\text{Pu}^{4+} > \text{Th}^{4+} > \text{Np}^{4+} \gg \text{U}^{\text{VI}}\text{O}_2^{2+} > \text{Cf}^{3+} > \text{Am}^{3+} > \text{Cm}^{3+}$.¹⁷ Experimental studies regarding the interactions of transferrin have been carried out with a variety of actinide (An) ions.^{18–25} It is observed from these experimental studies that tetravalent An ions are more tightly bound to sTf and also their coordination with the binding site of sTf is different to that of trivalent An ions. Even in the case of tetravalent ions, while Pu(IV) is reported bound to transferrin in the iron sites,²⁷ two Th(IV) ions have been reported to bind at two non-equivalent sites.²⁶ Although a huge amount of information is available for transferrin to bind and transport non-iron metal ions,¹⁴ there is hardly any specific information at the molecular level, especially for the An ions. To the best of our knowledge crystal structures of An loaded sTf are not yet available. Similarly, how physiological carbonate ion work in tandem with sTf to bind An ion is an unexplored area. Whereas this is an important issue to be probed at the molecular level, since it relates to the biological fate of An trafficking in human body through sTf. In effect, the structural and thermodynamic properties of An-sTf systems are of enormous importance in providing guidance on the structures, affinities, and design of potential specific chelating agents that might be used to eliminate an incorporated radionuclide before the initiation of toxic effects.

Because of their strong tendency to undergo hydrolysis at physiological pH values, An ions in living organisms can only exist in complexed form or as hydrolysed species possibly with different coordination than that of iron. Whereas it is generally believed

that coordination of all metal ions with sTf are identical with Fe(III). Molecular level understanding in combination with extended X-ray absorption fine structure (EXAFS) and X-ray absorption near edge structure (XANES) data analysis can lead to better understanding of metal protein binding sites.^{12,166} In the pursuit of molecular details of binding, a combination of DFT and MD simulation is a very attractive avenue.^{28,29} The work presented in this chapter focuses *in-silico* on the binding characteristics of two actinide ions [Th(IV) and Cm(III)] with the iron binding protein, sTf at the physiological pH of serum (pH=7.4) in order to obtain molecular level understanding of their speciation. Particularly in this work, a systematic study is carried out on the binding, structure of first two coordination shells, and dynamics of sTf loaded with An ions through a combination of DFT and MD methods. Additionally, well-tempered metadynamics (WtMetaD) simulations are performed to explore the energetics of their binding to sTf. The results are compared wherever possible with Fe(III) binding at physiological pH. Endeavour of this work is primarily to visualize the structural changes induced by heavier An ions on the sTf binding cleft and their binding characteristics, since arguably their coordination and hydration energies¹⁷⁴⁻¹⁸⁰ are different from Fe(III) in complexed form.

5.2 METHODS

The two sTf sub-domains of each of the two lobes (N and C) close upon iron capturing at serum pH. The full sTf with its two lobes is a 679 residue protein. However, high resolution (1.6 Å) structure of only N-lobe of iron-bound recombinant sTf is available in the crystal structure database.¹¹⁴ Apart from disulfide bonds and a longer hinge region in C-lobe than that found in N-lobe, the latter show similar binding and release characteristics when compared with the entire molecule.¹⁸¹ In view of this, the half molecule N-lobe sTf is used as the starting configuration of the iron-loaded protein (PDB ID 1A8E).¹¹⁴

5.2.1 Molecular dynamics study

Crystal structure of N-lobe of iron-bound human serum transferrin was chosen as a starting configuration for all simulations. Inside blood, pH of the medium is around 7.4. Protonation state of the amino acids involved in the binding site was studied by evaluating their pKa values.¹⁸² Only H249 and Y188 are the non-standard residues, while all other amino acids were in their standard protonation state. In particular, Y188 was in phenolate form and in H249 both ND1 and NE2 were deprotonated (doubly deprotonated imidazolate form). All other histidines were singly protonated in accordance with serum physiological pH, e.g., NE2 was protonated in H14, H207 and H300 residues, whereas ND1 was protonated in H25, H119, H242, H273 and H289 residues, such that, they maintain neutral forms.

The problem at hand is the interactions between protein and charged metal ions¹⁸³ (+3 and +4 in the present case), where polarization and charge-transfer effects are supposed to be at full dynamics display. Indeed, metal binding sites are usually located inside solvent inaccessible protein cavities and clefts, characterized by a low dielectric constant that enhances electrostatic metal-protein ligand interactions. For example, Fe(III) experiences high free energy gain upon ligation with anionic protein ligands, such as, deprotonated aspartic acid and tyrosine residues forming inner-sphere metal-sTf binding (*cf.* Figure 5.1). Consideration of polarization effects are, however, missing in standard MD force fields. In order to bring in their effects, one can think of a effective polarizable model, under the aegis of reduction of polarizable Hamiltonians into nonpolarizable ones. In this model the electronic screening effects are implicitly considered by scaling the charges of all ionized groups and ions by the inverse of the electronic part of the water dielectric constant ($1/\sqrt{\epsilon_{el}}$, $\epsilon_{el} = 1.78$).^{184,185} In order to reflect the protein interior, these charges can even be locally adjusted self-consistently during each MD steps such as the case in a mean-field polarizable (MFP) model of water.¹⁸⁵ In order to treat the highly charged An ions' binding with the protein interior,

here we have adopted the effective polarization in polarizable water model (MFP-TIP3P) in an otherwise standard nonpolarizable force field model system that is successfully applied in previous occasions.^{186,187}

All MD simulations are performed using Gromacs-4.0.7 suite of programme.¹⁸⁸ The amber99 force field¹⁸⁹ (ff99SB) was employed to build the topology of the protein. Amber force field parameters for deprotonated tyrosine, doubly deprotonated histidine and carbonate ion were not available in the force field library. They were evaluated using python based acpype script with antechamber package¹⁹⁰⁻¹⁹² and charges were calculated using GAMESS¹⁹³ and Restrained Electrostatic Potential (RESP)¹⁹⁴ tools. The non-bonded parameters of Cm(III) and Th(IV) were taken from literature.^{180,195} These parameters for the ions, explicitly dissolved in TIP3P water,¹⁹⁶ were obtained by targeting the experimental hydration free energies and ion-oxygen distances of the first solvation shell as touchstone. Note that amber99 force field, as is available in the Gromacs-4.0.7 distribution, which is subsequently modified to include MFP model of TIP3P water¹⁸⁵ and used here, is somewhat primitive. This may affect the results, although the qualitative trend may not alter if one uses more accurate recent force field (e.g. ff99SB-ILDN, ff14SB).

Simulation Protocol: Periodic boundary conditions were applied in all directions using a cubic cell, with a minimal distance between the protein and the wall of the cell set to 10 Å. The TIP3P water solvated systems with the added Na⁺ and Cl⁻ ions (to maintain electro-neutrality) are comprised of more than 63000 atoms. The energy of the entire system was minimized by successive applications of the steepest descents (15000 steps) and conjugate gradient (1000 steps) methods. Temperature of the system was slowly increased to 300 K. First, the water molecules were heated to this temperature for 1 ns simulation run, while the protein-ion complex remained fixed. Then, the simulation was restarted for heating the protein-ion complex to 300 K for a similar period with the already equilibrated water molecules. All bond lengths of protein, carbonate, and water

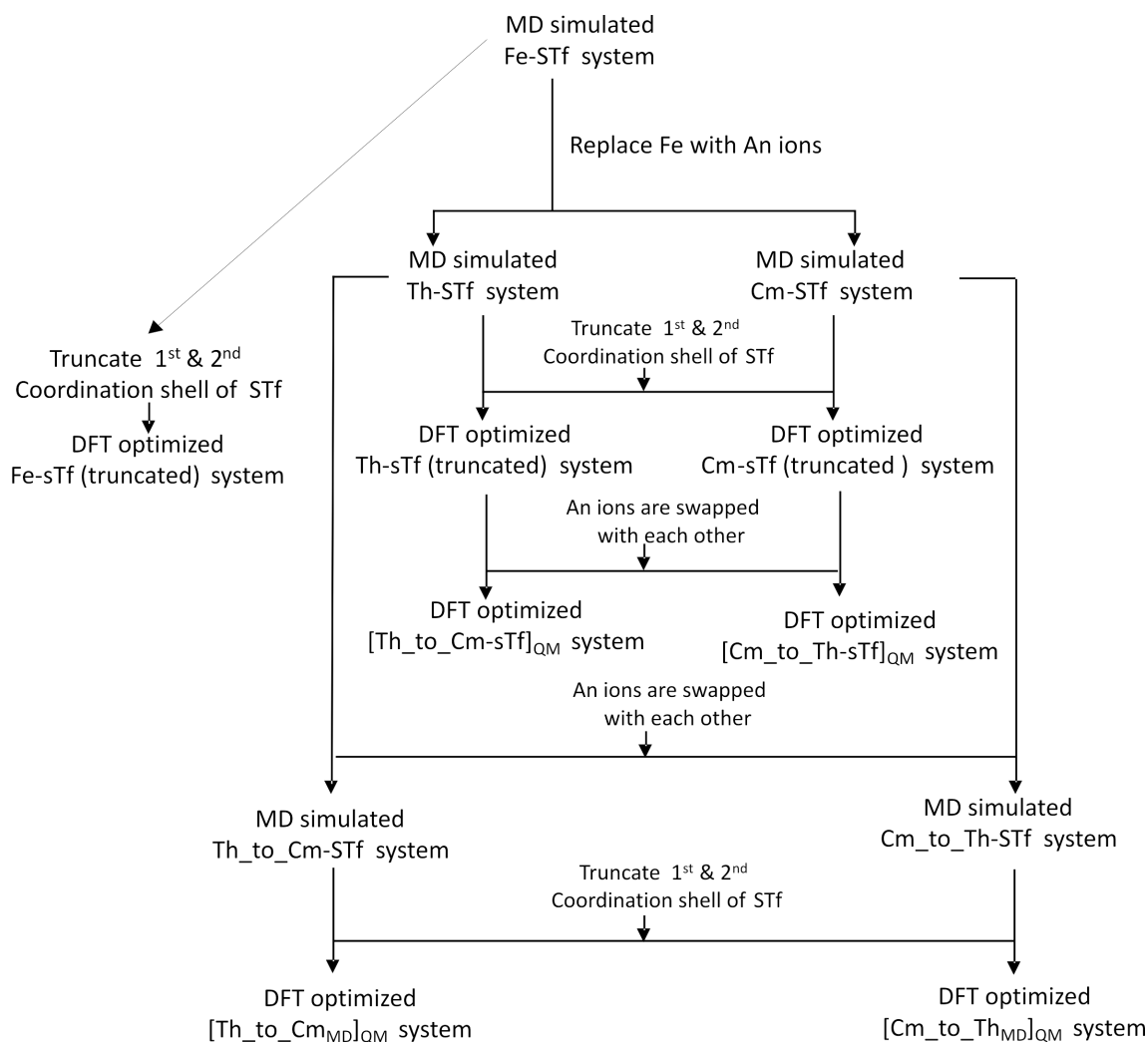


FIGURE 5.2: Flowchart of all the MD and QM calculations performed.

were constrained with Linear Constraint Solver (LINCS)¹⁹⁷ algorithm, allowing for an integration time step of 2 fs. Pressure was restrained to 1 atm using the Berendsen method with a coupling time of 0.5 ps. Finally, 1 ns equilibration was performed in the canonical thermodynamic ensemble (NVT), where the temperature of the water, ions and protein were independently coupled to 300 K temperature bath using velocity rescaling algorithm.¹⁹⁸ Long-range electrostatics were calculated using the smooth particle mesh Ewald (PME)^{199,200} method with a cutoff of 12 Å. A similar cut off was chosen for the van der Waals non-bonded interaction where the switch function was employed. Finally, MD simulations are performed for 100 ns for each of metal-bound sTf systems under

NPT conditions without applying any additional constraints at 1 atm and at 300 K.

The equilibrated Fe-sTf system was taken to prepare the An containing sTf by replacing ferric ion with the An ions. Each of the An-loaded sTf structures were then subjected to 100 ns MD simulation following the above protocol to generate Cm-sTf and Th-sTf equilibrium systems. Further to cross verify the structure and binding properties, we have interchanged the two An ions with one another in the sTf binding cleft to produce Cm_{-to}-Th-sTf and Th_{-to}-Cm-sTf systems. These systems were then MD simulated for 100 ns. Note that these An containing structures were used to prepare truncated structures like, [Cm_{-to}-Th_{MD}]_{QM} and [Th_{-to}-Cm_{MD}]_{QM} for QM calculations. See Figure 5.2 for a flowchart of all the MD and QM calculations performed. Five independent equilibrium simulations, starting with the same minimization but with different initial velocities, are performed for each of the metal loaded sTf systems.

In order to deal with the charged An ion's interaction with sTf cleft, all MD simulations were conducted in an effective polarization environment with MFP/TIP3P model of water.^{184–187} In view of this, charges on the ions were scaled by a factor of 0.75, such that they are reduced to +2.25 and +3 on Cm and Th ions, respectively. To compensate for the reduced charges on the An ions, the excess charge is delocalized equally on the coordinating oxygen and nitrogen atoms in the binding cleft. This technique introduces the electronic screening effect implicitly in the effective polarizable model in conjunction with MFP/TIP3P water. The atomic charges of the MFP water molecules are adjusted “on-the-fly” based on the local atmosphere in a self-consistent manner. This treatment captures the induced polarization of water in a non-uniform protein environment through the use of a damping scheme based on the average hydrogen bond lifetime (≈ 1 ps).¹⁸⁵ To achieve sufficient accuracy we have allowed 5 ps interval between two successive MD moves, such that, several hydrogen bonds break and form during two simulation steps and diffusion of water molecules in the protein interior can take place during this time interval. Through the charge scaling of the ions and use

of MFP model for TIP3P water, we expect to deal with local environment changes, which are experienced by the metal ions from binding cleft to the protein exterior.

5.2.2 Well-tempered metadynamics

All metadynamics simulations were conducted with Gromacs-4.0.7¹⁸⁸ patched with Plumed 1.2.²⁰¹ At serum pH (=7.4), as is the case here, it might take prohibitively long time (at least not in 100 ns that we have examined) for the protein to open in order to release the metal ion. This may not be accomplished by equilibrium simulation techniques within a reasonable computational time. Biased non-equilibrium simulation technique such as metadynamics (MtD) simulation can be an useful alternative towards this goal.²⁰² In MtD method, rare events such as, protein opening and unbinding of metal ions are accelerated by depositing Gaussian shaped history dependent biased potential along some chosen reaction coordinate, known as the collective variables (CV). We have chosen COM separations between (i) NI and NII sub-domains and that between (ii) N-lobe of sTf and metal ions along with their synergistic carbonate ion as the two CVs. COM of NI sub-domain is constituted of sTf residue number 1 to 91 and 245 to 313, while that of NII sub-domain is constituted of sTf residue number 92 to 244. The two sub-domains are connected to each other by a hinge consisting of two extended antiparallel β -strands (residues 91-101 and 241-252) that forms the binding cleft for the metal ion along with its synergistic carbonate anion. COM of the entire N-lobe of sTf is determined using all the residues (1 to 329) of the listed protein structure, 1A8E.¹¹⁴ The height (H) and width (σ) of the deposited Gaussians is a measure of the applied biased potential, which at the end of simulation can be quickly converted to potential mean force (PMF) of the metal release event without any reprocessing of the data.

However, convergence related issues are well known in MtD simulations. A well-tempered variant of MtD technique⁴⁶ provides a solution to this problem by

progressively scaling the height of the deposited Gaussian bias over time at a fictitious higher temperature, $T + \Delta T$, where ΔT can be regarded as a tuning parameter ranging between $\Delta T \rightarrow 0$ for equilibrium MD and $\Delta T \rightarrow \infty$ for standard MtD. $H=1$ kJ mole⁻¹ and $\sigma=0.05$ was chosen for the Gaussian hills, which were added after every 500 time step (1ps). Bias factor $[(T + \Delta T)/T]$ was taken as 15 and all the simulations were carried out at temperature 300 K. As the simulation progresses, we have noted a decreasing trend of added hill heights. This indicates the convergence of the resultant PMF profiles. Converged PMF profiles are obtained within 28, 25, and 12 ns of WtMetaDuns for Fe-, Th-, and Cm-loaded sTf systems, respectively.

5.2.3 Quantum mechanical study

Model Structures: The first coordination shell of the metal ion in the binding cleft comprises residues D63, Y95, Y188, H249 and the CO₃²⁻ ion, while T120, R124, K206 and K296 form the basis for second coordination shell (see Figure 5.1). The second shell residues; T120 and R124 are stably bound with the carbonate ion. K296 forms hydrogen bond with K206 and Y188. The two immediate coordination shells of the metal-carbonate system can be regarded as a reasonable representation of the metal-bound sTf binding cleft. The QM model starting structures are built in light of this by truncating the first and second coordination shells along with the metal ion and the synergistically bound carbonate anion. All crystallographic water molecules within 10Å from the metal ion were also considered in the starting structures. In the peptide junction of the truncated structure, the -CO-NH- groups were replaced with CH₃ to prevent unreasonable hydrogen bonding formation between nearby residues that may obscure the actual structural motifs of the binding cleft.¹⁴⁸ It is to be noted that relativistic mechanics is important to be considered for the heavier elements with high atomic numbers, ²⁴⁷Cm

and ^{232}Th . In view of this, a small core-relativistic effective core potentials were used for actinide ions during DFT treatments.

From the last frame of a chosen MD replica of Cm-sTf and Th-sTf systems, the QM calculations are initiated by truncating the equilibrated structures to obtain Cm-sTf (truncated) and Th-sTf (truncated) systems. In order to cross verify the results, we have also conducted QM calculations when An ions in the truncated structures are exchanged with one another and further the resulting structures were optimized at the DFT level. We call these sTf structures as $[\text{Cm}_{-10}\text{-Th-sTf}]_{\text{QM}}$ and $[\text{Th}_{-10}\text{-Cm-sTf}]_{\text{QM}}$. In another, the An ions in the MD equilibrated structures of Cm-sTf and Th-sTf are first interchanged with one another, MD equilibrated and the truncated structures are DFT optimized to produce $[\text{Cm}_{-10}\text{-Th}_{\text{MD}}]_{\text{QM}}$ and $[\text{Th}_{-10}\text{-Cm}_{\text{MD}}]_{\text{QM}}$ systems (see the flowchart in, Figure 5.2).

Optimization Protocol:

All starting structures were optimized using a pure generalized gradient approximated BP86 functional^{35,153} in protein medium using the continuum solvation model (with $\epsilon=5$) by applying COSMO algorithm as implemented in TURBOMOLE 6.6.¹⁵⁴ def-TZVP basis sets⁴³ and small core-relativistic effective core potentials were used both for iron and An ions. For other atoms in the system TZVP basis sets^{41,42} were used. For the actinides we have used relativistic small core potential to replace core electrons of actinide ions. C^α carbon atoms of the amino acid residues in the structures were kept frozen during DFT optimization in order to preserve the steric effect imposed by the protein. Furthermore, numerical frequency calculations were performed using the NUMFORCE module to verify the structure as the minima in the potential energy surface. Single point calculations are performed on the optimized structures using B3LYP functional^{36,155,203} along with the continuum solvation model (with $\epsilon=80$ & 5). Our strategy of using BP86 functional for structure optimization and B3LYP functional for single point calculation has been successfully adopted previously to predict accurate

structural and thermodynamic properties for several host-guest and metal-ligand complexes.²⁰⁴⁻²⁰⁷ Tighter SCF convergence criteria (10^{-8} Hartree) were applied for all geometry optimization calculations using $\epsilon = 5$. To validate the methodology, hydration free energies of An ions were estimated using the following equation (see subsection 5.3.3.2 for further detail).



Thermodynamic quantities such as changes in Gibbs free energies (ΔG) and entropy (ΔS) were derived. The entropic component of the binding cleft structures were determined through frequency calculations. It is important to note that the reported optimized structures are at their potential minima. Most of the structures were found to have no imaginary frequencies except for a few ranging between 5-40i, which can be attributed to the frozen coordinates. In accordance with the work of Siegbahn and co-worker,²⁰⁸ we believe that the presence of such a small imaginary frequency is expected to have a negligible effect on the structure and energetics trend.

5.3 RESULTS AND DISCUSSION

At serum pH, five equilibrium simulations are performed for each of the metal loaded sTf systems. The calculated parameters are found to be largely invariant with respect to the starting configurations of the MD runs. The results presented below are representatives of one such run, while in Table 5.1, the metal-ligand distances are presented by averaging over all the five independent runs.

5.3.1 Protein in closed conformation

Y95, Y188 and D63 residues of the first coordination shell of the metal ion are considered to be in anionic form, T120 and K206 of the second coordination shell in

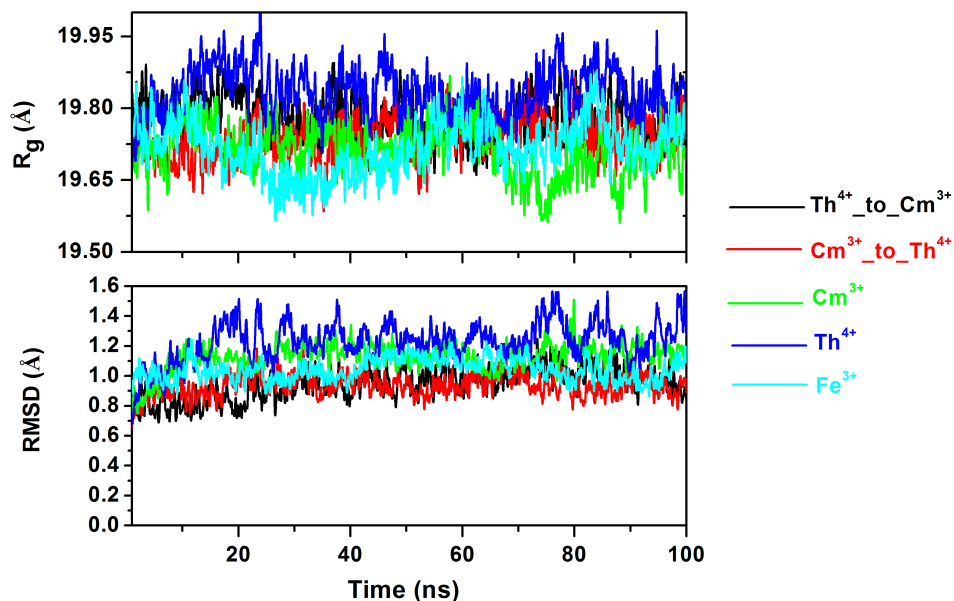


FIGURE 5.3: Time dependence of the radius of gyration, R_g (upper panel) of protein heavy atoms and RMSD of its C^α atoms (lower panel) from the crystal structure of the iron loaded (cyan) serum transferrin during the 100 ns equilibrium MD simulation is shown. Also shown are the same when Fe^{3+} ion in the binding cleft is replaced with Th^{4+} (blue), Cm^{3+} (green) and the equilibrated structures of Cm-sTf and Th-sTf are replaced with Th^{4+} (Cm^{3+} -to- Th^{4+} , red) and Cm^{3+} (Th^{4+} -to- Cm^{3+} , black) ions, respectively.

neutral form, while the synergistic carbonate ion is taken to be in dianionic form at this pH.¹³⁷ Residues K296 and R124 in second coordination shell are considered to be protonated (*cf.* Figure 5.1). First we have conducted a 100 ns simulation of iron loaded, Fe-sTf system. Next, five structures of Fe-sTf systems, at an interval of 20 ns, are selected in order to replace iron with thorium(IV) and curium(III) and to generate equal numbers of An-loaded sTf systems: Th-sTf and Cm-sTf. The resulting structures are simulated further for 100 ns. The deviation of sTf from the initial starting structure is assessed on the basis of root-mean-square deviation (RMSD) of its C^α atoms. For Fe-sTf system, the initial structure is the crystal structure, while for An-loaded systems they are equilibrium structures, obtained from the preceding simulations as stated above. In order to characterize the ensemble of closed states of the protein sub-domains, an ordered parameter, namely, size of sTf is measured through radius of gyration, R_g of its

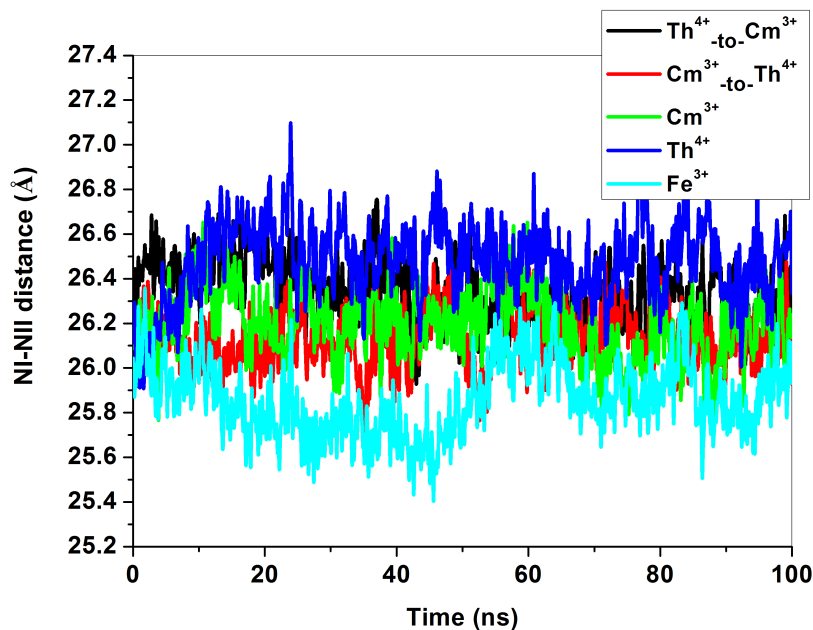


FIGURE 5.4: MD time evolution of distance between centre of mass of the NI and NII sub-domains of N-lobe of sTf, bound to the metal ions as indicated. Color legends are same as in Figure 5.3.

heavy atoms: $R_g = \sqrt{\sum_i (|\mathbf{r}_i|^2 m_i) / \sum_i m_i}$, where m_i is the mass of atom i and \mathbf{r}_i is the position of atom i with respect to COM of the molecule. The temporal dependence of both these parameters are presented in Figure 5.3. It can be seen in the figure that for all the systems studied, deviations of C^α atoms are within 1.5 Å and that they appear to be stabilized within 2 ns. This observation is a clear indication of convergence of the metal-protein systems and that An-loaded systems behaves similar to Fe-sTf system. The compactness [$R_g(t)$] of sTf in all the varieties of metal-bound cases are found to be within 19.80 ± 0.15 Å during the 100 ns period. The propensity towards a closed state of An-loaded protein, like the case of iron,^{137,139} is again evident from this result.

In order to characterize the opening of the protein,¹³⁷ the COM separation between NI and NII sub-domains of sTf is monitored (see Figure 5.4). The temporal profiles of this separation for An-sTf systems can be seen to vary within 1 Å when compared with Fe-sTf system. The average value of NI-NII distance for Fe-sTf, on the

other hand, is almost identical to that reported in the crystal structure (25.9 Å) of the closed form of the iron-loaded protein at serum pH.¹¹⁴ This means that, sTf, like in the case of iron, also remains in the closed form when it captures thorium(IV) or curium(III) ions. We believe that this a significant observation and throws light on the actinide speciation and regulation in human transferrin in conjunction with carbonate ion. The closed form structures are subsequently used for further analysis of the protein's binding cleft.

5.3.2 Structural analysis of An-loaded sTf binding cleft

Coordination of metal ions with immediate first and second shell residues of sTf binding cleft and with any available water molecules therein plays major role in regulating metal ions' concentration in the blood. In view of this, the results on the features of water penetration into the binding cleft of An-sTf systems are discussed here. Next detailed results on coordination sphere of Th (IV), Cm(III) in the cleft are provided. Later the cases of swapping of An ions (*viz.* Cm_{to}-Th and Th_{to}-Cm) in the cleft in order to cross verify their coordination characteristics are also discussed.

5.3.2.1 Water penetration into the binding cleft.

The sTf binding cleft is deeply buried in the closed configuration of the protein, resulting into a compact size of metal-sTf system at serum pH. During receptor-mediated endocytosis, at acidic pH, the protein opens up to allow the water molecules to enter the binding cleft. This helps in releasing the metal from the cleft. This sequence of events in the regulation of Fe(III) speciation, and transport in the blood are well known. The calculated radial distribution function (RDF) at serum pH, $g_{M-OH_2O}(r)$ of metal-water (Figure 5.5) for Fe-sTf system exhibits a very faint peak beyond (>7 Å) the radius of the first coordination shell of the cleft. This means that the binding cleft in Fe-sTf is devoid

of any water molecule. However, when ferric ion is replaced with An ions to generate Cm-sTf and Th-sTf systems, one water molecule enters into the first coordination shell of binding cleft in each of the two cases during equilibration; sharp peak in RDF profile appears well within the first coordination sphere, as shown in Figure 5.5. This result, in particular, signifies that like carbonate ion, water in the sTf binding cleft plays the synergistic role while capturing An ions. This water molecule completes seven coordination number requirements for Cm(III), while Th(IV) attains eight coordination, additionally by the participation of D63 in bidentate form (see below). Further, when the two An ions are interchanged with one another in the sTf binding cleft and were MD simulated, one more water molecule enters the first shell to satisfy the eight coordination number for Th^{4+} in Cm_{-to}-Th-sTf system (Figure 5.5), while D63 remained in monodentate form. On the other hand in Th_{-to}-Cm-sTf system, while retaining the water molecule in the cleft, D63 became monodentate so that Cm(III) again became seven coordinated. Below we provide further details of coordination sphere of each of An-sTf systems studied (see Figure 5.2). For each of the cations, we first present the results of equilibrium MD simulations (*cf.* Table 5.1) followed by DFT calculation (*cf.* Table 5.2). We will show that the results on hydration and coordination characteristics of the ions, as obtained by the two methods, corroborate well with each other.

5.3.2.2 Coordination sphere of Th (IV), Cm(III) in the cleft.

MD simulated Th-sTf system: R_g of the protein is stabilized at ~ 19.8 Å and RMSD is stabilized at ~ 1 Å (Figure 5.3). In Figures 5.6 (a)-(g), the distances between metal cations and the atoms of the residues in the first coordination shell of the protein binding pocket are shown, while distances between metal cations and the centre of mass separation of the first coordination shell are shown in panel (h). During the 100 ns MD simulation, Th^{4+} is seen to be ligated with Y95, Y188, H249, bidentate carbonate ion, one water molecule, and D63 in bidentate form in its first coordination shell. It can be

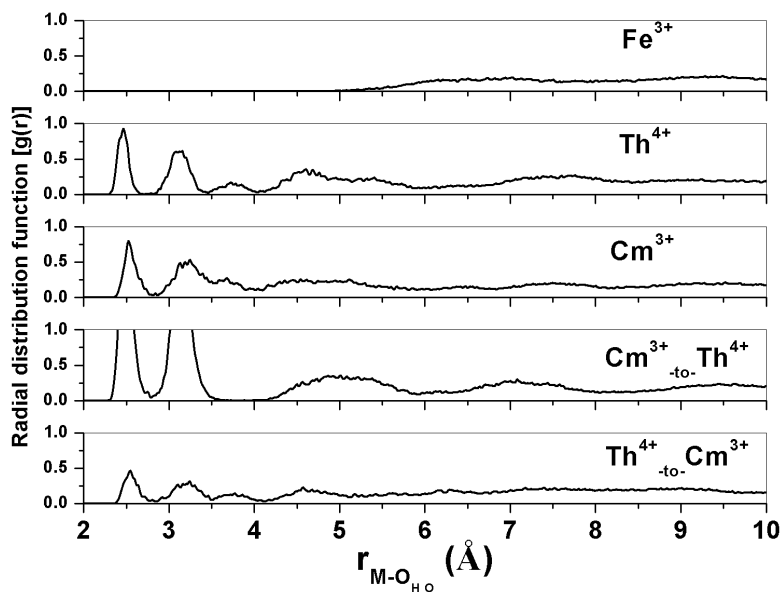


FIGURE 5.5: Water penetration into the protein's binding cleft for the case of metal-loaded sTf. Radial distribution function (RDF), $g_{M-O_{H_2O}}(r)$, calculated from 100 ns simulation data for the metals bound to the sTf protein as indicated are shown. From top to bottom panels: for Fe^{3+} , Fe^{3+} replaced with Th^{4+} and Cm^{3+} , MD-equilibrated Cm^{3+} structure is replaced with Th^{4+} , and MD-equilibrated Th^{4+} structure is replaced with Cm^{3+} .

observed in the figure that initially $OD2_{D63}$ is at a distance of around 4 Å but after ~ 200 ps its distance is reduced to an average value of 2.4 Å. Mean and standard deviation of distances between thorium(IV) ion and the first shell coordinating atoms are presented in Table 5.1. When compared with Fe(III), thorium(IV) ion is seen to coordinate with the ligand atoms with a larger bond lengths. This causes COM separation between thorium(IV) ion and the residues in the first shell of metal binding site (MBS) to be in slightly higher side.

DFT optimized Th-sTf (truncated) system: DFT optimized structures of the metal-coordinated first and second coordination shells of the cleft are presented in Figure 5.7 (A)-(C). Bond lengths between metal ions and the ligating atoms in the first shell of the DFT optimized structures are given in Table 5.2. Important distances between residues in the second shell are also shown in Figure 5.7 for the three metal-bound DFT optimized structures. The similarities and differences between the ligation characteristics

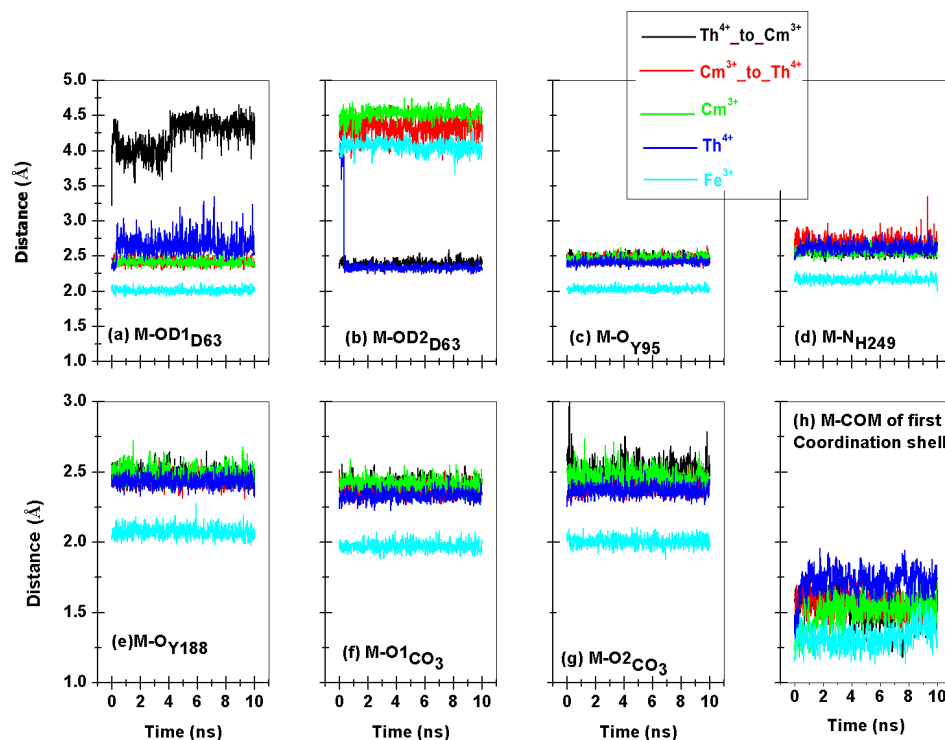


FIGURE 5.6: Temporal profiles of distances between metal cations and the atoms of the residues lining the first coordination shell of the protein binding pocket are shown as indicated. Since after initial 10 ns the distances vary monotonously for each of the MD runs, only the first 10 ns of a representative 100 ns MD data are plotted here. Also shown are distances between metal cations and the centre of mass separation of the first coordination shell. Colour legends shown for the variety of protein-bound metal ions considered are the same as in Figure 5.3.

TABLE 5.1: Mean and standard deviations of bond lengths (Å) of the metal ions ligated with atoms of the residues in the first coordination shell as calculated by averaging over five independent 100 ns MD simulations

Ions(M ⁿ⁺)	M-OD1 _{D63}	M-OD2 _{D63}	M-O1 _{CO₃}	M-O2 _{CO₃}	M-N _{H249}	M-O _{Y95}	M-O _{Y188}	COM _{M-MBS} ^a
Fe ³⁺	2.01 ± 0.05	4.07 ± 0.10	1.97 ± 0.04	2.01 ± 0.05	2.17 ± 0.06	2.03 ± 0.04	2.08 ± 0.05	1.33 ± 0.09
Th ⁴⁺	2.65 ± 0.17	2.38 ± 0.28	2.33 ± 0.05	2.37 ± 0.05	2.62 ± 0.08	2.42 ± 0.05	2.44 ± 0.05	1.72 ± 0.10
Cm ³⁺	2.46 ± 0.07	4.53 ± 0.10	2.42 ± 0.05	2.47 ± 0.08	2.57 ± 0.07	2.47 ± 0.06	2.49 ± .07	1.51 ± 0.11
Cm ³⁺ _{-to} -Th ⁴⁺	2.42 ± 0.06	4.35 ± 0.17	2.36 ± 0.05	2.39 ± 0.06	2.68 ± 0.12	2.46 ± 0.06	2.45 ± 0.06	1.56 ± 0.09
Th ⁴⁺ _{-to} -Cm ³⁺	4.22 ± 0.25	2.40 ± 0.06	2.40 ± 0.05	2.50 ± 0.09	2.57 ± 0.07	2.46 ± 0.06	2.48 ± 0.06	1.55 ± 0.11

^a Centre of mass separation between metal ions and the residues in the first coordination shell of the metal binding site (MBS)

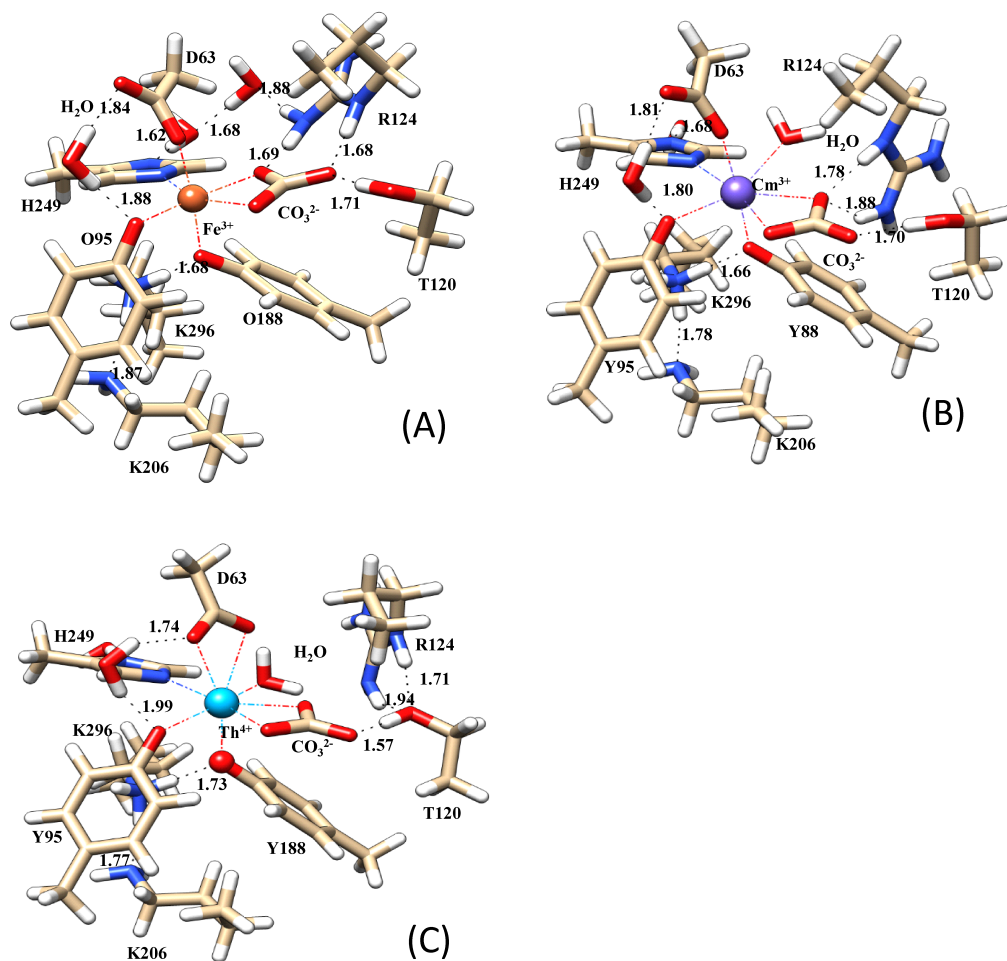


FIGURE 5.7: DFT optimized structures consisting of first and second coordination shell residues of sTf protein bound with the (A) Fe^{3+} , (B) Cm^{3+} , and (C) Th^{4+} ions. Various hydrogen bonds and their lengths are also depicted.

of Fe(III) and Th(IV) ions in the first shell can be clearly seen in optimized structures, which are in accordance with MD results. For example, both the ions coordinate with carbonate ion, Y95, Y188, and H249 residues in similar fashion. Whereas differences in coordination with D63 [monodentate in Fe(III) and bidentate in Th(IV)], and presence of one water molecule in the case of Th(IV) is quite evident.

The role of physiological anions, such as synergistic carbonate ion in iron-transferrin chemistry is well known. But the role of same anion in binding and transport of non-iron metals is an unexplored area. Here we found that as in the case of

specific binding requirement of Fe(III) to sTf, the carbonate is stably bound to an arginine (R124) and also with one threonine (T120) residues of the second coordination shell of Th(IV) (Figures 5.7). Two lysine residues, one in sub-domain NI (K296) and the other in NII (K206) play essential role to hold tight the captured Fe(III) ion.¹¹⁴ In particular, X-ray crystal structures revealed that these two deprotonated residues form a hydrogen bond interaction in the so-called dilysine bridge in the iron loaded protein at serum pH. This observation is also supported by the DFT optimized structure where the proximity of the two lysine residues can be clearly seen (Figure 5.7). Note that at endosomal acidic pH, the two lysine residues are protonated resulting into repulsion between them due to their positive charges, which facilitate the opening of the domain and release of the metal.²⁰⁹

MD simulated Cm-sTf system: For the Cm-loaded sTf, RMSD is seen to be stabilized at ~ 1 Å and radius of gyration at around 19.7 Å. Curium(III) in the binding cleft coordinates with oxygen atom of one water molecule and with the same six atoms of the first shell residues as in the case of Th(IV). As can be seen in Table 5.1 and Figure 5.6, the main difference between Th-sTf and Cm-sTf binding mode is that with respect to D63. While in the case of thorium(IV) it is bidentate, for curium(III) it is monodentate. Average bond lengths and their temporal variations with the coordinating atoms are almost similar to that found in the case of thorium(IV). In Figure 5.8 (a)-(c), we have presented the interatomic distances between oxygen atoms of the carbonate ion and the hydrogen atoms of the residues in the second coordination shell for various metal-bound sTf systems. In Figure 5.8 (d), the distances between the nitrogen atoms of K206 and K296 are also presented. One can observe that there is hydrogen bonding (HB) between O3 of carbonate ion and HG1 of T120, as distance between these atoms is maintained at ~ 1.7 Å throughout the 100 ns simulation. Also K206 and K296 are at 2.9 Å apart from each other maintaining dilysine bridge. Two water molecules, one each in the first and second shell of the Cm-sTf bound system at a distance of ~ 2.5 Å and ~ 3.5 Å,

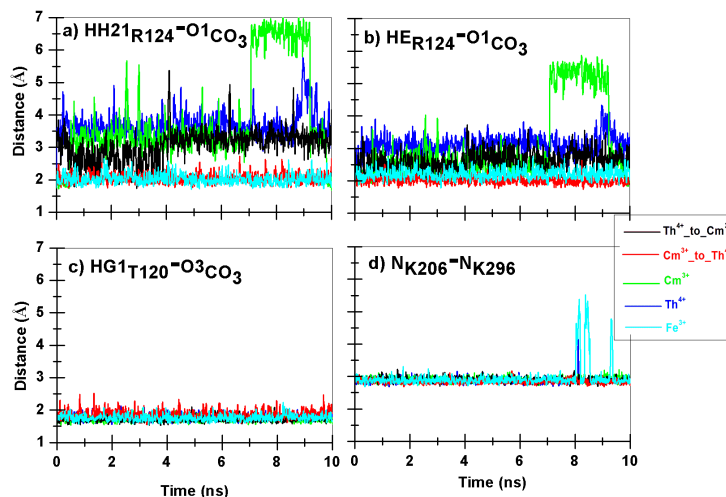


FIGURE 5.8: Temporal profiles of interatomic distances between oxygen atoms of the synergistic ion (CO_3^{2-}) and hydrogen atoms of residues in the second coordination shell, forming hydrogen bonds (a: $\text{HH21}_{\text{R124}}\text{-O1CO}_3$, b: $\text{HE}_{\text{R124}}\text{-O1CO}_3$, c: $\text{HG1}_{\text{T120}}\text{-O3CO}_3$) and that between nitrogen atoms of K206 and K296 residues (d: $\text{N}_{\text{K206}}\text{-N}_{\text{K296}}$). Colour legends shown for the variety of protein-bound metal ions are the same as in Figure 5.3. Since after initial 10 ns the distances varies monotonously for each of the MD runs, only the first 10 ns of a representative 100 ns MD data are plotted here.

respectively can be seen to be present (see the RDF plot for Cm-sTf in Figure 5.5).

DFT optimized Cm-sTf (truncated) system: DFT optimized structure of the truncated Cm-sTf bound system (Figure 5.7) is seen to follow the same binding trends as we have noticed in MD simulation. For example, the similarities in ion's seven coordinated structure with the same sets of atoms, monodentate form of D63 and presence of one water molecule in the first shell. Bond lengths between Curium(III) and the first shell coordinating atoms obtained through DFT method is given in the Table 5.2. Bond distances between atoms in the second shell clearly indicate T120 is making HB with O3 of CO_3^{2-} and R124 with O2 of CO_3^{2-} . Like in the case of thorium(IV) binding, dilysine bridge between K206 and K296 can be seen to be present in the structure. One extra water molecule in the second shell of curium(III) binding (RDF plot for Cm-sTf in Figure 5.5) that is observed during MD simulation is found to form water bridge with OD2 of D63 and O of Y95.

5.3.2.3 Swapping of An ions in the sTf binding cleft.

MD simulated Cm_{-10} -Th-sTf system, $[Cm_{-10}$ -Th-sTf]_{MD}: When curium(III) in equilibrated structure of Cm-sTf system is replaced with thorium(IV) and the resulting Cm_{-10} -Th structure is further MD equilibrated, one can observe that radius of gyration of the Th-bound protein is stabilized at ~ 19.8 Å and RMSD is stabilized at ~ 1 Å (Figure 5.3). For thorium(IV) substitution, from the RDF plot (Figure 5.5) it can be inferred that three water molecules, two in the first shell and one in the second shell of the binding site of sTf are present at a distance of ~ 2.5 Å and ~ 3.5 Å, respectively. Rest of the coordination pattern (see Table 5.1, Figures 5.6 and 5.8) in the binding cleft remained same as it was in the case of curium(III), except the coordination pattern of D63. D63, which was functioning as a bidentate ligand in Th-sTf system has now become monodentate, ligating with thorium(IV). However, two water molecule (in place of one) in the first binding shell make up the eight coordination number requirement of the substituted thorium(IV). In other words, D63, which was working as a monodentate ligand in Cm-bound sTf, remained so after thorium(IV) substitution of curium(III) in the binding cleft. It is interesting to note that even after this readjustment of binding pattern, the COM separation between the substituted thorium(IV) and first shell of MBS remains close to the values observed in Fe-, Cm-, and Th-sTf system (Table 5.1). HB between O3 of CO_3^{2-} and HG1 of T120, and dilysine bridge between K296 and K206 (Figure 5.8) also remained unaltered.

DFT optimized $[Cm_{-10}$ -Th-sTf]_{QM} system: In a separate study we have replaced curium(III) in DFT optimized Cm-sTf truncated structure (*cf.* Figure 5.7) with thorium(IV) and again optimized the resulting structure (*cf.* Figure 5.9(A)). In this structure thorium(IV), like curium(III), shows seven coordination. This is because D63 continues to exhibit its monodentate nature, both in curium(III) binding and in thorium(IV) binding, which is in accordance with the aforementioned MD result. Rest of

the binding pattern with the first shell residues is seen not to alter much when compared with other metal-bound sTf systems (Table 5.2).

DFT optimized $[Th_{-10}-Cm-sTf]_{QM}$ system: Similar switch over of coordination status of central An ion is also noticed in DFT calculation, when thorium(IV) in the optimized structure of Th-sTf(truncated) system is exchanged with curium(III) [*cf.* Figure 5.9(B)]. We have observed that after optimization, Cm(III) changes its coordination from octa-dentate to hepta-dentate by the movement of one water molecule away from the binding site. However, D63 remains in the bidentate mode.

DFT optimized $[Cm_{-10}-Th_{MD}]_{QM}$ system: Further, instead of exchanging An ions in the truncated structure of protein's binding cleft, we have taken the equilibrated structure of thorium(IV) substituted sTf protein ($Cm_{-10}-Th-sTf$), which was then truncated to extract An-bound binding cleft. The resulting truncated structure is DFT optimized to generate $[Cm_{-10}-Th_{MD}]_{QM}$ system. DFT optimized structure of such a system is provided in Figure 5.9(C) and bond distances of first shell coordination in Table 5.2. As we have discussed earlier when we interchange curium(III) with thorium(IV), its coordination number changed from seven to eight as one more water molecule enter into its first coordination shell.

MD simulated $Th_{-10}-Cm-sTf$ system, $[Th_{-10}-Cm-sTf]_{MD}$: Eight coordinated initial structure of thorium(IV) in Th-sTf complex quickly changes over to seven coordinated structure for curium(III) in the binding cleft of sTf when thorium(IV) is replaced with curium(III). The switch over in coordination number of the central An ion is assisted by the monodentate (in place of bidentate in Th-sTf) mode of complexation of D63 with curium(III) in the substituted sTf system. Like in the case of $Cm_{-10}-Th$ substitution in the binding cleft, R_g of the protein heavy atoms after the $Th_{-10}-Cm$ substitution is also stabilized at ~ 19.8 Å and RMSD at ~ 0.9 Å (Figure 5.3). Mean and standard deviation of distances between curium(III) and residues in the first coordination shell after the

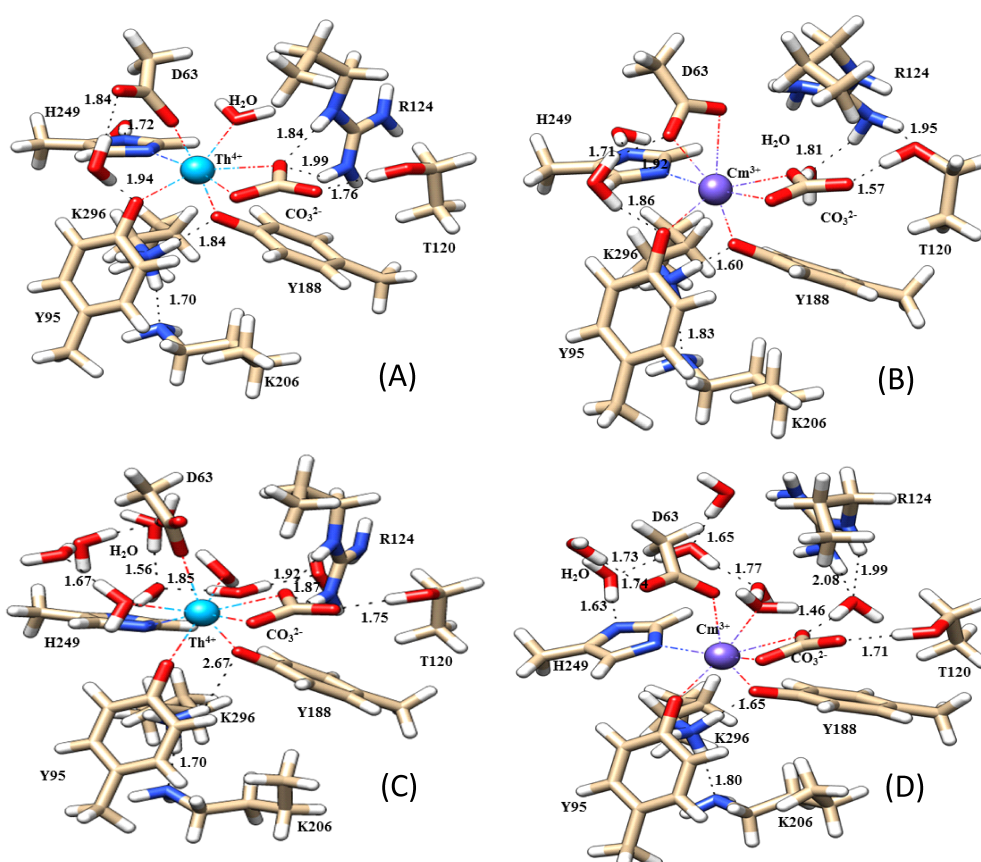


FIGURE 5.9: DFT optimized structures consisting of first and second coordination shell residues of actinide-bound sTf protein when structures, presented in Figure 5.7 of: Cm^{3+} is replaced with Th^{4+} , $[\text{Cm}_{\text{-to-}}\text{Th-sTf}]_{\text{QM}}$ (A); Th^{4+} is replaced with Cm^{3+} , $[\text{Th}_{\text{-to-}}\text{Cm-sTf}]_{\text{QM}}$ (B). The bottom panel shows the same when An ions in the equilibrated structures of An-bound sTf are first swapped with one another, MD equilibrated and then the truncated structures of An-bound binding cleft are DFT optimized: (C) $[\text{Cm}_{\text{-to-}}\text{Th}_{\text{MD}}]_{\text{QM}}$, (D) $[\text{Th}_{\text{-to-}}\text{Cm}_{\text{MD}}]_{\text{QM}}$. Various hydrogen bonds and their lengths are also depicted.

substitution are given in Table 5.1, which can be seen to compare well with the Cm-sTf system. This results into almost identical COM separation between curium(III) and the MBS for the $\text{Th}_{\text{-to-}}\text{Cm}$ substituted sTf complex as it was in the case of Cm-sTf system. Dilysine bridge between K296 and K206 and HB between atom O3 of CO_3^{2-} and HG1 of T120 are found to be intact throughout the 100 ns simulation post substitution (Figure 5.8).

DFT optimized $[\text{Th}_{\text{-to-}}\text{Cm}_{\text{MD}}]_{\text{QM}}$ system: In order to cross verify the DFT results, we have taken a truncated structure from the MD equilibrated and curium(III) substituted

TABLE 5.2: DFT optimized bond lengths (Å) of the metal ions ligated with atoms of the residues in the first coordination shell of protein's binding cleft

QM systems	Total charge (q)	Spin multiplicity (2S+1)	M-OD1 _{D63}	M-OD2 _{D63}	M-N _{H249}	M-O _{Y95}	M-O _{Y188}	M-O1 _{CO3}	M-O2 _{CO3}	H ₂ O
Fe-sTf (truncated)	-1	6	2.07 (2.03 ^a , 2.08 ^b)		2.37 (2.04 ^a , 2.16 ^b)	1.99 (1.8 ^a , 1.96 ^b)	2.08 (1.97 ^a , 1.97 ^b)	2.1 (2.06 ^a , 2.08 ^b)	2.01 (2.24 ^a , 2.22 ^b)	
Th-sTf (truncated)	0	1	2.54	2.61	2.54	2.29	2.29	2.39	2.41	2.72
Cm-sTf (truncated)	-1	8	2.34		2.56	2.34	2.31	2.46	2.46	2.6
[Cm ₁₀ -Th - sTf] ^{QM}	0	1	2.29		2.55	2.26	2.28	2.41	2.45	2.59
[Th ₁₀ -Cm - sTf] ^{QM}	-1	8	2.52	2.62	2.51	2.32	2.38	2.39	2.4	
[Cm ₁₀ -ThMD] ^{QM}	0	1	2.42		2.58	2.36	2.29	2.37	2.49	2.58, 2.63
[Th ₁₀ -CmMD] ^{QM}	-1	8	2.42		2.57	2.26	2.3	2.39	2.46	2.95

Values in parentheses are ^aexperimental form Ref.¹¹⁴ and ^bDFT results from Ref.¹³⁸

([Th₁₀-Cm-sTf]_{MD}) sTf structure, and then DFT optimize the resulting structure. We found that like in the case of Cm-sTf system, curium(III) again became hepta-coordinated as only one oxygen of D63 was found to coordinate with it. Important bond lengths between first shell residues are given in Table 5.2 and distances between second shell residues are given in Figure 5.9(D).

In summary, MD results on the coordination characteristics of the two An ions after their interchange in the sTf cleft and the results on their various levels of DFT optimization corroborates well with each other.

5.3.3 The binding and exchange energetics of metal ions at the cleft

The uptake of the metal ions from blood is governed by their binding strength to the sTf. In view of their different ionic charges, the metal-sTf binding can be thought to be dictated by the electrostatic interactions between the An ions and Lewis basic residues of the binding site. In addition, ionic potential (z/r) and their hydration number will play a major role towards metal binding to sTf. Indeed, actinides form variably stable complexes with plasma transferrin; Th(IV)-sTf complex being more stable than Cm(III)-sTf. In order to gain molecular level insights into experimental findings of their relative order of binding strengths to sTf,^{17,18} and to predict their ability to dislodge an already captured iron from sTf binding cleft, here we present the results of the binding and exchange energetics of the two An ions.

5.3.3.1 Ion binding :

While calculating binding of highly charged ions ($z > 1$) into protein interior, one must take electronic polarizability of the medium into account. To this effect, the use of MFP model of water¹⁸⁵ and implicit treatment of electronic screening effects¹⁸⁴ gives rise to an effective polarizable model for dissolved ions along with varying dipole moment of

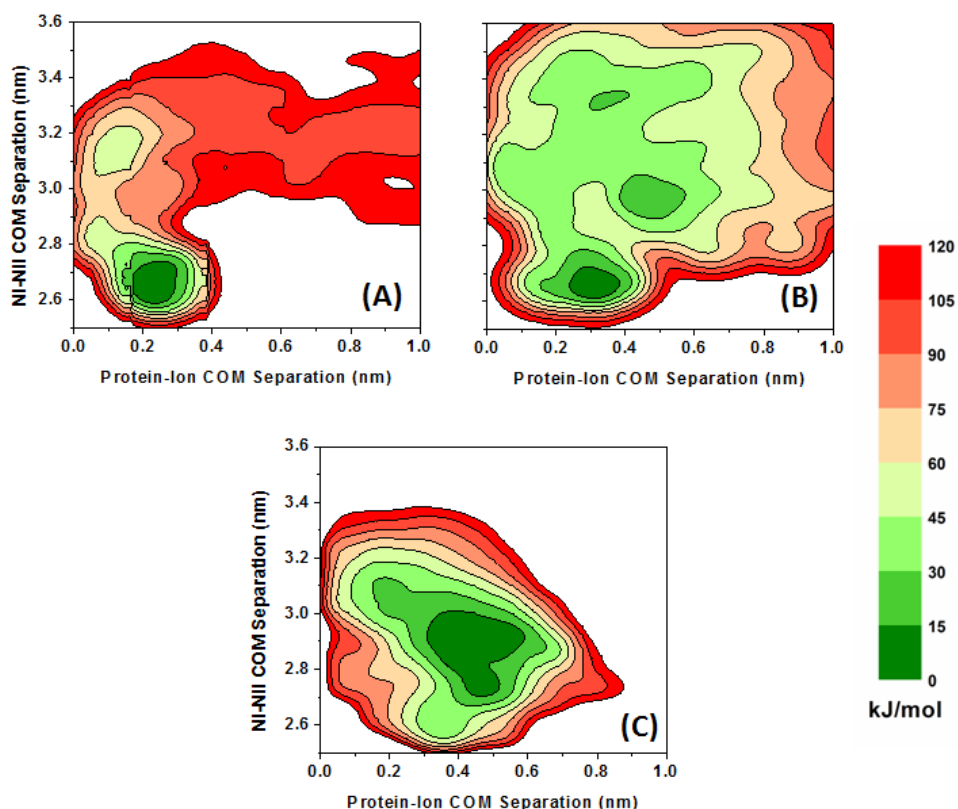


FIGURE 5.10: Well-tempered metadynamics-discovered free energy contour surface as a function of protein-ion centre of mass separation and centre of mass separation between the NI and NII sub-domain of sTf for unbinding transition of: (A) Cm^{3+} , (B) Th^{4+} and (C) Fe^{3+} in polarizable water medium are shown. Isoenergy lines are drawn every 15 kJ/mol as indicated by color bar. Green colored regions show the bound state of the ions; in contrast to trivalent ions, tetravalent thorium(IV) ion can be seen to remain attached to the transferrin at various locations even when NI and NII sub-domains are far apart and the protein is in the open state.

water from protein binding shell to its exterior.

In the above simulating environment, we have calculated the PMF profiles of the metal ions' unbinding from the cleft by utilizing MtD version of nonequilibrium enhanced sampling technique. The MtD runs were well-tempered along two chosen CVs, namely the COM separation between NI and NII sub-domains and that between the metal ion and the protein. The choice of the first CV is guided by the fact that the metal release process is triggered by substantial conformational changes of the protein, such

that the separation between NI and NII sub-domains increases and the protein opens up. The results of 2D PMF profiles are presented in Figure 5.10 for the unbinding transition of Cm(III), Th(IV), and Fe(III) ions in panels (A), (B), and (C), respectively. The minimum of the 2D unbinding free energy of each of the ion is used as a reference point to arrive at this plot. The very complex nature of the metal ion-sTf interacting system is quite evident in the figure. The large number of local minima (basins) and maxima (barriers) along the unbinding pathways are a manifestation of several influencing parameters, namely, structural fluctuations, electrostatic interactions, solvation, and van der Waals, HB, and protein-water-protein water bridge (WB) interactions. Th^{4+} , for example, with its higher ionic potential ($3.7 \text{ e}\text{\AA}^{-1}$) can be locally trapped in several binding pockets along the unbinding pathway. Whereas such a possibility for Cm^{3+} ion ($z/r = 2.7 \text{ e}\text{\AA}^{-1}$) can be seen to be rather rare. Ionic potential can be thought to stand for a proxy of measure of how strongly or weakly the ion will be electrostatically attracted to ions of opposite charge. Our treatment of electronic polarizability in the unbinding simulation ensured that water trapped inside the protein interior results in weaker protein-water-protein WB, stronger protein-metal ion interactions, both being facilitated by its lower dipole moment in the protein interior. This results into the subtlety of unbinding features of the An ions, with different ion potentials, to be unravelled in Figure 5.10. Note that even the trivalent iron ion ($z/r = 4.3 \text{ e}\text{\AA}^{-1}$) exhibits dissimilar binding feature when compared with trivalent curium ion.

The very virtue of well-tempered version of MtD allows one to reweight⁴ the resultant distribution for recovering equilibrium Boltzmann distribution of any unbiased variable. Utilizing this principle, from the 2D WtMetaD results, we have extracted the 1D free energy landscape of ions' unbinding from the first coordination shell of the protein's inter-domain cleft (Figure 5.11). Binding pattern of the ferric and the An ions in the first coordination shell (construct of D63, Y95, Y188, and H249 residues) is quite

remarkable. While the ferric ion ($z/e= 4.3 \text{ e}\text{\AA}^{-1}$) is strongly bound with well-defined free energy minima at the cleft and a large energy barrier thereafter, for An ions, especially for Cm(III) the binding at the cleft bottom is weaker with no free energy well that can be clearly observed. Difference in the binding features of the three ions can be quickly ascribed to their ionic potentials; the largest electrostatic effects in the ion coordination surface is caused by Fe(III), followed by Th(IV) and Cm(III). The order of binding strength of the ions are also manifested in the plots of their separation from the COM of the first coordination shell (Figure 5.11, right panel) as a function of WtMetaD run time; Cm(III) exits first ($\approx 7 \text{ ns}$), followed by Th(IV) ($\approx 21 \text{ ns}$) and Fe(III) ($\approx 33 \text{ ns}$). Based on these results of the two An ions studied here, one can conclude that Cm(III) can easily span the ion coordination surface in the first shell, thus providing a weak coordination. On the other hand, Th(IV) shows a much more stable coordination. However, none of these two ions can dislodge an already captured ferric ion. This result is in line with experimental observation that actinide complexes are less stable than Fe-sTf. Moreover, curium (III) is even more weakly bound than thorium (IV).^{17,18}

Present binding studies suggest that carbonate ion controls the chemical toxicity of the two An ions by firmly binding it to sTf protein, wherein it remained bound as a synergistic anion forming a fairly stable complex; Th-sTf-CO₃ being more stable than its curium(III) counterpart. Like Fe-sTf system, carbonate ion in synergism with sTf can capture An ions from the blood stream in a closed conformation of the protein at serum pH. Our more realistic polarizable simulating environment also ensures that it can provide additional stability towards potential ion-protein interactions at the cleft, which can act as possible local kinetic traps in the course of unbinding of the heavily charged thorium(IV) ion. In total, transferrin trafficking of the two An ions is found to follow the same mechanism, as is well known in the case of ferric ion, with subtle difference in their interactions with the protein.

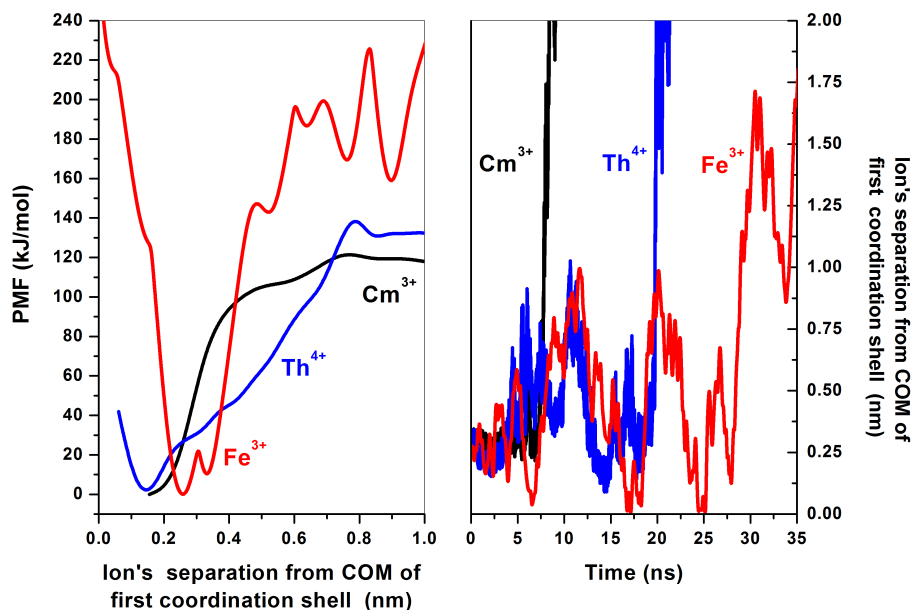


FIGURE 5.11: Left panel shows the PMF profiles of actinides (Th^{4+} and Cm^{3+}) and Fe^{3+} unbinding from the sTf binding cleft as a function of centre of mass separation between the residues in the first coordination shell of the protein's MBS and the metal ions, synergistically attached with the CO_3^{2-} ion. The profiles are obtained by reweighting⁴ the well-tempered metadynamics results in a polarizable water medium. Also shown at the right are ions' separation from centre of mass of first coordination shell of the MBS as a function of time.

5.3.3.2 Ion exchange energetics with DFT calculations

Here we further explore whether an already captured ferric ion in sTf binding cleft can be replaced with non-ferric An ions using DFT formalism. Using DFT is an attractive option since unlike MD methods, the results are independent of any parametrization protocol. However, the sheer size of the system often restricts application of DFT method, and like here, one usually formulates a realistic truncated model of the binding scenario. As stated above our truncated model is made up of first and second coordination shells of the binding cleft (*cf.* Figure 5.1) comprising total 123 atoms. Peptide junctions in the truncated model are capped with methyl group in order to stop unwanted HB formations that may render the structural motif of the cleft unintelligible. Note that total electronic charge in the model structure without metal ion is -4 (-1 from

each of the deprotonated D63, Y95, Y188, and H249 residues, +1 from each of the protonated residues, R124 and K296 in the second shell, and -2 from the synergistic carbonate ion) in accordance with the sTf protonation states at serum pH.^{114,137}

Metal Hydration: Before the truncated model of sTf is put to test for the calculations of ion exchange energetics, we have first considered hydration of the metal ions, since it plays a crucial role in the binding energy calculations. The DFT calculated results on the hydrated structure of metal ions showed that hydration sphere of Cm(III) is somewhat diffuse with 8-10 water coordination possible, whereas 9 and 6 water coordination for Th(IV) and Fe(III), respectively are almost always a possibility. This finding is in agreement with previously reported results.²¹⁰ We first obtain an average hydrated structure of the first coordination shell of the metal ions, dissolved in water, by MD simulations and then find an optimized hydrated structure of all the three ions by DFT calculations using B3LYP/def-TZVP basis set. While performing DFT optimization we have explicitly considered the primary hydration sphere, whereas implicit treatments of the rest of the solvent sphere are carried out.^{28,29} Analytical harmonic frequency calculations were performed for all structures to characterize the stationary points (potential minima). We found that hydration sphere of Cm³⁺ is somewhat diffuse with 8-10 water coordination possible, whereas 9 and 6 water coordination for Th⁴⁺ and Fe³⁺, respectively are almost always a possibility. This finding is in agreement with previously reported results.²¹⁰ Further, in order to validate the solvation model, we have calculated the hydration energies of the ions using the reaction scheme, presented in main text Eq. (1).



The optimized bond lengths of M-O_{water}, hydration energies of the metal ions with the corresponding values of n (electronic charge) and m (hydration number) in Eq. (1) are given in Table 5.3 and compared with available experimental and theoretical results. As can be observed, hydration energy of tetravalent thorium(IV) ion is more compared to

TABLE 5.3: Optimized range of M-O_{water} bond lengths and hydration free energies of metal hydrated systems

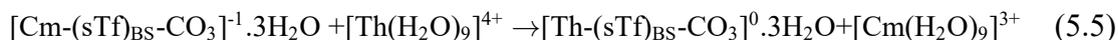
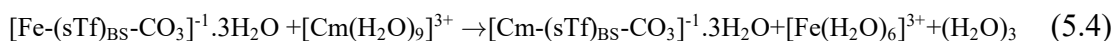
Hydrated metal ions	M-O _{water} bond length (Å)	Hydration energy (kJ/mol)
[Th(H ₂ O) ₉] ⁴⁺	2.53 - 2.54 (2.45) ^a	-5536 (-5815) ^d
[Cm(H ₂ O) ₉] ³⁺	2.53 - 2.55 (2.45-2.55) ^b	-3306 (-3334) ^e
[Fe(H ₂ O) ₆] ³⁺	2.07 - 2.08 (2.00) ^c	-4369 (-4265) ^d

values in parentheses are reported experimental/calculated values. ^a ref.,¹⁷⁴
^b ref.,^{174,175} ^c ref.,^{176,177} ^d ref.,¹⁷⁸ ^e ref.¹⁷⁹

trivalent ions. In case of Th⁴⁺ the deviation in the hydration energy from the reported result is less than 5%, while in case of Cm³⁺ ion the deviation is less than 1% and that for Fe³⁺ is less than 3%.

Ion Exchange Energetics: Note that due to the differences in the coordination characteristics (see section 3.2.3) of the An ions, thorium (IV) in the DFT optimized Th-sTf truncated structure (Figure 5.7) shows eight coordination number (for D63 being of bidentate nature) and is more stable than Cm_{-to}-Th substitution in sTf by around 10.5 kJ/mol. Similarly, the free energy of curium(III) substituted [Th_{-to}-Cm-sTf]_{QM} structure indicates that it is about 26.7 kJ/mol more stable compared to the DFT optimized Cm-sTf (truncated) structure. Based on these findings we set out to gain further insight into An versus ferric ion binding at the protein binding site. In particular, we have calculated the ion exchange free energies (ΔG_{ex}) using the truncated model of the of sTf cleft. The results, while providing thermodynamic feasibility of the ion exchange reactions on a relative basis, are also aimed at shedding light on the possibility of displacing an already captured iron by the two An ions. In addition, when compared with the MD results on the binding energetics of the ions involving the full protein (see above), the DFT calculated ΔG_{ex} values will verify the success and utility of the truncated model of the binding cleft. ΔG_{ex} between two metal ions at the sTf binding site (BS) are calculated

using the following exchange reaction schemes.



Note that in the left-hand side of above equations, the three water molecules arise from the choice of our QM model, which was prepared by selecting those molecules that appear within 10 Å of the central ions. These water molecules in addition to interacting with the BS atoms also interact between themselves through HB formation. In order to reflect their HB formation in the right-hand side of Eqs. 2 and 3, water molecules are represented as $(\text{H}_2\text{O})_3$. The free energy change associated with the above equations is given by,

$$\Delta G_{\text{ex}}^{\epsilon} = [\Delta G_{\text{solv}}^{\epsilon}]_{\text{product}} - [\Delta G_{\text{solv}}^{\epsilon}]_{\text{reactant}}, \quad (5.6)$$

where $\Delta G_{\text{solv}}^{\epsilon}$ is the free energy change in transferring the reactants or products from the gas phase to solution phase with the dielectric constant, ϵ . The dielectric constant of the BS at the protein interior is known to be different from that in the bulk. In view of this, two sets of calculations are performed, one at $\epsilon=5$ (mimicking the BS environment) and the other at $\epsilon=80$ for the bulk. Calculated thermodynamic parameters are given in Table 5.4 for the three ion exchange reactions using B3LYP/def-TZVP basis set for metal and TZVP basis set for all lighter atoms. The results for ΔG_{ex} values clearly show that at both the dielectric media, a bound Cm(III) can be replaced by Th(IV), however, a bound Fe(III) cannot be replaced by Cm(III). In the former case, the exchange reaction is enthalpy (sum of electronic energies, thermal energies including zero-point energy) driven whereas, for the later it is enthalpy forbidden. These results are in accordance with the MD results on PMF values involving the full sTf protein. However, substitution of a bound ferric ion by thorium (IV), as predicted by the DFT calculation (Table 5.4 with negative exchange free energy) of the truncated model is in contrast with the MD

TABLE 5.4: Calculated ion exchange energetics (kJ/mol) in the first binding shell of the protein cleft at different dielectric constant of the medium

Exchanging ions	ΔH		$T\Delta S$		ΔG_{ex}	
	$\epsilon=5$	$\epsilon=80$	$\epsilon=5$	$\epsilon=80$	$\epsilon=5$	$\epsilon=80$
$\text{Fe}^{3+} \rightarrow \text{Th}^{4+}$	-287.25	-6.45	37.61	38.20	-324.86	-44.65
$\text{Fe}^{3+} \rightarrow \text{Cm}^{3+}$	277.93	204.22	27.79	28.39	250.14	175.83
$\text{Cm}^{3+} \rightarrow \text{Th}^{4+}$	-565.18	-210.67	9.81	9.81	-574.99	-220.48

result for the reasons discussed below.

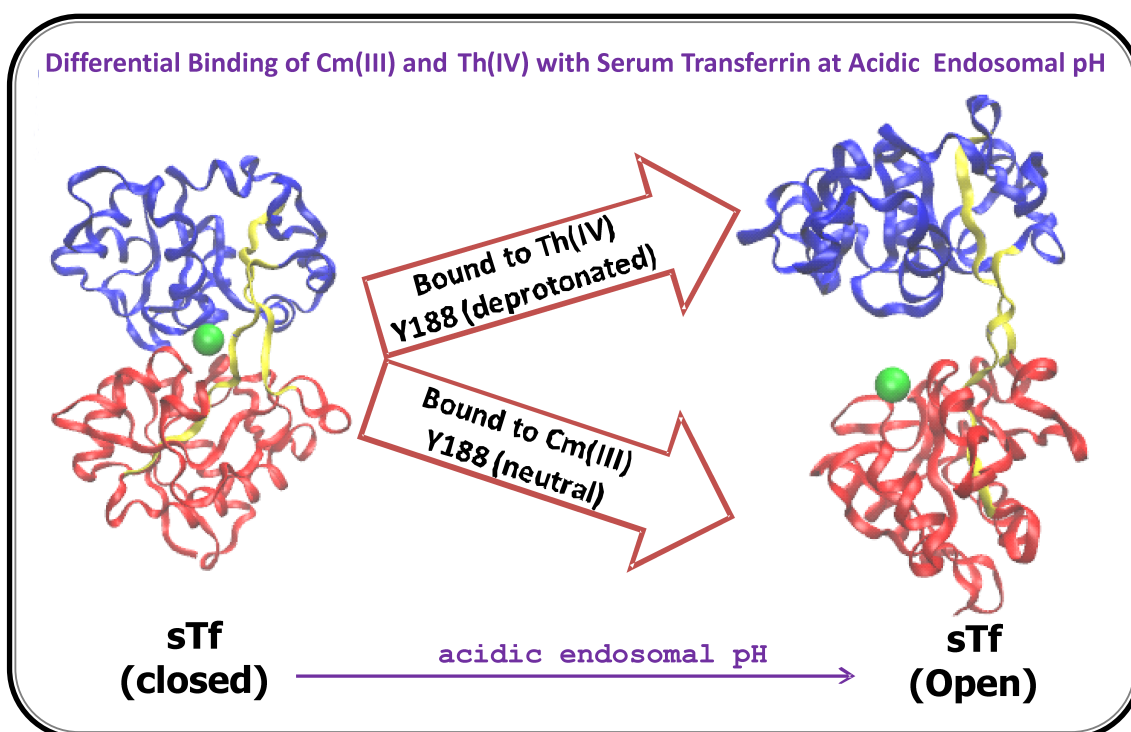
In the DFT method, the ion exchange energetics are obtained by free energy difference method (*cf.* Eqn 5.6) using a truncated model. Whereas in WtMetaD simulation, each of the ions are displaced along a physical pathway of unbinding, unravelling the complete mechanistic information of the process involved. These results into PMF profile (Figures 5.10, 5.11) along the unbinding pathway and unlike DFT method does not provide a free energy difference. Moreover, DFT results on the binding free energy are based on a fixed number of water molecules associated with the reaction scheme, Eqn (2)-(4), whereas in the MD simulations the water coordination (hydration) number of the ions continuously fluctuates realistically. Therefore, it is impracticable to expect that the DFT and WtMetaD results are comparable on a quantitative basis. However, the results from the two methods can be compared on a qualitative basis. The close correspondence between the MD results and the experimental trend^{17,18} on the stability order of the sTf complexes: $\text{Fe}^{3+} > \text{Th}^{4+} > \text{Cm}^{3+}$ is quite encouraging and is a testimony of the success of using the full N-lobe of the sTf protein in polarizable water model with effective polarization due to ions. On the other hand, the inconsistency in the DFT results on the said order between Fe^{3+} and Th^{4+} may be ascribed to the usage of a truncated stand-alone BS (*cf.* Figure 5.1), in which the synergistic of the nearby residues' structural fluctuations on the end-results are neglected.²⁸

5.4 CONCLUSIONS

Our structural, dynamical and binding studies of the two An ions indicate that the sTf protein binds them in a closed conformation. This mechanism closely follows that of the ferric ion trafficking pathway at serum pH. We have observed that in tandem with carbonate ion, Th(IV) is present in octa-dentate mode while Cm(III) prefers a hepta-dentate mode of coordination in the protein binding site. Like their ionic potential values, the relative order of stability of sTf complexes with Fe(III), Th(IV), and Cm(III) ions, as inferred from the WtMetaD discovered PMF values, are found to follow the same trend as are observed in experiments. This result in particular emphasizes that interaction between the An ions and sTf in the presence of explicit water molecules is mainly the Coulomb interaction between them, which gives rise to the difference in the binding characteristics of the ions. The shortfall in the DFT results on the said order between tetravalent Th ion and ferric ion may be ascribed to the oversimplified truncated model of the binding cleft, wherein the indirect influences of nearby residues on the ion binding is neglected. Further, the WtMetaD results revealed that out of the two An ions investigated here, thorium (IV) binds with sTf slightly more strongly than curium (III). As a result, it will be more difficult to release thorium(IV) from the binding cleft, which might suggest its lower cytotoxicity when compared with curium (III). In total, this work provides the atomistic detail of An ions' interaction with sTf at serum pH, which in future may prove to be useful for effective design of their decorporating therapeutics.

CHAPTER 6

Equilibrium MD Simulations for Binding of Cm(III) and Th(IV) with sTf at Endosomal pH



HIGHLIGHTS

- **Understanding Actinide (An) interaction with serum transferrin (sTf) assumes a greater significance for the development of safe and efficacious chelators for their removal from the blood stream.**
- **In this chapter, several 100 ns equilibrium MD simulations of sTf bound to Cm(III) and Th(IV) at various protonation states of the protein are performed to explore the possibility of the two An ions release and speciation. The results demonstrate that like in Fe(III)-sTf system at the acidic endosomal pH, variation in protonation state of dilysine pair (K206 and K296) and the tyrosine (Y188) residue is necessary for the opening of Cm(III)-bound protein and the release of this trivalent ion.**
- **For Th(IV), protonation of dilysine pair alone is found to be sufficient to cause conformational changes in protein for opening of the sub-domains. However, in none of the protonation states of the protein investigated, Th(IV) is found to be released.**
- **Analysis of hydrogen bond and water bridge correlation functions, in addition with the evaluation of potential of mean forces of the An ions' release from sTf, substantiate the differential behaviour of Cm(III) and Th(IV).**
- **The results provide insight in the regulation of Cm(III) and Th(IV) bioavailability that may prove useful for effective design of their decorporating agents and as well may help future design of radiotherapy based on tetravalent ions.**

6.1 INTRODUCTION

In the previous chapter 5 results of multi-scale modelling for sTf loaded with Th(IV) and Cm(III) at serum pH conditions are discussed. In the present chapter interaction of Th(IV) and Cm(III) with sTf for several protonation states of the protein at endosomal pH condition are explored using equilibrium molecular dynamics simulations.

Naturally occurring long lived actinide (An) isotopes ^{238}U , ^{232}Th , ^{244}Pu , called as primeval radionuclides and their decay products should be considered to be inherent constituent of the human body ever since the existence of Homo Sapience on this planet.^{24,166,168} An isotopes, unlike some other heavy metals, have no known essential role in the normal biochemical reactions occurring in living organisms. Isotopes of U, Th, Am, Pu, Cm and other actinides are routinely used in various processes involved in the front- and back-end of nuclear fuel cycle. Although there are stringent safety measures during these processes, there always remains a risk that these radionuclides can enter into human body through any of the routes, namely inhalation, ingestion and injection. Upon entry into the body they are transported to various tissues, cells via blood mainly through the iron carrier serum transferrin (sTf) protein.^{13,18,20–22,24,61,81,122,167,168} Most of the An isotopes especially, ^{228}Th , $^{238,239}\text{Pu}$, ^{241}Am , $^{242,244}\text{Cm}$ and ^{237}Np are mainly alpha emitters and are highly radiotoxic.¹⁶⁶ Biochemistry of these isotopes are not yet very clear. Such biochemical knowledge, especially interaction with sTf, however, becomes essential for the development of safe and efficacious therapeutic methods accelerating their slow, natural rate of elimination from human body in the event of an incidental contamination.

Role of the homologous iron-binding glycoproteins, known as transferrin family of proteins is to control the iron level in the human body. sTf is a member of this family which controls the transport of iron in the blood and its delivery into various absorption cells. Dietary iron in human body is mainly bound to sTf, then transported in the blood serum and finally delivered to cells through a process of receptor mediated endocytosis.

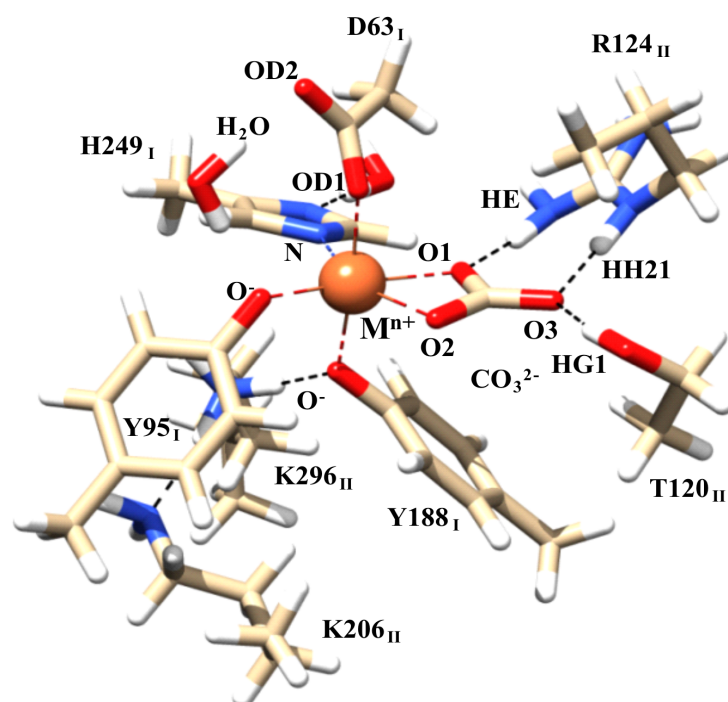


FIGURE 6.1: The first and the second coordination shells of metal ions ($M^{n+} = \text{Cm}^{3+}, \text{Th}^{4+}$) in human serum transferrin binding cleft is shown schematically. Various protonation states of the residues in the shells, for which equilibrium MD simulations are performed, are summarized in Table-6.1.

sTf protein is present at a concentration of approximately 3mg/ml in human serum and is about 30 % saturated with Fe (III). While this renders the blood serum accessible for certain therapeutic metal ions to bind and transport, it also become vulnerable for other toxic metals to follow the major iron acquisition pathway and subsequent receptor mediated endocytosis.¹²⁻¹⁵ About 30 other metal ions including actinides are found to make complexes with sTf.¹⁶

sTf forms a bilobal structure (N- and C-lobes) with its single-chain polypeptide having molecular mass of 80 kDa. Each lobe can accommodate one iron at the binding site formed by the inter-domain cleft due to two respective sub-domains, NI, NII and CI, CII. NI sub-domain is constituted of sTf residue number 1 to 91 and 245 to 313, while NII sub-domain is constituted of sTf residue number 92 to 244. The two sub-domains are connected to each other by a hinge consisting of two extended anti-parallel β -strands

TABLE 6.1: Protonation states of residues in the first and second coordination shells of the metal ions in the protein binding cleft. Only changes in protonation states with respect to the crystal structure (PDB ID: 1A8E) are indicated

	Serum pH	Endosomal pH		
		<i>acid I</i>	<i>acid II</i>	<i>acid III</i>
First Coordination Shell (D63, Y95, Y188, H249, CO ₃ ²⁻)	H249 (doubly deprotonated) ^a Y95, Y188 (phenolate)	HCO ₃ ⁻ H249 (neutral) ^a	HCO ₃ ⁻ Y188 (protonated) H249 (neutral) ^a	HCO ₃ ⁻ Y188 (protonated) H249 (neutral) ^a
Second Coordination Shell (T120, R124, K206, K296)	no change	K206 (protonated) K296 (protonated)	K206(protonated) K296 (neutral)	K206 (neutral) K296 (protonated)

^a all other histidine residues are protonated following Rinaldo and Field¹³⁹ and Mujika et.al.¹³⁷

(residues 91-101 and 241-252) that forms the binding cleft for the metal ion.¹¹⁴ The first coordination shell of the binding cleft is in octahedral shape where two tyrosine (Y95 and Y188) phenolate oxygen atoms, one histidine (H249) imidazole nitrogen atom, one carboxylic oxygen atom from an aspartate (D63) residue, and the synergistic carbonate anion are ligated with the central metal atom. The second coordination shell in the binding cleft is comprised of residues: threonine T120, arginine R124, two lysines K206, and K296 (*Cf.* Figure6.1 and Table-6.1). The two coordination spheres together complete the binding of the metal ions at physiological serum pH. Other synergistic anions in place of carbonate, such as citrate is reported to coordinate with non-iron metal ion, Ti(IV),¹⁶⁹ while a large number of inorganic anions those can bind with transferrin are recently reviewed.¹⁷⁰ Recently molecular dynamics (MD) simulation of the effects of synergistic and non-synergistic anions on the iron binding has been reported.¹⁷¹

Several experimental studies on the interactions of transferrin are carried out with a variety of actinide ions.^{18,19,23-25} For example, interaction of Cm(III) and Am(III)²⁰⁻²² with transferrin are recently studied by time-resolved laser fluorescence and EXAFS spectroscopy. It is evident from these experimental studies that tetravalent An ions' binding characteristics are different to that of trivalent An ions. Even amongst the tetravalent ions, the binding features are found to be different, e.g., Pu(IV)²⁷ vs.

Th(IV).²⁶ Although experimental data on binding and transport of non-iron metal ions¹⁴ including that of the An ions are available aplenty, there is hardly any specific information at the molecular level. In addition, how physiological carbonate ion work in tandem with sTf to bind An ion is unknown. Whereas, in order to gain deeper understanding on the biological fate of sTf mediated An trafficking, molecular level investigation is of utmost importance.

In the pursuit of molecular details of binding, a combination of density functional theory (DFT) and MD simulation is a very attractive avenue.^{28,29} Theoretical studies for sTf bound with other non-iron metal ions including that of the actinides are very scarce. A few DFT studies for complexes of transferrin with metal ions, such as, Fe(III), $V^{IV}O^{2+}$, UO_2^{2+} have been successfully attempted.^{109,122,138,172} Recently through a combination of DFT and MD methods¹⁶⁵ we have observed that in tandem with carbonate ion, Th(IV) prefers an octa-dentate mode while Cm(III) prefers a hepta-dentate mode of coordination in the sTf binding cleft.(*cf. Chapter4.4*) This coordination profile of the An ions is radically different from that of the Fe(III) ion. Further, from well-tempered metadynamics discovered potential of mean force (PMF) values at serum pH, we have observed that the relative order of stability of sTf complexes with Fe(III), Th(IV),and Cm(III) ions follow the same trend [Fe(III) >Th(IV) >Cm(III)] as are observed in experiments.

The transferrin molecule undergoes a significant conformational change during the process of binding and releasing iron: from open (the iron free Apo-protein)–to closed (iron loaded at physiological serum pH)–to open (releasing iron upon binding to transferrin receptor at the endosomal pH) conformations. Mujika *et al.*¹³⁷ have investigated the release of metal from an Fe(III) and Al(III) loaded N-lobe of serum transferrin by MD simulations. They have observed that in addition to the variations in the protonation state of the dilysine pair (K206 and K296), the protonation of Y188 is indispensable for prompting the conformational change of the protein and release of the

metal ions. Whether similar mechanism will hold true in the case of release of An ions is yet to be explored. In this work, this central issue is probed for the two test cases: a trivalent [Cm(III)] and a tetravalent [Th(IV)] ions at the endosomal pH (pH=5.5) using equilibrium MD simulations.

The binding cleft of sTf is located inside the protein where the polarization environment experienced by the bound metal ions will be different from that prevailing in the solvent exposed protein surface. While carrying out classical MD simulations for charged metalloproteins¹⁸³ the consideration of dielectric heterogeneity of the medium thus become important.¹⁶⁵ Essentially this becomes paramount of importance while dealing with heavily charged metal ions (such as, +3 and +4 in the present case). However, in standard MD force fields, the generic electronic screening effects due to water are treated as fixed charge nonpolarizable water. As a result, the nonpolarizable water models overlook the local environment changes from the bulk to the protein surface to its interior. In order to bring in the changes in local dielectric environment of the An ions in a more realistic fashion, here the MD simulations are conducted by utilizing a mean-field polarizable (MFP) model of water,^{184,185} which has been successfully applied in several other occasions.^{29,186,187} In this work, several 100 ns equilibrium MD simulations are conducted at different protonation states of the sTf binding cleft (*acid I*, *acid II*, and *acid III*, see Table-6.1) when the protein is bound to the An ions: Th(IV) and Cm(III). The work is primarily aimed at delineating the binding, release and speciation of the two ions at endosomal acidic conditions. One of the important finding is that protonation of Y188 residue alongside that of the dilysine pair is essential for the protein to undergo conformational changes prompting Cm(III) to be released. Whereas in the case of Th(IV), the protonation of the dilysine pair is enough for the protein to undergo the conformational changes. However, Th(IV) is never found to be released from the protein interior in any of the protonation states studied. Through a host of analysis (hydrogen bond (HB), water bridge (WB) dynamics, PMF profiles for

the metal release from the binding cleft, An ion-protein residue electrostatic interaction) we have underpinned the mechanistic details of the tetravalent *vs.* trivalent An ion's interaction with sTf. This work provides insight that may help designing improved An chelators. In a broader sense, it also shed light on the futuristic design of targeted radio therapy with the help of sTf.

6.2 METHODS

Serum transferrin consists of a single-chain polypeptide of 679 amino acids with a molecular mass of 80 kDa. The single-chain polypeptide forms a bilobal structure with its N- and C-lobes. The sub-domains in each of the lobes (NI, NII and CI, CII) form one metal binding site in their inter-domain clefts. Except that a disulfide bond and a longer hinge region in C-lobe than that found in N-lobe, the later show similar binding and release characteristics when compared with the entire molecule.¹⁸¹ The high resolution (1.6 Å) structure of only N-lobe of iron-bound recombinant sTf is available in the crystal structure data base.¹¹⁴ In view of this, we have chosen only the N-lobe sTf as the starting configuration of the protein (PDB ID: 1A8E).

6.2.1 Molecular dynamics

Model Structures: The sTf binding cleft consists of two coordination shells that hold tight the central metal ion. The first coordination shell of the metal ion is comprised of D63, Y95, Y188, H249 and the CO_3^{2-} ion. While T120, R124, K206 and K296 form the basis for second coordination shell (*cf.* Figure 6.1). The residues in the second shell; T120 and R124 are stably bound with the carbonate and while K296 forms hydrogen bond with K206, also is bound to Y188. The two immediate coordination shells of the metal-carbonate system can be regarded as a reasonable representation of the

metal-bound sTf binding cleft. In extracellular medium, the pH of the blood serum is around 7.5. At this pH, the metal-loaded sTf maintains a closed configuration.^{137,165} At the acidic endosomal pH (around 5.5), during iron/aluminium release protonation states of metal coordination shells are known to undergo change.^{137,139} Following this the protonation state of the amino acids involved in the binding site is studied by evaluating their pKa values¹⁸² at the acidic pH condition. We have carried out equilibrium MD simulations of the N-lobe of sTf, loaded with Th(IV) and Cm(III) in three protonation states of their coordination shells: (1) *acid I*, (2) *acid II* and (3) *acid III* (*cf.* Figure 6.1 and Table-6.1). Note that in our previous study,¹⁶⁵ at serum pH, Y95 and Y188 were in phenolate form, H249 was in imidazolate (doubly deprotonated) form, while all other histidines were protonated accordingly which is similar to Mujika *et al.*¹³⁷ In the present work at the endosomal acidic environment, carbonate is protonated to bicarbonate, H249 is in the neutral form while all other residues are similar to that in the serum pH condition, except that, (1) in *acid I*, both the lysine residues (K206 and K296), (2) in *acid II*, Y188 and K206 and (3) in *acid III*, Y188 and K296 are protonated. Protonation of the residues were initiated from the previously obtained equilibrated structures of Cm(III)- and Th(IV)-loaded sTf at serum pH.¹⁶⁵

Simulation Protocol: All MD simulations are performed using Gromacs-4.0.7 suite of programme.¹⁸⁸ The amber99 force field¹⁸⁹ (ff99SB) is employed to build the topology of the protein. Amber force field parameters for deprotonated tyrosine and bicarbonate ion were evaluated using python based acpype script with antechamber package¹⁹⁰⁻¹⁹² as these were not available in the force field library. Charges of these residues were calculated using GAMESS¹⁹³ and Restrained Electrostatic Potential (RESP)¹⁹⁴ tools. The non-bonded parameters of Cm(III) and Th(IV) were taken from literature.^{180,195} These parameters for the ions, explicitly dissolved in TIP3P water,¹⁹⁶ were obtained by targeting the experimental hydration free energies and ion-oxygen

distances of the first solvation shell as metric. Details of the MD simulation protocol is described in the fifth chapter of the thesis and also can be found elsewhere.^{165,226}

6.2.2 Umbrella sampling simulations

In order to study the thermodynamics of An ions' unbinding from sTf we have conducted umbrella sampling (US) simulations.⁴⁷⁻⁴⁹ We have generated a series of configurations along chosen reaction coordinates between the interacting An ion and sTf. The chosen reaction coordinates, as discovered through equilibrium MD simulation, are centre-of-mass (COM) separation between NI and NII sub-domains of sTf and that between An ion and entire N-lobe of sTf protein. While the former is a signature of protein's opening up transition, the latter is An ion's unbinding transition from the protein interior. These reaction coordinates serve as sampling windows, wherein independent simulations are conducted to generate an ensemble of structures. For a reaction coordinate, say χ , the potential energy is modified as: $U(\mathbf{R}) \rightarrow U(\mathbf{R}) + V_b(\chi_i)$, where \mathbf{R} is a vector representing all coordinates. To enhance the sampling of certain regions of coordinate span, a biasing potential,^{50,51} $V_b(\chi_i) = \frac{1}{2}k(\chi - \chi_i)^2$ is added, where k is a harmonic constant and χ_i is the position along χ around which the sampling is enhanced.

From the equilibrium MD simulations at certain protonation states, 8 Å COM separation between NI and NII sub-domains and 25 Å between an An ion and sTf were achieved. From these trajectories, snapshots were taken to initiate US simulations in 100 sampling windows in each of the coordinates. An asymmetric distribution of sampling windows is used, such that the window spacings at certain instances were even less than 0.08 Å and 0.25 Å along the NI-NII and An-sTf COM separation coordinates, respectively. In each window, 10 ns of MD is performed for a total simulation time of 1 μ s along each of the coordinates. k is set to 1000 kJ mol⁻¹ nm⁻². This resulted into a set

of 100 partially overlapping histograms, each of them providing a probability distribution function $\rho_i(\chi)$. The unbiased probability distribution, $\rho_u(\chi)$ ⁵² is recovered from the biased ones by the weighted histogram analysis method (WHAM)^{49,54-57} as implemented in the Gromacs tool. Finally the PMF, $F(\chi)$, or the change in free energy along the coordinate χ is obtained by, $F(\chi) = -k_B T \ln \langle \rho^u(\chi) \rangle$.^{50,53}

6.2.3 Hydrogen bond and water bridge correlation functions

To elucidate the dynamics of HB formation between the residues in the protein and that between HCO^- and the protein we have calculated their correlation function. Similar to this, a WB is formed between two residues when one water molecule forms concurrent HBs with two residues. WB time-correlation function elucidates the protein-water interaction dynamics. Methodology to calculate these correlation functions is given in the first chapter.

6.3 RESULTS AND DISCUSSIONS

Six equilibrium MD simulations are performed for Th(IV)- and Cm(III)- loaded sTf system at the endosomal acidic pH as described in the methodology section. For each of the actinides, three protonation states: (1) *acid I*, (2) *acid II* and (3) *acid III* are used as starting structures for subsequent 100 ns MD simulations. We began by replacing Fe(III) of the Fe-sTf crystal structure with Th(IV) and Cm(III), respectively to get the An-sTf equilibrated structures in the physiological serum pH condition.¹⁶⁵ The protonation states of the binding cleft (first and second coordination shells, *cf.* Table-6.1) are then changed to generate the Th(IV)- and Cm(III)- loaded sTf structures at these acidic conditions.

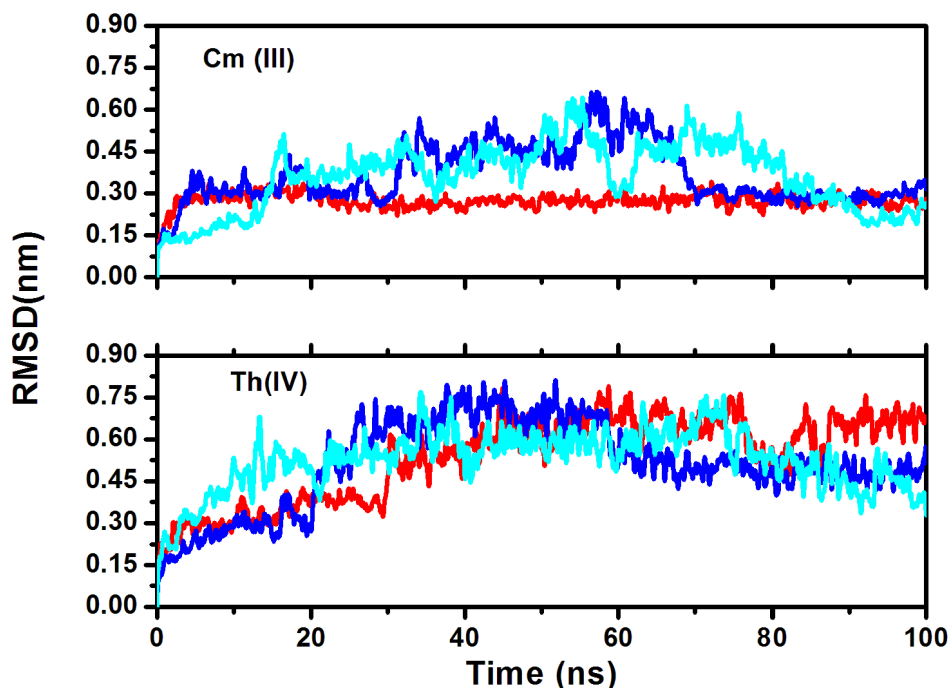


FIGURE 6.2: Time dependence of the RMSD of backbone C^α atoms of the An-sTf systems from their starting structures during the 100 ns equilibrium MD simulation. Upper panel shows the RMSD profiles for Cm(III)- and lower panel for Th(IV)-loaded sTf systems. Colour labels representing different protonation states (*cf.* Table-6.1) of the coordination shells of the An ions in the protein binding cleft are (i) red; *acid I*, (ii) blue: *acid II*, and (iii) cyan: *acid III*.

6.3.1 Structure and dynamics of the An-sTf systems.

The structural deviations of the An-sTf systems from their initial starting structures are assessed on the basis of root-mean-square deviation (RMSD) of its backbone C^α atoms as depicted in the Figure 6.2. While it is an important criterion to test the convergence of the simulating system, this can also serve as an indicator for large conformational change, if any. Previously in another study it has been verified that at the physiological serum pH, the RMSD of C^α atoms are within 0.16 nm and that they appear to be stabilized within 20 ns for both the An-sTf systems.¹⁶⁵ This observation is a clear indication of convergence of the An-protein simulating system and that the protein does

TABLE 6.2: Mean and standard deviations of distances (Å) between the An ions and the ligating atoms of the residues in the first coordination shell of the protein during 100 ns MD simulations at various protonation states

Ions	M-OD1 _{D63}	M-OD2 _{D63}	M-O1 _{HCO₃⁻}	M-O2 _{HCO₃⁻}	M-N _{H249}	M-O _{Y95}	M-O _{Y188}	MBS ^a	NI-NII ^b
Cm(III) _{acid I}	4.42±0.17	2.43±0.14	2.9±0.67	2.82±0.36	2.82±0.16	2.54±0.08	2.53±0.08	1.33±0.22	27.64±0.41
Cm(III) _{acid II}	6.63±2.37	5.81±2.61	18.39±12.79	18.16±12.96	7.25±1.81	11.47±2.90	10.61±2.55	8.82±2.23	28.18±1.48
Cm(III) _{acid III}	12.28±9.58	11.45±10.31	16.83±16.03	16.85±16.04	13.7±10.79	14.48±10.78	14.82±8.9	13.68±11.26	29.1±1.48
Th(IV) _{acid I}	3.98±0.59	2.36±0.05	12.01±8.42	12.18±8.54	5.63±0.89	8.22±2.95	8.97±4.44	6.43±2.6	31.05±1.61
Th(IV) _{acid II}	4.06±0.5	2.35±0.05	8.98±3.79	9.04±3.77	5.86±0.78	8.97±2.69	10.33±2.69	7.74±2.04	30.88±1.64
Th(IV) _{acid III}	4.23±0.25	2.35±0.05	8.88±2.44	9.25±2.73	5.53±0.89	8.41±2.39	11.95±2.71	7.21±2.23	31.13±1.14

^a Centre of mass separation between metal ions and the residues in the first coordination shell of the metal binding site (MBS)

^b Centre of mass separation between residues in NI and NII sub-domains

not undergo any noticeable structural changes at the serum pH. In the endosomal acidic condition, however, the temporal profiles of RMSD can be seen to be different. For example, in *acid I* protonation state (red lines in Figure 6.2), the deviation of RMSD in the case of Th(IV)-loaded sTf is substantially larger than that in Cm(III)-loaded sTf protein. It serves as a signature of structural changes or bonds/atoms motion during the equilibrium MD simulation of the protein when bound to Th(IV). In other two protonation states (*acid II* and *acid III*) RMSD profile exhibit almost similar pattern and maximum deviation goes upto 0.82 nm for thorium and 0.7 nm for curium structures. To investigate the structural changes at the endosomal pH conditions, we have carried out detailed structural analysis as presented below.

The structural changes of the An-loaded sTf systems during the 100 ns equilibrium MD simulation can be gauged from the mean and standard deviations of the distances between the An ions and the ligating atoms of the residues in the first coordination shell of the protein at the three protonation states. The results are summarized in Table-6.2. At the physiological serum pH where the An-loaded protein is known to preserve its closed conformation, earlier we have found that all the residues maintain a ligand-An distances within 2.63 Å during the 100 ns of simulation time.¹⁶⁵ However, at the acidic endosomal pH quite a number of interesting observations can be made. In *acid I* protonation state, while Cm(III) maintains a bound structure, as is evident from all the measured distances (except in Cm-OD1_{D63}) and the COM separation

between Cm(III) and the metal binding site (MBS), Th(IV)-loaded sTf binding cleft can be seen to be distorted. For the latter, all the calculated distances (except Th-OD2_{D63}) are substantially larger and the synergistic effect of the bicarbonate ion can even be seen to be lost. The distortion of the first coordination shell of the Th(IV)-bound sTf structure corroborates well with the RMSD result (*cf.* Figure 6.2). In other two protonation states (*acid II* and *acid III*) Cm (III) can be seen not to coordinate with any of the first shell residues, while in the case of Th(IV), only D63 is seen to be coordinated to it with its OD2 oxygen atom. This again reasserts the higher RMSD values for both the An ions in the two protonation states. Our observation of the compact structure of Cm(III)-loaded sTf system in *acid I* protonation state is similar to other trivalent metal's [Fe(III) and Al(III)] behaviour, in the sense, that without protonation of Y188 the metal ion cannot be released from the binding cleft.¹³⁷ The mean and standard deviations of the COM separation between the NI and NII sub-domains (see further below) of Th(IV)-sTf system in all the three protonation states are larger than those in the case of Cm(III)-loaded system. This signifies that for Th(IV)-loaded sTf, with or without the protonation of Y188, the protein can open up, which can subsequently assist the tetravalent An ion's release from the protein interior. This is in contrast to the trivalent metal-bound sTf, where without the protonation of Y188 the protein is seen to maintain closed configuration.^{137,165} Note however, as we will discuss below in greater detail, that in none of protonation states, Th(IV) is seen to be set free from the binding influence of the protein interior.

The protein's dynamics invariably involves local and global motions, which can be quantified convincingly by principal component analysis (PCA). Mujika *et al.* have concluded in their PCA study that while the first principal component of the global motion represents the hinge-bending motion, the second component entails hinge-twisting step.¹³⁷ The hinge-bending motion can be further associated with the COM separation between the NI and NII sub-domains of sTf, since these two

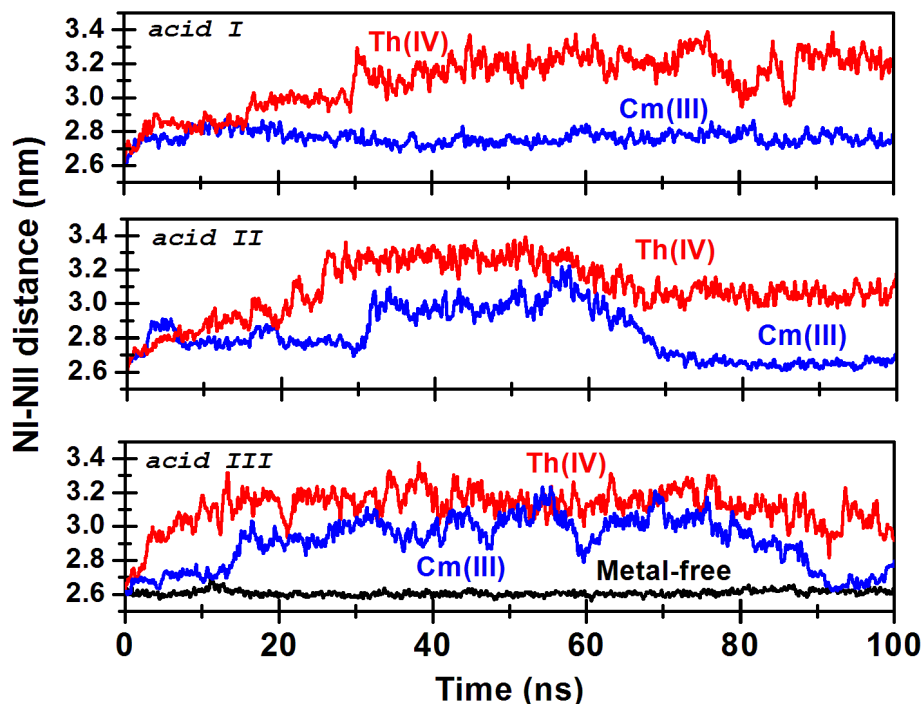


FIGURE 6.3: MD time evolution of distance between center of mass of the NI and NII sub-domains of An-sTf systems in various protonation states: (from top to bottom) *acid I*, *acid II* and *acid III*. Lines in red colour are for Th(IV)-loaded and blue ones are for Cm(III)-loaded sTf. Also shown the same in black line for the metal-free apo-sTf system at *acid III* protonation state.

sub-domains are connected to each other by the hinge. In Figure 6.3 we have presented the time evolution of the COM separation in the three protonation states of the An-loaded sTf. As can be observed in this figure, for the Th(IV)-bound sTf the NI-NII COM separation is always larger than that in the case of Cm(III)-bound sTf in all of its protonation states studied in this work. This is in line with the measured RMSD values of the protein (*Cf.* Figure 6.2). Higher values of RMSD and NI-NII COM separation from the starting structure can together be ascribed to opening of the protein. It is interesting to note in these Figures (Figures 6.2, 6.3) that in *acid I* protonation state, even without the protonation of Y188, the protein can open up while loaded with tetravalent thorium ion, which is in sharp contrast with the trivalent curium, iron or aluminium ions.¹³⁷ Put in other words, variation in the protonation of dilysine (K206 and K296)

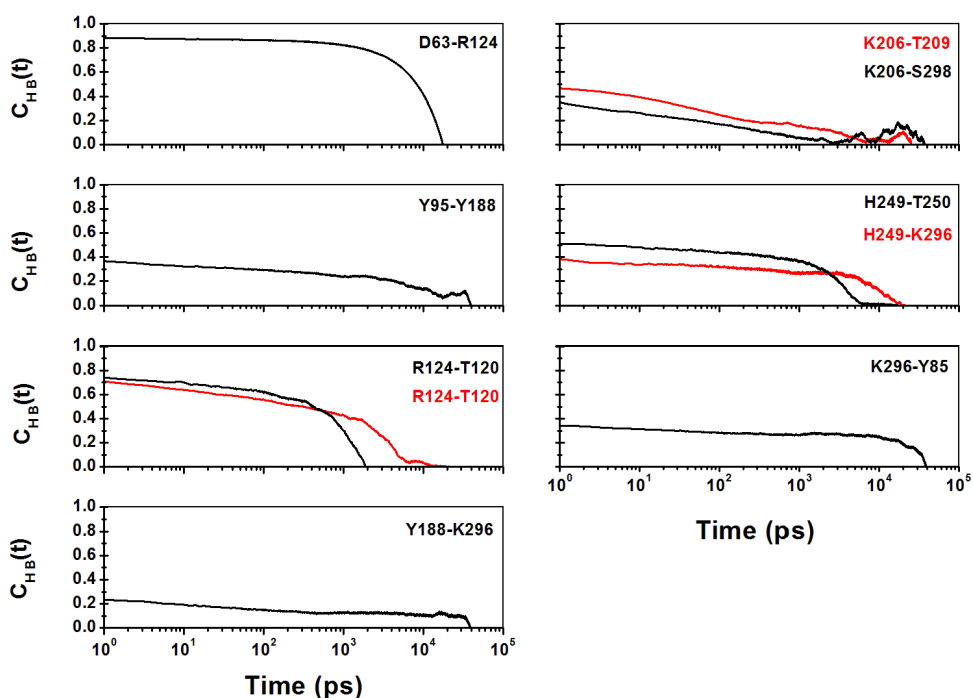


FIGURE 6.4: Time dependence of HB lifetime correlation function for the hydrogen bonds formed by the residues in the binding cleft of sTf in *acid III* protonation state of the protein are shown for metal-free (black line) and Th(IV)-sTf (red lines) systems. Higher HB lifetimes in the case of metal-free condition implies that the protein maintains its closed and compact structure in this acidic state, while Th(IV)-loaded protein opens up (*cf.* Figures 6.3) with less number of similar HBs to report upon.

trigger alone is sufficient to trigger the conformational changes of the Th(IV)-loaded sTf. While protonation of Y188 residue (as in *acid II* and *acid III* state) is a necessity, along with that of the dilysine trigger, to initiate similar conformational changes in the case of trivalent ion containing protein.

In the *acid I* protonation state, the residues in the first coordination shell of the binding cleft i.e., aspartate D63, both the tyrosines Y95, Y188, and the synergistic bicarbonate anion are unit negatively charged while histidine H249 is neutral. Thus, the total charge in the first coordination shell of the Cm(III)-loaded binding cleft is -1, which becomes zero when bound to Th(IV). In the immediate second coordination shell, on the other hand, each of the residues R124, K206 and K296 are unit positively charged

whereas T120 is neutral. The difference in the electronic charge distribution between the two coordination shell (negative *vs.* positive) for the Cm(III)-bound sTf can be thought to result into a compact structure of the binding cleft due to electrostatic attraction between the two shells and hence the protein is seen to maintain a closed structure during 100 ns simulation time. Whereas such additional electrostatic attraction between the two shells (neutral *vs.* positive) of Th(IV)-loaded sTf is missing, which resulted into opening of the protein. In *acid II* and *acid III* protonation states Y188 is protonated. This results into no net charge in Cm(III)-loaded sTf and +1 charge in Th(IV)-loaded sTf in their first coordination shell. As a result, neutralization of Y188 deforms the binding cleft containing either of the An ions, more so for the tetravalent thorium ion. This triggers the opening of the protein for either of An-bound sTf in these protonation states.

In order to justify the above argument that the electronic charge distribution in the coordination shells of the An ions is a governing factor for the protein's conformation changes, we have also evaluated NI-NII COM separation for the metal-free apo-sTf in *acid III* protonation state (black line in the lower most panel of Figure 6.3) and found it to be about 2.6 nm. This value is similar to that in metal-loaded sTf at the physiological serum pH,^{114,137,165} which can be readily inferred as a closed conformation of the metal-free protein. The closed and open conformational states of the protein can be further judged from an analysis of inter-residue HB time correlation function, $C_{HB}(t)$. In Figure 6.4 the temporal profiles of $C_{HB}(t)$ between the residues comprising the coordination shells of the metal ion in *acid III* protonation state of the protein with [Th(IV)] and without any An ion are presented. All the possibilities of HB formation between the residues in the coordination shells are also explored. A strong HB between D63 and R124 lasting ≈ 50 ns is noticed exclusively in metal-free sTf. In Th(IV)-bound sTf, protonated Y188 pushes apart R124 from its original position resulting into T120-R124 HB, which is also seen to be present in metal-free sTf. Protonation of K296 residue breaks the HB with K206 ("dilysine trigger") in either of the two cases studied.

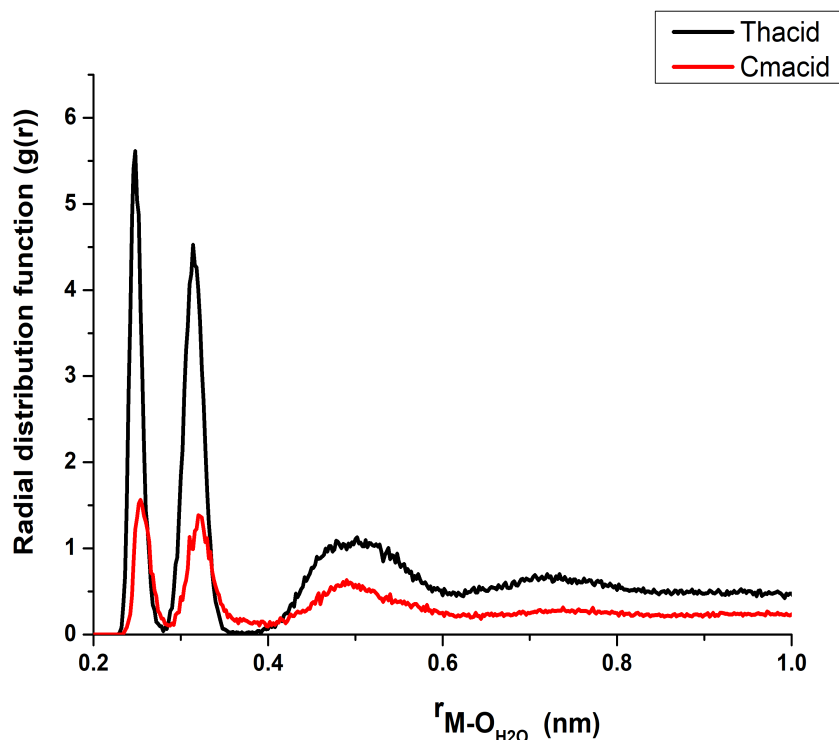


FIGURE 6.5: Water penetration into the binding cleft of the An-bound protein in *acid I* protonation state. Radial distribution function (RDF), $g_{M-O_{H_2O}}(r)$ of water around the An ions (Th(IV) in black and Cm(III) in red line), calculated from 100 ns simulation data are shown. Opening up of the protein while bound to Th(IV) ion is evident.

However, both the lysine residues continue to form varying degree of HB with other nearby residues. For example, K296 forms HB with Y188 and Y85, exclusively in the case of metal-free sTf. Similarly, the two tyrosine residues Y95 and Y188 are seen to be engaged in HB between them in metal-free sTf, which is seen to be absent in Th(IV)-bound sTf. Extensive nature of HB formations in metal-free sTf (in comparison to Th(IV)-bound sTf) can be regarded to maintain a compact structure of the binding cleft and a closed conformation of the protein.

In summary, the global conformational changes of the protein is seen to be governed in a complex manner by a host of factors: the presence of the metal ions, its charge, and various protonation states of the binding cleft.

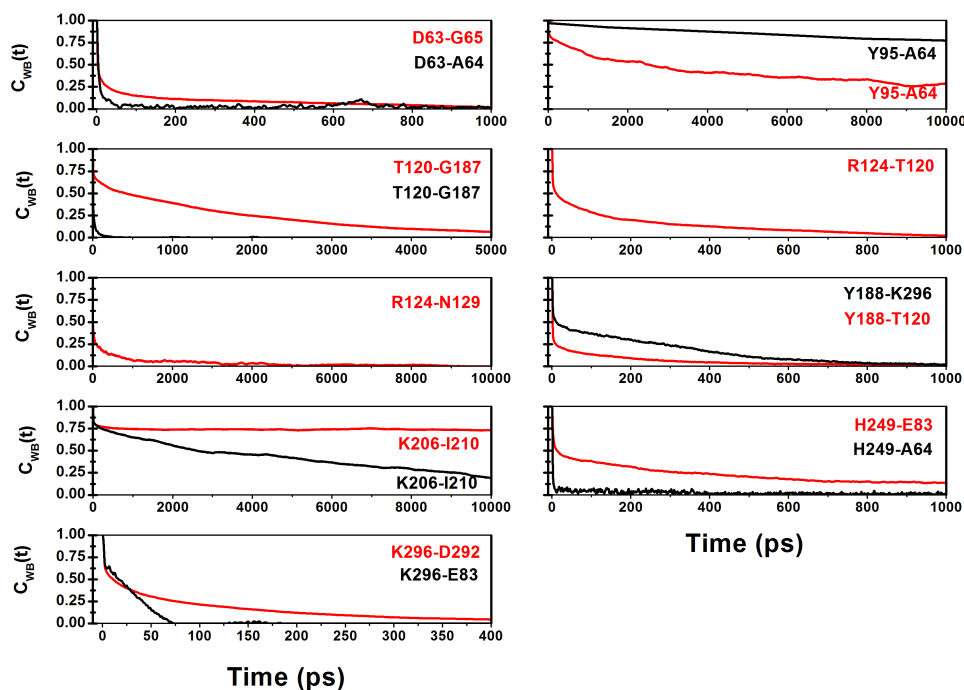


FIGURE 6.6: Time dependence of WB lifetime correlation function of the residues in the sTf binding cleft in *acid I* protonation state is shown. Red and black lines represents $C_{WB}(t)$ for Th(IV)- and Cm(III)-loaded sTf systems, respectively. Opening of the protein (Figure 6.3) at this acidic condition in Th(IV)-sTf system allows extensive WB formation due to abundance of water molecules in the protein interior in comparison to Cm(III)-loaded sTf.

6.3.2 Water penetration into the binding cleft.

The conformational changes of sTf is expected to give leeway for the water molecules to enter the binding cleft region. The radial distribution function (RDF), $g_{M-O_{H_2O}}(r)$ of water molecules around the An ion is a direct measure of the possibility of water penetration into the protein interior. In Figure 6.5 the RDF results, when the protein is in *acid I* protonation state, are presented. As discussed above (*cf.* Figure 6.3), under this acidic condition, sTf bound to Th(IV) completely opens up, whereas Cm(III) containing sTf does not. The extent of conformational changes due to the two An ions is clearly reflected in their $g_{M-O_{H_2O}}(r)$ plots. From the calculated profiles it is observed that about 10

water molecules enters the binding cleft forming hydration shell of radius 6 Å around the central Th(IV) ion. In Cm(III)-sTf system the corresponding number of water molecules reduces to 3.

Water plays crucial role in the conformational flexibility of a protein by making HB and WB with its residues. Water exhibits different dipole moments on the surface and in the interior of a protein,¹⁸⁵ e.g. binding cleft of sTf. The different dielectric properties of water in the bulk, in the surface and inside a protein molecule, has been further reinforced by a recent study that dielectric constant of small water clusters is different from the bulk water.^{211,212} It is also well known that the interior of the protein is quite hydrophobic in contrast to the hydrophilic surface.^{186,213–217} This dielectric heterogeneity of water in the protein interior leads to the stabilization of electrostatic interaction, e.g., HB between the protein residues and other ions. Gao *et al.* have observed that the breaking of HB in the hydrophobic environment requires 1.2 kcal/mol more energy.²¹⁸ Note that the TIP3P water in this work through its polarizable (MFP) treatment ensures that the dielectric heterogeneity of water in the medium is properly captured.^{184,185} The success and utility of this approach has been verified by us recently.^{186,187} Water molecules present in the hydrophobic metal binding cleft act as a lubricant by inserting into broken HBs between protein residues and forming one or two (during WB formation) concurrent HBs (in place of it) using two of its hydrogen atoms. This helps in facilitating further conformational changes of the protein and the unbinding of the metal ions.^{219,220} Hence, lubricating water molecules decrease the energy barrier during the metal liberation process. Thus, the dynamical balance between making and breaking of HBs and WBs finally controls the unbinding transition of metal.

In view of this, in Figure 6.6 WB time correlation function, $C_{WB}(t)$ between the residues in the binding cleft of the protein in *acid I* protonation state are presented. As is evident in Figure 6.3 that at this acidic condition, sTf, bound to the tetravalent thorium ion undergoes larger conformational changes as compared to its trivalent curium

counterpart causing more water molecules to be accessible (*cf.* Figure 6.5) at the binding cleft. Hence the likelihood of WB formation is more in the case of Th(IV)-loaded sTf. Data presented in Figure 6.6 meets this expectation. At this acidic condition the two positively charged lysine residues (K206 and K296) would repel each other facilitating the opening of the binding cleft.^{137,139} The freed lysine residues can be seen in Figure 6.6 to form WB with nearby residues. What is important to notice here is that both the dilysine forms stronger WB with longer lifetimes in case of Th(IV)-sTf system as compared to its Cm(III) counterpart. Similarly, the second shell residue R124 is seen to form WB with T120 and also with nearby N129 residue in Th(IV)-sTf system but none in the case of Cm(III)-sTf system. The extensive nature of WB formation in the binding cleft of the Th(IV) containing sTf further substantiates that the tetravalent An ion causes larger conformational changes of protein even without the protonation Y188, although distortion of the binding cleft in presence of curium ion cannot be ruled out.

6.3.3 Actinide release and their potential of mean force.

In view of their different ionic charges and ionic potential (z/r) values, the An-sTf binding can be thought to be largely governed by the electrostatic interactions experienced by the An ions in the binding cleft. Indeed, actinides form variably stable complexes with plasma transferrin; Th(IV)-sTf complex being more stable than Cm(III)-sTf at the serum pH.¹⁶⁵ Release of metal ions from transferrin inside cells is governed by the change in the protonation state of the coordination shells of the binding cleft and that of the synergistic anion due to decrease in pH of the medium. Here we explore release and speciation of the two An ions in the three protonation states of the protein and also evaluate the associated PMFs.

Parting away of the NI and NII sub-domains of sTf is a first step towards the An release. As discussed above the separation between these sub-domains is feasible in all the three protonation states of the protein when bound to the tetravalent thorium ion.

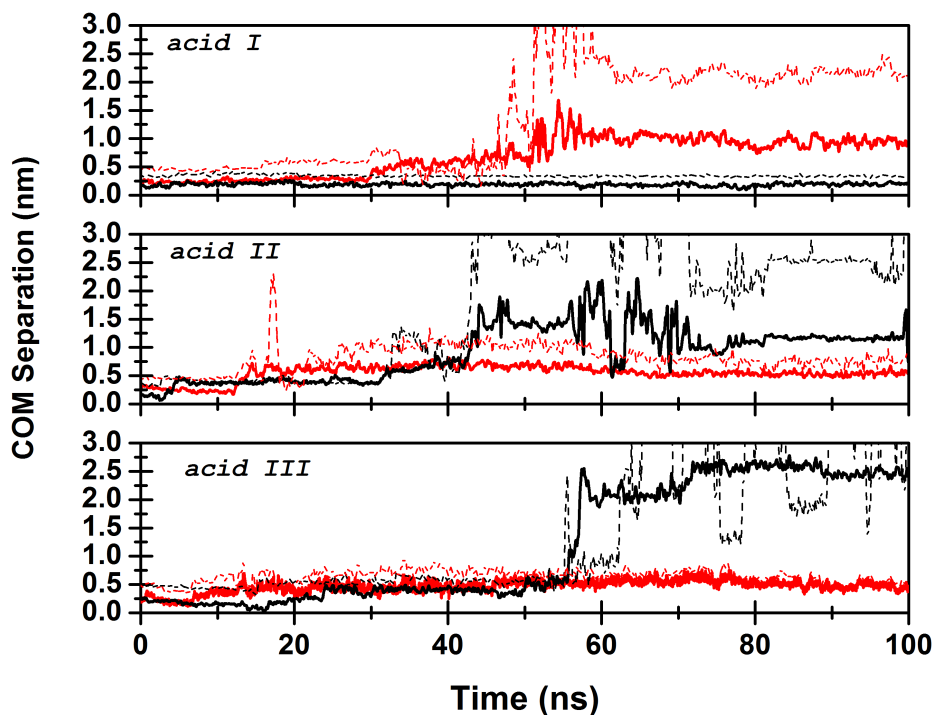


FIGURE 6.7: Temporal profile of the COM separation of the actinides (solid lines) and the synergistic HCO_3^- ion (dashed lines) from the protein in acidic conditions: *acid I*, *acid II*, and *acid III*, as indicated. Red lines are for Th(IV)-loaded and black lines are for Cm(III)-loaded sTf systems. The synergistic effect of HCO_3^- ion is seen to be lost as the An ions moves out of binding cleft.

However, protonation of Y188 (*cf. acid II* and *acid III* protonation states) is an essential prerequisite for the Cm(III)-loaded protein to open up. COM separation between an An ion (or the synergistic bicarbonate anion) and the protein is a suitable measure of the possibility of An release/speciation. Their temporal evolution in all the three protonation states are presented in Figure 6.7. It is interesting to note in this figure that opening of protein does not necessarily guarantee the release of an An ion. For example, Th(IV) in *acid I* protonation state reaches a maximum COM separation ≈ 1.5 nm at 55 ns, which then reduces to ≈ 1 nm in the 100 ns simulated time, although the synergistic influence of bicarbonate ion is lost. Similar observation can be made for Cm(III) in the *acid II* protonation state (middle panel, Figure 6.7). These COM separation data imply that none of the An ions are set free to the bulk solvent, even though the protein opened up in both

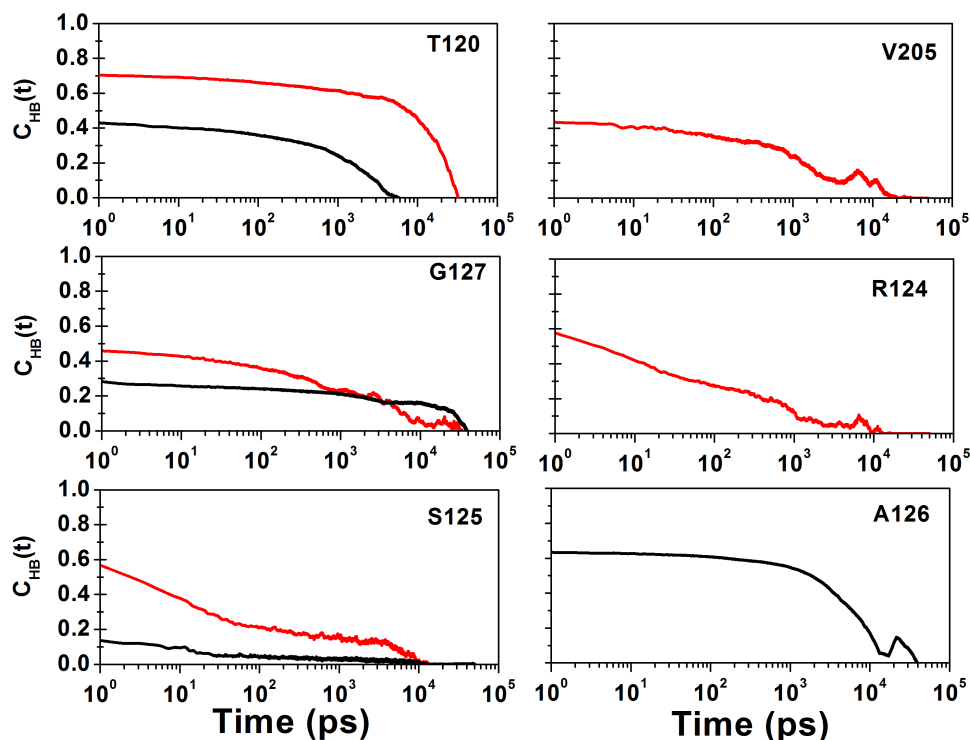


FIGURE 6.8: Hydrogen bond correlation function between HCO_3^- ion and residues of sTf in *acid I* protonation state is shown. Hydrogen bonds between all possible donor-accepter pairs are considered. Red and black lines represent $C_{\text{HB}}(t)$ for Th(IV)- and Cm(III)-loaded sTf, respectively. Extensive nature of hydrogen bonding of HCO_3^- with residues in Th(IV)-sTf system imply that the synergistic anion is detached from An ion while the later forms strong electrostatic interaction with D63 residue in the first coordination shell (see below). This renders Th(IV) not to leave the protein interior even though the protein opened up in *acid I* protonation state (*cf.* Figure 6.3) and Th(IV) is freed from the synergistic influence of the bicarbonate ion (*cf.* Figure 6.7).

occasions. In *acid III* protonation state, however, Cm(III) can be seen to be fully released from sTf interior coupled with loss of synergism with the bicarbonate ion. It is important to emphasize here that when Y188 is protonated (*acid II* and *acid III* protonation states) thorium remained tightly bound to the cleft with the synergistic influence of bicarbonate ion intact. This can be explained on the basis of highly positive charge of thorium ion that can readily form strong electrostatic interaction with the first shell residue, aspartate D63 (also see below).

In order to investigate the fate of the bicarbonate ion after it loses its influence on

the captured An ion, we have monitored its hydrogen bonding pattern with the residues in the cleft and nearby. In Figure 6.8 we have presented the corresponding HB time correlation function in *acid k* protonation state for the captured An ions in sTf cleft. It can be clearly seen that HCO^- goes on forming strong HB (surviving up to ≈ 40 ns) with a number of residues in the Th(IV)-loaded protein interior. The extensiveness of HB formation in this case is more prominent than that in Cm(III)-loaded sTf, barring one: HB between HCO^- and A126. The latter HB, in fact, strengthens the synergistic influence by holding the bicarbonate anion in tight spot with the captured curium ion.

In order to investigate special role played by D63 in regulating An ion speciation

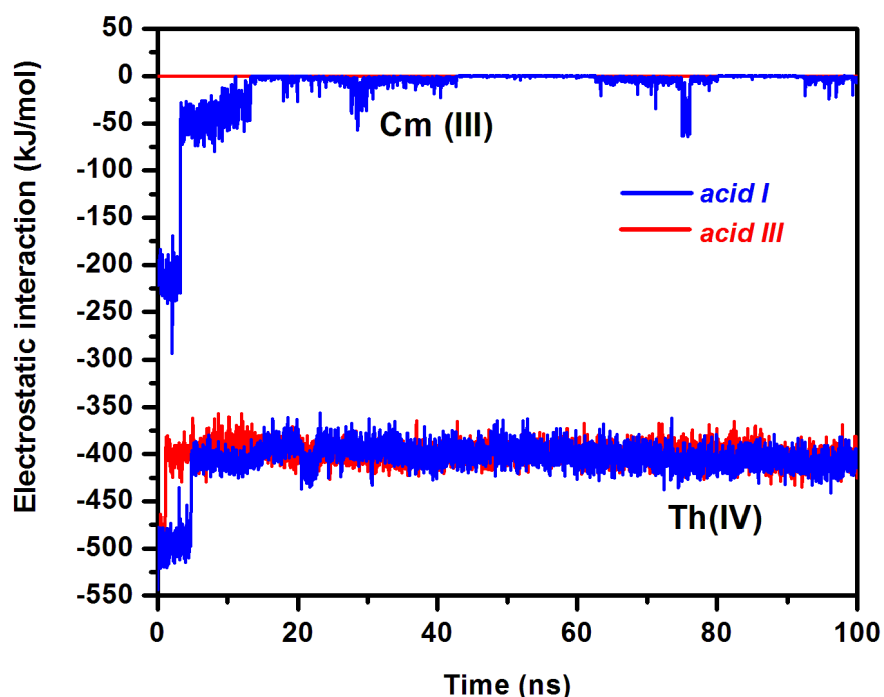


FIGURE 6.9: Short-range electrostatic interaction energy between Th(IV) and D63 and between Cm(III) and D63 are plotted as a function of time in *acid I* (blue lines) and *acid III* (red lines) protonation states of sTf. Strong electrostatic interaction between D63 and Th(IV) in both the protonation states of sTf does not allow the An ion to completely come out of the protein interior (*cf.* Figure 6.7), even though the protein opens up in both the acidic situations (*cf.* Figure 6.3). Whereas, Cm(III), in particular at *acid III* condition is free from such interaction and hence can be released from the protein.

in blood, we have monitored its short-range electrostatic interaction energy with the two An ions. Figure 6.9 show their temporal evolution. It can be readily seen in this figure that after an initial decrease (within ≈ 5 ns) the interaction energy stabilizes at about -400 kJ/mol in both the protonation states (*acid I* and *acid III*) for the bound Th(IV) ion. This highly attractive interaction can be thought to hold back the tetravalent An ion, even though the protein opens up in each of this acidic states. This result is in sharp contrast to Cm(III)-loaded sTf, where it can be seen that the said interaction of D63 has minimum influence on the trivalent An ion: in *acid I* it quickly attains a zero value with intermittent exhibition of attraction; in *acid III* with no interaction during the entire time period of simulation.

An important proposition can be made from the above results and discussion. sTf

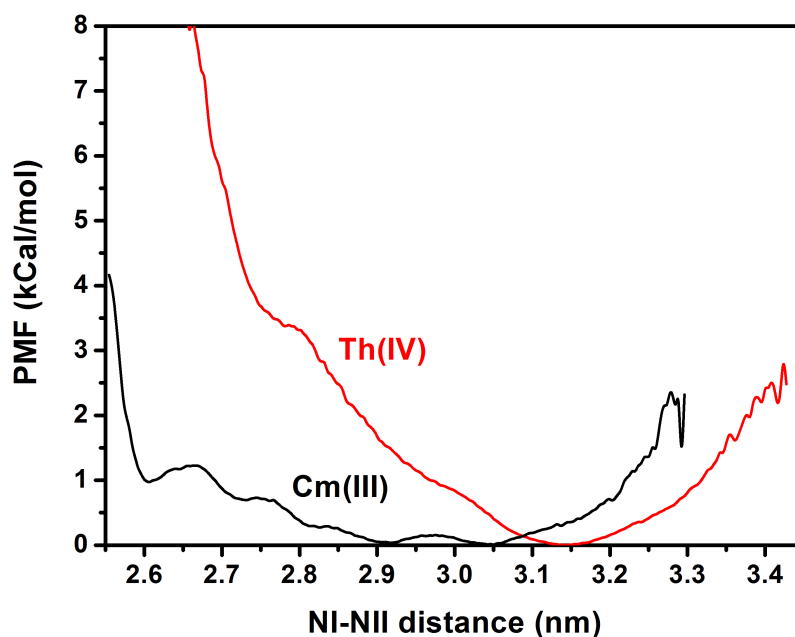


FIGURE 6.10: Potential of mean force (PMF) profiles for distance between COM of NI and NII sub-domains, characterizing the opening of sTf protein in *acid III* protonation state is shown. Red line is for Th(IV)- and black line is for Cm(III)-loaded protein. The profiles are obtained by performing US simulation along the NI-NII distance coordinate, as obtained from equilibrium MD simulations and shown in Figure 6.3.

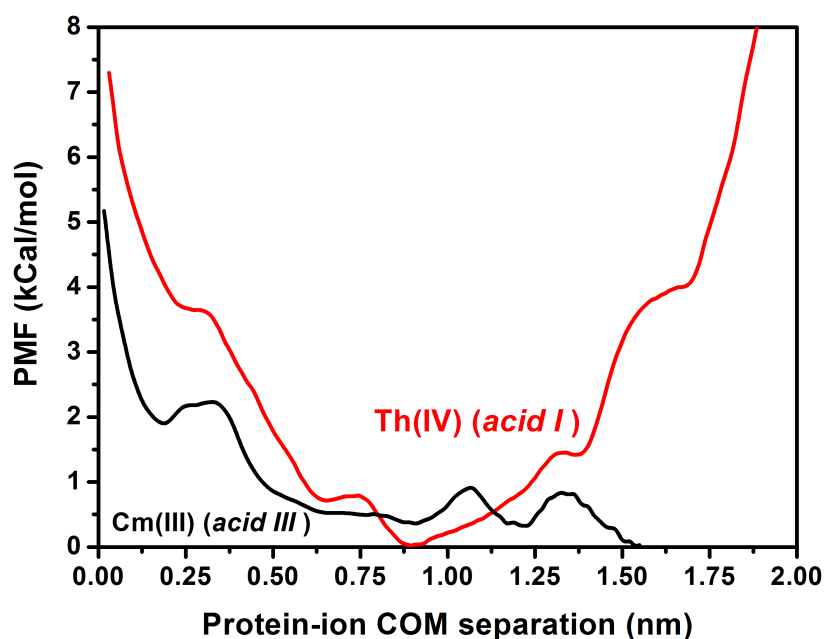


FIGURE 6.11: PMF profiles of An ions' unbinding transitions from the sTf protein as obtained through US runs. Red line represents PMF for Th(IV) unbinding in *acid I*, while black line represents Cm(III) unbinding in *acid III* protonation state of the protein. The US simulations were performed along the COM separation coordinate between the protein and the An ions (*cf.* equilibrium MD results in Figure 6.7).

that can bind dietary iron can also bind An ions with the help of bicarbonate ion at serum pH. Transport of a metal by the blood serum is finally destined to be delivered to cells through receptor mediated endocytosis at the acidic pH. What we found in this work is that while the trivalent curium, like iron, can be released into cells, the tetravalent thorium cannot. Stability of Th(IV)-sTf complex may attenuate its cytotoxic property in which both bicarbonate and D63 residue play critical role towards the tetravalent ion's speciation in serum. This may also open up the possibility of future design of radioactive tracer compounds based on tetravalent radionuclides.

In order to further substantiate that Th(IV) facilitates opening of the protein at the acidic endosomal pH yet it remained attached to the protein interior, we have evaluated its binding energetics (PMF) by US simulation. We have chosen two reaction

coordinates (RC), one that signifies the conformational changes of the protein, as measured by the COM separation between NI and NII sub-domains (Figure 6.10). And the other is the COM separation between the protein and the An ions (Figure 6.11). In the determination of a PMF using the US technique, the starting conformation of the system used at each umbrella window is key because the conformational sampling may be inadequate in cases where the free energy surface is complex and contains multiple wells. Usually these starting structures are generated from non-equilibrium techniques, such as, steered MD (SMD),²²¹ metadynamics (MtD)²²² or other suitable sampling methods. In SMD in order to perform pulling simulations, the RC is need to be known a priori. MtD on the other hand can be regarded as an efficient path sampling method. Once the reaction pathway is identified, the PMF along it can then be calculated using US simulations. MtD, however, makes the technique susceptible to errors introduced by the Gaussian bias deposition protocol along the user chosen set of collective variables. Fortunately, in the present work, by virtue of the acidic endosomal pH medium, the identification of the aforementioned two RC is a natural outcome of the 100 ns equilibrium MD simulations. As a result, the use of non-equilibrium techniques in search of RC could be avoided. In other words, the two RC in the present work can be regarded to correctly represent the problem of interest.

In Figure 6.10, the PMF profile for the opening of the protein in *acid III* protonation state is presented. In this protonation state maximum COM separation between NI and NII has been observed for both the An ions (*cf.* Figure 6.3). In the closed protein structure, when both the sub-domains are about 2.6 nm apart, a shallow minimum at about 1 kCal/mol for curium is observed. The separation increases thereafter and the PMF reaches a global minimum at around 3.05 nm. This can be considered to be the energetically most stable structure of Cm(III)-loaded sTf. Similarly, for Th(IV)-loaded sTf, the most stable structure is found when NI-NII COM separation is about 3.15 nm with a shallow minimum at 2.75 nm. Therefore, the US-discovered positions of PMF

minima along the NI-NII COM separation RC of the An-loaded sTf indicates preferable opening of the protein in the case for thorium compared to curium.

PMF for protein-ion COM separation is evaluated and presented in Figure 6.11. For thorium, *acid I* and for curium, *acid III* protonation state of sTf is considered. This is because at these conditions, An-sTf COM separations are found to be largest for the respective An ions (*cf.* Figure 6.7). The very complex nature of the An-sTf interacting system is quite evident in the figure. The large number of local minima (basins) and maxima (barriers) along the ion separation pathways are a manifestation of several influencing parameters, namely, structural fluctuations, electrostatic interactions, solvation, van der Waals, hydrogen bond (HB), and water bridge (WB) interactions. Th(IV), for example, with its higher ionic potential ($3.7 \text{ e}\text{\AA}^{-1}$) can be locally trapped in several binding pockets along the unbinding pathway. Whereas such a possibility for Cm(III) ion ($z/r = 2.7 \text{ e}\text{\AA}^{-1}$) can be seen to be rather less. Most stable structure for thorium is found when protein-ion COM separation is about 0.9 nm. Beyond this the tetravalent An ion faces huge barrier to exit from the protein interior. As discussed in detail above, this is mainly caused by the electrostatic pulling attraction of D63 residue in the first coordination shell of the cleft. Whereas in the case of curium, the discovered PMF tends towards zero when the trivalent ion reaches $> 1.5 \text{ nm}$ separation from the COM of sTf; large enough to be set free into the bulk.

6.4 CONCLUSIONS

The equilibrium MD simulations of actinide-loaded serum transferrin protein is performed in MFP/TIP3P water. In variation from nonpolarizable TIP3P water, its MFP version allows one mimic the dielectric heterogeneity of water in the protein interior, its surface and in the bulk. Thus, the data presented here can be considered to be physically more realistic. The results on varieties of protonation states of Cm(III)- and

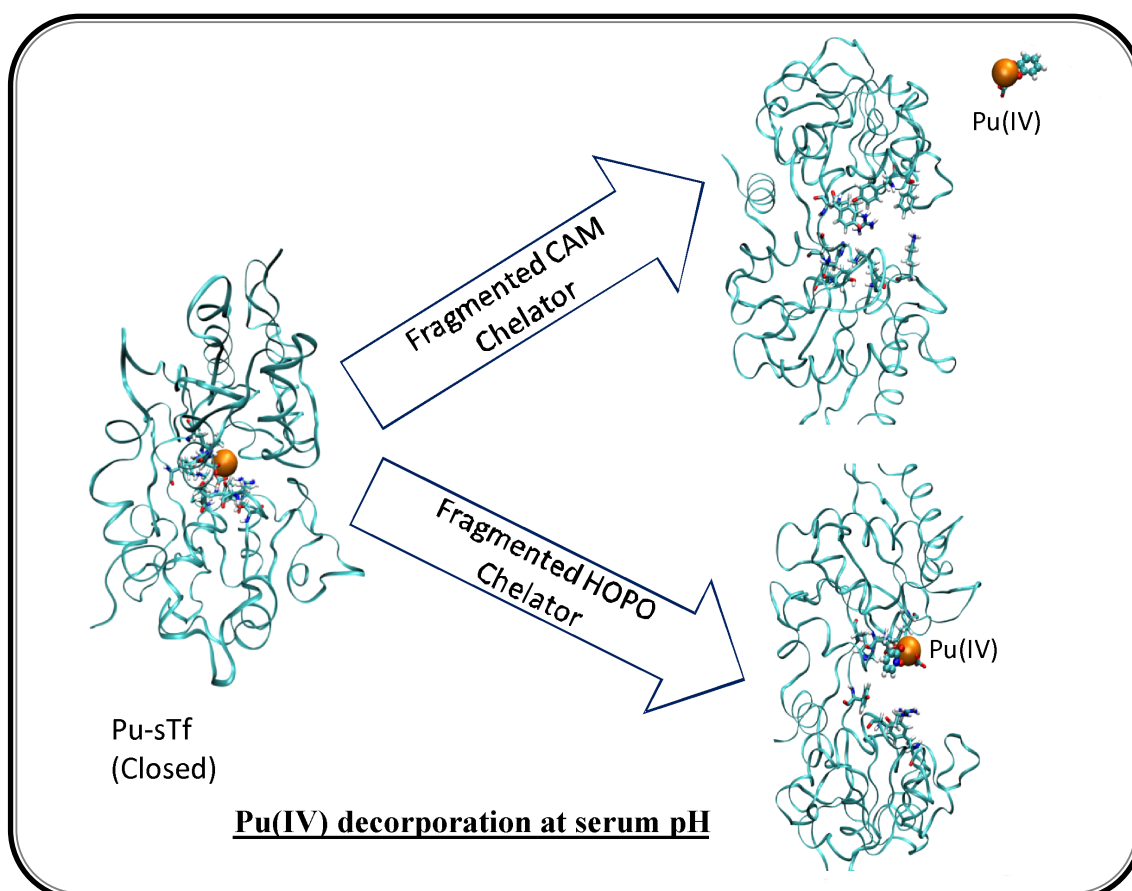
Th(IV)-loaded human transferrin at the acidic endosomal pH indicate that their structure and dynamics are widely different from each other. The presence of tetravalent An can trigger opening of the protein even without protonation of Y188 residue. Whereas, like the trivalent iron, protonation of Y188 is found to be an essential prerequisite for the protein to open up when bound to curium ion. Interestingly in none of the three protonation states of the sTf cleft, Th(IV) is seen to be set free from its binding influence. Combined influences of synergistic bicarbonate and aspartate residue D63 is seen to play major role during the speciation of the tetravalent An ion in the blood serum. Cm(III), on the other hand, like Fe(III) is seen to undergo complete release from sTf. This result may indicate that the risk of cytotoxicity due to Cm(III) is more than that due to Th(IV). Moreover, this property of Th(IV) may be utilized to design newer radio tracers containing tetravalent ion.

Findings of the present work are further supported by the evaluation of PMF of An ions' release. In this endeavour, both the determination of the reaction coordinates and subsequent US runs along these coordinates, the ergodicity is maintained throughout. This is because in both the steps, diffusive dynamics of the systems are maintained with a reasonable computational effort in the spirit of an equilibrium run. This work provides the molecular detail of An ions' interaction with sTf, which in future may prove to be useful for effective design of their decorporating therapeutics.

CHAPTER 7

In-silico Investigations for Pu(IV) Binding and its

Decorporation from sTf



HIGHLIGHTS

- **Transportation of Plutonium (Pu) to various organs/cells is mainly carried through serum transferrin (sTf), by receptor-mediated endocytosis. Understanding the Pu-sTf interaction is a primary step toward future design of its decorporating agents.**
- **In this chapter MD simulations of Pu(IV) binding with sTf are reported and its decorporation is investigated at extracellular pH using suitable ligands in polarizable water environment at different protonation states of the protein.**
- **Results unravel that Pu(IV) is bound to sTf binds in closed conformation at extracellular serum pH with carbonate as synergistic anions, and change in protonation state of dilysine (K206 and K296)-trigger and carbonate ion at endosomal pH induces conformational changes in protein, conducive for the heavy ion to be released, however strong electrostatic interaction between D63 and Pu(IV) does not allow the ion to be free.**
- **In an endeavour to decorporate Pu(IV), fragmented molecular form of hydroxypyridinone (HOPO) and catecholamide (CAM) based ligands are docked at the binding site (BS) of the protein and metadynamics simulations are conducted.**
- **Pu(IV) binding at BS is found to be so strong that it is not detached from BS with the docked HOPO. However, for the identical set of simulation parameters, CAM is found to facilitate dislodging the heavy ion from the protein's binding influence. Differential behaviour of the two chelators are further explored.**

7.1 INTRODUCTION

This chapter is aimed at computational study on the serum transferrin (sTf) loaded with Pu(IV), one of the most important radionuclides in nuclear fuel cycle program. First, binding of this ion with sTf is investigated for various protonation states at serum and endosomal pH conditions and then its decorporation from the binding pocket of the protein is explored with and without chelating ligands.

In civilian energy production, plutonium (Pu) is generated as a by-product of the processes that are based primarily on uranium fission. While plutonium can be introduced into the environment via accidents at nuclear facilities, trace amount of plutonium is also found in the environment as is evidenced in natural nuclear reactors and its nuclear waste products in an underground uranium deposit at Oklo (Gabon, Africa).²²³ World wide production of plutonium is also increasing due to the increase in number of running nuclear reactors to meet up the never ending energy demand. There are very stringent industrial safety measures both in the front- and in the back-end processes of the nuclear fuel cycle program, yet risk of internal contamination due to plutonium cannot be ruled out.^{61,81} The need for therapies to isolate inhaled, ingested or injected Pu or other actinides was previously considered an issue solely of concern for trained radiation workers, but the potential for radioactive exposure of actinides to members of the public as the result of an accidental release or an intentional dissemination caused by sabotage exists, unfortunately.²²⁴ Pu isotopes, unlike some other heavy metals, have no known essential role in the normal biochemical reactions occurring in living organisms. Upon entering human body they are absorbed by blood and transported to various organ cells (*viz.* liver, skeleton etc.) mainly through iron carrier serum transferrin (sTf) protein.^{13,18,168,225} Most of the isotopes of Pu, especially ²³⁸Pu, ²³⁹Pu, ²⁴⁰Pu, ²⁴²Pu are mainly α emitters and are highly radiotoxic¹⁶⁶ due to their high linear energy transfer to the tissues. Interaction of Pu with various biomolecules present in the blood serum is obscure as studies are limited due to its radioactive nature.

Such biochemical knowledge, especially interaction with sTf becomes essential for understanding sTf mediated transport of Pu to various cells and for the design of safe and efficacious therapeutic methods, accelerating their slow natural rate of elimination from human body.

sTf is an important member of the homologous iron-binding glycoproteins family, which is responsible for control of iron level in the body. Dietary iron in human body is delivered to cells by sTf through a process of receptor mediated endocytosis. sTf protein is present at a concentration of approximately 3mg/ml in human serum and is about 30 % saturated with Fe (III). While this renders the blood serum accessible for certain therapeutic metal ions to bind and transport, it also become vulnerable for other toxic metals to follow the major iron acquisition pathway.^{12–15} About 30 other metal ions, including Pu(IV) are found to make complexes with sTf.¹⁶

sTf (molecular mass 80 kDa) is a single-chain polypeptide of 679 amino acid

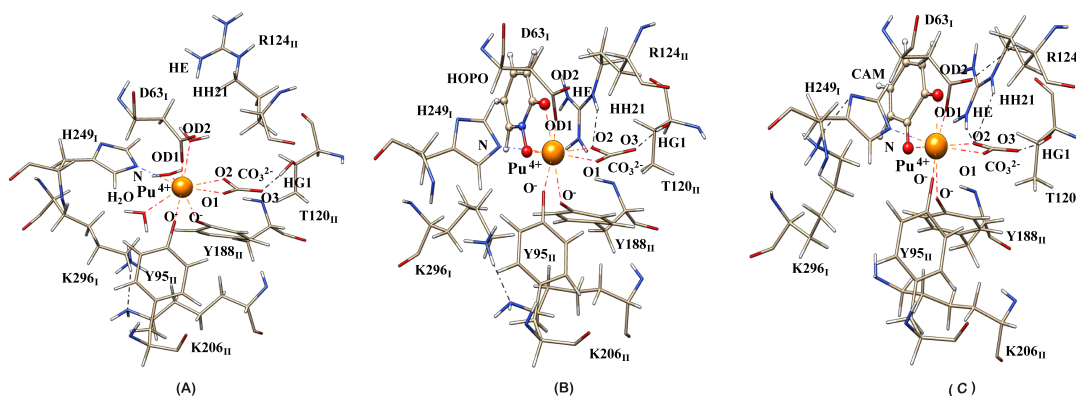


FIGURE 7.1: Schematic view of the binding-cleft of Pu(IV)-bound human serum transferrin at serum pH are presented (A) without ligand, and with the fragmented (B) HOPO, and (C) CAM ligands. The suffixes I and II in the residue labels point to the sub-domains I and II of the N-lobe of the protein that they belong to.

residues that forms a bilobal structure, to be known as N- and C-lobes respectively. Each lobe can capture one iron ion at the binding site, formed by the inter-domain cleft due to the two respective sub-domains, NI, NII and CI, CII of the lobes. In each lobe, two

sub-domains are connected by a hinge consisting of two anti parallel β -strands, which form a cleft where the metal ion can bind. In particular, NI sub-domain (residue number 1 to 91 and 245 to 313) is connected to NII sub-domain (residue number 92 to 244) by a hinge consisting of two extended anti parallel β -strands (residues 91-101 and 241-252) that forms the binding cleft for the metal ion.¹¹⁴ At physiological (*phy*) serum pH, Fe(III) at the binding cleft makes coordinate bonds with phenolate oxygen atoms of two tyrosine residues (Y95 and Y188), one carboxylate oxygen atom of aspartate (D63) and one imidazolate nitrogen atom of histidine (H249).¹³⁷ Octahedral shape of the first coordination shell of the binding cleft is completed with the participation of a bidentate synergistic carbonate anion. Recently we have observed similar binding pattern of Cm(III) and Th(IV) with the sTf binding cleft.^{165,226} Besides carbonate, other synergistic anions, such as citrate is reported to coordinate with non-iron metal ion, Ti(IV).¹⁶⁹ A large number of inorganic anions those can bind with sTf are recently reviewed.¹⁷⁰ Molecular dynamics (MD) simulation of the effects of synergistic and non-synergistic anions on the iron binding cleft are also reported.¹⁷¹ In the immediate vicinity of the binding cleft, the second coordination shell is comprised of residues threonine T120, arginine R124 and two lysines K206, and K296 (see Figure 7.1).

Experimental studies focusing on the interactions of transferrin with Pu(IV) and other actinide (An) ions can be found in the literature.^{14,18,19,23–25,126,166,225,227} For example, capillary electrophoresis coupled with an inductively coupled plasma mass spectrometer is applied for the first time to determine the binding constant of human transferrin (Tf) with Pu(IV).¹²⁶ In another study by Duffield *et al.*, binding of Pu to human apo-transferrin and to rat serum was investigated following delivery of the metal to the protein.²²⁸ It is observed from these experimental studies that Pu(IV) binds with sTf and also their coordination with the binding site (BS) of sTf is different from that of the native iron ion. Although huge amount of information are available for transferrin to bind and transport non-iron metal ions,¹⁴ molecular-level specific information are rather

scarce.^{165,226} To the best of our knowledge crystal structures of Pu-loaded sTf are not yet available. Similarly, how synergistic carbonate ion work in tandem with sTf to bind Pu(IV) is an unexplored area. Also as is well known, the transferrin molecule undergoes a significant conformational change during the release of metal ions: from closed (metal-loaded at physiological serum pH) to open (upon binding to transferrin receptor at the endosomal pH).¹³⁷ How sTf, while bound to Pu(IV), will respond to the acidic endosomal pH (pH=5.5) condition remained hitherto unexplored. Whereas this is an important issue to be probed at the molecular level since it relates to the biological fate of Pu trafficking in human body through sTf. A combination of density functional theory (DFT) and MD simulation is a very attractive avenue towards unravelling molecular details of metal-sTf binding.^{28,29,165} Recently we have carried out DFT studies on the structures and spin Hamiltonian parameters of iron transferrin using isolated and embedded clusters models.¹⁰⁹ Although few DFT studies on sTf complexes with metal ions, especially Fe(III), $V^{IV}O^{2+}$, UO_2^{2+} are found in the literature,^{122,138,172} An-sTf complexes are not much explored with MD, DFT or similar other tools.

Previously, at serum pH (pH=7.4) we have observed that in association with carbonate ion, Th (IV) binds in octa-dentate mode while Cm (III) prefers a hepta-dentate mode of coordination in the sTf binding cleft.¹⁶⁵ From well-tempered metadynamics (WtMetaD) discovered potential of mean force (PMF) values, we have further found the relative order of stability of sTf complexes with Fe (III), Th (IV) and Cm (III) ions to follow the same trend as are observed in experiments.¹⁶⁵ Mujika *et al.*¹³⁷ have investigated the release of metal from an Fe(III)- and Al(III)-loaded N-lobe of sTf by MD simulations. They have observed that the protonation of Y188 is indispensable for prompting the conformational change of the protein and release of metal ion from the protein. In another work we have used equilibrium MD simulations for understanding the detachment mechanism of Cm(III) and Th(IV) from the binding cleft of sTf at the endosomal acidic pH condition.²²⁶ We have observed that presence of tetravalent Th(IV)

can trigger opening of the protein even without protonation of Y188 residue. Whereas, like the trivalent iron, protonation of Y188 is found to be an essential prerequisite for the protein to open up when bound to curium ion. Interestingly in none of the three protonation states of the sTf cleft investigated, Th(IV) is seen to be set free from its binding influence. Enabled with this background information on An-sTf interactions, here we set out to investigate the decorporation of one of the most toxic An ion in nuclear fuel cycle, Pu(IV) from sTf binding cleft at serum pH with two plausible chelator ligands, fragmented form of hydroxypyridinone (HOPO) and catecholamide (CAM) molecules. Relaxed configurations of the Pu(IV)-sTf binding cleft with and without the ligands at serum pH are shown in Figure 7.1. We found that while CAM based chelator could be an effective decorporating agent for Pu(IV), HOPO-based chelator is not, although their chemical skeleton differs from one another with respect one single nitrogen atom, to be found in HOPO. We also investigate in detail the binding features of Pu(IV) with three protonation states of the sTf cleft at endosomal pH. Relaxed equilibrium configurations of the Pu(IV)-bound sTf cleft at this pH are given in Figure 7.2.

Polarization and charge-transfer effects are supposed to be important for interactions between protein and charged metal ions (+4 in the present case) while carrying out classical MD simulations for charged metalloproteins.¹⁸³ Indeed metal binding sites are usually located inside solvent inaccessible protein cavities and clefts, characterized by a low dielectric constant. In order to bring in the dielectric heterogeneity of the medium^{184,185} and treat the highly charged An ions' binding with the protein interior, here we have adopted the effective polarization in polarizable water model in an otherwise standard nonpolarizable force field model system that has been successfully applied in other occasions.^{186,187} In the present study several 100 ns equilibrium MD simulations are performed for the sTf complex with Pu (IV) for each of the four different protonation states of the protein. Hydrogen bond (HB) and water

molecule N-lobe of sTf (PDB ID: 1A8E) as the starting configuration for all calculations.

Protonation states of the amino acids in the BS (*cf.* Figure 7.1) at the serum and endosomal pH are determined by evaluating their pKa values.¹⁸² Four different starting structures: (1) *phys*, (2) *acid I*, (3) *acid II*, and (4) *acid III* are accordingly chosen, which differ from one another with respect to the protonation states of the residues in the first and second coordination shells of the central metal ion. In the *phys* structure, Y95 and Y188 are in phenolate form, H249 is in doubly deprotonated imidazolate form, while all other histidines are protonated following Mujika *et al.*¹³⁷ In *acid I* state carbonate is protonated to bicarbonate, H249 is in the neutral form. While all other residues in the first coordination shell are similar to that in *phys* structure, both K 206 and K296 in the second coordination shell are protonated. Protonation state of *acid II* structure is different from that in *acid I* state in the sense that Y188 is protonated and K296 is in the neutral form. Similarly in *acid III* structure, protonation of all residues are similar to that in *acid II* except that protonation states of K206 and K296 are interchanged.

7.2.1 Docking of ligands at the binding cleft of sTf

Autodock is used to produce initial coordinates of the Pu-sTf-ligand complexes.²³⁰ Different conformations are generated by employing the Lamarckian genetic algorithm (LGA). The energy-based autodock scoring function is used to find the possible BS of the HOPO and CAM ligands. The scoring function is composed of parameters like, electrostatic interaction, solvation and loss of entropy due to drug binding, short-range van der Waals and HB interactions. Region around the binding cleft of the sTf protein is considered for docking. The grid size of $60 \times 60 \times 60$ along the x, y, and z axes, respectively, with a grid spacing of 0.375 Å is used to find the possible BS of the ligands. The maximum number of energy evaluation is set to 2.5×10^6 in the LGA run. Root-mean-square (with 0.2 nm tolerance) clustering is carried out on the resulting conformers of the Pu-sTf-ligand complexes. The resulting conformers are then ranked

according to their energy values. The lowest-energy conformer of the Pu-sTf-ligand complex is then used as a docked structure for subsequent MD simulations. A relaxed conformation of the docked complex is shown in Figure 7.1.

7.2.2 Equilibrium molecular dynamics

All MD simulations are performed using Gromacs-4.0.7 suite of programme.¹⁸⁸ Details of the MD simulation protocol is described in the fifth chapter of the thesis and also can be found elsewhere.^{165,226} Amber force field parameters for deprotonated tyrosine, doubly deprotonated histidine, synergistic carbonate and bicarbonate anions and chelating agents are evaluated using python based acpype script with antechamber package¹⁹⁰⁻¹⁹² as these are not available in the force field library. Charges of these residues are calculated using GAMESS¹⁹³ and Restrained Electrostatic Potential (RSEP)¹⁹⁴ tools. The non-bonded parameters of Pu (IV) are taken from literature.¹⁹⁵

7.2.3 Hydrogen bond and water bridge dynamics

Hydrogen bond (HB) between amino acid residues and water bridge (WB), formed by a water molecule using two of its hydrogen atoms simultaneously to form HB with ligand/protein residues are calculated based on geometric criteria. HB and WB time-correlation functions elucidate the protein-protein and protein-water interaction dynamics. Methodology to calculate these correlation functions is described in the first chapter.

7.2.4 Well-tempered metadynamics

All metadynamics simulations are conducted with Gromacs-4.0.7,¹⁸⁸ patched with Plumed 1.2.²⁰¹ The well-tempered metadynamics parameters used in these simulations are similar

as given in the fifth chapter.

7.3 RESULTS AND DISCUSSION

7.3.1 Binding of Pu(IV) with human serum transferrin

7.3.1.1 Binding without ligand

Structures. Equilibrium MD simulations are performed for Pu(IV) loaded sTf system at each of the four protonation states of the protein's binding cleft. In order to deal with highly charged ions ($z \gg 1$), where electronic polarizability of the medium is known to play very important role on the fate of the captured ions, we have conducted the simulations in an effective polarizable environment. This ensures a more realistic picture of the varying dipole moment of water from protein binding shell to its exterior to emerge, while working with otherwise standard nonpolarizable force field models.^{184,185} Figure 7.1(A) shows a schematic configuration of the Pu(IV)-bound ligand-free sTf cleft at serum pH. Similar structures for the three acidic states at endosomal pH can be seen in Figure 7.2. At serum pH, an MD simulated relaxed state show Pu(IV) making coordinate bonds with oxygen atoms of D63, Y95, and Y188, NE2 atom of the H249 in imidazolate form, and the two oxygen atoms of the bidentate CO_3^{2-} . Also 2-3 water molecules are seen to enter the first shell BS of Pu(IV) making up its usual 8-9 coordination. In the second coordination shell, T120 and R124 are found to making HBs with the synergistic carbonate ion, while K206 and K296 are hydrogen bonded to form the di-lysine bridge. In all the three protonation states at endosomal pH, on the other hand, Pu(IV) is initially found to be in hexa-coordinated mode. During the equilibrium MD simulations, the residues Y95, Y188, H249 and HCO_3^- , except D63 are seen to push apart and the BS gets somewhat distorted. This allows water molecules to penetrate, once again making up the 8-9 coordination of the bound Pu(IV). Calculations of radial distribution function (RDF)

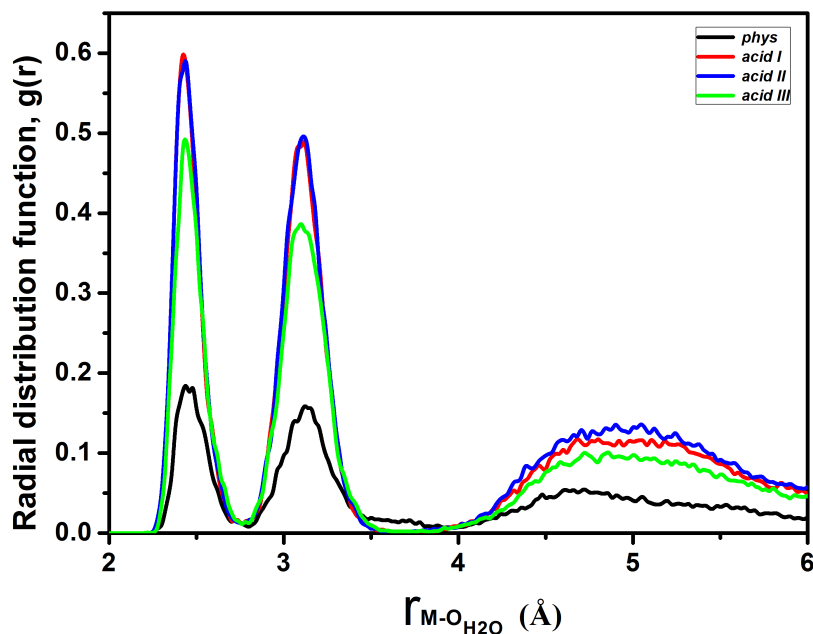


FIGURE 7.3: Water penetration into the ligand-free protein's binding cleft. Radial distribution function, $g_{M-O_{H_2O}}(r)$, of water around the Pu(IV) ion during the 100 ns simulation for various protonation states of the protein, as indicated: *phys* at serum pH (black), and at acidic endosomal pH *acid I* (red), *acid II* (blue), and *acid III* (green), are shown. Opening up of the protein in *acid I* protonation state can be seen to be most prominent.

of water around the central metal ion, $g_{M-O_{H_2O}}(r)$ shown in Figure 7.3 reaffirms the differential water penetration pattern in the four protonation states of sTf cleft. At serum pH, RDF of metal-water exhibits very small peaks at 2.5 Å and at 3.3 Å, the radius of the first and second coordination shells of the cleft, respectively. In contrast, in all three acidic protonation states, the peak intensity is seen to be increased and maximum height of the peaks is observed for *acid I* structure, where around 12 water molecules are calculated to be present up to a distance of 3.5 Å. Similarly, in *acid II* and *acid III* structures, around eight water molecules are present in the binding cleft.

The temporal evolution of the deviation of Pu(IV)-sTf structures from their initial starting structures are assessed on the basis of root-mean-square deviation (RMSD) of

TABLE 7.1: Mean and standard deviations of bond lengths (Å) of the metal ions ligated with atoms of the residues in the first coordination shell as calculated from MD simulations

Pu(IV) _{protonation state}	M-OD1 _{D63}	M-OD2 _{D63}	M-O1 _{CO₃}	M-O2 _{CO₃}	M-N _{H249}	M-O _{V95}	M-O _{V188}	MBS ^a	NI-NII ^b
Pu(IV) _{phys}	2.37±0.06	4.46±0.09	2.31±0.05	2.34±0.06	2.58±0.09	2.39±0.07	2.43±0.07	1.31±0.11	26.59±0.29
Pu(IV) _{acid I}	4.18±0.23	2.30±0.05	25.51±15.62	25.65±15.56	5.77±0.75	8.59±2.62	9.24±2.62	6.86±2.29	30.92±1.24
Pu(IV) _{acid II}	4.13±0.21	2.30±0.05	23.16±16.28	23.15±16.36	6.99±0.93	11.21±2.00	11.47±2.34	9.34±2.35	31.25±1.11
Pu(IV) _{acid III}	4.00±0.32	2.31±0.05	13.84±10.19	13.81±10.21	5.16±0.52	10.63±2.17	14.07±2.55	8.51±2.02	31.11±1.11
Pu(IV) _{HOPO}	2.31±0.05	4.43±0.08	2.30±0.05	2.31±0.05	2.55±0.08	2.38±0.05	2.39±0.06	1.16±0.07	26.37±0.16
Pu(IV) _{CAM}	2.34±0.05	4.46±0.08	2.33±0.06	2.30±0.05	2.54±0.08	2.42±0.05	2.40±0.06	1.19±0.08	26.08±0.16

^a COM separation between metal ions and the residues in the first coordination shell of the metal binding site (MBS)

^b COM separation between residues in NI and NII sub-domains NI-NII

their backbone (C_α) atoms. As mentioned earlier, the initial structures are prepared by the replacement of ferric ion in an equilibrated Fe(III)-sTf structure with Pu(IV) ion. The time dependence of RMSD can be found in Figure 7.4. It can be seen in the Figure that at physiological serum pH (*phys*; black line), deviations of C_α atoms are within 2 Å and that they appear to be stabilized within 2 ns. This observation is a clear indication of convergence of the metal-protein systems. In acidic conditions, however, deviations between backbone (C_α) atoms goes up to 7 Å for all the three (*acid I*, *acid II*, and *acid III*) protonation states. The results are a signature of significant structural rearrangements of the protein at the acidic endosomal pH. In order to substantiate this finding, the compactness of the structures are measured by radius of gyration: $R_g = \sqrt{\sum_i (||\mathbf{r}_i||^2 m_i) / \sum_i m_i}$, where m_i is the mass of the heavy atom i and \mathbf{r}_i is the position of atom i with respect to COM of the molecule. Temporal profile of R_g is shown in the lower panel of Figure 7.4 for all the structures. Clearly the data corroborates well with the RMSD profiles: Pu-sTf protein is less compact in acidic structures than in *phys* structure.

In order to investigate further on the differences between structures of the BS at serum and endosomal pH, we have carried out detailed structural analysis. Namely, the mean and standard deviation of the distances between metal and ligating atoms of the residues in the first coordination shell in all four protonation states are evaluated. From

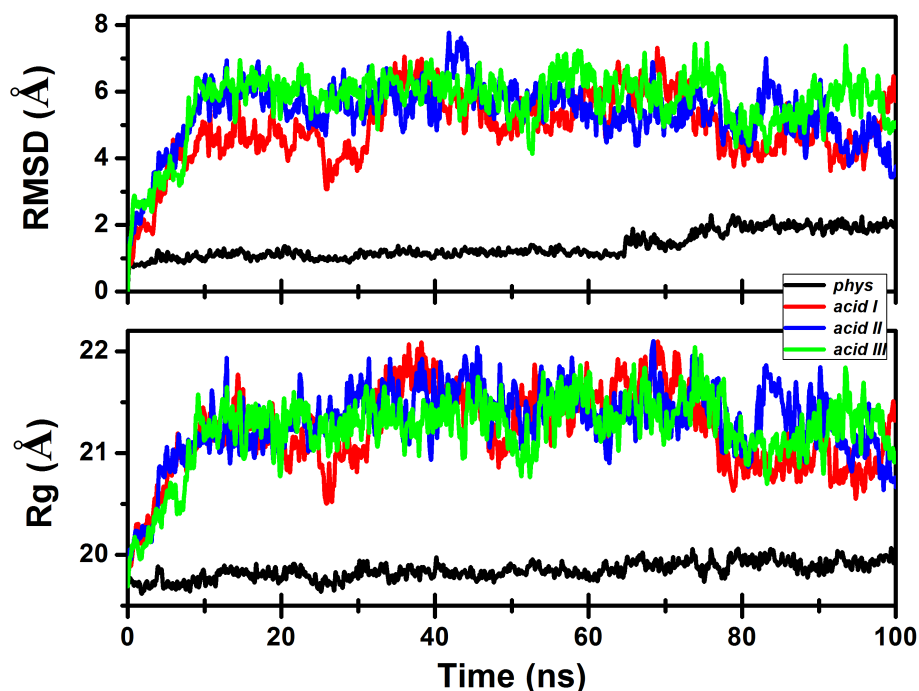


FIGURE 7.4: Time dependence of root mean square deviation (RMSD) of backbone C_{α} atoms (upper panel) and the radius of gyration, R_g of protein heavy atoms (lower panel) from the starting structure of the ligand-free and Pu(IV)-loaded serum transferrin during the 100 ns equilibrium MD simulation are shown at various protonation states of the protein binding-cleft. Colour legends are same as in Figure 7.3.

the data, presented in Table 7.1, one can find that all the residues are in a compact bound state at physiological serum pH, since metal-ligand bond lengths are always within 2.58 Å. Whereas in endosomal acidic conditions, ligating residue atoms, except O2_{D63}, go away from the binding cleft, distorting the bound state, which results in more deviation of the backbone atoms of protein. The coordination pattern of Pu(IV) that we observe here is very similar to our earlier work on tetravalent Th(IV).²²⁶ Notably, in *acid I* protonation state, the data reveals that Pu(IV) can be released from the influence of the binding cleft even without protonating Y188, which contradicts the observations for trivalent metals, found earlier.^{137,226}

Opening of the protein. Recently Mujika *et al.* have concluded from the principal component analysis of their equilibrium MD trajectory that the first major eigenvalue

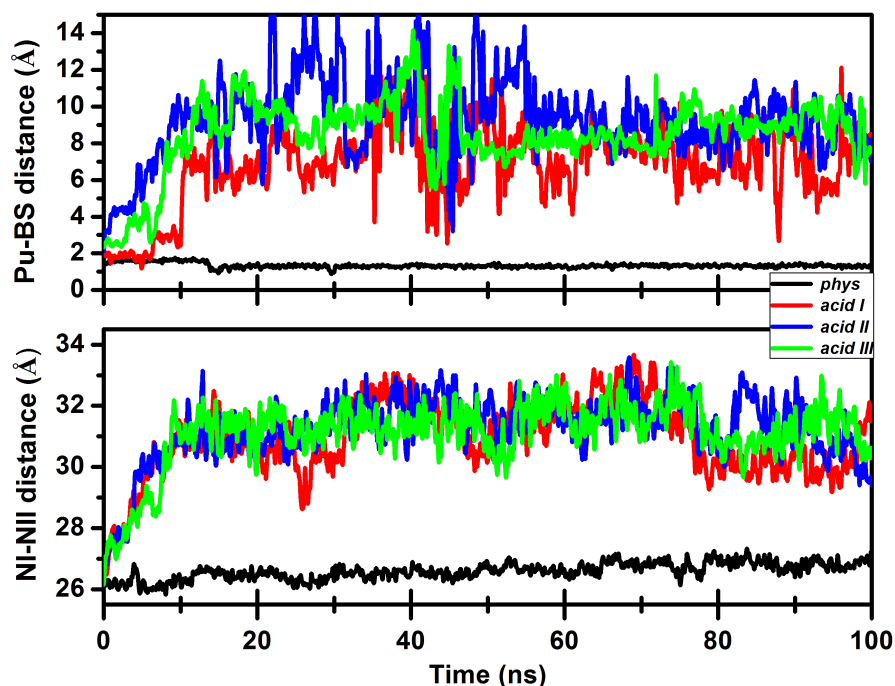


FIGURE 7.5: MD time evolution of distance between the tetravalent metal ion and centre of mass (COM) of residues in the binding site (BS) cleft (upper panel), and the COM separation between NI and NII sub-domains (lower panel) of the ligand-free and Pu(IV)-loaded sTf protein are shown at various protonation states of the cleft: *phys* at serum pH (black), and at acidic endosomal pH *acid I* (red), *acid II* (blue), and *acid III* (green).

can be associated with the bending motion of the hinge region.¹³⁷ Since NI and NII sub-domains are connected by the hinge region, this key global motion can also be attributed to their COM separation. The temporal profiles of NI-NII distance of ligand-free Pu-sTf systems in all the protonation states of the protein are shown in Figure 7.5. Opening of the two sub-domains at the acidic endosomal pH, which can facilitate the release of the captured ion, is evident in this figure. However, for *phys* structure at serum pH, the two sub-domains are practically closed till 100 ns. This result is also in accord with the observed RMSD deviations and R_g values (Figure 7.4). In view of the major structural changes at acidic endosomal pH, the separation of Pu(IV) from the COM of first shell residues of the cleft (see the upper panel of Figure 7.5) is monitored. At serum pH (structure, *phys*) Pu(IV) can be seen to be in the bound state with Pu-BS

distance always within 2Å, whereas in all three acidic structures (*acid I*, *acid II* and *acid III*) the central metal ion is clearly losing its coordination atmosphere in the first binding shell within 20 ns (c.f. Table 7.1). Although Pu(IV) is dislodged from the BS, we have noticed that the heavy ion is unable to completely unbind from the protein in any of the studied acidic states because of its strong electrostatic interaction with D63. Due to the high positive charge of the metal ion, its electrostatic interaction with the Lewis basic residues of the BS can be thought to dictate the final outcome of the unbinding event. We have monitored the Pu(IV)-BS and Pu-D63 electrostatic interactions in the *phys* and *acid I* protonation state and depicted in Figure 7.6. The interactions are always found to be attractive and Pu(IV)-BS interaction is found to reduce to that prevailing between Pu(IV) and D63 at ~ 80 ns in the *acid I* protonation state. This result implies that in *acid I* state the central ion is completely dislodged from the BS, however, its sticky electrostatic interaction with D63 holds it back in the protein periphery.

HB and WB dynamics. Further insight into the structural differences between the various protonation states can be gained from a simple consideration of charge distribution in the binding cleft. For example, in *acid I* state, residues in the first shell i.e., D63, Y95, Y188, and the bicarbonate ion are all unit negatively charged, while H249 is neutral. Thus the first shell of the Pu(IV)-bound cleft is electronically neutral. However, in the immediate second shell, each of the residues R124, K206 and K296 are unit positively charged, whereas T120 is neutral. The positively charged second shell residues will undergo repulsive interactions between themselves. This will render disrupting influences on the compact structure of the Pu(IV)-bound sTf cleft that eventually triggers the opening of the protein. In contrast, in the *phys* structure at serum pH, -5 charge (c.f. due to the bidentate carbonate ion in place of bicarbonate ion) of the first shell residues makes attractive electrostatic interaction with Pu(IV) ion, while repulsive interaction between the two lysine residues is absent. This would render a compact and efficient coordination sphere for the Pu(IV) ion. In the same vein, in *acid II*

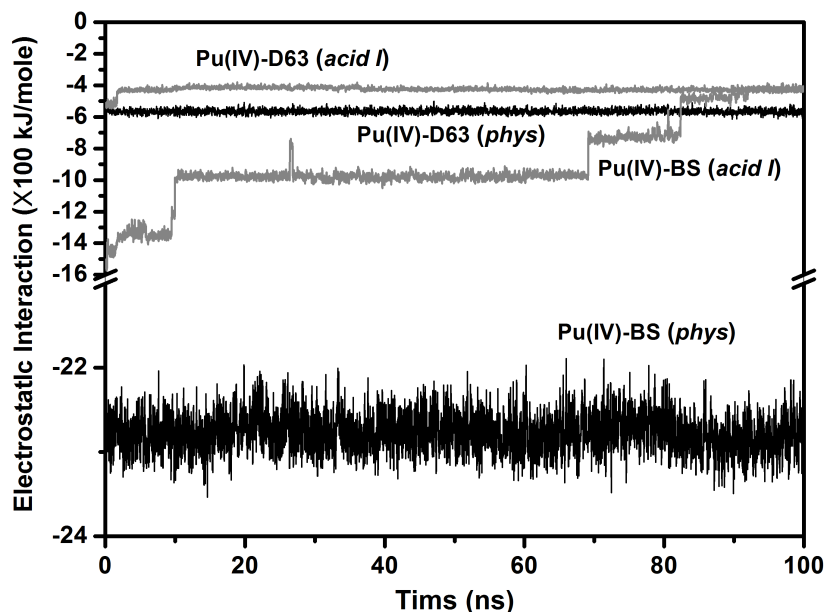


FIGURE 7.6: Time dependence of HB (Short-range electrostatic interaction energy of Pu(IV) with D63 and with the binding site (BS) residues of ligand-free sTf are plotted as a function of time in *phys* serum and *acid I* protonation states. Stronger electrostatic interaction as experienced by Pu(IV) both with BS and with D63 residue at *phys* protonation state compared with the *acid I* variant is evident. Note that in *acid I* state, Pu(IV)-BS interaction strength reduces to that prevailing between Pu(IV) and D63 at about 80 ns. However, interaction strengths are always seen to be attractive, which does not allow the An ion to completely come out of the protein interior, even though the protein opens up in *acid I* protonation state (*cf.* Figure 7.5) for the tetravalent ion to be released.

and *acid III* structures, protonation of the coordinating O atom of Y188 weakens its interaction with Pu(IV) ion. This in addition to repositioning of R124 residue in second shell, away from the bicarbonate ion, initiate the protein opening.¹³⁷ The complex nature of binding with respect to the variations in the protonation states can also be assessed from the inter-residue HB time correlation functions of the sTf cleft (see Figure 7.7). For example, repositioning of the second shell residue, like R124, in all the three acidic states allow it to form a strong HB (longer lifetime) with nearby residue, L122. Similarly, displacement of H249 and K296 at *acid I* state is quite remarkable as it allows them to form HB with Y85 and E83, respectively, both of which survives even beyond 10 ns.

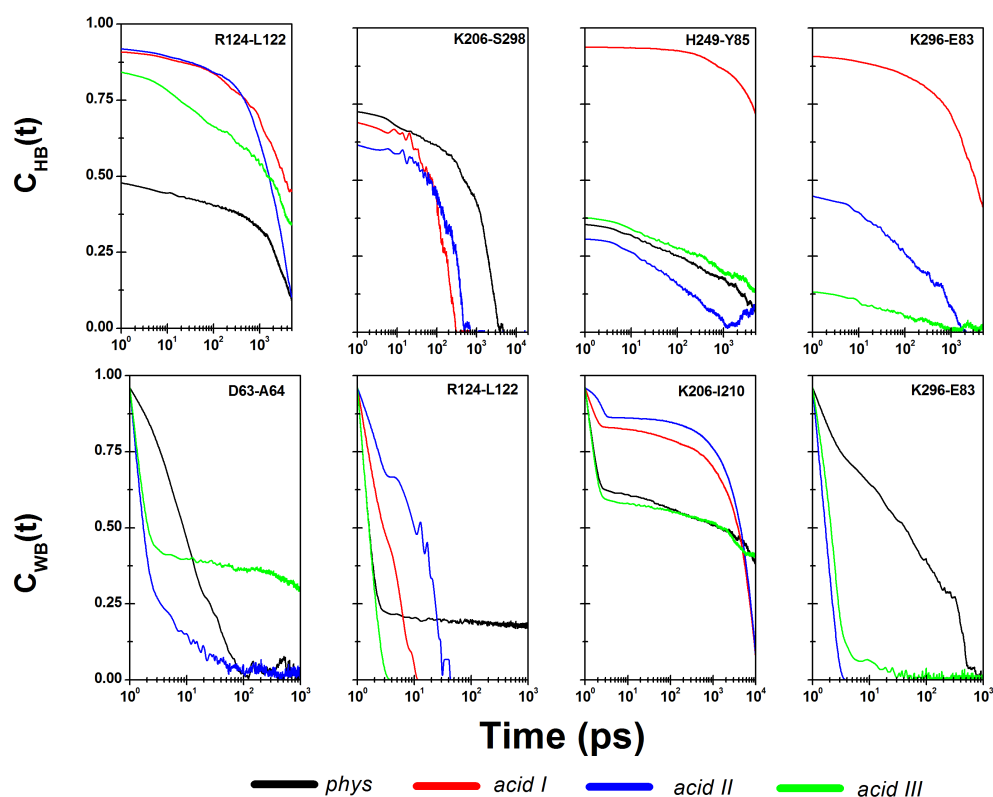


FIGURE 7.7: Time dependence of HB (upper panel) and WB (lower panel) lifetime correlation functions between residues of ligand-free sTf, bound to the tetravalent ion, are shown in all the four protonation states of the protein. Results for D-A pairs (as indicated) which are extensively engaged in HB and WB formation in polarizable water medium are presented. Colour legends, as indicated are same as in Figure 7.5.

In aqueous medium, water plays crucial role on the binding event by forming WB in place of a broken inter-residue HB. In other words, water can be considered to act as lubricant facilitating opening of the protein.^{219,220} The complex nature of the repositioning of binding cleft residues with respect to their protonation states is again evident from their WB dynamics (see bottom panel Figure 7.7). Note that at serum pH, as discussed, even though the protein maintains its closed configuration throughout the production run, a couple of water molecules enters the binding cleft during the equilibration step in order to satisfy central ion's coordination. The WB data at serum pH involves these cleft water molecules. At acidic endosomal pH condition, on the other

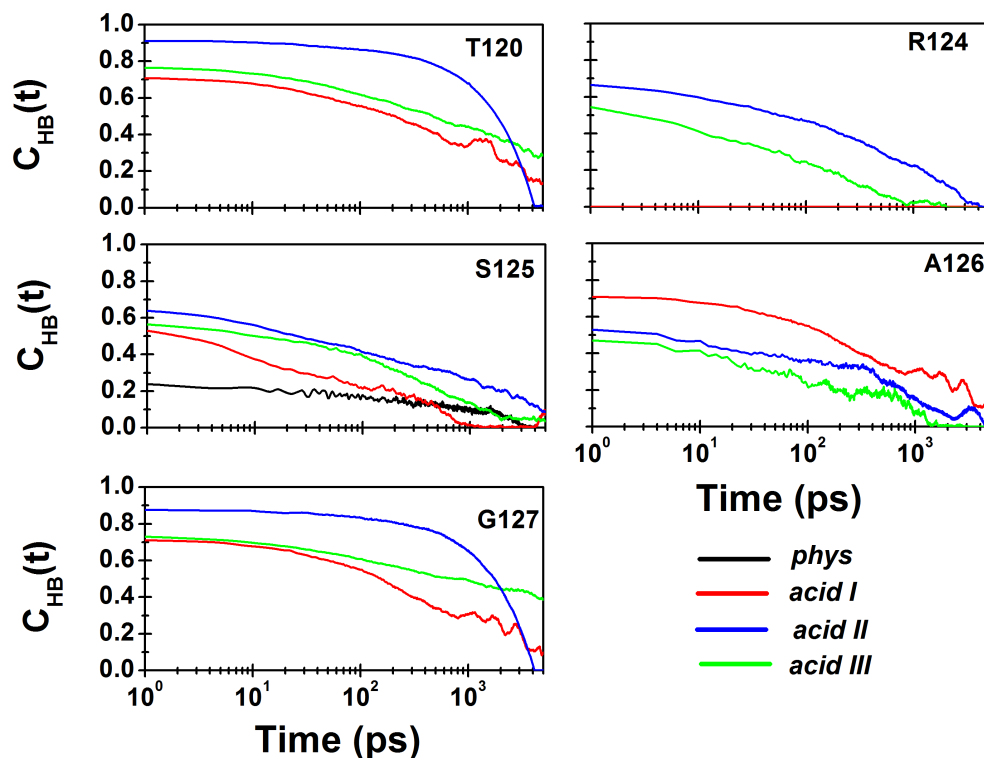


FIGURE 7.8: Time dependence of HB lifetime correlation functions between residues of sTf which are extensively engaged in HB formation with the synergistic ion (carbonate and bicarbonate) are shown for ligand-free Pu(IV)-sTf bound system at all four protonation states of the protein. Colour legends used are as mentioned.

hand, the protein opens up to allow the water molecules to enter and leave the binding cleft during receptor-mediated endocytosis. Opening of the protein is also reflected in the extensive nature of HB between the synergistic bicarbonate ion with protein residues at acidic endosomal pH as shown in Figure 7.8. Put in other words, at all the three acidic structures, the close and compact coordination of the bicarbonate ion with central heavy ion is weakened. It is worthwhile to mention that, the interior of the protein is quite hydrophobic in contrast to the hydrophilic surface.^{186,213–217} Gao *et al.* have observed that the breaking of HB in the hydrophobic environment requires 1.2 kcal/mol more energy with respect to hydrophilic.²¹⁸ Our treatment of TIP3P water at the MFP level ensures a realistic treatment of the dielectric heterogeneity in the protein

medium.^{184,186,187} Thus the data presented here for HB and WB dynamics, which together controls the fate of a captured metal ion can be considered to reflect this assessment.

7.3.1.2 Binding with ligand

Ligand docked structures. Any effort towards the lead compound discovery for the decorporation of An ions from sTf protein should be aimed at physiological serum pH, before the receptor mediated endocytosis could begin. This is because inside the cell their presence can cause highly undesirable radiolytic events. Plutonium, for example, has very high linear energy transfer capacity for its α emission feature. In this endeavour we have identified two plausible chelators, HOPO and CAM. Hereafter, we will focus on their binding at the Pu(IV)-loaded sTf cleft and will explore their suitability as Pu(IV) decorporating agents through the calculations of unbinding PMF at *phys* serum pH.

Linear hydroxypyridinone (LI-HOPO), especially 3,4,3-(LI-1,2- HOPO) and linear catecholamide (CAM) *viz.*, 3,4,3-LICAM and its derivatives are promising candidates for actinide chelation and are being used in in-vitro studies and as well as in animal studies.^{228,231-240} These ligands, are generally multi-dentate chelators, composed of a spermine backbone coupled with four HOPO or CAM groups for metal binding. These ring-like structures are found to bind metal ions in aqueous medium or free metal ions present in the blood serum. However, these chelators due to their incommensurate size and shape cannot reach the interior of sTf protein. Fortunately, there are evidences that suggest when large sized drug compounds are injected/ingested, they are broken into small fragments and these small fragments are found to bind with protein interior in place of whole large compound.^{241,242} Details on DFT calculations of the ion exchange [Fe(III) \rightarrow Pu(IV)] energetics by the full sized ligands in absence and also in presence of the binding influence of a truncated sTf (cleft) are given in subsequent sections of this chapter. In view of their incommensurate sizes, we have first docked one single CAM and HOPO group at the binding cleft of Pu-sTf at serum pH and subsequently using

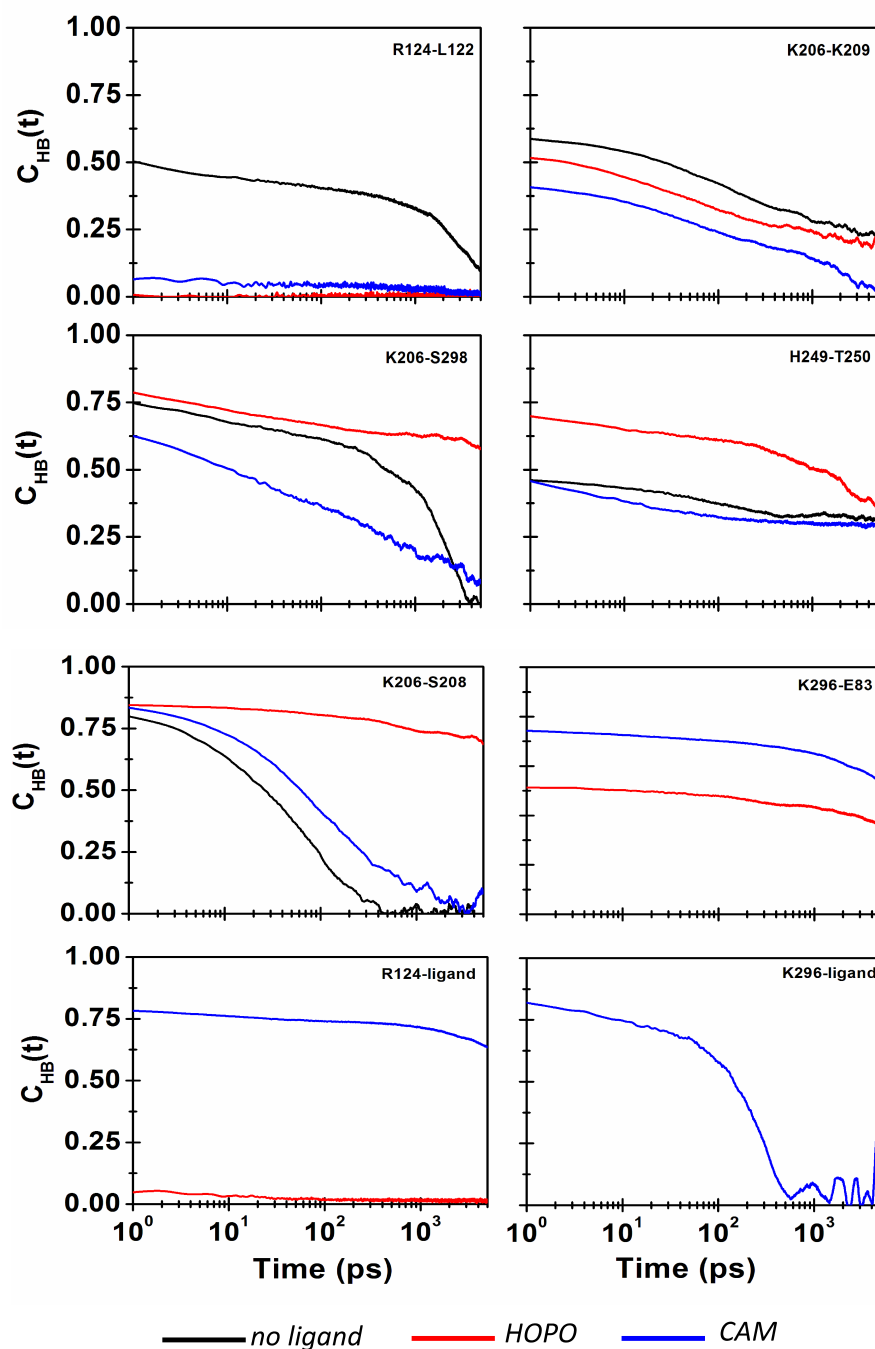


FIGURE 7.9: Time dependence of HB lifetime correlation functions between residues of sTf which are extensively engaged in HB formation between themselves and with the ligand molecules are shown for Pu(IV)-sTf bound system at *phys* serum pH. The results are presented without (black lines) and with ligands (red lines: HOPO, blue lines: CAM). HB formation pattern in presence of the two ligand molecules can be seen to be strikingly different from each other. HB formation between all possible D-A pairs are considered in polarizable water.

these docked configurations as initial structures, we have performed equilibrium MD simulations for 100 ns each to explore their binding behaviour at the Pu(IV)-sTf cleft. We have found that these ligands are bound to the Pu(IV)-sTf cleft while the protein maintains its closed conformation. Moreover, both the chelator ligands are found to coordinate in bidentate mode, thus making octa-coordination for Pu(IV) in the initial structure (see Figure 7.1 (B) and (C)). Other residues in the first- and second coordination shells are present in the same binding mode as they are in absence of any ligand at serum pH. We have also observed that after 100 ns simulations, water does not penetrate into the first coordination shell (in contrast to the case of ligand-free binding) to fulfil the coordination requirement of central heavy ion. Mean and standard deviations of various bond lengths at the binding cleft are provided in the last two rows of Table-7.1, which are to be compared with the listings for Pu(IV)_{phys}. It can be seen in the table that the values closely resemble each other. Most importantly, NI and NII sub-domains are at a mean distance of about 26 Å, indicating closed conformation of the Pu(IV)- and chelator-loaded protein.

HB and WB dynamics. In order to understand changes at the molecular level due to the presence of these ligands at the BS, we have estimated HB (Figure 7.9) and WB (Figure 7.10) correlation functions for residues which are extensively engaged in them. Repositioning of the residues in the binding cleft to accommodate the ligand molecules when compared with the ligand-free Pu(IV)-sTf system at serum pH (*cf.* Figure 7.7, Figure 7.8) is quite evident. Namely, often the participating residues are changed and also between a given residue pair, their HB and WB dynamics markedly differ from one another. A close scrutiny of Figures 7.9 and 7.10 reveals the differential binding pattern of the two ligands. From the slower K206-S298, K206-S208, and H249-T250 HB dynamics (see Figure 7.9), one can infer that HOPO position itself close to the second shell residue, K206 and the first shell residue, H249 by pushing them towards nearby residues, S298, S208 and T250, respectively. The realignment of K206 is also evidenced

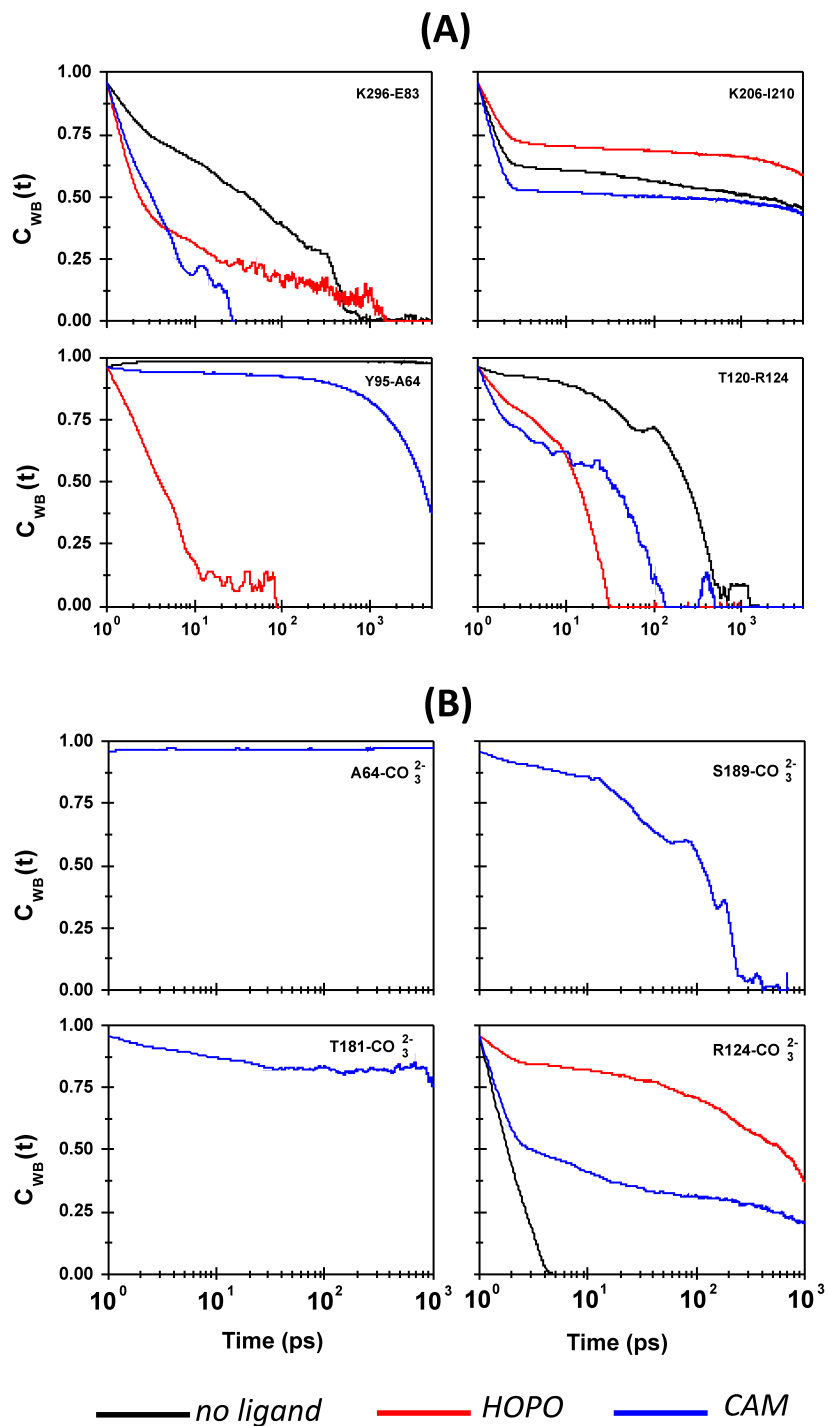


FIGURE 7.10: (upper panel, A) Time dependence of WB lifetime correlation functions between residues of sTf which are extensively engaged in WB formation between themselves are shown for Pu(IV)-sTf bound system at *phys* serum pH. (lower panel, B) Same as panel (A) except that WB between residues of sTf with the synergistic ion, CO_3^{2-} are shown. Colour legends are same as in Figure 7.9. Remarkable difference in WB formation behaviour due to single-atom nitrogenation of catechol-based CAM ligand in hydroxypyridinone-based HOPO ligand is quite evident.

from its enhanced WB interaction with I210 (see Figure 7.10). However, HOPO by itself is not seen to form HB with nearby residues in the bound state. CAM, on the other hand, position itself close to second shell residues, R124 and K296 such that it can participate in HB formation with them. CAM also pushes K296 towards E83 (see the HB dynamics between the two residues in Figure 7.9) and Y95 towards A64 (see the WB dynamics between the two residues in Figure 7.10). Both the ligands can be seen to disrupt the R124-CO₃²⁻ coordination, prevailing in ligand-free Pu(IV)-sTf system, by introducing one water molecule between them, which can be inferred from enhanced WB between them.

Note that parting away of R124 from CO₃²⁻ in *acid II* and *acid III* state (i.e., Y188 is protonated) in ligand-free sTf is known to trigger the opening of the protein.^{137,226} As discussed above, similar repositioning of R124 with respect to the carbonate ion is also seen here at serum pH due to the placement of the ligands in the binding cleft. However, in the present case this event is found not enough to initiate the protein opening and subsequent Pu(IV) release, at least not during the 100 ns simulation time. In order to expedite Pu(IV) release and thereby to study the plausibility of the two ligands as suitable decorporating agents, metadynamics simulations are conducted and the results are discussed below.

7.3.2 Unbinding of Pu(IV) at serum pH

The metadynamics runs are well-tempered along two chosen CVs, namely the COM separation between NI and NII sub-domains of sTf and that between the metal ion and the protein. The choice of the first CV is guided by the fact that the metal release process is triggered by substantial conformational changes of the protein, such that the separation between NI and NII sub-domains increases to facilitate central ion's release. The PMF contour profiles for the unbinding transition of Pu(IV) without any ligand, with HOPO and with CAM ligands are presented in Figure 7.11 along the two chosen CVs, while

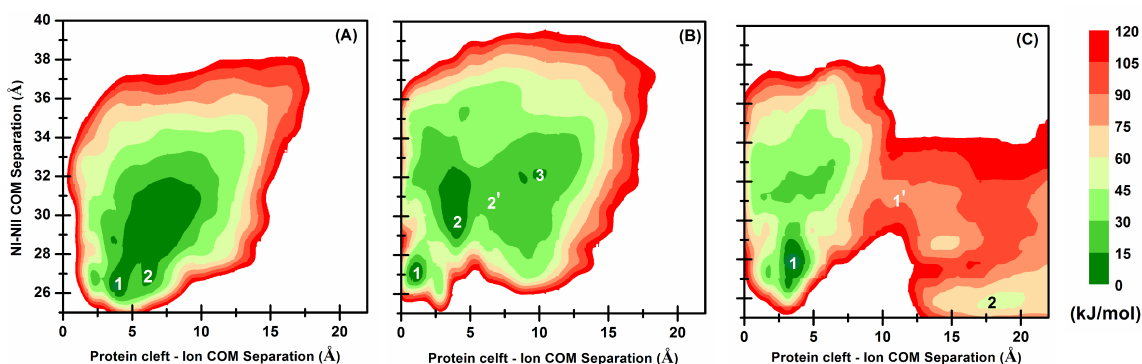


FIGURE 7.11: Two-dimensional contour plot for the unbinding transition of Pu(IV) from the binding-cleft of serum transferrin at serum pH are shown (A) without ligand, (B) with HOPO, and (C) with CAM ligands. The 2D free-energy landscape is generated from WtMetaD runs, employing ordinate and abscissa of the plots as CVs. Isoenergy lines are drawn every 15 kJ/mol. Numerals without and with prime indicate major basins and barriers along the unbinding pathway. See Figures 7.13, 7.14, 7.15 for structural snapshots of them.

Figure 7.12 represent their one-dimensional variant along the ion-protein COM separation. In these Figures, the local minima (basins) and maxima (barriers) along the unbinding pathways are a manifestation of several influencing parameters, namely, structural fluctuations, electrostatic interactions, solvation, van der Waals, HB, and WB interactions. Pu(IV) with its high ionic potential ($Z/r = 4.4 \text{ e}\text{\AA}^{-1}$) can be thought to be locally trapped in binding pockets (minima) along the unbinding pathway. Additions of enough number of Gaussian hills could liberate it from a local minima, which after passing through a barrier can again be trapped in another minima. Their positions in the CV landscape and as well as their depth and height without and with the ligands markedly differ from each other. Below we discuss them in detail.

7.3.2.1 Without ligand

When there is no ligand attached to the BS of Pu(IV)-sTf system, the COM separation between NI and NII sub-domains can be seen in Figure 7.11(A) to increase up to $\sim 38 \text{ \AA}$. At this large separation, although the protein is fully in the open state, the maximum

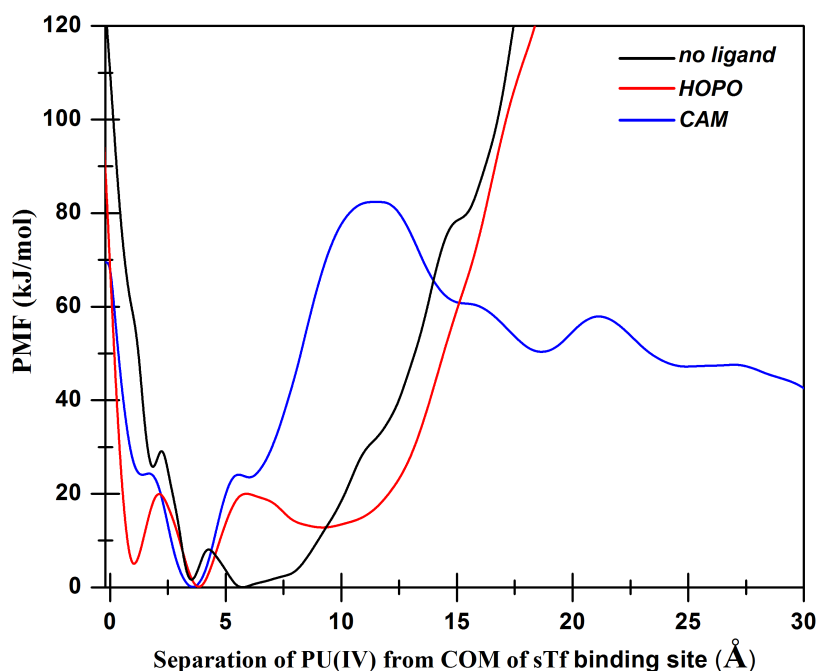


FIGURE 7.12: PMF profile for the unbinding transition by employing COM separation between protein binding-cleft and Pu(IV) ion as a CV (*cf.* abscissa in Figure 7.11) are shown without and with the ligands. Colour legends are same as in Figure 7.10. The PMF profile are generated from the converged WtMetaD simulation.

separation of the heavy ion from protein's COM reaches ~ 15 Å (see Figure 7.12). From a visual inspection of the unbinding trajectory we conclude that even in the fully opened state of sTf, Pu(IV) is not completely knocked out of the protein as it is seen to undergo electrostatic interactions at the protein's periphery. In fact, Pu(IV) binding with sTf is found to be so strong that in our WtMetaD simulation, even after addition of 2×10^5 hills (till 200 ns), it was unable to be freed from the binding influence of the protein completely. With similar WtMetaD parameters, in a recent study we have observed complete release of Th(IV) and Cm(III) from sTf within few tens of ns simulations.¹⁶⁵

Two major basins (indicated by numerals in Figure 7.11), intervened by a tiny barrier along the unbinding pathway of Pu(IV) from the ligand-free sTf can be seen in Figure 7.12. Snapshots of the two basins are displayed in Figure 7.13. In *basin 1*, Y95

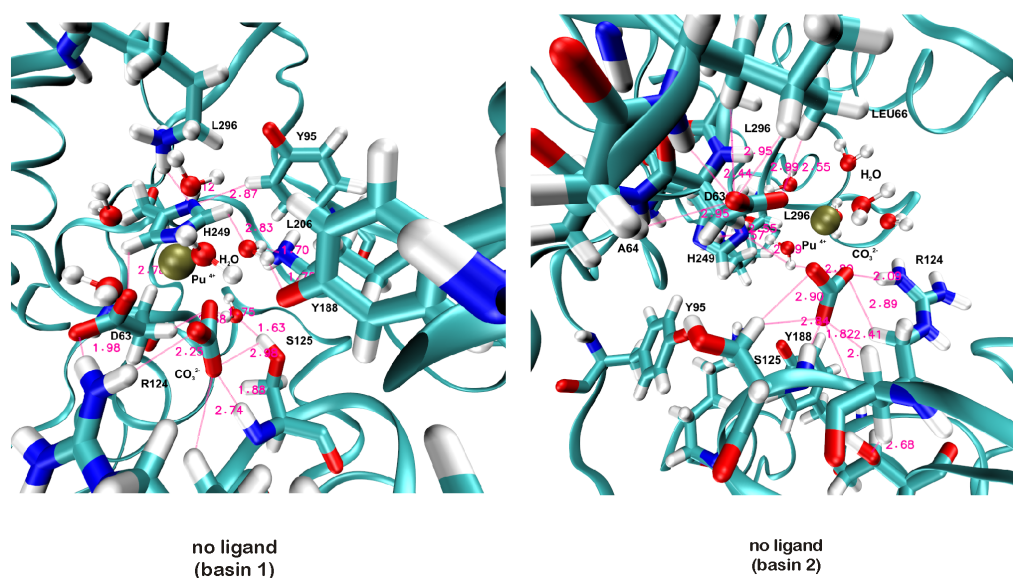


FIGURE 7.13: Snapshots of the two energetic basins, as marked in Figure 7.11 (A) for the unsuccessful attempt of unbinding transition of Pu(IV) without the ligands in polarizable water medium are shown. Only those residues of sTf that stabilizes these states and are responsible for Pu(IV) binding are depicted. The dotted lines marked with separation distance (Å) indicate HBs and WBs.

can be seen to be pushed out of BS and four water molecules enter, which along with H249, D63, CO_3^{2-} , and Y188 make up 8-9 coordination for the bound Pu(IV) ion. Several HBs between H249-Y95, H249-K296, D63-R124, R124- CO_3^{2-} and WBs between S125- CO_3^{2-} , Y188-K206, Y188-H249, H249-Y188 give rise to a energetically stable Pu(IV)-bound sTf structure. Similar to this, in *basin 2*, Y95, Y188, and H249 are seen to be pushed out of BS and six water molecules enters into the cleft, which along with D63 and CO_3^{2-} satisfy 9 coordination number for Pu(IV). Old HB between H249-Y95 in *basin 1* is broken (causing the tiny barrier to occur) and several newer ones are found (H249-D63, D63-L66, D63-G65, T120-R124, and S125- CO_3^{2-}). In addition to this, WBs between D63-Y95, H249- CO_3^{2-} , R124- CO_3^{2-} , and D63- CO_3^{2-} give rise to a sufficiently strong binding pocket for the captured heavy ion in *basin 2*, such that, it cannot be dislodged from the pocket in the future course of the simulation.

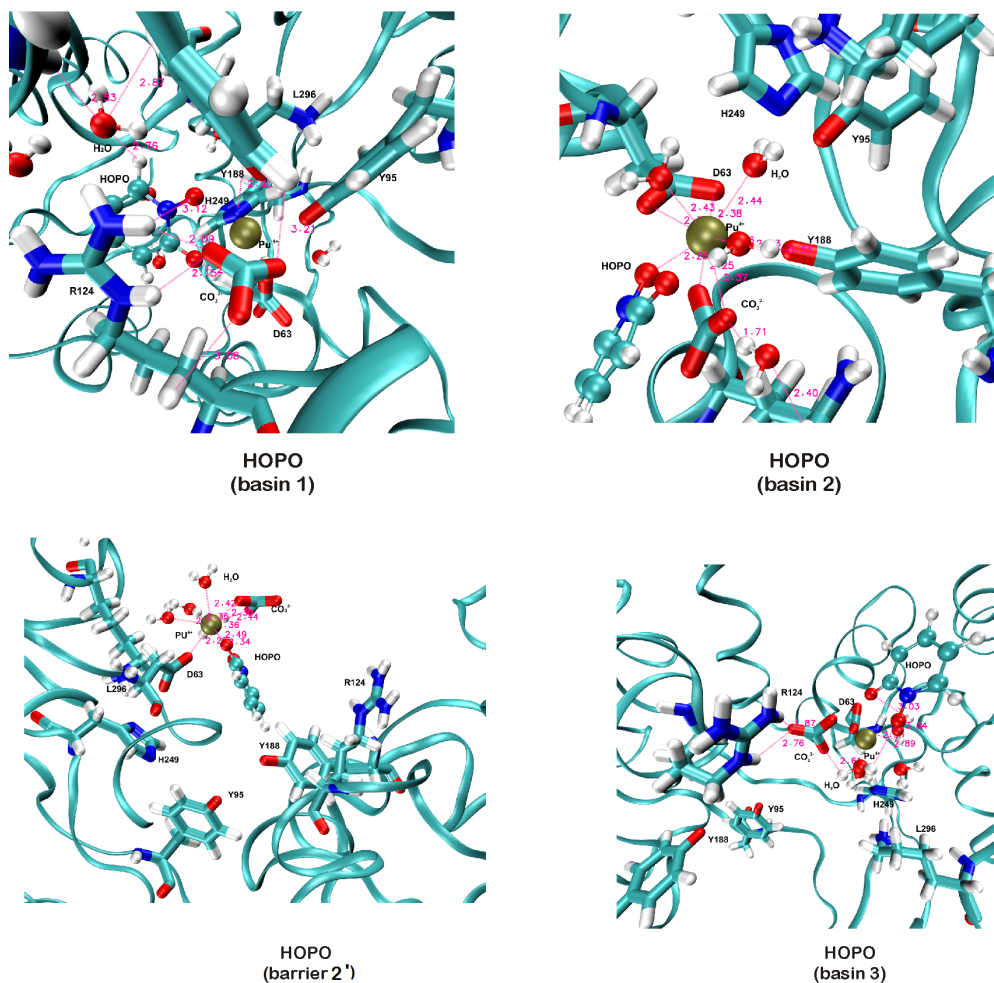


FIGURE 7.14: Snapshots of the energetic basins and barriers, as marked in Figure 7.11 (B) for an attempt to unbind Pu(IV) from sTf cleft when docked with HOPO ligand in polarizable water medium are shown. Only those residues of sTf that stabilizes these states and are responsible for Pu(IV) binding are depicted. The dotted lines marked with separation distance (\AA) indicate HBs and WBs.

7.3.2.2 With HOPO

When HOPO is docked into the BS, the PMF profile for Pu(IV) unbinding exhibits three major minima with two small barriers in between (Figure 7.12). Snapshots of the three basins and one barrier, as marked with numerals in Figure 7.11(B), are presented in Figure 7.14. *Basin 1*, is identified when the protein is in its closed conformation and

Pu(IV) is tightly bound to the cleft. No water in the BS is found to enter and the 8 coordination number of Pu(IV) ion is seen to be satisfied by H249, Y95, Y188, D63 residues in association with the bidentate HOPO and CO_3^{2-} . Several HBs, notably between H249-L296, Y95-L296, R124- CO_3^{2-} and D63-HOPO are observed. In *basin 2*, H249 and Y95 are pushed away from the binding pocket and Pu(IV) attains 9 coordination sphere with D63, Y188, HOPO, CO_3^{2-} and with three water molecules that entered the BS. HBs between H249-K296, R124-Y188, H249-D63, Y95-D63, R124- CO_3^{2-} , HOPO- CO_3^{2-} , and WBs between HOPO-D63, HOPO-Y188 are noticed. *Basin 3* is reached from *basin 2* by crossing through a small barrier. In this barrier (*barrier 2'*, Figure 7.14), H249, Y188, and Y95 are seen to be pushed away, NI and NII sub-domains part away from each other, and four water molecules entered the BS. Older HBs in *basin 2* are broken and a new one, D63-HOPO is formed. Similarly, new WBs between D63-K296, HOPO- CO_3^{2-} are also formed. The breaking of the old HBs and WBs, prevalent in *basin 2*, can be thought to give rise to structure in *barrier 2'*, which quickly gets trapped in *basin 3*. The structure at *basin 3* is stabilized by the restoration of multiple HBs between R124- CO_3^{2-} and D63-H249. The new binding environment for Pu(IV) at *basin 3* is again found to be strong enough to hold back the ion in the new environment, even after subsequent addition of sufficient number of hills in the unbinding WtMetaD run (*cf. basin 2* with no ligand).

7.3.2.3 With CAM

With CAM docked into the BS of Pu(IV)-sTf system, an attempt to unbind the heavy ion by WtMetaD simulation is seen to be successful with two major basins and one barrier (see Figures 7.11(C) and 7.15). The most stable structure in *basin 1* is similar to the *basin 2* of the HOPO bound Pu-sTf structure. H249 is pushed away from its position in the ligand-free structure and one water molecule enters into the first shell, which satisfies 8 coordination number of the central metal ion along with other nearby residues. HBs

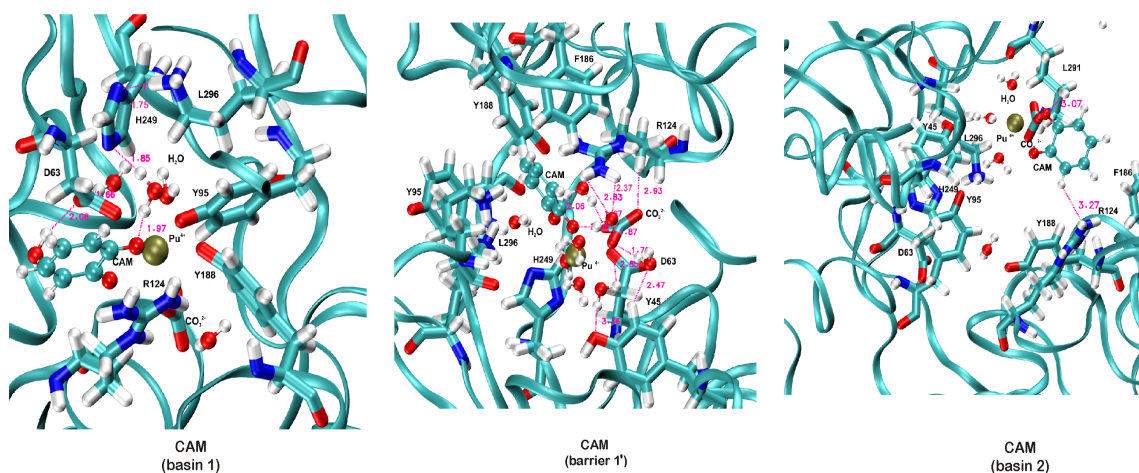


FIGURE 7.15: Snapshots of the energetic basins and barriers, as marked in Figure 7.11 (C) for successful unbinding of Pu(IV) from sTf cleft when docked with CAM ligand in polarizable water medium are shown. Only those residues of sTf that stabilizes these states and are responsible for Pu(IV) binding are depicted. The dotted lines marked with separation distance (\AA) indicate HBs and WBs.

between H249-K296, R124-CO₃²⁻ and Y188-CO₃²⁻, WBs between H249-CAM, D63-CAM. D63-Y95, D63-Y188 are noteworthy. *Barrier 1'* is characterized with 7-coordinated Pu(IV) while H249, Y95 and Y188 is pushed away from BS and three water molecules entered in the first shell. Old HB between H249-K296 and R124-CO₃²⁻ in *basin 1* are somewhat weakened because of the participation of H249 with D63 and R124 with CAM in similar HB formation. Similarly, only WB between H249-CAM survives in *barrier 1'*. Breaking of old WBs and weakening of HBs in *basin 1* until the participating residues find new HB partner cause the *barrier 1'* to appear with ~ 80 kJ/mol height at ~ 11.5 \AA (see Figure 7.12) along the COM of Pu-sTf BS separation coordinate, when NI-NII COM separation is large enough (32 \AA) for the protein to be considered in open configuration. Crossing the barrier, Pu(IV) can be trapped in a shallow well (*basin 2*) where Pu(IV) is again seen to engage in 7 coordination, and HB between R124-CO₃²⁻ is broken. The structure in this shallow basin is stabilized by HBs between L291-CAM and R124-CAM with no additional inter-residue HB to report upon. Breaking of these HBs along the unbinding pathway liberates the captured Pu(IV) ion completely from the

binding influence of sTf. Thus the present simulation results suggest that catechol based compounds could be promising potential molecules for the decorporation of Pu(IV) ion from sTf at serum pH.

7.3.3 DFT calculations for ion exchange energetics

Most promising alternative to DTPA that can decorporate Pu(IV), or in general the actinide ions, from blood serum are linear hydroxy-pyridinone (LIHOPO), especially 3,4,3-LI(1,2-HOPO) and linear catecholamide 3,4,3-LICAM chelator ligands. Before the acquirement by sTf, capture of free aquated Pu(IV) ion from the blood serum, is an outcome of the chelating strengths of the ligands with respect to water molecules. Using the following reaction scheme we have calculated the binding free energies (BFE) of Pu(IV) with the chelators.



where values of m are 5 and 1 and that of n are 4 and 0 for LICAM and LIHOPO, respectively.

The free energy change associated with the above equations is given by,

$$\Delta G_{ex}^\epsilon = [\Delta G_{solv}^\epsilon]_{product} - [\Delta G_{solv}^\epsilon]_{reactant}, \quad (7.2)$$

where ΔG_{solv}^ϵ is the free energy changes associated with transferring a reactant or product partner from gas phase to solution phase with dielectric constant, ϵ . Further, in another heuristic analysis we have estimated the changes in the thermodynamic parameters for the detachment of Pu(IV) from the sTf binding cleft (see Figure 17.1) with these chelating ligands as shown in the following equation,



Electronic structure calculations are carried out to estimate the free energy

TABLE 7.2: Estimated ion exchange, Fe(III) \rightarrow Pu(IV) free energies (in kJ/mol) by the chelating ligands, in the absence of sTf binding cleft, at different dielectric constant of the medium.

Ligand	Thermodynamic Parameters (kJ mol ⁻¹)					
	ΔH		$T\Delta S$		ΔG_{ex}^ϵ	
	$\epsilon=80$	$\epsilon=5$	$\epsilon=80$	$\epsilon=5$	$\epsilon=80$	$\epsilon=5$
3,4,3-L1(1,2-HOPO)	-216.56	-495.29	43.42	43.42	-259.98	-538.71
3,4,3-L1CAM	-378.66	-880.58	56.76	56.76	-435.42	-937.34

changes associated with the above ion exchange [Fe(III) \rightarrow Pu(IV)] reactions (Eqs. 7.1 and 7.3) with the help of Equation 7.2. All the structures are optimized at BP86 functional.^{35,153} A def-triple zeta valence augmented by polarization function (TZVP) basis set⁴³ and small core-relativistic effective core potentials are used for actinide ion. For other atoms in the system TZVP basis sets^{41,42} are used. The optimized structures are verified as minima by computing their harmonic vibrational frequencies. Energies are evaluated using B3LYP functional^{36,155,203} in conjunction with the continuum COSMO solvation model (with dielectric constant, $\epsilon=80$ and $\epsilon=5$) as implemented in TURBOMOLE 6.6.¹⁵⁴ The calculated parameters for the formation of Pu-Ligand complexes, representing the capture of aquated Pu(IV) by the ligands (*cf.* Equation 7.1), are presented in Table 7.2. As is evident from the table that that Pu-LICAM complex is more stable than Pu-LIHOPO complex.

TABLE 7.3: Estimated ion exchange, Fe(III) \rightarrow Pu(IV) free energies (in kJ/mol) by the chelating ligands, inside the sTf binding cleft, at different dielectric constant of the medium

Ligand	Thermodynamic Parameters (kJ mol ⁻¹)					
	ΔH		$T\Delta S$		ΔG_{ex}^ϵ	
	$\epsilon=80$	$\epsilon=5$	$\epsilon=80$	$\epsilon=5$	$\epsilon=80$	$\epsilon=5$
3,4,3-L1(1,2-HOPO)	-117.07	-106.53	-43.57	-43.57	-73.50	-62.96
3,4,3-L1CAM	-279.17	-491.83	-30.23	-30.23	-248.94	-461.59

In Table 7.3 we have presented the similar ion exchange energetics when the Pu(IV) ion is bound to the sTf binding cleft (*cf.* Equation 7.3). The DFT calculations clearly shows that both the chelating agents can remove Pu(IV) from the sTf binding cleft and that LICAM is a more plausible candidate for Pu(IV) chelation as its complex with Pu(IV) is more stable than LIHOPO-Pu(IV) complex. This result also corroborates well with our main finding (described above) that the fragmented molecular form of CAM based ligand could be a plausible decorporating agent for sTf-bound Pu(IV) ion.

7.4 CONCLUSIONS

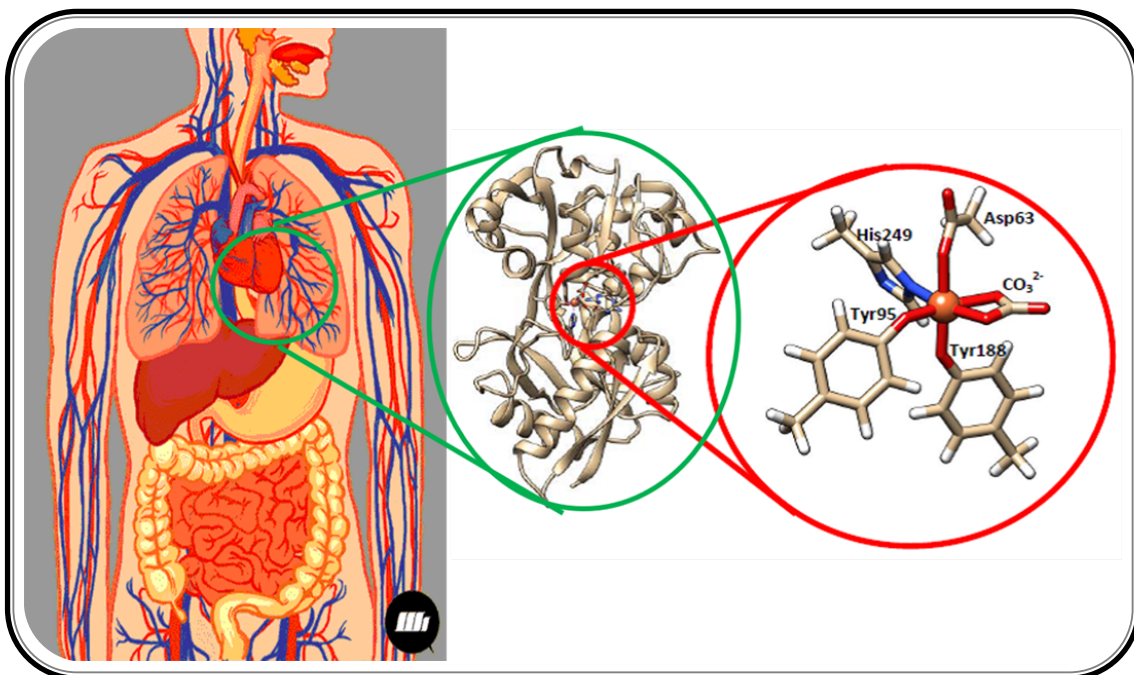
Equilibrium MD simulations of Pu(IV) binding with human serum transferrin (sTf) at physiological and at endosomal acidic pH are performed. At physiological serum pH we found that sTf binds the heavy ion in closed conformation, which is very reminiscent to the ferric ion trafficking pathway. At acidic pH, on the other hand, we found that sTf binding cleft is somewhat distorted and that the central heavy ion is released from the cleft even without protonation of Y188. This result is similar to our earlier findings for Th(IV) binding but in contradiction to observations made for trivalent curium or native iron ions. However, in none of the three protonation states of the protein at the acidic pH, Pu(IV) is ever seen to be completely set free from the protein's binding influence. The Coulomb interaction between the tetravalent ion and the aspartate residue, D63 is seen to play major role in the ion's speciation. The results are based on mean-field polarizable model of water, which allow one to mimic the more realistic picture of dielectric heterogeneity of water in the protein interior, its surface and in the bulk.

Any attempt towards lead compound discovery for the decorporation of Pu(IV) ion should be primarily aimed at serum pH, before the receptor mediated endocytosis could initiate. Because the later can cause highly undesirable radiolytic events inside the cells/tissues. In this endeavour we have studied the possibility of two chelators: fragmented form of hydroxypyridinone and catecholamide ligands, to act as suitable unbinding agents for Pu(IV) in blood serum. The equilibrium MD simulations of the

docked chelators in Pu(IV)-sTf system show variedly rich HB and WB dynamics, which significantly differ from each other. The metadynamics simulation results along the chosen CVs show differential unbinding pattern of the metal ion from the sTf cleft by the two ligands. The free energy barriers associated with the inter-basin transitions along the transition pathways are also found to be different. Following the discovered PMF profiles for the ion's unbinding, we conclude that catecholamide based ligands could be promising chelator for the Pu(IV) ion decorporation. While any comment on the chemical toxicity of these compounds is beyond the scope of present study, this study may help in understanding the Pu(IV) chelation mechanism in blood serum and designing new decorporating agents. In total, this work provides the molecular detail of Pu(IV) ions' interaction with sTf at serum and endosomal pH conditions and its removal at serum pH, which in future may prove to be useful for effective design of its therapeutic decorporating agents.

CHAPTER 8

Summary and Future Scope



HIGHLIGHTS

- The present thesis is aimed to develop a methodology for quick estimation of Pu/Am in biological samples. This thesis also focuses on finding optimum *in-vivo* monitoring geometry out of Lungs, Liver, and knee such that lowest intake can be estimated at various time intervals post inhalation of Pu/Am compounds.
- Iron carrier, serum transferrin (sTf) which is also responsible for transport of Pu and other actinides within the body, is studied using various computational techniques. Much debated structure of the binding cleft of iron loaded sTf is studied using isolated and embedded clusters models and spin Hamiltonian parameters are estimated from DFT calculations.
- This thesis extensively discusses about the speciation, dynamics, binding and structures of various actinide ions present in the binding cleft of the sTf at serum and endosomal pH conditions.
- In an endeavour to decipher decorporation mechanism of plutonium ion Pu(IV), by fragmented molecular form of hydroxypyridinone (HOPO) and catecholamide (CAM) based ligands, docking of the ligands at the binding site (BS) of the sTf protein and metadynamics simulations are conducted. A detailed mechanism of the ligands decorporation characteristics are explored.
- The findings of present thesis can in principle be useful in future for effective design of decorporating therapeutics for Pu and actinides' in general, based on CAM or its derivatives.

8.1 SUMMARY AND FUTURE SCOPE

In the final and concluding chapter, all the major findings and conclusions of the thesis are summarized. This chapter is also aimed to provide a futuristic outlook and possible future extensions of the present work.

The first chapter is introductory in nature, which describes various terminology and methods used in the present thesis. Direct method of internal dose assessment, important dosimetric quantities, how to solve biokinetic models and estimate committed effective dose (CED) using methodology given by committee on medical internal radiation dose (MIRD) are discussed in brief. Current decorporating agent for decorporation of important actinides (An) and their limitations are also discussed. Various multi-scale modelling techniques which are used for computational investigations for binding and decorporation of various actinide ions are introduced in this chapter e.g. basics of QM especially DFT, basis sets, equilibrium MD simulations and enhanced sampling methods like umbrella sampling (US), well-tempered metadynamics (WtMetaD), hydrogen bond (HB), water bridge (WB) dynamics etc. Finally, objectives and goals of the present thesis are discussed.

Chapter 2 describes a methodology which is developed for quick estimation of Pu/Am in biological samples using HPGe detectors and its comparison with conventional technique based on radio-chemical separation followed by alpha counting. In this work, gamma/x-rays detection method is applied to estimate Pu and ^{241}Am deposited in biological sample. First, depth of contaminant in biological sample is estimated by comparing relative transmission of 26.3 and 59.5 keV photons emitted by ^{241}Am . Then ^{241}Am activity is estimated using calibration factor at calculated depth. Finally, Pu activity is estimated by applying appropriate correction for ^{241}Am contribution in 17.2 keV L_{β} X-rays region and Pu/ ^{241}Am ratio is calculated. Also methodology for estimating ^{241}Pu in small biological sample is standardized. The method is fast as it does not involve chemical separation of Pu and Am as required in the

alpha-spectrometric method. This study will be useful for assessment and medical management of Pu/²⁴¹Am embedded in tissues.

In Chapter 3, a geometry optimization protocol is presented to find the organ whose in-vivo counting will correspond to minimum intake and CED values at different time intervals post inhalation of Pu/Am compounds. In-vivo measurement of Pu/²⁴¹Am in workers is carried out by placing suitable detector above lungs, liver and skeleton, as major fraction of Pu/Am is transferred to liver and skeleton, after its retention in entry organ. CED due to inhalation of minimum detectable activity (MDA) equivalent type M and S ²³⁹Pu/²⁴¹Am compounds deposited in these organs are estimated and a monitoring protocol of organ measurement giving lowest CED at different time intervals post inhalation is described. It is observed, for type M compounds, lung measurement is most sensitive method during initial days after inhalation exposure. Liver measurement yields lowest CED between 100 to 2000 days and beyond that bone measurement gives lowest CED. Whereas for type S compounds, lung measurement remains most sensitive method even up to 10,000 days post inhalation. This study is expected to be useful for the assessment of CED due to internally deposited ²³⁹Pu/²⁴¹Am in radiation workers.

Pu/Am and other actinides are deposited to various organs *viz.* lungs, liver, bone, lymph nodes etc. Molecular mechanism about their transport within the body is still obscure. It is observed that iron carrier serum transferrin (sTf), transports An ions to various sites of the deposition within body by forming suitable complexes with them. In order to have molecular level understanding about An-sTf structures, binding, speciation and dynamic properties, various multi-scale modelling studies are performed and presented in next four chapters. This thesis not only focus on the interaction of Pu with sTf but also on this protein's interaction with two other important radionuclides Th, and Cm.

Chapter 4 discusses about the optimized model structure for the binding site (BS) of native protein Fe-sTf. Before studying structural, speciation, binding and

thermodynamic characteristics of actinide bound sTf complexes, DFT based calculations using large cluster models are carried out to elucidate the ground state electronic structure of iron bound transferrin. In this chapter, the results of electronic structure calculations help in understanding the much debated geometric structure of Fe-sTf. It is observed that the use of gas phase geometry optimization predicts a wrong penta-coordinated geometric structure and thus an incorrect electronic structure, whereas the geometry predicted within the continuum solvation model is hexa-coordinate which is also found in the crystal structure. Various spin Hamiltonian parameters are evaluated for Fe-sTf and Cu-sTf binding site and found to be in good agreement when compared with experimental values. This study guided in selecting suitable computational solvation models, basis sets and other parameters which can be used for QM studies on actinide bound sTf complexes.

In the fifth Chapter, results of the multi-scale modelling for Binding of Cm(III) and Th(IV) with sTf at Serum pH are presented. From structural, dynamical and binding studies of the two ions it is observed that sTf binds both the heavy ions in a closed conformation with carbonate as synergistic anions and the An loaded sTf maintains its closed conformation even after 100 ns of equilibrium molecular dynamics (MD) simulations. Th(IV) is found to be present in octa-dentate mode while Cm(III) prefers a hepta-dentate mode of coordination in the protein binding site. Well-tempered metadynamics results of the ions' binding energetics show that the studied An-sTf complexes are less stable than Fe-sTf which are in line with reported experimental observations. Additionally, Cm(III) is found to bound more weakly than Th(IV). As a result, it will be more difficult to release thorium(IV) from the binding cleft, which might suggest its lower cytotoxicity when compared with curium (III). This result in particular emphasizes that interaction between the An ions and sTf in the presence of explicit water molecules is mainly the Coulombic one, which gives rise to the difference in the binding characteristics of the ions.

Chapter 6 is focused on studying the binding of Cm(III) and Th(IV) with sTf at Endosomal pH. In this chapter, several 100 ns equilibrium MD simulations of sTf bound to Cm(III) and Th(IV) at various protonation states of the protein are performed to explore the possibility of the two An ions release and speciation. The results demonstrate that like in Fe(III)-sTf system at the acidic endosomal pH, variation in protonation state of dilysine pair (K206 and K296) and the tyrosine (Y188) residue is necessary for the opening of Cm(III)-bound protein and the release of this trivalent ion. For Th(IV), although the protonation of dilysine pair alone is found to be sufficient to cause conformational changes in protein for opening of the sub-domains, in none of the protonation states of the protein investigated, Th(IV) is found to be released. The findings are further supported by the evaluation of potential mean force (PMF) of An ions' release using US runs along the chosen reaction coordinates. This chapter provides the molecular detail of An ions' interaction with sTf at endosomal pH condition, which in future may prove to be useful for effective design of their decorporating therapeutics which is the subject matter of next chapter.

The seventh chapter of the thesis, is devoted to *In-Silico* investigations for Plutonium binding and its decorporation from sTf. In this chapter, equilibrium MD simulations for binding of Pu(IV) with human serum transferrin at physiological and at endosomal acidic pH are discussed. Results unravel that Pu(IV) is bound to sTf in closed conformation at extracellular serum pH with carbonate as synergistic anions, and change in protonation state of dilysine -trigger (K206 and K296) and carbonate ion at endosomal pH induces conformational changes in protein, to initiate release of the heavy ion from sTf BS. However strong electrostatic interaction between D63 and Pu(IV) does not allow the ion to be free. The possibility of two chelators: fragmented form of hydroxypyridinone and catecholamide ligands, to act as suitable unbinding agents for Pu(IV) in blood serum is discussed. The equilibrium MD simulations of the docked chelators in Pu(IV)-sTf system show variedly rich HB and WB dynamics, which

TABLE 8.1: Ionic potential and non-bonded parameters of the investigated metal ions

Metal ion	Ionic potential Z/r ($e\text{\AA}^{-1}$)	Non-bonded parameters	
		σ (nm)	ϵ (kJ/mol)
Th(IV)	3.7	3.04E-01	6.00E-01
Pu(IV)	4.4	2.96E-01	4.75E-01
Fe(III)	4.3	2.08E-01	5.61E-01
Cm(III)	2.7	3.70E-01	5.43E-02

significantly differ from each other. The metadynamics simulation results along the chosen collective variables (CVs) show differential unbinding pattern of the metal ion from the sTf cleft by the two ligands. The free energy barriers associated with the inter-basin transitions along the transition pathways are also found to be different. Following the discovered PMF profiles for the ion's unbinding, it is concluded that catecholamide based ligands could be promising chelator for the Pu(IV) ion decorporation. While any comment on the chemical toxicity of these compounds is beyond the scope of present study, this study may help in understanding the Pu(IV) chelation mechanism in blood serum and designing new decorporating agents.

Results in chapter 5, 6, 7 are largely presented on the basis of ionic potential, rather than electronic charges alone. In classical MD stimulations, van der Waals interactions are incorporated through non bonded parameters. The ionic potential and non-bonded parameters of the trivalent and tetravalent ions are now provided in tabular form 8.1. The ionic potential as well as the non-bonded parameter, epsilon is the least for Cm(III) amongst all the four metal ions, which causes its binding weakest at the binding site. In case of tetravalent ions Pu(IV) and Th(IV), although the non-bonded parameters are similar, the high ionic potential of Pu(IV) makes its binding stronger than Th(IV). This can also be observed in the PMF plots for their separation from binding site using well-tempered metadynamics.

To summarize, this thesis is aimed in developing experimental methods for quick estimation of Pu/Am internal contamination in human body. To gain insight into the

transport mechanism of Pu, *in-silico* investigations are carried out. This thesis also focus on studying the binding and transport mechanism of tetravalent thorium as well as trivalent curium ions. Several multi-scale modelling studies are carried out to understand the molecular mechanism of binding of Pu(IV), Th(IV) and Cm(III) with serum transferrin protein at serum and endosomal pH conditions. The possibility of two chelators: fragmented form of hydroxypyridinone and catecholamide ligands, to act as suitable unbinding agents for Pu(IV) in blood serum is also addressed which might help in developing new decorporating agents of actinides in general.

The present thesis can be considered as a step towards molecular level understanding of the binding of few actinides with sTf and their decorporation mechanism. In order to study the complexes formed by transferrin receptor (TfR) with the full sTf protein having both N and C lobes, coarse grained molecular dynamics simulations can be explored. Also more efficient hybrid QM/MM methods can be focused to investigate these complexes at molecular level without compromising the atomistic details at the binding sites of the protein. The knowledge gained during the thesis work will help in future for design and development of suitable chelating agents for decorporation of actinides from our body. The gained knowledge will also help in developing methods for targeted delivery of certain metal therapeutics.

List of Abbreviations

AF	Absorbed Fraction
ALI	Annual Limit on Intake
An	Actinides
BFE	binding free energies
BS	Binding Site
CAM	Catechol
CED	Committed Effective Dose
CGTO	Contracted Gaussian Type Orbital
CN	Coordination Number
COM	Centre of Mass
CV	Collective Variables
CWT	Chest Wall Thickness
DAC	Derived Air Concentration
DC	Dose Coefficient
DFT	Density Functional Theory
ECF	Effective Core Potential
EPR	Electron Paramagnetic Resonance
FES	Free Energy Surface
FDA	Food and Drug Administration
GI	Gastrointestinal
GTO	Gaussian Type Orbital
HATM	Human Alimentary Tract Model
HB	Hydrogen Bond
HFCC	Hyperfine Coupling Constant
HN	Hydration Number
HOPO	Hydroxypyridinone
HRTM	Human Respiratory Tract Model

List of Abbreviations

ICRP	International Commission on Radiation Protection
LGA	Lamarckian genetic algorithm
LICAM	Linear Catecholamide
LI-HOPO	Linear Hydroxypyridinone
LINCS	Linear Constraint Solver
LLNL	Lawrence Livermore National Laboratory
MB	Mössbauer
MBS	Metal Binding Site
MD	Molecular Dynamics
MDA	Minimum Detectable Activity
MEQ-CWT	Muscle Equivalent Chest Wall Thickness
MFP	Mean Field Polarizable
MIRD	Committee on Medical Internal Radiation Dose
MM	Molecular Mechanics
MtD	Metadynamics
PBC	Periodic Boundary Condition
PES	Potential Energy Surface
PME	Particle Mesh Ewald
PMF	Potential of Mean Force
QM	Quantum Mechanism
RDF	Radial Distribution Function
RMSD	Root-Mean-Square Deviation
ROI	Region of Interest
RSEP	Restrained Electrostatic Potential
SEE	Specific Effective Energy
SH	Spin Hamiltonian
sTf	Serum Transferrin
STO	Slater Type Orbital
Tf	Transferrin
US	Umbrella Sampling
WB	Water Bridge
WtMetaD	Well-Tempered Metadynamics

Bibliography

- [1] Ingólfsson, H. I.; Arnarez, C.; Periole, X.; Marrink, S. J. *J. Cell Sci.* **2016**, *129*, 257–268.
- [2] Bussi, G.; Branduardi, D. *Reviews in Computational Chemistry Volume 28*; John Wiley & Sons, Ltd, 2015; Chapter 1, pp 1–49.
- [3] Nadar, M.; Patni, H.; Akar, D.; Mishra, L.; Singh, I.; Rao, D.; Sarkar, P. *Radiat. Prot. Dosim.* **2013**, *154*, 148–156.
- [4] Bonomi, M.; Barducci, A.; Parrinello, M. *J. Comput. Chem.* **2009**, *30*, 1615–1621.
- [5] *International commission on radiological protection. Individual monitoring for internal exposure of workers. ICRP Publication 78.*; 1997; Vol. 27.
- [6] *International Commission on Radiological Protection. Human respiratory tract model for radiological protection. ICRP Publication 66.*; 1994; Vol. 24.
- [7] *International Commission on Radiological Protection. Limits for Intakes of Radionuclides by Workers. ICRP Publication 30. Part 1.*; 1979; Vol. 3-4.
- [8] *International Commission on Radiological Protection. Human Alimentary Tract Model for Radiological Protection. ICRP Publication 100*; 2006; Vol. 36.
- [9] *NCRP Report No. 156 : Development of a Biokinetic Model for Radionuclide-Contaminated Wounds for Their Assessment, Dosimetry and Treatment*; 2006.

-
- [10] *International commission on radiological protection. Dose coefficients for intake of radionuclides by workers. ICRP Publication 68.*; 1994; Vol. 24.
- [11] *The 2007 Recommendations of the International Commission on Radiological Protection. ICRP Publication 103.*; 2007; Vol. 37.
- [12] Ansoborlo, E.; Prat, O.; Moisy, P.; Den Auwer, C.; Guilbaud, P.; Carriere, M.; Gouget, B.; Duffield, J.; doizi, D.; Vercouter, T.; Moulin, C.; Moulin, V. *Biochimie* **2006**, *88*, 1605–1618.
- [13] Sun, H.; Li, H.; Sadler, P. J. *Chem. Rev.* **1999**, *99*, 2817–2842.
- [14] Vincent, J. B.; Love, S. *Biochim. Biophys. Acta, Gen. Subj* **2012**, *1820*, 362–378.
- [15] Harris, W. R.; Messori, L. *Coord. Chem. Rev.* **2002**, *228*, 237–262.
- [16] Dennis Chasteen, N. *Coord. Chem. Rev.* **1977**, *22*, 1–36.
- [17] Durbin, P. W. *The chemistry of the actinide and transactinide elements. Springer, Heidelberg, 3rd Edition*; 2006; p 3339.
- [18] Jeanson, A.; Ferrand, M.; Funke, H.; Hennig, C.; Moisy, P.; Solari, P.; Vidaud, C.; Den Auwer, C. *Chem.: Eur. J* **2010**, *16*, 1378–1387.
- [19] Sturzbecher-Hoehne, M.; Goujon, C.; Deblonde, G. J.-P.; Mason, A. B.; Abergel, R. J. *J. Am. Chem. Soc.* **2013**, *135*, 2676–2683.
- [20] Bauer, N.; Frohlich, D. R.; Panak, P. J. *Dalton Trans.* **2014**, *43*, 6689–6700.
- [21] Bauer, N.; Panak, P. J. *New J. Chem.* **2015**, *39*, 1375–1381.
- [22] Bauer, N.; Smith, V. C.; MacGillivray, R. T. A.; Panak, P. J. *Dalton Trans.* **2015**, *44*, 1850–1857.
- [23] Michon, J.; Frelon, S.; Garnier, C.; Coppin, F. *J. Fluoresc.* **2010**, *20*, 581–590.

-
- [24] Taylor, D. M.; Farrow, L. C. *Int. J. Radiat. Appl. Instrum. Part B* **1987**, *14*, 27–31.
- [25] Racine, R.; Moisy, P.; Paquet, F.; Metivier, H.; Madic, C. *Radiochim. Acta* **2003**, *91*, 115.
- [26] Harris, W. R.; Carrano, C. J.; Pecoraro, V. L.; Raymond, K. N. *J. Am. Chem. Soc.* **1981**, *103*, 2231–2237.
- [27] Li, H.; Sadler, P. J.; Sun, H. *Eur. J. Biochem.* **1996**, *242*, 387–393.
- [28] Sadhu, B.; Sundararajan, M.; Bandyopadhyay, T. *J. Phys. Chem. B* **2015**, *119*, 12783–12797.
- [29] Sadhu, B.; Sundararajan, M.; Bandyopadhyay, T. *Phys. Chem. Chem. Phys.* **2017**, *19*, 27611–27622.
- [30] Hohenberg, P.; Kohn, W. *Phys. Rev.* **1964**, *136*, B864–B871.
- [31] Kohn, W.; Sham, L. J. *Phys. Rev.* **1965**, *140*, A1133–A1138.
- [32] St.-Amant, A.; Cornell, W. D.; Kollman, P. A.; Halgren, T. A. *J. Comput. Chem.* **1995**, *16*, 1483–1506.
- [33] Perdew, J. P.; Wang, Y. *Phys. Rev. B* **1992**, *45*, 13244–13249.
- [34] Stephens, P. J.; Devlin, F. J.; Chabalowski, C. F.; Frisch, M. J. *J. Phys. Chem.* **1994**, *98*, 11623–11627.
- [35] Becke, A. D. *Phys. Rev. A* **1988**, *38*, 3098–3100.
- [36] Lee, C.; Yang, W.; Parr, R. G. *Phys. Rev. B* **1988**, *37*, 785–789.
- [37] Vosko, S. H.; Wilk, L.; Nusair, M. *Can. J. Phys.* **1980**, *58*, 1200–1211.
- [38] Jensen, F. *Introduction to Computational Chemistry, 3rd Edition*; John Wiley & Sons, 2017.

-
- [39] Hehre, W. J.; Stewart, R. F.; Pople, J. A. *J. Chem. Phys.* **1969**, *51*, 2657–2664.
- [40] McLean, A. D.; Chandler, G. S. *J. Chem. Phys.* **1980**, *72*, 5639–5648.
- [41] Schäfer, A.; Horn, H.; Ahlrichs, R. *J. Chem. Phys.* **1992**, *97*, 2571–2577.
- [42] Schäfer, A.; Huber, C.; Ahlrichs, R. *J. Chem. Phys.* **1994**, *100*, 5829–5835.
- [43] Weigend, F.; Ahlrichs, R. *Phys. Chem. Chem. Phys.* **2005**, *7*, 3297–3305.
- [44] Weigend, F. *Phys. Chem. Chem. Phys.* **2006**, *8*, 1057–1065.
- [45] Laio, A.; Parrinello, M. *Proc. Natl. Acad. Sci.* **2002**, *99*, 12562–12566.
- [46] Barducci, A.; Bussi, G.; Parrinello, M. *Phys. Rev. Lett.* **2008**, *100*, 020603.
- [47] Torrie, G. M.; Valleau, J. P. *J. Chem. Phys.* **1977**, *66*, 1402–1408.
- [48] Torrie, G. M.; Valleau, J. P. *Chem. Phys. Lett.* **1974**, *28*, 578–581.
- [49] Valleau, J. P.; Torrie, G. M. A. *A Guide for Monte Carlo for Statistical Mechanics. In statistical Mechanics Part A*; Plenum Press: New York, 1977.
- [50] Chandler, D. *J. Chem. Phys.* **1978**, *68*, 2959–2970.
- [51] Chandler, D. *Introduction to Modern Statistical Mechanics*; Oxford University Press Inc.: New York, 1987.
- [52] Roux, B. *Comput. Phys. Commun.* **1995**, *91*, 275–282.
- [53] Allen, M. P.; Tildesley, D. J. *Computer Simulation of Liquids*; Oxford University Press Inc.: New York, 1987.
- [54] Kumar, S.; Rosenberg, J. M.; Bouzida, D.; Swendsen, R. H.; Kollman, P. A. *J. Comput. Chem.* **1992**, *13*, 1011–1021.
- [55] Woolf, T. B.; Roux, B. *J. Am. Chem. Soc.* **1994**, *116*, 5916–5926.

-
- [56] Haydock, C.; Sharp, J. C.; Prendergast, F. G. *Biophys. J.* **1990**, *57*, 1269–1279.
- [57] Shen, J.; McCammon, J. A. *Chem. Phys.* **1991**, *158*, 191–198.
- [58] Luzar, A.; Chandler, D. *The Journal of Chemical Physics* **1993**, *98*, 8160–8173.
- [59] Luzar, A.; Chandler, D. *Phys. Rev. Lett.* **1996**, *76*, 928–931.
- [60] Bagchi, B. *Chem. Rev.* **2005**, *105*, 3197–3219.
- [61] Singh, I. S.; Mishra, L.; Yadav, J. R.; Nadar, M. Y.; Rao, D. D.; Pradeepkumar, K. S. *Appl. Radiat. Isot.* **2015**, *104*, 49–54.
- [62] Griffith, R.; Bergmann, H.; Fry, F. A.; Hickman, D.; Genicot, J. L.; Malatova, I.; Neton, J.; Rahola, T.; Wahl, W. *Report 69, Journal of the International Commission on Radiation Units and Measurements*; 2003; Vol. 3.
- [63] Pendharkar, K. A.; Bhati, S.; Singh, I. S.; Sawant, P. D.; Satyabhama, N.; Nadar, M. Y.; Vijaygopal, P.; Patni, H. K.; Kalyane, G. N.; Prabhu, S. P. *BARC Newsletter* **2008**, *296*, 9–23.
- [64] Singh, I. S.; Nadar, M. Y.; Kalyane, G. N.; Bhati, S.; Pendharkar, K. A. *Radiat. Prot. Environ.* **2008**, *31*, 379–381.
- [65] *International commission on radiological protection. Guide for the practical application of the ICRP human respiratory tract model. ICRP Supporting Guidance 3*; 2002; Vol. 32.
- [66] *International commission on radiological protection. Age-dependent doses to members of the public from intake of radionuclides: Part 2. Ingestion dose coefficients. A report of a Task Group of Committee 2 of the International Commission on Radiological Protection. ICRP Publication 67.*; 1993; Vol. 23.

-
- [67] White, D. R.; Booz, J.; Griffith, R. V.; Spokas, J. J.; Wilson, I. J. *Report 44, Journal of the International Commission on Radiation Units and Measurements*; 1989; Vol. os23.
- [68] Singh, I. S.; Nadar, M. Y.; Mishra, L.; Rao, D. D. *Proceedings of DAE-BRNS symposium on nuclear and radiochemistry. V. 2* **2011**,
- [69] Nadar, M.; Singh, I.; Bhati, S. *Radiat. Prot. Environ.* **2010**, 33, 213–215.
- [70] Yadav, J. R.; Rao, D. D.; Hegde, A. G.; Aggarwal, S. K. *Radiat. Prot. Dosim.* **2008**, 129, 403–410.
- [71] Ranjeet, K.; Yadav, J.; Rao, D.; Lal, C. *J. Radioanal. Nucl. Chem.* **2010**, 283, 785–788.
- [72] Aggarwal, S. K.; Saxena, M. K.; Jain, H. C. *J. Radioanal. Nucl. Chem.* **1992**, 156, 111–118.
- [73] Rao, D. D.; Sudheendran, V.; Sarkar, P. K. *Appl. Radiat. Isot.* **2012**, 70, 1519–1525.
- [74] Currie, L. A. *Anal. Chem.* **1968**, 40, 586–593.
- [75] Genicot, J.-L.; Hardeman, F.; Oberstedt, S. *Appl. Radiat. Isot.* **1995**, 46, 199–203.
- [76] Palmer, H. E.; Rhoads, M. *Health Phys.* **1989**, 56, 249–252.
- [77] Andreaco, M. S.; Seymour, R. S.; Martin, G. N. *J. Radioanal. Nucl. Chem.* **1992**, 156, 323–340.
- [78] Patra, S.; Agarwal, C.; Chaudhury, S.; Newton Nathaniel, T.; Gathibandhe, M.; Goswami, A. *Appl. Radiat. Isot.* **2013**, 78, 139–144.
- [79] *International Commission on Radiological Protection. Radionuclide Transformations - Energy and Intensity of Emissions. ICRP Publication 38.*; 1983; Vol. 11-13.

-
- [80] Mishra, L.; Singh, I. S.; Anilkumar, S.; Rao, D. D. *Proceedings of the 7th DAE-BRNS biennial symposium on emerging trends in separation science and technology, SESTEC2016 held at IIT-Guwahati, India during May 17-20, 2016* **2016**,
- [81] Mishra, L.; Singh, I. S.; Patni, H. K.; Rao, D. D. *Radiat. Prot. Dosim.* **2018**, *181*, 168–177.
- [82] *International Commission on Radiological Protection. Occupational Intakes of Radionuclides: Part I. ICRP Publication 130.*; 2015; Vol. 44.
- [83] Newton, D.; Talbot, R. J.; Kang, C.; Warner, A. J. *Radiat. Prot. Dosim.* **1998**, *80*, 385–395.
- [84] Ham, G. J.; Harrison, J. D. *Radiat. Prot. Dosim.* **2000**, *87*, 267–272.
- [85] Luciani, A.; Polig, E. *Health Phys.* **2000**, *78*, 303–310.
- [86] Suslova, K. G.; Khokhryakov, V. F.; Tokarskaya, Z. B.; Nifatov, A. P.; Krahenbuhl, M. P.; Miller, S. C. *Health Phys.* **2002**, *82*, 432–444.
- [87] Singh, I. S.; Sharma, R. C.; Abani, M. C. *Radiat. Prot. Dosim.* **2003**, *105*, 361–364.
- [88] Leggett, R. W.; Eckerman, K. F.; Khokhryakov, V. F.; Suslova, K. G.; Krahenbuhl, M. P.; Miller, S. C. *Radiat. Res.* **2005**, *164*, 111–122.
- [89] Birchall, A.; Dorrian, M.-D.; Suslova, K. G.; Sokolova, A. B. *Radiat. Prot. Dosim.* **2016**,
- [90] Khalaf, M.; Brey, R. R.; Derryberry, D. *Health Phys.* **2013**, *104*, 57–62.
- [91] Kramer, G.; Bureau, R. P. **2006**,
- [92] Griffith, R. V.; Anderson, A. L.; Dean, P. N.; Fisher, J. C.; Sundbeck, C. W. *Tissue-equivalent torso phantom for calibration of transuranic-nuclide counting facilities.*; 1987; pp 293–314.

-
- [93] Newton, D.; Wells, A. C.; Mizushita, S.; Toohey, R. E.; Sha, J. Y.; Jones, R.; Jefferies, S. J.; Palmer, H. E.; Rieksts, G.; Anderson, A. L. *Assessment of radioactive contamination in man. Vienna: IAEA* **1985**, 183–199.
- [94] Nadar, M.; Akar, D.; Patni, H.; Singh, I.; Mishra, L.; Rao, D.; Pradeepkumar, K. *Radiat. Prot. Dosim.* **2014**, *162*, 469–477.
- [95] Sharma, R. C.; Surendran, T.; Haridasan, T. K.; Sunta, C. M. *Bull. Radiat. Prot.* **1989**, *12*, 41–56.
- [96] Castellani, C. M.; Marsh, J. W.; Hurtgen, C.; Blanchardon, E.; Bérard, P.; Giussani, A.; Lopez, M. A. **2013**, *EURADOS Re.*
- [97] *Intercomparison Exercise on Internal Dose Assessment, Final report of a joint IAEA–IDEAS project, IAEA-TECDOC-1568; 2007.*
- [98] Konzen, K. *Health Phys.* **2016**, *111*, 22–29.
- [99] Birchall, A.; James, A. C. *Health Phys.* **1989**, *56*, 857–868.
- [100] Singh, I. S.; Sharma, R. C.; Abani, M. C. *Radiat. Prot. Environ.* **2001**, *24*, 628–641.
- [101] Garg, S. P.; Singh, I. S.; Sharma, R. C.; Harikumar, M. *Radiat. Prot. Environ.* **2001**, *24*, 135–140.
- [102] Nadar, M.; Singh, I.; A., C.; Kantharia, S.; Bhati, S. *Proc. of NSRP-18* **2009**, 284–285.
- [103] Snyder, S. F.; Traub, R. J. *Health Phys.* **2010**, *98*, 459–465.
- [104] Mishra, L.; Singh, I. S.; Nadar, M.; Kalyane, G. N.; Rao, D. D. *Book of abstracts of DAE-BRNS fifth symposium on nuclear analytical chemistry, NAC-V held at BARC, Mumbai during January 20-24* **2014**, 160–161.

- [105] Mishra, L.; Singh, I. S.; Rao, D. D. *Proceedings of the 32nd IARP international conference, IARPIC2016 held at IGCAR, Tamilnadu, during February 22-25, 2016* **2016**, 95.
- [106] Lobaugh, M. L.; Spitz, H. B.; Glover, S. E. *Health Phys.* **2015**, *108*, 67–75.
- [107] Kathren, R. L.; Lynch, T. P.; Traub, R. J. *Health Phys.* **2003**, *84*, 576–581.
- [108] Birchall, A.; Jarvis, N. S.; Peace, M. S.; Riddell, A. E.; Battersby, W. P. *Radiat. Prot. Dosim.* **1998**, *79*, 107–110.
- [109] Mishra, L.; Sundararajan, M. *J. Chem. Sci.* **2019**, *131*, 15.
- [110] Crichton, R. R.; Charloteaux-Wauters, M. *Eur. J. Biochem.* **1987**, *164*, 485–506.
- [111] Cook, J. D.; Skikne, B. S.; Baynes, R. D. *Annu. Rev. Med.* **1993**, *44*, 63–74.
- [112] Sun, H.; Li, H.; Sadler, P. J. *Chem. Rev.* **1999**, *99*, 2817–2842.
- [113] Princiotto, J. V.; Zapolski, E. J. *Nature* **1975**, *255*, 87.
- [114] MacGillivray, R. T. A.; Moore, S. A.; Chen, J.; Anderson, B. F.; Baker, H.; Luo, Y.; Bewley, M.; Smith, C. A.; Murphy, M. E. P.; Wang, Y.; Mason, A. B.; Woodworth, R. C.; Brayer, G. D.; Baker, E. N. *Biochemistry* **1998**, *37*, 7919–7928.
- [115] Mason, A. B.; Halbrooks, P. J.; James, N. G.; Connolly, S. A.; Larouche, J. R.; Smith, V. C.; MacGillivray, R. T. A.; Chasteen, N. D. *Biochemistry* **2005**, *44*, 8013–8021.
- [116] Aisen, P.; Aasa, R.; Redfield, A. G. *J. Biol. Chem.* **1969**, *244*, 4628–4633.
- [117] Gaber, B. P.; Miskowski, V.; Spiro, T. G. *J. Am. Chem. Soc.* **1974**, *96*, 6868–6873.
- [118] Zak, O.; Aisen, P. *Biochemistry* **1988**, *27*, 1075–1080.
- [119] Tinoco, A. D.; Valentine, A. M. *J. Am. Chem. Soc.* **2005**, *127*, 11218–11219.

-
- [120] Kay, C. W. M.; Mkami, H.; Cammack, R.; Evans, R. W. *J. Am. Chem. Soc.* **2007**, *129*, 4868–4869.
- [121] Vidaud, C.; Gourion-Arsiquaud, S.; Rollin-Genetet, F.; Torne-Celer, C.; Plantevin, S.; Pible, O.; Berthomieu, C.; Quéméneur, E. *Biochemistry* **2007**, *46*, 2215–2226.
- [122] Benavides-Garcia, M. G.; Balasubramanian, K. *Chem. Res. Toxicol.* **2009**, *22*, 1613–1621.
- [123] Hémadi, M.; Ha-Duong, N.-T.; El Hage Chahine, J.-M. *J. Phys. Chem. B* **2011**, *115*, 4206–4215.
- [124] El Hage Chahine, J.-M.; Hémadi, M.; Ha-Duong, N.-T. *Biochim. Biophys. Acta, Gen. Subj.* **2012**, *1820*, 334–347.
- [125] Abergel, R. J.; Ansoborlo, E. *Nat. Chem.* **2016**, *8*, 516.
- [126] Sauge-Merle, S.; Lemaire, D.; Evans, R. W.; Berthomieu, C.; Aupiais, J. *Dalton Trans.* **2017**, *46*, 1389–1396.
- [127] Borisenko, G. G.; Kagan, V. E.; Hsia, C. J. C.; Schor, N. F. *Biochemistry* **2000**, *39*, 3392–3400.
- [128] Steere, A. N.; Miller, B. F.; Roberts, S. E.; Byrne, S. L.; Chasteen, N. D.; Smith, V. C.; MacGillivray, R. T. A.; Mason, A. B. *Biochemistry* **2012**, *51*, 686–694.
- [129] Rottman, G. A.; Doi, K.; Zak, O.; Aasa, R.; Aisen, P. *J. Am. Chem. Soc.* **1989**, *111*, 8613–8618.
- [130] Doctor, K. S.; Gaffney, B. J.; Alvarez, G.; Silverstone, H. J. *J. Phys. Chem.* **1993**, *97*, 3028–3033.
- [131] Seidel, A.; Bill, E.; Haggstrom, L.; Nordblad, P.; Kilar, F. *Arch. Biochem. Biophys.* **1994**, *308*, 52–63.

-
- [132] Gaffney, B. J. In *High Resolution EPR: Applications to Metalloenzymes and Metals in Medicine*; Berliner, L., Hanson, G., Eds.; Springer New York: New York, NY, 2009; pp 233–268.
- [133] Mathies, G.; Gast, P.; Chasteen, N. D.; Luck, A. N.; Mason, A. B.; Groenen, E. J. J. *J. Biol. Inorg. Chem.* **2015**, *20*, 487–496.
- [134] Spartalian, K.; Oosterhuis, W. T. *J. Chem. Phys.* **1973**, *59*, 617–622.
- [135] Tsang, C. P.; Boyle, A. J. F.; Morgan, E. H. *Biochim. Biophys. Acta, Protein Struct.* **1973**, *328*, 84–94.
- [136] Tsang, C. P.; Bogner, L.; Boyle, A. J. F. *J. Chem. Phys.* **1976**, *65*, 4584–4589.
- [137] Mujika, J. I.; Escribano, B.; Akhmatskaya, E.; Ugalde, J. M.; Lopez, X. *Biochemistry* **2012**, *51*, 7017–7027.
- [138] Rinaldo, D.; Field, M. J. *Aust. J. Chem.* **2004**, *57*, 1219–1222.
- [139] Rinaldo, D.; Field, M. J. *Biophys. J.* **2003**, *85*, 3485–3501.
- [140] Kumar, R.; Mauk, A. G. *J. Phys. Chem. B* **2012**, *116*, 3795–3807.
- [141] Aasa, R.; Aisen, P. *J. Biol. Chem.* **1968**, *243*, 2399–2404.
- [142] Zweier, J. L. *J. Biol. Chem.* **1978**, *253*, 7616–7621.
- [143] Eaton, S. S.; Dubach, J.; Eaton, G. R.; Thurman, G.; Ambruso, D. R. *J. Biol. Chem.* **1990**, *265*, 7138–7141.
- [144] Gaffney, B. J.; Eaton, G. R.; Eaton, S. S. *J. Phys. Chem. B* **1998**, *102*, 5536–5541.
- [145] Smith, C. A.; Anderson, B. F.; Baker, H. M.; Baker, E. N. *Biochemistry* **1992**, *31*, 4527–4533.

- [146] Periyasamy, G.; Sundararajan, M.; Hillier, I. H.; Burton, N. A.; McDouall, J. J. W. *Phys. Chem. Chem. Phys.* **2007**, *9*, 2498–2506.
- [147] Lancaster, K. M.; Zaballa, M.; Sproules, S.; Sundararajan, M.; DeBeer, S.; Richards, J. H.; Vila, A. J.; Neese, F.; Gray, H. B. *J. Am. Chem. Soc.* **2012**, *134*, 8241–8253.
- [148] Sundararajan, M.; Sinha, V.; Bandyopadhyay, T.; Ghosh, S. K. *J. Phys. Chem. A* **2012**, *116*, 4388–4395.
- [149] Sundararajan, M.; Neese, F. *Inorg. Chem.* **2015**,
- [150] Siegbahn, P. E. M.; Borowski, T. *Acc. Chem. Res.* **2006**, *39*, 729–738.
- [151] Siegbahn, P. E. M.; Blomberg, M. R. A. *Chem. Rev.* **2000**, *100*, 421–438.
- [152] Siegbahn, P. E. M.; Himo, F. *WIREs Comput. Mol. Sci.* **2011**, *1*, 323–336.
- [153] Perdew, J. P. *Phys. Rev. B* **1986**, *33*, 8822–8824.
- [154] Ahlrichs, R. et al. *TURBOMOLE V6.6, a development of University of Karlsruhe and Forschungszentrum Karlsruhe GmbH, TURBOMOLE GmbH, 2011; available from <http://www.turbomole.com>; 2011. Last accessed 4 March, 2016.*
- [155] Becke, A. D. *J. Chem. Phys.* **1993**, *98*, 5648–5652.
- [156] Neese, F. *Inorg. Chim. Acta* **2002**, *337*, 181–192.
- [157] Sinnecker, S.; Slep, L. D.; Bill, E.; Neese, F. *Inorg. Chem.* **2005**, *44*, 2245–2254.
- [158] Römelt, M.; Ye, S.; Neese, F. *Inorg. Chem.* **2009**, *48*, 784–785.
- [159] Froncisz, W.; Aisen, P. *Biochim. Biophys. Acta, Protein Struct. Mol. Enzymol.* **1982**, *700*, 55–58.
- [160] Sinnecker, S.; Neese, F. *J. Comput. Chem.* **2006**, *27*, 1463–1475.

-
- [161] Astashkin, A. V.; Neese, F.; Raitsimring, A. M.; Cooney, J. J. A.; Bultman, E.; Enemark, J. H. *J. Am. Chem. Soc.* **2005**, *127*, 16713–16722.
- [162] Cox, N.; Pantazis, D. A.; Neese, F.; Lubitz, W. *Acc. Chem. Res.* **2013**, *46*, 1588–1596.
- [163] Cox, N.; Retegan, M.; Neese, F.; Pantazis, D. A.; Boussac, A.; Lubitz, W. *Science* **2014**, *345*, 804.
- [164] Lohmiller, T.; Krewald, V.; Navarro, M. P.; Retegan, M.; Rapatskiy, L.; Nowaczyk, M. M.; Boussac, A.; Neese, F.; Lubitz, W.; Pantazis, D. A.; Cox, N. *Phys. Chem. Chem. Phys.* **2014**, *16*, 11877–11892.
- [165] Mishra, L.; Sawant, P. D.; Sundararajan, M.; Bandyopadhyay, T. *J. Phys. Chem. B* **2019**, *123*, 2729–2744.
- [166] Taylor, D. M. *J. Alloys Compd.* **1998**, *271*, 6–10.
- [167] Peter, E.; Lehmann, M. *Int. J. Radiat. Biol.* **1981**, *40*, 445–450.
- [168] Taylor, D.; Duffield, J.; Williams, D.; Yule, L.; Gaskin, P.; Unalkat, P. *Eur. J. Solid State Inorg. Chem.* **1991**, *28*, 271–274.
- [169] Tinoco, A. D.; Saxena, M.; Sharma, S.; Noinaj, N.; Delgado, Y.; Gonzalez, E. P. Q.; Conklin, S. E.; Zambrana, N.; Loza-Rosas, S. A.; Parks, T. B. *J. Am. Chem. Soc.* **2016**, *138*, 5659–5665.
- [170] Harris, W. R. *Biochim. Biophys. Acta, Gen. Subj.* **2012**, *1820*, 348–361.
- [171] Ghanbari, Z.; Housaindokht, M. R.; Bozorgmehr, M. R.; Izadyar, M. *J. Mol. Graph. Model.* **2017**, *78*, 176–186.
- [172] Justino, G. C.; Garribba, E.; Pessoa, J. C. *J. Biol. Inorg. Chem.* **2013**, *18*, 803–813.

- [173] Mujika, J. I.; Lopez, X.; Rezabal, E.; Castillo, R.; Marti, S.; Moliner, V.; Ugalde, J. M. *J. Inorg. Biochem.* **2011**, *105*, 1446–1456.
- [174] David, F. H.; Vokhmin, V. *New J. Chem.* **2003**, *27*, 1627–1632.
- [175] D'Angelo, P.; Martelli, F.; Spezia, R.; Filipponi, A.; Denecke, M. A. *Inorg. Chem.* **2013**, *52*, 10318–10324.
- [176] Best, S. P.; Forsyth, J. B. *Dalton Trans.* **1990**, 395–400.
- [177] Jarzecki, A. A.; Anbar, A. D.; Spiro, T. G. *J. Phys. Chem. A* **2004**, *108*, 2726–2732.
- [178] Marcus, Y. *J. Chem. Soc., Faraday Trans.* **1991**, *87*, 2995–2999.
- [179] Heinz, N.; Zhang, J.; Dolg, M. *J. Chem. Theory Comput.* **2014**, *10*, 5593–5598.
- [180] Atta-Fynn, R.; Bylaska, E. J.; Schenter, G. K.; de Jong, W. A. *J. Phys. Chem. A* **2011**, *115*, 4665–4677.
- [181] Li, Y.; Harris, W. R.; Maxwell, A.; MacGillivray, R. T.; Brown, T. *Biochemistry* **1998**, *37*, 14157–14166.
- [182] Anandakrishnan, R.; Aguilar, B.; Onufriev, A. V. *Nucleic Acids Res.* **2012**, *40*, W537–W541.
- [183] Dudev, T.; Lim, C. *Chem. Rev.* **2003**, *103*, 773–788.
- [184] Leontyev, I. V.; Stuchebrukhov, A. *J. Chem. Phys.* **2014**, *141*, 014103.
- [185] Leontyev, I. V.; Stuchebrukhov, A. *J. Chem. Theory Comput.* **2012**, *8*, 3207–3216.
- [186] Pathak, A. K.; Bandyopadhyay, T. *J. Phys. Chem. B* **2015**, *119*, 14460–14471.
- [187] Pathak, A. K.; Bandyopadhyay, T. *J. Phys. Chem. B* **2018**, *122*, 3876–3888.
- [188] Hess, B.; Kutzner, C.; van der Spoel D.; Lindahl, E. *J. Chem. Theory Comput.* **2008**, *4*, 435–447.

- [189] Lindorff-Larsen, K.; Piana, S.; Palmo, K.; Maragakis, P.; Klepeis, J. L.; Dror, R. O.; Shaw, D. E. *Proteins: Struct., Funct., Bioinf.* **2010**, *78*, 1950–1958.
- [190] Sousa da Silva, A. W.; Vranken, W. F. *BMC Research Notes* **2012**, *5*, 367.
- [191] Wang, J.; Wang, W.; Kollmann, P.; Case, D. *J. Comput. Chem.* **2005**, *25*, 1157–1174.
- [192] Wang, J.; Wang, W.; Kollman, P. A.; Case, D. A. *J. Mol. Graphics Modell.* **2006**, *25*, 247–260.
- [193] Gordon, M. S.; Schmidt, M. W. *Chapter 41 - Advances in electronic structure theory: GAMESS a decade later A2 - Dykstra, Clifford E*; 2005; pp 1167–1189.
- [194] Dupradeau, F.-Y.; Pigache, A.; Zaffran, T.; Savineau, C.; Lelong, R.; Grivel, N.; Lelong, D.; Rosanski, W.; Cieplak, P. *Phys. Chem. Chem. Phys.* **2010**, *12*, 7821–7839.
- [195] Li, P.; Song, L. F.; Merz, K. M. *J. Phys. Chem. B* **2015**, *119*, 883–895.
- [196] Jorgensen, W. L.; Chandrasekhar, J.; Madura, J. D.; Impey, R. W.; Klein, M. L. *J. Chem. Phys.* **1983**, *79*, 926–935.
- [197] Hess, B.; Bekker, H.; Berendsen Herman, J. C.; Fraaije Johannes, G. E. M. *J. Comput. Chem.* **1997**, *18*, 1463–1472.
- [198] Bussi, G.; Donadio, D.; Parrinello, M. *J. Chem. Phys.* **2007**, *126*, 014101.
- [199] Darden, T.; York, D.; Pedersen, L. *J. Chem. Phys.* **1993**, *98*, 10089–10092.
- [200] Essmann, U.; Perera, L.; Berkowitz, M. L.; Darden, T.; Lee, H.; Pedersen, L. G. *J. Chem. Phys.* **1995**, *103*, 8577–8593.
- [201] Bonomi, M.; Branduardi, D.; Bussi, G.; Camilloni, C.; Provasi, D.; Raiteri, P.; Donadio, D.; Marinelli, F.; Pietrucci, F.; Broglia, R. A.; Parrinello, M. *Comput. Phys. Commun.* **2009**, *180*, 1961–1972.

- [202] Barducci, M., A. and Bonomi; Parrinello, M. *Wiley Interdiscip. Rev. Comput. Mol. Sci.* **2011**, *1*, 826–843.
- [203] Miehllich, B.; Savin, A.; Stoll, H.; Preuss, H. *Chem. Phys. Lett.* **1989**, *157*, 200–206.
- [204] Sundararajan, M.; Neese, F. *J. Chem. Theory Comput.* **2012**, *8*, 563–574.
- [205] Sadhu, B.; Sundararajan, M.; Velmurugan, G.; Venuvanalingam, P. *Dalton Trans.* **2015**, *44*, 15450–15462.
- [206] Verma, P. K.; Pathak, P. N.; Kumari, N.; Sadhu, B.; Sundararajan, M.; Aswal, V. K.; Mohapatra, P. K. *J. Phys. Chem. B* **2014**, *118*, 14388–14396.
- [207] Verma, P. K.; Pathak, P. N.; Mohapatra, P. K.; Aswal, V. K.; Sadhu, B.; Sundararajan, M. *J. Phys. Chem. B* **2013**, *117*, 9821–9828.
- [208] Liao, R.-Z.; Siegbahn, P. E. M. *Chem. Sci.* **2015**, *6*, 2754–2764.
- [209] Dewan, J. C.; Mikami, B.; Hirose, M.; Sacchettini, J. C. *Biochemistry* **1993**, *32*, 11963–11968.
- [210] Spezia, R.; Jeanvoine, Y.; Beuchat, C.; Gagliardid, L.; Vuilleumier, R. *Phys. Chem. Chem. Phys.* **2014**, *16*, 5824–5832.
- [211] Pathak, A. K. *Mol. Phys.* **2015**, *113*, 3345–3352.
- [212] Pathak, A. K.; Samanta, A. K. *Mol. Phys.* **2017**, *115*, 2508–2514.
- [213] Pal, S. K.; Zewail, A. H. *Chem. Rev.* **2004**, *104*, 2099–2124.
- [214] Meyer, E. A.; Castellano, R. K.; Diederich, F. *Angew. Chem. Int. Ed.* **2003**, *42*, 1210–1250.
- [215] Tiwary, P.; Limongelli, V.; Salvalaglio, M.; Parrinello, M. *Proc. Natl. Acad. Sci. USA* **2015**, *112*, E386.

-
- [216] Pathak, A. K.; Bandyopadhyay, T. *Phys. Chem. Chem. Phys.* **2017**, *19*, 5560–5569.
- [217] Isom, D. G.; Cannon, B. R.; Castañeda, C. A.; Robinson, A.; García-Moreno E, B. *Proc. Natl. Acad. Sci. USA* **2008**, *105*, 17784.
- [218] Gao, J.; Bosco, D. A.; Powers, E. T.; Kelly, J. W. *Nat. Struct. Mol. Biol.* **2009**, *16*, 684.
- [219] Sinha, V.; Ganguly, B.; Bandyopadhyay, T. *PLoS One* **2012**, *7*, e40188.
- [220] Schmidtke, P.; Luque, F. J.; Murray, J. B.; Barril, X. *J. Am. Chem. Soc.* **2011**, *133*, 18903–18910.
- [221] Lemkul, J. A.; Bevan, D. R. *J. Phys. Chem. B* **2010**, *114*, 1652–1660.
- [222] Zhang, Y.; Voth, G. A. *J. Chem. Theory Comput.* **2011**, *7*, 2277–2283.
- [223] Cowan, G. A. *Sci. Amer.* **1976**, *235*, 36–47.
- [224] Sutcliffe, W. G.; Condit, R. H.; Mansfield, W. G.; Myers, D. S.; Layton, D. W.; Murphy, P. W. *A Perspective on the Dangers of Plutonium*; Lawrence Livermore National Laboratory: Livermore, CA, 1995.
- [225] Jensen, M. P.; Gorman-Lewis, D.; Aryal, B.; Paunesku, T.; Vogt, S.; Rickert, P. G.; Seifert, S.; Lai, B.; Woloschak, G. E.; Soderholm, L. *Nat. Chem. Biol.* **2011**, *7*, 560–565.
- [226] Mishra, L.; Bandyopadhyay, T. (*submitted*). **2019**,
- [227] Lehmann, M.; Culig, H.; Taylor, D. M. *Int. J. Radiat. Biol. Relat. Stud. Phys. Chem. Med.* **1983**, *44*, 65–74.
- [228] Duffield, J. R.; Taylor, D. M.; Proctor, S. A. *Int. J. Nucl. Med. Biol.* **1986**, *12*, 483–7.
- [229] Barducci, A.; Bonomi, M.; Parrinello, M. *WIREs Comput. Mol. Sci.* **2011**, *1*, 826–843.

- [230] Morris, G. M.; Huey, R.; Lindstrom, W.; Sanner, M. F.; Belew, R. K.; Goodsell, D. S.; Olson, A. J. *J. Comput. Chem.* **2009**, *30*, 2785–2791.
- [231] Abergel, R. J.; Raymond, K. N. *Inorg. Chem.* **2006**, *45*, 3622–3631.
- [232] Volf, V. *Int. J. Radiat. Biol. Relat. Stud. Phys. Chem. Med.* **1985**, *49*, 449–462.
- [233] Xu, J.; Durbin, P. W.; Kullgren, B.; Ebbe, S. N.; Uhlir, L. C.; Raymond, K. N. *J. Med. Chem.* **2002**, *45*, 3963–3971.
- [234] W Durbin, P.; Kullgren, B.; Xu, J.; N Raymond, K. *Multidentate hydroxypyridinonate ligands for Pu(IV) chelation in vivo: Comparative efficacy and toxicity in mouse of ligands containing 1,2-HOPO or Me-3,2-HOPO*; 2000; Vol. 76; pp 199–214.
- [235] Guilmette, R. A.; Hakimi, R.; Durbin, P. W.; Xu, J.; Raymond, K. N. *Radiat. Prot. Dosim.* **2003**, *105*, 527–34.
- [236] Santos, M. A.; Chaves, S. *Future Med. Chem.* **2015**, *7*, 383–410.
- [237] Durbin, P. W.; White, D. L.; Jeung, N.; Weitzel, F. L.; Uhlir, L. C.; Jones, E. S.; Bruenger, F. W.; Raymond, K. N. *Health Phys.* **1989**, *56*.
- [238] Turcot, I.; Stintzi, A.; Xu, J.; Raymond, K. N. *J. Biol. Inorg. Chem.* **2000**, *5*, 634–641.
- [239] Stradling, G. N.; Stather, J. W.; Gray, S. A.; Moody, J. C.; Ellender, M.; Hodgson, A. *Exp. Pathol.* **1989**, *37*, 83–88.
- [240] Stradling, G. N.; Stather, J. W.; Gray, S. A.; Moody, J. C.; Ellender, M.; Hodgson, A. *Hum. Toxicol.* **1986**, *5*, 77–84.
- [241] Captain, I.; Deblonde, G. J.-P.; Rupert, P. B.; An, D. D.; Illy, M.-C.; Rostan, E.; Ralston, C. Y.; Strong, R. K.; Abergel, R. J. *Inorg. Chem.* **2016**, *55*, 11930–11936.

- [242] Allred, B. E.; Rupert, P. B.; Gauny, S. S.; An, D. D.; Ralston, C. Y.; Sturzbecher-Hoehne, M.; Strong, R. K.; Abergel, R. J. *Proc Natl Acad Sci USA* **2015**, *112*, 10342.